

**NASA CONTRACTOR
REPORT**



NASA CR-135096

R-0 7/77
9-15-77
11-15-77
2/78
5-78
6-78
8-78

NASA CR-135096

(NASA-CR-135096) ADDITIONAL STUDIES OF
EXTERNALLY BLOWN FLAP NOISE (United
Technologies Research Center) 174 p

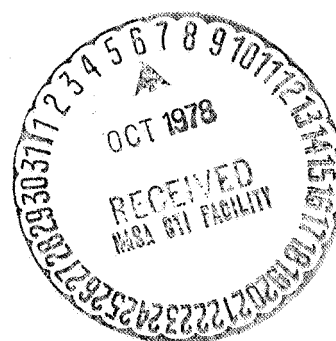
N78-78753

00/71 Unclass
32834

**ADDITIONAL STUDIES OF EXTERNALLY
BLOWN FLAP NOISE**

By Martin R. Fink

Prepared by
UNITED TECHNOLOGIES RESEARCH CENTER
East Hartford, CT. 06108
for Lewis Research Center



NATIONAL AERONAUTICS AND SPACE ADMINISTRATION, WASHINGTON, D.C. AUGUST 1976

CONTENTS

	<u>Page</u>
SUMMARY.	1
SYMBOLS.	2
INTRODUCTION	3
CROSSCORRELATION STUDY OF EBF NOISE MECHANISMS	4
Apparatus and Procedure	4
Nozzle and Airfoil Model	4
Acoustic Instrumentation	5
Crosscorrelations	6
General Discussion	6
Under-the-Wing, 9° Deflection.	8
Upper-Surface-Blowing, 9° Deflection	10
Under-the-Wing, 30° Deflection	12
FORWARD FLIGHT EFFECTS ON EBF NOISE.	14
Method of Approach.	14
Apparatus and Procedure	14
Test Apparatus	14
Calibration of Test Installation	16
Test Conditions.	17
Evaluation of Forward Flight Effects.	18
Expected Effects of Forward Flight	18
Effects on Flow Field.	19
Acoustic Results for Short-Chord Airfoil	21
Acoustic Results for Long-Chord Airfoil.	26
Prediction of Forward Flight Effects.	28
Method for Calculating Forward Flight Effects.	28
Comparison With Available Data	30
COMPARISONS OF MEASURED AND PREDICTED EBF NOISE FOR LARGE-SCALE MODELS	33
Discussion of Large-Scale Test Configurations	33
Spectrum Correlations for Ground Reflection	34
EBF Noise Prediction Methods.	36
ANOPP Method	36
GELAC Method	37

	<u>Page</u>
Noise Component Method	37
Under-the-Wing Mixer Nozzle	39
Under-the-Wing Three-Flap Model	42
Upper Surface Blowing	47
Noise Radiation Patterns	47
Spectra in Flyover Plane	49
PAPERS GENERATED DURING CONTRACT YEAR.	51
CONCLUSIONS.	52
REFERENCES	53
FIGURES 1 Through 74	57

ADDITIONAL STUDIES OF EXTERNALLY BLOWN FLAP NOISE

Martin R. Fink
United Technologies Research Center
East Hartford, Connecticut

SUMMARY

Crosscorrelations were obtained among surface pressures on both sides of externally blown flap models and far-field acoustic pressures. Tests were conducted with both under-the-wing and upper-surface-blowing configurations. For both types of configurations at small deflection, the crosscorrelations showed that convection of jet exhaust turbulence to the trailing edge produces sound waves of opposite phase above and below the flap. These waves travel forward along the airfoil and outward to the far field. For under-the-wing at larger flap deflection, dipole sound is generated by convection of turbulence past the forward part of the flap. This sound propagates downstream along the flap upper surface, with opposite phase to the sound waves moving below the flap toward the far field. These results slightly modify the concept of trailing-edge and lift-fluctuation surface radiation processes.

Forward flight effects on externally blown flap noise were evaluated at ratios of wind tunnel velocity to exhaust jet velocity from 0 to $1/2$ in increments of $1/8$. Profiles of mean velocity and turbulence level were obtained along with surface pressure spectra and far-field acoustic spectra. The surface-radiated portion of far-field noise spectra was found to be predicted from spectra measured at zero tunnel speed by decreasing the amplitude and increasing the frequency. The resulting predictions of forward speed effects on externally blown flap spectra and overall sound pressure levels agree with available data.

Free-field directivity and spectra of large externally blown flap configurations were compared with predictions by the noise component method previously developed under this contract and with predictions by other methods. Good agreement was obtained with the noise component method for a mixer nozzle and two-flap under-the-wing configuration, a turbofan engine and three-flap under-the-wing configuration, and a turbofan engine with an upper-surface-blowing canted nozzle and short flap. All methods underpredicted the noise measured with an upper-surface-blowing circular nozzle, deflector, and long flap.

SYMBOLS

a	Speed of sound, m/sec
c	Airfoil chord, m
f	Frequency, Hz
H	Ratio of airfoil half-chord to acoustic wavelength
R	Far field distance, m
t_a	Time for an acoustic wave to travel from the trailing edge to an airfoil surface position, sec
t_c	Time for a turbulent eddy to be convected from an airfoil surface position to the trailing edge, sec
t_{ff}	Time for an acoustic wave to travel from the airfoil to the far field, sec
u'	Root mean square fluctuation of velocity in mean flow direction, m/sec
U	Exhaust jet velocity, m/sec
V	Local mean velocity, m/sec
V_i	Impingement velocity, m/sec
V_{ia}	Impingement velocity at zero flight speed, m/sec
V_J	Exhaust jet velocity, m/sec
V_O	Wind tunnel velocity, m/sec
x	Chordwise distance from leading edge, m
δ	Exhaust jet deflection angle, deg
θ	Azimuthal angle from upstream direction in flyover plane, deg
ϕ	Measurement direction angle relative to sideline plane, deg

INTRODUCTION

For the past three years, an analytical and experimental study of turbo-machinery strut noise and externally blown flap noise has been conducted for NASA Lewis Research Center. The basic approach of this study is that noise from such configurations can be represented by a sum of noise generated by several simple aeroacoustic mechanisms. Investigations of these individual noise components for externally blown flap (EBF) configurations, conducted under this contract, were reported in references 1-4. Other EBF noise component methods have been developed by McKinzey (reference 5) and Reddy, et al (reference 6). Those studies gave strong but not conclusive indication of the EBF noise components. A semi-empirical prediction method based on those components was shown in reference 3 to give good to fair prediction of acoustic data for fourteen small under-the-wing and upper surface blowing models tested by NASA Lewis Research Center at zero flight speed. After a description of the major EBF noise components was obtained, additional cross-correlation measurements could be formulated to examine these assumed processes.

Two deficiencies of the EBF noise prediction method given in reference 3 were the absence of an experimentally justified procedure for calculating the effect of flight speed and the lack of comparisons with acoustic data for large-scale models. The investigation described herein therefore comprises (1) crosscorrelation studies of both under-the-wing and upper-surface-blowing EBF noise mechanisms, (2) experimental studies of forward flight effects on local flow properties and noise radiation from simple EBF models, and formulation of a method for calculating forward flight effects on EBF noise, and (3) comparison of measured and predicted EBF noise for nominal half-scale and full-scale configurations at zero flight speed. The obvious next step, a comparison of measured and predicted EBF noise for full-scale configurations over a range of flight speed, could not be done because such tests have not been conducted.

Task VIII of the subject Contract NAS3-17863 comprised the portion of this report entitled "CROSSCORRELATION STUDY OF EBF NOISE MECHANISMS". Tasks IX and X, tests of forward flight effects on short-chord and long-chord models, are both described in the sections entitled "Method of Approach", "Apparatus and Procedure" and "Evaluation of Forward Flight Effects" within "FORWARD FLIGHT EFFECTS ON EBF NOISE". Task XI is reported in the section entitled "Prediction of Forward Flight Effects" within "FORWARD FLIGHT EFFECTS ON EBF NOISE". The results of Task XII are given in the portion of this report entitled "COMPARISONS OF MEASURED AND PREDICTED EBF NOISE FOR LARGE-SCALE MODELS".

CROSSCORRELATION STUDY OF EBF NOISE MECHANISMS

Apparatus and Procedure

Nozzle and Airfoil Model

Clean dry air for jet exhaust tests was obtained from a large air storage system at $2.7 \times 10^3 \text{ kN/m}^2$ (400 lb/in.²) nominal supply pressure. This air passed through flow control valves, flow straighteners, noise mufflers, and a straight pipe. The straight pipe downstream of the mufflers was approximately 2.9 m (9.5 ft) long and had an 0.15 m (6 in.) inside diameter. It ended at a fitting that provided smooth transition to an 0.049 m (1.925 in.) exit diameter axisymmetric nozzle contoured to give uniform exit flow. The pipe passed into an anechoic chamber and was aimed at a door in this chamber. This door was opened to allow undisturbed exit of the jet. The nozzle centerline was 1.07 m (42 in.) above the tips of the floor anechoic wedges. Jet noise data obtained with the nozzle and test arrangement have been shown (reference 1) to agree with predictions by standard methods.

Exhaust velocity was defined as that for isentropic expansion from the stagnation pressure and temperature measured near the start of the straight pipe to a static pressure equal to ambient pressure in the chamber. Stagnation temperatures for these tests generally ranged from about 4 C to 10 C (40 F to 50 F) as did the static temperature within the anechoic chamber. Velocity was set by maintaining the difference between stagnation pressure and atmospheric static pressure at predetermined values within about 2.5 mm (0.1 in.) of water at pressure differences less than about 16 kN/m² (70 in. of water) and about 2.5 mm (0.1 in.) of mercury at larger pressure differences. Exhaust velocities of 125 and 250 m/sec (410 and 820 ft/sec) were used in this test program.

Externally blown flaps were simulated by installing a single unslotted airfoil slightly downstream of the jet exhaust nozzle. This airfoil model is shown in figure 1. It has 23 cm (9 in.) chord, 53 cm (21 in.) span, and an NACA 0018 airfoil section. Sliders at 30% and 70% chord within the model could be moved manually within keyhole-shaped slots that extend to the airfoil surface. A 0.635 cm (1/4 in.) flush-mounted microphone with its right-angle adaptor and preamplifier could be contained within each slider and traversed along the airfoil span. Four fixed flush-mounted microphones were installed in a chordwise row at one-third span and 20, 38, 62, and 80% chord. (The number of active microphones was limited by space available for cables and preamplifiers.) The exhaust nozzle centerline was at the spanwise position of the fixed microphones. The two slider microphone positions were not used in this phase of the tests. Small pressure-sensitive semiconductor integrated circuit pressure transducers having an 0.22 cm (0.085 in.) active diameter were installed on the opposite surface from the fixed microphones at the same

four chordwise locations. Each gage was mounted in a recessed steel baseplate 0.635 cm (0.25 in.) wide, 1.40 cm (0.55 in.) long, and 0.99 cm (0.035 in.) deep. These baseplates were cemented into slots in the airfoil surface, with the gage active surface flush with the surface. Wires from each gage were led through holes in the airfoil and were brought out the end of the airfoil alongside the microphone cables. The steel baseplates could be pried away from the cement without damages to the gage.

The airfoil was mounted between circular endplates and could be rotated about 30% chord within a support stand. For tests representing an under-the-wing externally blown flap, the leading edge at zero deflection was 2.5 cm (1.0 in.) beneath and 2.5 cm (1.0 in.) downstream of the lip of a 4.9 cm (1.925 in.) diameter convergent nozzle. Airfoil position relative to the nozzle is sketched in figure 2 for 9° and 30° deflection. At 9° the scrubbed surface was in line with the nozzle lip where pressure fluctuations would be largest. The larger angle placed the airfoil trailing edge in line with the nozzle opposite lip. For tests that represented an over-the-wing (upper surface blowing) externally blown flap, the leading edge at zero deflection was 2.5 cm (1.0 in.) above and 2.5 cm (1.0 in.) downstream of the nozzle lip. Airfoil position relative to the nozzle for this installation is sketched in figure 2 for 9° deflection angle. Because the airfoil leading edge moved into the jet as deflection angle was increased, the jet became split between the airfoil surfaces at larger deflection angles and did not properly simulate an upper surface blowing installation. Data were not taken at those larger angles.

Acoustic Instrumentation

Far-field noise spectra, and surface pressure spectra on the airfoil surface opposite from the nozzle, were measured with commercially available 0.635 cm (1/4 in.) condenser microphones. Frequency response of these microphones to pressure fluctuations is flat from 6 Hz to 20,000 Hz. Free-field directivity corrections at grazing (90°) incidence are less than 0.2 dB at frequencies to 16,000 Hz and about 0.5 dB at 20,000 Hz without the protecting grid. Far-field microphones were oriented at grazing incidence and used without the protecting grid. To permit flush mounting the microphones in the airfoil models as sketched in figure 1, right-angle adaptors were used. Each microphone and adaptor was clamped in a bracket that was attached to the airfoil by set screws. These set screws were adjusted to optically aline the microphone diaphragm with the airfoil surface.

Atmospheric attenuation of the far-field acoustic data was calculated as about 0.1 dB at 10 kHz and 0.4 dB at 20 kHz. Because this correction is approximately equal and opposite to that for free-field directivity of the microphones, no corrections were applied to the measured spectra.

Far-field sound pressure levels and surface pressure fluctuation levels, cited herein as SPL and surface SPL, respectively, were measured in decibels

referenced to 2×10^{-5} newtons per square meter (2×10^{-4} microbar). All microphones were calibrated daily with a 250 Hz pistonphone.

Far-field microphones were located at three positions on an arc of 2.14 m (7 ft) radius in a vertical plane through the jet nozzle centerline. The microphones were at 60° , 90° , and 120° angular position relative to the nozzle centerline. The microphone arc was centered at the middle of the nozzle exit plane.

Crosscorrelations

General Discussion

Crosscorrelation of acoustic signals can provide several kinds of information about the relationships between surface and far field acoustic pressures. Normalized peak amplitude of a crosscorrelation will show whether the two measured quantities were associated with the same noise mechanism. Use of only the peak amplitude, without regard to delay time or crosscorrelation signal shape, has a major disadvantage. It cannot distinguish between pressures that are related because one signal is in an acoustic source region and the other in an acoustic radiation field, or pressures which are related because both signals include an acoustic field radiated from some other location.

As shown by Siddon (reference 7), surface-radiated noise source strength can be determined from the crosscorrelation slope at a particular delay time. Crosscorrelation slope cannot be measured accurately, for the near full scale exhaust velocities and small model sizes used in EBF tests, unless long data sampling times appropriate to short time intervals are used. The surface distribution of dipole strength, and therefore the location of noise sources, can be measured if a sufficiently large number of surface transducer locations are available. Unfortunately, it may be impractical to install sufficient transducers to measure the dipole source locations when several noise mechanisms occur simultaneously.

This approach can be generalized by recognizing that maximum dipole source strength is associated (reference 7) with maximum slope of the crosscorrelation. The sign of this slope depends on the expected phase between the surface and far-field positions. Thus the delay time at which maximum slope occurs can be plotted against streamwise distance. The extrapolated or interpolated position which gives a delay time equal to the far field acoustic propagation time then is the source location. Also, the shape of the crosscorrelation curve can often indicate whether one signal is part of the dipole noise-radiating surface that produced the sound measured by the other signal, or whether both signals are sound waves radiated from a source located elsewhere.

Some of these features are shown in figure 3. The test configuration, sketched in the upper part of the figure, has an exhaust jet scrubbing an airfoil lower surface. Acoustic pressures are measured by transducers at the same chordwise position on both the upper and lower surface and in the far field below the airfoil. Three important times are defined by this geometry. The eddy convection time t_c is the time required for a turbulent eddy to be convected within the attached exhaust jet from the transducer to the trailing edge. The surface acoustic time t_a is the time for an acoustic wave to travel from the trailing edge to the upper-surface transducer. The far-field acoustic time t_{ff} is the time required for a sound wave to travel from any point on the airfoil to the far field microphone. It is assumed that the far-field microphone is on a line approximately perpendicular to the airfoil chord and at a large distance relative to the chord, so t_{ff} is independent of transducer chordwise position.

Crosscorrelations between each of the two surface pressures and the far-field acoustic pressure are sketched for two possible noise mechanisms. The center part of the figure shows the signals expected for noise caused by fluctuations of airfoil lift. The lift force response of the airfoil to the exhaust jet turbulence then is assumed to resemble that for an airfoil immersed in a turbulent airstream. Each signal has the antisymmetric shape expected (references 7 and 8) for dipole noise. The crosscorrelation from the lower surface to the far field has a positive peak followed by a negative peak. Crosscorrelation from the upper surface to the far field has a negative peak followed by a positive peak. Both signals cross at zero amplitude and maximum absolute value of the slope. This crossing occurs when the surface signal is delayed by the far-field acoustic time t_{ff} relative to the far-field signal. Such behavior occurs because the pressure fluctuations on both the upper and lower surface are directly proportional in magnitude, but opposite in sign, to the lift force fluctuation which causes the noise.

The lower part of figure 3 shows crosscorrelations for trailing edge noise that is generated by exhaust-jet turbulence convected past the trailing edge. If a pressure transducer could be installed on the airfoil lower surface very near the trailing edge, its cross correlation with the far field would be identical to that shown above for fluctuating lift noise. For a more practical location upstream of the trailing edge, the transducer would sense the turbulence pressure field at a time t_c before each turbulent eddy reaches the trailing edge and generates noise. The crosscorrelation between the airfoil lower surface and the far field then has a positive peak followed by a negative peak; it crosses through zero at a delay time $t_{ff} + t_c$, the sum of the far-field acoustic time and the eddy convection time.

The resulting trailing edge noise is radiated above and below the airfoil with opposite phase. Sound waves which originated at the trailing edge at the same time would reach the upper-surface transducer after traveling for the

surface acoustic time t_a and would reach the far-field microphone after the far-field acoustic time t_{ff} . The crosscorrelation of those two signals, shown as a dotted line in the lower part of figure 3, has a negative peak (opposite phase) at a delay time $t_{ff} - t_a$. If the trailing edge noise was caused by turbulence convected along the wing upper surface as with an upper-surface-blowing externally blown flap, each signal would be that shown for the opposite surface but reversed in sign. That is, the crosscorrelation from upper surface to far field would have a negative peak followed by a positive peak, bracketing a zero crossing at time $t_{ff} + t_c$. The crosscorrelation from lower surface to far field would have a positive peak at time $t_{ff} - t_a$.

No matter which side the exhaust jet is located, crosscorrelations between the upper and lower surface at the same chordwise position should show trailing edge noise as a negative peak followed by a positive peak, with the zero crossing at delay time $t_c + t_a$.

Under-the-Wing, 9° Deflection

This configuration was taken as a reasonable starting point because its noise processes are fairly simple. Overall sound pressure levels were expected to be dominated by trailing edge noise. Crosscorrelations of pressure signals measured at the same chordwise position on the airfoil upper and lower surfaces are given in figure 4. The crosscorrelator traces for 125 and 250 m/sec exhaust velocity and 62% chord, shown in figure 4(a), are typical of those for the three forward positions. Crosscorrelations had near zero amplitude at zero delay time, and changing the velocity changed the sign of the slope. Therefore the surface pressures were not dominated by a lift-fluctuation type of loading. These crosscorrelations had an approximately antisymmetric shape, with a negative peak at small delay time of the lower-surface signal followed by a positive peak at larger times. The positive delay time, and positive slope at zero amplitude, correspond to production of an upper-surface acoustic pressure by a lower-surface turbulence pressure. Doubling the exhaust velocity reduced the zero-amplitude delay time by less than half. These delay times are given by the sum of the eddy convection time t_c and the surface acoustic time t_a defined in the upper part of figure 3.

Crosscorrelations at 80% chord, shown in figure 4(b), had an approximately symmetric shape dominated by a positive peak at positive delay time. It is probable that the important feature of these traces is the positive slope and zero amplitude at small positive delay time. Alternate features such as the positive peak at larger time (related pressure signals of the same sign on both the upper and lower surface) and the negative peak at zero delay time (lift fluctuation caused by convection turbulence) at one but not both velocities are not consistent with the trailing edge noise process.

Maximum values of normalized crosscorrelation coefficient are plotted in figure 5. This quantity is the maximum absolute value of the crosscorrelation signal, divided by the square root of the product of the two autocorrelations evaluated at zero delay time. It can vary between zero and one. The test configuration, showing microphones located in the far field and at the same chordwise distance on both the upper and lower surface, is sketched in figure 5(a). As shown in figure 5(b), normalized crosscorrelation between the airfoil upper and lower surfaces decays with distance from the trailing edge and decreases with increasing exhaust velocity. The solid curves were calculated as an exponential decay for which the argument of the exponential varies directly with distance from the trailing edge and inversely with velocity, $\exp(-K(1-x/c)/U_J)$. These curves approximately match the data. Measured normalized crosscorrelation coefficients between the far field and the airfoil lower surface, given in figure 5(c), are also matched by the same solid-line exponential decay. Crosscorrelation coefficients between the far field and the airfoil upper surface are given in figure 5(d). These coefficients decayed slowly as distance from the trailing edge to the upper-surface pressure transducer was increased, until the leading edge was approached. Such results would occur if both the far-field acoustic pressures and the upper-surface near-field pressures were generated by turbulence occurring near the airfoil lower-surface trailing edge.

Delay times at which significant events occurred in crosscorrelations between the far field and airfoil surfaces are plotted in figure 6. Times at which zero amplitude and large negative slope occurred in the crosscorrelations between the lower surface and far field are given in figure 6(a). This feature of a crosscorrelation corresponds to acoustic radiation from a surface directly facing the far field. Delay times for measurements at the four chordwise positions and two exhaust velocities were given by the sum of the eddy convection time and the far-field acoustic time. That is, surface pressure disturbances were convected to the neighborhood of the airfoil trailing edge and then caused noise radiation.

It was not obvious what event should be taken as significant for crosscorrelations between the upper surface and far field. Times for both peak positive and peak negative amplitude are shown in figure 6(b). The time for positive peaks was approximately given by the sum of far-field acoustic time and the time required for an acoustic wave to travel from the leading edge to the surface position. No acoustic process was envisioned that would cause that time delay for acoustic waves having the same sign on both the airfoil upper surface and the far field beneath the lower surface. Zero amplitude and positive slope, which corresponds to dipole noise radiation, would occur roughly midway between the two peaks at approximately the far-field acoustic time. However, these times clearly increased at a slope corresponding to chordwise travel of an acoustic wave. The interpretation consistent with all of the other data is that the delay times at peak negative amplitude are

given by the far-field acoustic time minus the time for a sound wave to travel upstream from the trailing edge. These times were approximately independent of exhaust velocity. They correspond to trailing edge noise, which has opposite sign (negative crosscorrelation amplitude) above and below the airfoil. Therefore, all features of the crosscorrelations for a small-deflection under-the-wing configuration show that overall noise was dominated by trailing edge noise.

Upper-Surface-Blowing, 9° Deflection

Crosscorrelations among surface pressures measured at 80% chord on both the upper and lower surface, and far field acoustic pressure, are given in figure 7 for the upper-surface-blowing configuration. The test configuration is sketched in the upper right portion of the figure. Crosscorrelations between the lower surface and far field are shown in figure 7(a) for 125 and 250 m/sec exhaust velocities. These approximately symmetric peaks represent noise having the same phase and reaching the far field after it reached the airfoil lower surface.

Crosscorrelations between the upper surface and far field, given in figure 7(b), clearly have an antisymmetric shape. Zero amplitude and maximum positive slope occurred at a slightly larger time for 125 m/sec than for 250 m/sec velocity. This shape can be recognized as that for turbulence convected along the upper surface and causing downward-radiated noise of opposite sign when it reaches the trailing edge. The crosscorrelation between upper and lower surfaces, given in figure 7(c), is antisymmetrical. Delay time at zero amplitude and maximum positive slope were small and were approximately halved by doubling the exhaust velocity. This result is consistent with trailing edge noise caused by upper-surface flow.

Crosscorrelations between the airfoil lower surface and far field are shown in figure 8 for all chordwise locations and both velocities. These shapes could not be easily categorized as either symmetric or antisymmetric. Peak positive amplitude occurred at a delay time that increased as chordwise distance from the leading edge increased. These times were less than the far field acoustic travel time. Delay times for zero amplitude and large negative slope increased above this travel time. Crosscorrelations between the far-field and the upper-surface microphones at 38% and 62% chord were erratic due to intermittent electrical faults in those surface pressure transducers. The semiconductor diaphragms apparently were damaged by small particles within the exhaust jet. Crosscorrelations between the far field and the two intact upper surface microphones were antisymmetric with positive slope at zero amplitude, as expected for far-field noise caused by turbulence near a surface.

Delay times at which two possible significant events occurred in cross-correlations between the far field and USB surfaces are shown in figure 9. Because some crosscorrelations resembled both an antisymmetric dipole source and a symmetric acoustic-wave pattern, delay times for both types of event are shown. Delay times at zero amplitude and large slope (positive slope for the upper surface and negative slope for the lower) are given in the upper part of this figure. These times were approximately the same for both 125 and 250 m/sec flow velocities. They increased with increasing distance downstream from the leading edge. At each chordwise position and for both the upper and lower surface, these delay times were given by the sum of the time for an acoustic wave to travel from the surface microphone to the leading edge and the far field travel time. This would represent a situation in which a loading fluctuation at each position along the airfoil caused a change of loading near the leading edge. The signal to produce this change would have traveled upstream at the speed of sound, and the loading fluctuation near the leading edge would have caused the far-field noise. Alternately, delay times for zero crossings measured at the two forward microphones would be consistent with noise radiation caused by lift force fluctuations at each position. The longer delay times measured at the two aft microphones then would not be explained.

Delay times at peak positive amplitude for the lower surface are shown in the lower part of this figure. These times also have a slope which corresponds to forward propagation of sound waves along the airfoil lower surface. They can be interpreted as representing the generation of noise at or ahead of the trailing edge, followed by travel of those waves along the wing lower surface and to the far field.

Normalized crosscorrelation coefficients for these tests are presented in figure 10. The crosscorrelation between the far field and lower surface, given in figure 10(c), approximately follows the exponential decay curves previously shown in figure 5(c) for UTW. The large values near the trailing edge, and rapid decrease with upstream distance, is consistent with the viewpoint that USB far-field noise is dominated by trailing edge noise. Limited correlations between the upper surface and either the lower surface (figure 10(b)) or the far field (figure 10(d)) were smaller than those shown in figure 5 for UTW. The small magnitude of the crosscorrelation between the far field and the forward position on the airfoil surface, shown in figure 10(d), contradicts the possible interpretation of delay times as representing changes of loading near the leading edge which then cause noise radiation.

These measurements unfortunately have done little to define precisely the basic mechanism of USB noise. This noise clearly is shown to be generated near the trailing edge, but measured USB directivity is found to be relatively uniform as compared with the rapid aft decay expected for edge noise. Perhaps the reason is that directivity for trailing edge noise from a finite-chord flat plate differs from that for a semi-infinite plate. A solution for this

finite-chord problem was developed by Tam and Yu in reference 9. Sound waves traveling forward along the plane chord are diffracted around the leading edge, causing phase cancellations. Calculated solutions for directivity of mean square acoustic pressure were plotted in figures 13 and 14 of reference 9 for ratios H of plate half-chord to acoustic wavelength equal to 5 and 10. These curves, matched in amplitude at 90° direction angle, are plotted as solid lines in figure 11. Phase cancellations and reinforcements cause multi-lobed patterns. The envelope of the peaks, and a mean value through the peaks and valleys, is reasonably close to the asymptotic shape for infinite H (semi-infinite plate). Presumably, the peaks and valleys would average out for the range of frequencies within a $1/3$ octave band. Calculated directivity was shown to approach that of a lift dipole as the ratio H approached zero. Peak amplitude of an USB noise spectrum may occur at a frequency which corresponds to a low enough value of H such that neither the directivity function for a compact-source semi-infinite plate (H approaching infinity) nor that for a compact-source lift dipole (H approaching zero) is valid.

Under-the-Wing, 30° Deflection

The major problem in analyzing crosscorrelations for under-the-wing models at large deflections is that several noise processes combine to cause a complicated variation with time. Data taken at large exhaust velocities also have the disadvantage that the crosscorrelator output oscillates at a relatively high frequency, causing the signal to consist of closely spaced jagged peaks. A further complication was caused by damage to the surface pressure transducers at 38% and 62% chord on the lower surface. Signals from these locations in the impingement region became progressively erratic during the test program, and generally had to be discarded.

Crosscorrelations between surface pressures at the same positions on the upper and lower surface are shown in figure 12. Sample crosscorrelation traces at 125 m/sec velocity are given in figure 12(a). The measurement for 15% chord was a symmetric peak having maximum negative amplitude at zero delay time. Pressure fluctuations on opposite sides of the airfoil had opposite sign at each instant of time. This is what would be expected if fluctuations of lift force were induced by the exhaust jet. In contrast, the measurement for 38% chord had a very small negative peak at zero delay time and an antisymmetric shape at larger times. This signal corresponds to a small fluctuation of loading and a larger acoustic pressure fluctuation generated on the upper surface by pressures convected along the lower surface. This same pattern occurred at 62% and 80% chord, with the delay times decreasing as distance from the trailing edge was decreased. The times at which zero magnitude and positive slope occurred are plotted in figure 12(b). These times were less than halved when exhaust velocity was doubled. They were approximately equal to the sum of the time t_c required for an eddy in the lower-surface exhaust jet to be convected to the trailing edge and the time t_a for a sound wave to move from the trailing edge to the upper-surface microphone.

Crosscorrelations of airfoil surface pressures and far field acoustic pressures for this configuration at 125 m/sec velocity are given in figure 13. Signals from three chordwise positions on the lower surface are shown in figure 13(a). For the two more forward locations (15% and 38% chord), zero amplitude and large negative slope occurred at the far-field acoustic travel time t_{ff} . After several small oscillations, these traces had another negative-slope zero crossing at the sum of that time and the eddy convection time t_c . Cross-correlation of the signal from 80% chord had positive slope at time t_{ff} but zero amplitude and negative slope at roughly the sum of t_{ff} and t_c . Previous tests (reference 2) had obtained similar results.

Crosscorrelations between the upper surface and far field are plotted in figure 13(b). In contrast to the complicated traces for the lower surface adjacent to the jet, these traces had only one dominant region. The signal for 15% chord had an antisymmetric pair of peaks, with zero amplitude and positive slope at time t_{ff} . The traces for other chordwise locations more closely resemble positive symmetric peaks at times that increase as the trailing edge is approached. However, that interpretation would require that acoustic signals of the same sign were radiated to both the near-field upper surface and far-field lower surface. A more plausible interpretation is that the zero-amplitude positive-slope portions represent an upper-surface pressure fluctuation that is part of an acoustic dipole source. These delay times increased above the far field acoustic travel time as downstream distance was increased, at a speed corresponding to the chordwise motion of an acoustic wave. Therefore the local pressure fluctuations on both the airfoil upper and lower surfaces (caused by convection of turbulent eddies in the jet) did not directly produce acoustic radiation at each chordwise position. They produced a readjustment of airfoil loading distribution, by pressure signals which were transmitted along the chord at the speed of sound. These changes of loading would be expected to be largest along the single airfoil's forward region, and this region radiated noise to the far field.

Surface-radiated EBF noise had been regarded in references 1 and 3 as a sum of radiation from a fluctuating-lift noise source distributed along the chord and a trailing-edge compact noise source. This simplified description is modified as a result of these crosscorrelation tests. There seems to be a noise source at the trailing edge which is relatively independent of flap deflection, and another near the leading edge which increases as the flap is initially deflected. Sound waves from each source are transmitted around the airfoil. A classical lift dipole associated with convected turbulence within the exhaust jet appeared to exist over the forward part of the flap but not along the rear half of the chord.

FORWARD FLIGHT EFFECTS ON EBF NOISE

Method of Approach

Tests were conducted to examine the effects of forward flight on aeroacoustic mechanisms that generate EBF noise. To assure that the various fluid-flow processes which affect noise radiation would be examined, measurements were made of mean and fluctuating velocity profiles across the exhaust jet. Surface pressure spectra and far-field acoustic spectra also were measured. It was expected that the two major effects on local exhaust jet flow would be a decrease of turbulence level and an increase of mean velocity within those portions of the jet mixing region which cause noise radiation. Two airfoil models therefore were tested. One had a chord length roughly equal to the length of the jet potential core at zero flight speed. Changes in noise radiation from this model would be expected to be dominated by changes of turbulence level. The other model was twice as long; increased mean velocity in noise-generating regions of the flow would be expected to partially counteract the effect of reduced turbulence level. The two ratios of airfoil chord to nozzle diameter bracket the range of EBF geometries tested by NASA and of practical interest.

Apparatus and Procedure

Test Apparatus

Tests were conducted in the UTRC acoustic wind tunnel. This open-circuit wind tunnel, shown in figure 14 and described in reference 10, has an open test section located within an anechoic chamber. This test section is shown in figure 15. For these tests the open jet was 0.79 m (31 in.) wide and 0.53 m (21 in.) high. The tunnel inlet section used with this test section size has a contraction ratio of 16.5 and a honeycomb and screens to provide less than 0.2% turbulence level in the test section. An air supply duct, connected to a regulated supply of high-pressure air, enters the tunnel inlet section downstream of the honeycomb and screens but upstream of the area contraction. This cantilevered duct extends downstream along the test-section nozzle centerline. The duct has about 20 cm (8 in.) inside diameter at a location 0.9 m (3 ft) upstream of the nozzle exit. A nozzle extension duct provides a smooth converging inner duct with 4.9 cm (1.925 in.) exit diameter and a smoothly contoured outer duct shape ending in a circular arc boattail.

A circular jet collector with approximately 1.1 m (42 in.) diameter, having a rounded lip lined with acoustic absorbing material, was located 3.6 m (12 ft) downstream of the nozzle inlet. Sidewalls 1.5 m (5 ft) long, supported by brackets outside the airflow, constrained the forward portion of the open

jet. The test airfoil was mounted between these sidewalls to assure that all of the airfoil noise was caused by the controlled-turbulence test airflow. This open jet configuration differs from that described in reference 10 by having a larger collector further downstream of the nozzle exit.

One airfoil model was the instrumented flat plate used in the measurements of incidence fluctuation noise described in references 3 and 4. This long-chord model, shown in figure 16, had 46 cm (18 in.) chord and 53 cm (21 in.) span. It had constant 2.54 cm (1.0 in.) thickness except at the cylindrical leading edge and the aft 6.35 cm (2.5 in.) region. This had circular arc upper and lower surfaces and less than 0.05 cm (0.02 in.) trailing-edge thickness. Model thickness had been chosen to allow easy installation within the airfoil of conventional 0.635 cm (1/4 in.) diameter condenser microphones mounted on right-angle adaptors and preamplifiers. Microphones were flush-mounted without protective grids on both the upper and lower surfaces at positions offset ± 0.5 cm (0.2 in.) from midspan at two chordwise locations: 23 cm (9 in.) and 41 cm (16 in.) downstream of the leading edge. Tests were conducted with the airfoil mounted between horizontal sidewalls with its centerline at zero angle of attack. One surface therefore was nearly in line with the nozzle exit lip.

The short-chord airfoil model was the 23 cm (9 in.) chord NACA 0018 airfoil used in the externally blown flap crosscorrelation tests and shown in figure 1. The sliders at 30% and 70% chord were positioned such that their flush-mounted microphones were at midspan along the exhaust jet centerline. At zero deflection, the airfoil leading edge was vertical and was positioned 2.5 cm (1.0 in.) downstream and 2.0 cm (0.8 in.) to the side of the nozzle lip. Thus the high-turbulence portion of the exhaust jet was approximately tangent to the airfoil maximum-thickness region. The airfoil was tested between horizontal sidewalls at 9° deflection (trailing edge toward the exhaust jet) on both the near side and the far side of the nozzle exhaust jet as sketched in figure 17(a). These cases represent an USB and an UTW installation, respectively. A deflection angle of 0° had been used in preliminary tests, but wind tunnel airspeed ratios greater than about 1/4 tended to blow the jet off the airfoil surface. At 9° deflection, the airfoil aft surface was approximately in line with the extended nozzle lip and the jet remained attached. The short-chord airfoil was also tested as an UTW installation at 30° deflection as sketched in figure 17(b). The center of rotation at 30% chord on the airfoil centerline was kept at the same position for all deflections. At 30° deflection, the airfoil trailing edge just barely obstructed the horizontal line-of-sight view of the nozzle lip. The long-chord airfoil was tested in both an UTW and USB installation, shown in figure 17(c). A photograph of the long-chord UTW installation is presented in figure 15.

Far-field measurements were obtained with conventional 0.635 cm (1/4 in.) diameter microphones placed on an arc of 3.05 m (10 ft) radius centered at the nozzle exit. The microphones were located at 70°, 90°, and 120° angular positions relative to the nozzle centerline direction. Far-field sound pressure levels and surface pressure fluctuation levels, cited as SPL and surface SPL, respectively, were measured in decibels referenced to 2×10^{-5} newtons per square meter (2×10^{-4} microbar). All microphones were calibrated daily with a 250 Hz pistonphone.

Flow-field traverses were obtained across the jet exhaust in the midspan plane of symmetry. A miniature hot-film gage, more rugged than a hot-wire gage, was used for measuring mean and root mean square fluctuating streamwise velocities. Because the exhaust jet temperature generally differed from the wind tunnel airstream temperature, a thermocouple also was traversed to obtain the temperature correction needed for measuring mean velocity. As sketched in figures 17(a) and (c), traverses were taken normal to the nozzle centerline for the short-chord airfoil at 9° deflection and the long-chord airfoil at zero deflection. These traverses were taken 22.9 cm (9.0 in.) downstream of the nozzle exit plane for both airfoils and also 40.6 cm (16.0 in.) downstream for the long-chord airfoil. Local surface slope of the short-chord airfoil at the traverse location and 9° deflection was nearly normal to the traverse line. For the short-chord airfoil at 30° deflection, the traverse line was rotated only 20° so that it would still be approximately normal to the airfoil surface. This position is sketched in figure 17(b). The extended traverse line intersected the nozzle centerline 22.9 cm (9.0 in.) downstream of the nozzle exit plane as with the other configurations. One basic assumption in planning these tests was that surface-radiated noise was caused by turbulence generated in the jet mixing region near the airfoil and convected past the airfoil. Noise is also generated by turbulence within the thin shear layer that forms downstream of the trailing edge. This region was not traversed in these tests. It was assumed that turbulence generated downstream of a surface would not cause acoustic radiation from that surface, and that the effect of forward speed on turbulence and quadrupole noise would be the same for both the initial exhaust jet mixing region and this other mixing region.

Calibration of Test Installation

The wind tunnel installation is shown in figure 15. It differed from that for previous tests in that the test section was rotated 90° such that the airfoil pitching axis was vertical. Microphones could then be mounted on supports attached to the anechoic-chamber floor at 3.05 m (10 ft) radius rather than being suspended overhead at 2.13 m (7 ft) radius. This installation used a relatively massive structure on the far side of the test section to support both ends of the airfoil models. Acoustic calibration of the various components were obtained at zero tunnel speed prior to this test program. Noise from the exhaust jet in the test section without sidewalls was

found to match that for a different installation which had a shorter, larger-diameter air supply duct. Thus the wind tunnel's air supply duct did not affect jet noise radiation. Adding the sidewalls caused a small noise increase up to 500 Hz one-third-octave center frequency. Evidently, the jet's axisymmetric broadband noise radiation caused weak standing waves between the sidewalls. Measured spectra at 90° and 120° directions generally matched within ± 2 dB those of previous tests and those calculated by the method of reference 11. Measurements at 60° from the nozzle upstream direction were systematically low. The wind tunnel nozzle lip may have shielded the jet exhaust nozzle region at this direction angle. Changing the microphone position to 70° eliminated this problem.

The exhaust jet was then tested with an undeflected airfoil mounted between the horizontal sidewalls but without the large support structure. Low-frequency noise caused by jet turbulence passing the airfoil was more than 10 dB larger than that from the jet alone. These spectra matched those which had been previously obtained for this configuration out of the wind tunnel and without sidewalls. Airfoil-radiated noise should be directed parallel to the sidewalls, so it is reasonable that such noise would not excite standing waves between the walls. Adding the airfoil support structure, for which all portions not shielded by the sidewalls were wrapped with acoustic absorbing material, did not alter this noise.

As a further check on possible noise reflection from the airfoil support structure, a small loudspeaker was used in place of the airfoil and jet. The loudspeaker output was about 10 dB stronger in front of the speaker cone than behind it, both in the free field and between the sidewalls. The speaker was placed at the airfoil nominal center position and aimed at the acoustically wrapped support structure. Pink-noise spectra obtained with the supports in place exceeded those without the supports by at most 3 dB above 8000 Hz frequency. Because of the speaker's directivity, this meant that the acoustically wrapped support reflected at most 10% of the incident noise. Spectra from a noise source that radiated equally in directions toward the microphones and toward the support could then be about 0.4 dB too high at high frequencies. This small error was regarded as acceptable.

Test Conditions

The range of jet exhaust velocities and tunnel airspeeds tested was picked to provide velocity ratios of practical interest, plus a larger range of velocity ratio to establish the trends. Full-scale EBF configurations are likely (reference 12) to operate at ratios of flight velocity to exhaust velocity near 0.25 during both takeoff and approach. Exhaust velocities would be near 250 and 200 m/sec (near 800 and 650 ft/sec) during takeoff and approach, respectively. It is difficult to obtain hot-wire or hot-film traverses of

turbulence intensity at these high subsonic speeds. Profiles of mean and rms streamwise turbulence velocity therefore were measured at 160 m/sec (525 ft/sec) exhaust velocity at practical velocity ratios of 0, 1/8, 1/4, and 3/8. Surface pressure spectra and far-field acoustic pressure spectra were measured at these four velocity ratios for both 160 and 250 m/sec (525 and 820 ft/sec) exhaust velocities. To establish trends more clearly, acoustic and flow-field measurements also were taken at 125 m/sec (410 ft/sec) exhaust velocity and velocity ratios of 0, 1/4, 1/2, and 3/4.

Evaluation of Forward Flight Effects

Expected Effects of Forward Flight

Surface-radiated noise is believed to be generated by turbulence produced in the jet mixing region and convected along the wing and past the trailing edge. Turbulence intensity in the direction normal to the wing surface is known to be much larger in this free shear layer than in the boundary layer adjacent to the wing surface. A crude approximation to estimating the effect of forward flight on shear-layer turbulence intensity would be to assume this intensity to be directly proportional to the difference in mean velocity across the shear layer. For axial distances smaller than the nominal potential core, the inner velocity can be taken as the jet exhaust velocity V_J . Then a flight velocity V_O would cause the turbulence velocity in the shear layer to be $(1-V_O/V_J)$ times that for zero flight speed.

The measured effect of external velocity on turbulence of an isolated axisymmetric subsonic jet (reference 13) was less of a decrease than would be predicted by that simple assumption. The multiplying factor was found to be closer to $(1-V_O/V_J)^{0.7}$ for experimental velocity ratios from 0.1 to 0.5. These higher levels were attributed to the turbulent boundary layer generated on the nozzle outer wall and convected into the free shear layer at nonzero simulated flight speeds.

Another effect of forward flight is increased axial extent of the jet's high-velocity potential core. Convection velocity of the turbulence which generates surface-radiated noise would therefore be increased by forward flight if the wing chord is much longer than the jet potential core. Length of this core for subsonic exhaust velocities, zero flight speed, and an isolated jet is about 4 or 5 diameters. Most under-the-wing EBF configurations have a distance of about 7 or 8 diameters from the nozzle exit to the deflected trailing edge. Thus a small increase of maximum mean velocity in the impingement region would be expected. Tunnel background noise in each 1/3 octave band was at least 10 dB below the measured noise for all test conditions except 125 m/sec exhaust velocity and velocity ratios of 3/4, and the two lowest 1/3

octave bands at a velocity ratio of $1/2$. Corrections for tunnel background noise therefore were not needed.

Forward flight should decrease the spreading rate of the free shear layer. If turbulence integral scale length is proportional to the shear-layer thickness, noise amplitudes would be decreased and peak frequency would be increased. This change of frequency would shift the full-scale spectra in the direction of increased annoyance.

Additional causes of EBF noise could include surface-radiated noise generated by turbulence in the wall boundary layer between the jet and the wing, quadrupole noise from the undistorted initial region of the jet, quadrupole noise from impingement of the jet against the wing, and quadrupole noise from the portion of the jet which develops from the wall boundary layer downstream of the trailing edge. The effect of forward speed on the wall boundary layer and the impingement region should be small. Quadrupole noise from the initial portion of the jet should vary as $60 \log (1 - V_0/V_J)$ as for an isolated jet (reference 11). Quadrupole noise from the region downstream of the trailing edge should be increased for long-chord wings because of the longer potential core and decreased by the above relative-velocity factor. A discussion of the effects of forward speed on these components is available in reference 14.

Effects on Flow Field

The effects of forward flight on mean velocity profiles measured normal to the surface near the trailing edge of the short-chord airfoil are shown in figure 18 for 125 and 160 m/sec exhaust velocities and 9° and 30° deflections. The velocity profiles for 9° deflection under-the-wing should also be a reasonable approximation for a small-chord small-deflection upper-surface-blowing configuration. All of these velocity profiles contained a potential core with maximum velocity equal to the nominal jet exhaust velocity except (figure 18(c)) for a velocity ratio of $3/4$ at 30° deflection. The smaller peak velocity and flat velocity profile near the surface for this case correspond to locally separated flow. Increasing the velocity ratio always decreased the maximum velocity gradient.

Profiles of mean velocity across the exhaust jet for two axial positions along the long-chord undeflected airfoil are given in figure 19. These profiles include a potential core with constant maximum velocity nearly equal to jet exhaust velocity.

Maximum velocities near the trailing edge of the long-chord airfoil (figure 19(c) and (d)) were less than the nozzle exhaust velocity. They generally increased as tunnel velocity ratio was increased. It should be noted that different results have been obtained by other investigators in tests of deflected long-chord airfoils. Reduced maximum velocity of the exhaust jet,

caused by viscous decay in the shear layer, may not allow the attached jet to overcome the adverse pressure gradient caused by the deflected flap in forward flight. An upper-surface-blowing configuration optimized for aerodynamics and acoustics at zero flight speed was described in reference 15 as having separated flow near the trailing edge at a tunnel velocity ratio near $1/4$.

Profiles of rms axial turbulence velocity divided by jet exhaust velocity are given in figure 20 for the short-chord model. These profiles have two peaks, one near the airfoil surface within the boundary layer and one in the free shear layer at the outer portion of the jet. The presence of the airfoil solid surface is known to prevent large turbulence levels normal to the surface, but turbulence levels in the free shear layer are nearly equal in all directions. Axial turbulence levels generally were larger than those in the boundary layer but their amplitude decreased more rapidly as tunnel velocity ratio was increased. The approximately 2% turbulence level in the potential core above the boundary layer agrees with the data of reference 13.

The effect of velocity ratio on maximum measured turbulence level in the shear layer of these configurations is shown in figure 21. No consistent difference existed between maximum levels for 9° deflection (open symbols) and 30° deflection (solid symbols). Also shown as square symbols are data from reference 13 for turbulence levels in an isolated axisymmetric exhaust jet at close to these test conditions. Maximum turbulence levels in the shear layer of a short-chord externally blown flap were approximately equal to those for an isolated exhaust nozzle. Turbulence levels for velocity ratios from zero to $3/8$ are fairly well predicted by a linear decay, shown by a solid line. This behavior would be expected if the rms turbulence velocity is proportional to relative velocity across the shear layer, $V_J - V_O$. The turbulence-decay expression given in reference 13, $(1 - V_O/V_J)^{0.7}$, shown by a dash line, is closer to the data for turbulence levels of $1/2$ and $3/4$. Slower decay at large velocity ratios was explained in reference 13 as being caused by the turbulent boundary layer generated on the compressed-air supply duct and jet nozzle outer wall. This turbulence is convected into the shear layer and increases the measured turbulence levels above what would exist in free flight with a practical nacelle length. For velocity ratios of practical interest (closer to $1/4$ than $1/2$), a dependence of surface-radiated acoustic intensity on turbulence level squared can therefore be represented by a dependence on $(1 - V_O/V_J)^2$.

Turbulence profiles for the long-chord airfoil at two axial positions and two jet velocities are given in figure 22. Turbulence profiles at midchord on the long-chord airfoil were a few percent larger than those for the short-chord airfoil at the same distance from the nozzle exit plane (figures 20(c) and (d)). Maximum turbulence levels near the trailing edge of the long-chord airfoil (figures 22(c) and (d)) are smaller than those near the trailing edge of the short-chord airfoil (figures 21(a) and (b)).

The presence of a potential core at midchord can be inferred from the measured flat minimum with near 2% turbulence level in figures 22(a) and (b). In contrast, minimum turbulence levels between the boundary layer and shear layer as measured near the trailing edge were about 6% to 7% at zero tunnel speed. As shown in figures 22(c) and (d), these minimum levels decreased to about 2% at velocity ratios larger than $1/4$. The jet potential core probably extended to this aft measurement position at these larger velocity ratios. The wavy turbulence profile for a velocity ratio of $3/4$ at 125 m/sec exhaust velocity in figures 22(a) and (c) may have resulted from oscillating separation and reattachment of the exhaust jet.

Effects of tunnel velocity ratio on maximum measured turbulence level in the jet shear layer of the long-chord airfoil are shown in figure 23. Maximum levels at midchord were roughly equal to those measured in the shear layer of an isolated subsonic exhaust jet (reference 11) at the same axial position. Midchord maximum levels at zero velocity ratio were about 17%, as compared with an average near 14.5% for the same axial position with the short-chord airfoil (figure 21). However, there was little difference between data for the two different airfoils at this same ratio of axial position to nozzle diameter for velocity ratios from $1/4$ to $1/2$. Maximum turbulence velocities near the trailing edge of the long-chord airfoil were only about $2/3$ those at midchord within the potential core. These levels decreased approximately linearly with increasing velocity ratio at both measurement positions. Therefore, noise which varies with turbulence levels squared should vary with $20 \log (1 - V_0/V_J)$ as with the short-chord airfoil.

Acoustic Results for Short Chord Airfoil

Effects of flight velocity ratio on one-third octave far-field sound pressure levels for the 23 cm chord 90° deflection UTW configuration are plotted in figures 24-26 for 125, 160, and 250 m/sec exhaust velocities. Spectra for the highest velocity ratio of $3/4$, shown in figure 24, were much larger than those for other velocity ratios. These high levels are believed to be a combination of incident-turbulence noise from the airfoil due to the exhaust nozzle supply duct's boundary layer, and intermittent separation of the exhaust jet from the airfoil surface. Data for this highest velocity ratio will not be shown for all configurations because they do not represent practical flow conditions.

Amplitudes of the far-field acoustic spectra at 90° from the nozzle inlet in an under-the-wing configuration were expected to be dominated by trailing edge noise at Strouhal numbers up to about one. Therefore, spectra measured at different jet velocities V_J but the same ratio of wind tunnel velocity to flight velocity V_0/V_J should coalesce if amplitudes were scaled with jet velocity to the fifth power. Spectra measured at three jet velocities and zero

tunnel velocity are plotted in figure 27(a). They are adjusted to the levels that would be expected at 100 m/sec jet velocity by being decreased $50 \log (V_J/100 \text{ m/sec})$. These adjusted spectra agree for Strouhal numbers up to 0.8 but systematically differ at larger Strouhal numbers. At those larger Strouhal numbers the measured spectra are a combination of directly radiated quadrupole noise from the exhaust jet, quadrupole noise reflected from the wing surface, and surface-radiated noise. This combination varies approximately with velocity to the seventh power. These same spectra for Strouhal numbers larger than one are shown in figure 27(b) to be brought into agreement when decreased by $70 \log (V_J/100 \text{ m/sec})$.

As a crude approximation, the major effect of flight velocity on trailing edge noise would be expected to be a reduction of intensity caused by the decreased turbulence level. Thus the velocity-adjusted levels would be adjusted for the change of turbulence level squared by being decreased $20 \log (1-V_0/V_J)$. Spectra for these three jet velocities and a tunnel velocity ratio of $1/4$, adjusted in this manner, are compared in figure 27(c) with an average curve drawn through the data for zero tunnel velocity. The data symbols match this curve in shape and peak amplitude, but they are displaced to larger Strouhal numbers. Notice that if Strouhal number had been defined in terms of relative velocity $U_J - U_0$ rather than jet velocity, or jet potential core length rather than jet diameter, the data points for nonzero velocity ratio would be displaced further from the curve. However, if Strouhal number had been arbitrarily multiplied by the relative velocity ratio $(1-V_0/V_J)$, the data points for a velocity ratio of $1/4$ would have approximately matched the adjusted spectrum for zero tunnel speed. This type of comparison will be shown later.

Although surface-radiated noise should have an intensity that varies with turbulence level squared (reference 1), quadrupole noise should vary with relative velocity and therefore turbulence level to the sixth power (reference 11). As shown in figure 27(d), use of a nominal fourth power average dependence on relative velocity ratio coalesces the measured spectra without need for an adjustment to Strouhal number.

The effects of flight velocity ratio on one-third octave far-field sound pressure levels for this configuration inverted to an USB position are plotted in figures 28-30 for the three test velocities. At frequencies below and somewhat beyond that for peak amplitude, these spectrum levels closely match those for the UTW position as given in figures 24-26. The USB spectra decay more rapidly than the UTW spectra at higher frequencies. This difference occurs because quadrupole noise from the forward 4.7 diameters of the exhaust jet was shielded by the USB wing.

If the USB spectrum is dominated by surface-radiated noise, the adjustment for forward flight effects on amplitude and frequency of such noise should coalesce the spectra over the entire frequency range. This comparison was made by increasing measured amplitudes by $-20 \log (1-V_0/V_J)$ and multiplying the one-third octave center frequencies by $(1-V_0/V_J)$. That is, spectra measured at nonzero tunnel speeds were adjusted to predict the zero-flight-speed spectrum. These adjusted spectra at 90° measurement direction are plotted in figure 31 for velocity ratios of 0, $1/8$, $1/4$, and $3/8$. Spectra for 160 m/sec exhaust velocity, given in figure 31(a), are coalesced within about 2 dB except at low frequencies. Incident-turbulence noise from the jet nozzle supply duct boundary layer convected past the airfoil, which would be unimportant for flight-length nacelles, caused the added low-frequency noise at higher velocity ratios. For 250 m/sec exhaust velocity, given in figure 31(b), the adjusted spectrum for a velocity ratio of $1/4$ fell somewhat below that for ratios of 0 and $1/8$ at high frequencies. Quadrupole noise from the exhaust jet downstream of the trailing edge is important at this high subsonic exhaust velocity. For this portion of the noise, adjusted levels should have been increased somewhat more and should not have been changed in frequency. The adjusted spectrum for a velocity ratio of $3/8$ at this exhaust velocity is not shown. Its levels were relatively high. They were probably increased by incident-turbulence noise at low frequencies and incipient separation of the exhaust jet at high frequencies. They may also have been increased by locally supersonic flow caused by the combination of a high subsonic exhaust jet and moderate subsonic external flow about the relatively thick airfoil.

Surface pressure spectra at 30% and 70% chord on the side of the airfoil adjacent to the exhaust jet are plotted in figure 32. Increased flight velocity ratio caused small decreases of peak amplitude. Spectra became narrower, but the frequency at peak amplitude was not changed.

Overall sound pressure levels were approximately the same for both the USB and UTW positions. These levels do not give a realistic measure of forward flight effects at velocity ratios larger than $1/4$ because of the large contribution of incident-turbulence noise. However, overall surface pressure levels seemed to be reasonable for velocity ratios to $1/2$. The effect of flight velocity on overall sound and surface pressure levels for this configuration is shown in figure 33. Sound pressure levels were adjusted for a fifth-power velocity dependence as expected for trailing edge noise. Surface levels were adjusted for the fourth-power dependence expected for surface and near-field acoustic pressures. All levels decreased approximately $20 \log (1-V_0/V_J)$, as expected for a dependence on turbulence level squared.

Effects of flight velocity ratio on far-field sound pressure levels for 30° deflection of the UTW configuration are plotted in figures 34-35. Data for the measurement direction 70° from the nozzle inlet (approximately perpendicular to the airfoil aft surface) should be least affected by quadrupole noise. Adjusted spectra for this direction are given in figure 37. As shown in figure 37(a), spectra for zero tunnel velocity and three different jet velocities are coalesced for Strouhal numbers less than 0.8 when adjusted for a fifth-power velocity dependence. Velocity-adjusted spectra for these three jet velocities at tunnel velocities $1/4$ the jet velocity are shown in figure 37(b) to coalesce except for the highest velocity at Strouhal numbers near peak amplitude. Use of a relative-velocity-squared correction for turbulence level brought the adjusted peak amplitudes into agreement with those for zero tunnel speed. However, the spectra were displaced to higher Strouhal numbers at nonzero velocity ratio.

The comparison of adjusted far-field spectra for this configuration and a direction 120° from the nozzle inlet is given in figure 38. Spectra for Strouhal numbers up to 0.5 and zero tunnel speed are shown in figure 38(a) to match when adjusted for a sixth-power velocity dependence. Spectra for Strouhal numbers above 1.0 and zero tunnel speed would be expected to be dominated by quadrupole noise. A ninth-power velocity dependence would be reasonable for this angle of about 50° relative to the aft direction of the deflected jet. This velocity exponent is shown in figure 38(b) to coalesce the spectra. Adjusted spectra for a velocity ratio of $1/4$ and low Strouhal numbers are given in figure 38(c). As with the other comparisons, peak level was matched with that for zero tunnel speed by correcting for turbulence level but the spectrum was shifted to larger Strouhal numbers. Spectra for this velocity ratio but large Strouhal numbers, given in figure 38(d), did not collapse into a smooth curve when adjusted for a ninth-power velocity dependence. The spectra for the two lower velocities, uncorrected for turbulence level, approximately matched those for zero tunnel velocity. The effect of velocity ratio on the portion of an EBF spectrum which is dominated by quadrupole noise from a deflected jet therefore was not clearly determined. It is likely that much of this noise comes from distortion of the portion of the jet mixing region which impinges against the airfoil surface. This region is located between the airfoil surface and the jet potential core. Its mean velocities, turbulence levels, and turbulence scale lengths would not be expected to be affected by simulated flight velocity. For longer configurations having the impingement region downstream of the potential core at zero flight speed, the effect of flight speed would be an increase of local mean velocities. Therefore the direct and reflected quadrupole noise from practical under-the-wing EBF configurations might increase as velocity ratio is increased.

Adjustment to both frequency and amplitude to coalesce USB far-field spectra had been shown in figure 32. The portion of UTW spectra that is produced by surface-radiated noise should be brought into agreement by the same process. Use of this adjustment for UTW acoustic spectra at 160 m/sec exhaust jet velocity and both 9° and 30° deflection angle is shown in figure 39. The spectra were compared at the measurement direction nearly perpendicular to the deflected aft surface. Data are shown for frequencies up to 5000 Hz corresponding to Strouhal numbers up to 1.6. Good agreement was obtained near peak amplitude for the test range of velocity ratios from 0 to $3/8$, with better agreement at the larger deflection.

Effects of flight velocity ratio on surface pressure spectra at 30% and 70% chord for UTW 30° deflection are plotted in figure 40. These spectra showed different trends at the two measurement positions. Spectra for 30% chord, adjusted for a fourth-power jet velocity dependence and relative velocity ratio squared, are plotted in figure 41. The spectra for zero tunnel velocity, shown in figure 41(a), form a sharply-decaying adjusted spectrum typical (reference 1) of surface pressure spectra upstream of the nominal impingement point. Adjusted spectra for a velocity ratio of $1/4$ are given in figure 41(b). They approximately match the spectra for zero tunnel velocity in the region of peak amplitude and rapid decay but are narrower at low Strouhal numbers. This change of shape resembles that for a more upstream location. One effect of increased velocity ratio is an axial stretching of the jet potential core and reduced spreading of the jet. The surface pressure distribution at this position and a velocity ratio of $1/4$ apparently corresponds to that for a more upstream location in a flow field with zero tunnel velocity.

Surface pressure spectra for this configuration and 70% chord, adjusted for a fourth-power velocity dependence but not adjusted for relative velocity ratio, are plotted in figure 42. The symbols for spectra measured at a velocity ratio of $1/4$ form a curve parallel to, but larger than, the average curve for zero tunnel speed. This increase of surface pressure level was given by $40 \log (1+V_o/V_J)$. Nonzero flight speed therefore can increase the surface pressure levels in the impingement region of a highly deflected under-the-wing externally blown flap.

Effects of flight velocity on overall sound and surface pressure levels for this UTW 30° deflection configuration are shown in figure 43. Overall sound pressure levels adjusted for a sixth-power velocity dependence, shown in figure 43(a), decreased as expected for a dependence on turbulence level squared. Overall surface pressure levels adjusted for a fourth-power velocity dependence, given in figure 43(b), had opposite trends for 30% and 70% chord. The relatively low levels at 30% chord decreased rapidly, varying approximately with $40 \log (1-V_o/V_J)$. Those measured at 70% chord, in the impingement

region, increased as velocity ratio was increased to $3/8$ and then decreased at a velocity ratio of $1/2$. This increase was approximately given by $-30 \log (1 - V_o/V_J)$. In agreement with this prediction, overall surface pressure levels at a velocity ratio of $3/8$ were 6 dB larger than at zero tunnel speed. This increase corresponds to a doubling of rms static pressure fluctuations from about 3% to 6.5% of the exhaust jet dynamic pressure. At this deflection angle and axial position, static pressure fluctuations at zero tunnel speed were shown in reference 1 to have a local minimum along the centerline. They increased to about 6.5% of the exhaust jet dynamic pressure near the edge of the jet. This higher level agrees with the maximum static pressure fluctuation in the mixing region of an isolated exhaust jet. It is not known whether static pressure fluctuations on the airfoil surface near the edge of the jet would also be doubled by forward speed.

Acoustic Results for Long-Chord Airfoil

Effects of flight velocity ratio on one-third octave far-field sound pressure levels for the 46-cm long chord airfoil in the USB configuration are plotted in figures 44-46 for 125, 160, and 250 m/sec jet velocities. Spectrum shape near peak amplitude varied irregularly as velocity ratio was increased. The spectra at zero tunnel speed had two mild peaks at low frequencies. The peak which occurred at the lowest frequency decreased rapidly in amplitude as velocity ratio was increased. Less change occurred near the other peak. All of these spectra, except those for the largest velocity ratios, decayed approximately inversely with frequency squared at high frequencies. This behavior is expected (reference 4) for trailing edge noise.

Effects of flight velocity ratio on one-third octave far-field sound pressure levels for the long-chord airfoil in the UTW configuration are plotted in figures 47-49. Near peak amplitude, these spectra are nearly identical to those of figures 44-46 for USB. However, their decay rate at high frequency is only about half as large. This portion of the UTW spectra is dominated by quadrupole noise generated in the jet exhaust mixing region. The long-chord airfoil reflects this noise when in the UTW configuration but shields it for USB. Effects of flight velocity ratio on one-third octave surface pressure levels on the surface adjacent to the exhaust jet at midchord and near the trailing edge are plotted in figure 50.

The effect of flight velocity on overall sound pressure level directly below the long-chord airfoil in both UTW and USB configurations is shown in figure 51. Both configurations had approximately the same OASPL. Adjusting these OASPL's for the fifth-power velocity dependence expected for trailing edge noise produced agreement among data taken at 125, 160, and 250 m/sec exhaust velocities. Increasing the ratio of tunnel velocity to exhaust jet

velocity from 0 to $3/8$ caused a more rapid decrease of OASPL than that shown in figure 42 for the short-chord configuration. This faster decrease was approximately given by a dependence on relative velocity to the third power, $30 \log (1-V_0/V_J)$. The cause of this decrease is not known. Measured turbulence levels had decreased with relative velocity squared (figure 23), and mean velocity at the trailing edge had not varied systematically with relative velocity (figure 19). Perhaps the width of the noise-producing region of this long-chord model was proportional to relative velocity.

Because of the change of peak-region spectrum shape with velocity ratio, far-field spectra near peak amplitude were not coalesced by use of an assumed variation of intensity with relative velocity cubed. The high-frequency portion of the USB spectra appeared to have the same amplitude and frequency dependence on velocity ratio that occurred for surface-radiated noise of the short-chord model. As with figures 31 and 39 for the short-chord model, both amplitude and frequency were adjusted such that data for nonzero velocity ratios were used for predicting the zero-tunnel-speed spectrum. Amplitudes were adjusted for a fifth-power dependence on jet velocity, and frequency was taken as Strouhal number, so that results obtained for different jet velocities could be compared. Spectra measured directly beneath the long-chord USB configuration and adjusted in this manner are shown in figure 52 for 160 and 250 m/sec jet velocities. Good agreement is shown in figure 52(a) for velocity ratios from 0 to $1/4$ at adjusted Strouhal numbers $(1-V_0/V_J)(fD/V_J)$ greater than 0.2 and 160 m/sec jet velocity. About 8 dB scatter occurred for adjusted Strouhal numbers less than 0.1. The same procedure applied for 250 m/sec jet velocity (figure 52(b)) caused less scatter at small Strouhal numbers. An arbitrary average curve drawn through the data of figure 52(a) is plotted in figure 52(b). This curve matches the low-frequency data points at velocity ratios of 0 and $1/8$, and the high-frequency data at a velocity ratio of $1/4$.

Use of this adjusted frequency and amplitude for correlating spectra measured beneath the long-chord UTW configuration is shown in figure 53. Spectra measured at velocity ratios from 0 to $3/8$ and 160 m/sec jet velocity, shown in figure 53(a), are brought into good agreement for Strouhal numbers less than one. Within this range, they match the average curve from figure 52(a) for USB at this jet velocity. Adjusted spectra had a smaller slope at larger Strouhal numbers, and amplitudes generally decreased with increasing velocity ratio. This portion of the spectra was dominated by both surface-radiated and quadrupole noise. It would be better correlated (not shown here) by the fourth power of relative velocity, as shown in figure 27(d) for the short-chord airfoil.

Spectra measured at 250 m/sec exhaust jet velocity for this long-chord UTW configuration are shown in figure 53(b). As with spectra for USB, the adjustments to frequency and amplitude produce less agreement among data for different velocity ratios and slightly worse agreement with the 160 m/sec average curve. At high Strouhal numbers, use of an averaged surface and quadrupole-noise adjustment to amplitude without an adjustment to frequency would have produced agreement among spectra for velocity ratios of 0, 1/8, and 1/4.

Prediction of Forward Flight Effects

Method for Calculating Forward Flight Effects

From the viewpoint of a noise component method (reference 3), the complicated noise radiation from an EBF is regarded as the sum of radiation from several basic noise processes. These processes are of two major types - surface-radiated and quadrupole. Noise radiated from a solid surface can be further approximated as a sum of two compact-source noise processes, fluctuating lift noise and trailing edge noise. They vary with velocity to the sixth power and fifth power, respectively, and both are proportional to turbulence level squared (reference 4). Approximating both velocity exponents by a sixth-power dependence, the effect of forward flight on surface-radiated one-third octave noise spectra then is a decrease of amplitude by $10 \log (V_i/V_{i0})^6 (1-V_0/V_J)^2$. This decrease should be applied at constant frequency for UTW and at an increased frequency given by $f/(1-V_0/V_J)$ for USB. Here, V_i is the impingement velocity (the velocity along the isolated jet centerline at the axial location of the trailing edge or where the extended nozzle centerline intersects a flap surface), and V_{i0} is its value at zero forward speed. Simple methods for calculating the effect of forward speed on V_i are not available, except for short-chord models where V_i can be regarded as equal to V_J . It is recommended that impingement velocity, or maximum exhaust velocity at the trailing edge, be measured as part of EBF wind tunnel aerodynamic test programs.

Surface-radiated noise generally dominates the low-frequency and peak-amplitude portions of measured spectra directly beneath an EBF configuration. Quadrupole noise is important at higher frequencies. Such noise is produced by the initial undeflected part of the exhaust jet, by the jet deflection region, and by the high-intensity shear layer downstream of the aft flap trailing edge. Quadrupole noise caused by impingement of the jet against a deflecting surface is important for UTW. Its amplitude depends on relative velocity between the jet and surface V_i . Such noise should have its amplitude increased by about $80 \log (V_i/V_{i0})$. The changes of frequency associated with the change in V_i probably can be neglected for reasonable configurations and velocity ratios.

The other two quadrupole noise processes depend on relative velocity between the jet and the external air. For directions perpendicular to the jet exhaust, the method of reference 11 specifies that OASPL varies with $60 \log (1-V_0/V_J)$. Amplitudes in other directions are calculated by basing the convection Mach number on relative velocity V_J-V_0 . Based on data cited in reference 11, normalized spectrum shapes are not changed and Strouhal number continues to be defined in terms of absolute jet velocity. For practical purposes, the effect of forward flight on these kinds of quadrupole noise at all directions should then be approximated as a $60 \log (1-V_0/V_J)$ decrease of amplitude at constant frequency. However, the limited data obtained under this program and shown in figures 27(d) and 38(d) would indicate a dependence on $40 \log (1-V_0/V_J)$ for small-deflection flaps and about $10 \log (1-V_0/V_J)$ at moderate deflection. The recommended procedure for quadrupole noise is a nominal $20 \log (1-V_0/V_J)$ decrease.

It should be noted that low-frequency surface-radiated one-third octave surface pressure levels often vary approximately with frequency squared. Therefore the low-frequency adjustment to USB zero-flight-speed spectra caused by decreasing the amplitude and increasing the frequency can be approximated by a $40 \log (1-V_0/V_J)$ decrease of amplitude at constant frequency. For USB configurations, the high-frequency portion of the surface-radiated noise spectrum varies approximately inversely with frequency squared so the adjustment merely shifts the calculated point along the zero-flight-speed spectrum. At frequencies for which quadrupole noise should dominate, the adjustment would be a $20 \log (1-V_0/V_J)$ decrease at constant frequency. This and the $40 \log (1-V_0/V_J)$ decrease at low frequencies would be faired to an arbitrary maximum. The peak would occur at the zero-flight-speed peak frequency divided by $(1-V_0/V_J)$.

This discussion does not include possible noise increases such as might arise from separated flow past the deflected flap at nonzero flight speed. Forward flight will generate increased aerodynamic lift on the wing flaps, producing an adverse pressure gradient on the aft part of the flap surfaces. Large-scale high-intensity turbulence generated in separated flow is known to cause surface-radiated noise. Direction of the deflected exhaust jet may also be changed, moving the angular location of peak quadrupole noise which occurs below the deflected jet.

The above method for calculating forward flight effects yields the spectra in a coordinate system moving with the airframe. These spectra should be Doppler-shifted for prediction of spectra measured by a stationary observer of a moving aircraft, using the equation given in reference 16.

Methods for predicting forward flight effects on EBF noise also are discussed in both the NASA Aircraft Noise Prediction Program (reference 16) and a method developed by Lockheed-Georgia Co. (GELAC) for the Federal

Aviation Administration (reference 17). The NASA ANOPP method specifies that in a coordinate system moving with the airframe, forward flight effects on USB noise frequency and amplitude can be neglected. For UTW the effect on frequency is neglected; the OASPL amplitude is adjusted by $10 k \log (1 - V_o/V_J)$ where the parameter k varies with flap deflection and measurement angle. The value of k is equal to 6 for directions near the deflected exhaust jet, as for jet exhaust noise (reference 11). In the forward quadrant it is equal to 4 for takeoff flap deflection and 1 for approach deflection. The empirical value of 1 gives a smaller decrease than the value of 2 recommended here. The large velocity exponent for takeoff flap deflection is believed to have been caused by one specific test configuration. It is discussed in the following section of this report, "Comparison With Available Data". The GELAC method described in reference 17 recommends that no adjustment for forward-flight source effects be applied to UTW or USB noise. For other types of STOL aircraft such as jet flaps, having noise radiation dominated by jet exhaust noise, the forward flight correction to such noise is specified.

Comparison With Available Data

Results of an investigation of forward velocity effects on under-the-wing EBF noise were reported in reference 18. A two-flap wing was tested at both takeoff and approach deflection with both a conical and a mixer nozzle. Forward flight was simulated by use of a large free jet having a diameter 6.5 times that of the conical nozzle. Tests were conducted at nominal airspeeds of 0, 43, and 53 m/sec and jet exhaust velocities from 208 to 290 m/sec, giving velocity ratios from 0.15 to 0.25. As shown in figures 9-12 of reference 18, normalized spectra measured with both flap deflections and both exhaust nozzles were unaffected by simulated flight speed at constant exhaust velocity. That is, there was no frequency shift for the spectra of under-the-wing configurations. The entire forward flight effect can be regarded as producing a decrease of overall sound pressure level (OASPL).

For these configurations and zero flight speed, OASPL was previously found to vary with exhaust velocity to approximately the seventh power. The axial distance from the nozzle exit plane to the flap impingement point was more than seven nozzle diameters, so the exhaust jet local velocity was decreased by viscous mixing as it approached the flaps. For the high subsonic exhaust velocities of these tests, the observed variation with exhaust velocity to the seventh power corresponded approximately to the expected dipole-noise variation with local impingement velocity to the sixth power. Conical nozzles and mixer nozzles have different variations of local maximum velocity with axial distance. It had been expected that simulated forward speed would change these variations differently for the two nozzle shapes. Instead, reductions of OASPL for the two nozzle shapes were nearly identical for each flap deflection but differed markedly for takeoff and approach deflections.

For approach deflection, OASPL was shown in figure 6 of reference 18 to vary with relative velocity to approximately the 1.4 power at constant exhaust jet velocity. This measured dependence of OASPL was within 0.7 dB of the second-power variation predicted herein and based on the decrease of turbulence intensity. Also, the turbulent boundary layer generated on the outside of the nozzle's long supply duct may have increased the jet shear layer turbulence level as described in reference 11. Based on the turbulence data from reference 13 for an isolated jet, a dependence on relative velocity to the 1.4 power rather than second power would have been predicted. For takeoff deflection, the variations shown in figure 5 of reference 18 were with relative velocity to the 3.5 and 4.9 powers for the conical and mixer nozzle. These exponents are larger than those inferred from any other test program, and formed the basis of the empirical prediction in reference 12.

One possible cause of this large difference between measured forward speed effects for the two flap deflections is the external airflow past the wing and flaps. The wing leading edge was 1.8 nozzle diameters above the nozzle upper lip. Simulated forward-speed airflow could pass between the wing lower surface and the exhaust jet, deflecting the jet below the wing and flaps. At takeoff flap deflection, the aft flap trailing edge did not extend much below the nozzle centerline. Relatively small vertical displacement of the exhaust jet by the wing lower-surface flow field could have caused a relatively large increase of distance between the noise-radiating aft flap panel and the exhaust jet. At approach flap deflection, the aft flap panel extended nearly two nozzle diameters below the nozzle centerline. The wing airflow pattern could not prevent the exhaust jet from passing through the external flow and pressing against this deflecting surface. Flow-field velocity measurements are not available to check the validity of this explanation. It should be noted that if this interpretation of the data is correct, then noise from a flap configuration which extends further into the exhaust jet at takeoff deflection would have closer to a relative-velocity-squared dependence.

Forward flight effects on noise from several types of STOL configurations have been measured in the NASA Ames Research Center 40 x 80 ft wind tunnel. The effect of forward speed on noise of a large under-the-wing EBF model in the landing configuration was given in reference 19. Measured maximum dynamic pressure in the jet exhaust upstream of the flap was shown in figure 3 of that reference to increase about 7% when forward speed was increased from zero to a typical approach speed. The larger value was equal to the jet dynamic pressure expected for the measured thrust, without viscous decay. It was noted in reference 19 that the resulting 19% increase in local velocity to the sixth power would be expected to cause about 0.75 dB increase of noise. Measured spectra for these forward speeds of zero and 31 m/sec at 115 m/sec jet exhaust velocity were given in figure 4 of reference 19 and are reproduced in figure 54(a) herein. These data are for a measurement direction 120° from the inlet in the flyover plane, where maximum OASPL occurred. The noise reduction

caused by decreased turbulence intensity at this velocity ratio of 0.27 would be $20 \log (1-V_O/V_J)$ or about 2.7 dB. Combining this with the effect of increased local velocity on surface-radiated noise causes a 2 dB predicted noise reduction. As can be seen from figure 54(a), applying this reduction to the static spectrum closely predicts the forward-flight spectrum between 50 Hz and 1000 Hz frequency. Below 50 Hz, tunnel background noise caused the spectrum to be louder at nonzero forward speed. Between 1600 Hz and 4000 Hz there was no effect of forward speed on SPL. At higher frequencies the spectrum was dominated by tones from the turbofan engines which powered the model. Nonzero tunnel speed decreased the turbulence ingested by the fans, greatly reducing that noise. The 2 dB decrease of flap impingement noise cited in that paper therefore was predicted as a combination of the effects of decreased turbulence level and increased local mean velocity. Measured spectrum shape in forward flight was predicted by correcting the amplitude but not changing the frequency. Apparently, adjustment to frequency is not needed for noise of highly deflected flaps.

The effect of forward speed on a large upper-surface-blowing model tested in this wind tunnel at simulated takeoff conditions was given in figure 8 of reference 12. Spectra for velocity ratios of zero and 0.165 are reproduced in figure 54(b). Adjusting both the measured amplitude and measurement frequency for the static-velocity spectrum (solid curve) yields the predicted spectrum in forward flight (dash curve). This prediction matched the data within ± 2 dB except at frequency bands containing engine tones. The predicted 1.6 dB reduction of OASPL agreed with the measured 2 dB decrease.

Effects of forward flight on noise of an upper-surface-blowing model at takeoff deflection as measured at the Boeing Co. were reported in reference 14. These tests used a nearly sonic (305 m/sec) jet exhaust velocity, so quadrupole noise should be important at high frequencies. Forward flight was simulated by placing the wing and exhaust jet in front of a large low-velocity subsonic exhaust nozzle. Measured spectra for zero forward velocity and for velocity ratios of 0.16 and 0.26 are given in figure 55(a), taken from figure 14 of reference 14. Adjusting the measured static spectrum in amplitude and frequency at low frequencies for surface-radiated noise, in amplitude only for a combination of surface and quadrupole noise, and in frequency for an arbitrary faired flat peak yields the two predicted solid-line spectra in figure 55(b). These predictions agreed with data for low frequencies and for high frequencies. Spectrum shape near peak amplitude was poorly predicted, and peak amplitudes were underpredicted by 2 to 4 dB. Measured SPL reductions were about 4 and 7 dB near peak amplitude, as shown in figure 55(a). These reductions due to simulated flight velocity agree with the 4.5 and 7.8 dB reductions expected (reference 14) for decreased quadrupole noise of an isolated exhaust jet. It is not obvious how to include this behavior near peak amplitude in a prediction of forward flight effects. The two spectra for different flight velocity ratios

clearly need different adjustments for low frequencies, high frequencies, and near peak amplitude. This same change in spectrum shape from a broad, approximately single-peaked spectrum to a double-peaked shape, and more rapid decrease of the lower-frequency peak as velocity ratio was increased, also occurred for the long-chord configuration reported herein.

Forward flight effects on noise of an upper-surface-blowing model tested by Lockheed-Georgia Co. were shown in figure 13 of reference 15. Data were given for velocity ratios of zero and 0.25. These data are shown in figure 56. The dash curve represents the measured static spectrum (solid curve) adjusted in both amplitude and frequency for prediction of the spectrum in forward flight. Agreement between this prediction and the measured spectrum was within 1 dB for most of the frequency bands. Although these data were for a relatively high subsonic (250 m/sec) exhaust velocity, use of a quadrupole-noise decrease of predicted amplitude at high frequencies would have caused worse agreement between predictions and forward-flight data.

COMPARISON OF MEASURED AND PREDICTED EBF NOISE FOR LARGE-SCALE MODELS

Discussion of Large-Scale Test Configurations

Extensive acoustic data have been obtained by NASA Lewis Research Center for under-the-wing externally blown flaps with a nominal half-scale 0.33 m (13 in.) diameter conical exhaust nozzle using unheated compressed air. Data for two-flap and three-flap configurations, altered vertical spacing between the nozzle and flap, and several nozzle types were given in reference 20. Maximum flyover noise was found to be relatively insensitive to these geometry variations at approach flap deflection. However, some differences occurred at takeoff flap deflection. This air supply also was used in tests of an under-the-wing (UTW) configuration having a mixer nozzle and an upper-surface-blowing (USB) configuration having a conical nozzle with deflector plate.

Acoustic data also have been obtained at NASA Lewis Research Center with nominal full-scale installations. The exhaust jet supply for those tests was a noise-suppressed TF-34 engine with 6:1 bypass ratio. These data include all full-scale effects that might be associated with viscous mixing phenomena of the exhaust jet. They also contain whatever compressibility, turbulence, and refraction effects might be caused by a hot core jet containing engine combustion products. Such data provide the best evaluation of prediction methods based on data obtained with small unheated jets. Configurations tested with this engine are a three-flap UTW model with a variety of coannular, decayer, and mixer-decayer nozzles and an USB model with circular and 4:1 slot nozzles and two different flap lengths.

Large-scale configurations designated by NASA Lewis Research Center for comparisons of predicted and measured EBF noise were the half-scale mixer nozzle and two-flap UTW, full-scale three-flap UTW, full-scale circular-nozzle long-flap USB, and slot-nozzle short-flap USB. It is also intended that comparisons will be made with data for the QCSEE (Quiet Clean STOL (or Short-haul) Experimental Engine) UTW and USB configurations.

Spectrum Corrections for Ground Reflection

Spectrum corrections for ground reflection were investigated with the noise-suppressed TF-34 engine and an under-the-wing externally blown flap at NASA Lewis Research Center. For this comparison of data and predictions, tabulated data were supplied by NASA for the engine with a mixer-conic nozzle and the wing with 0° - 20° - 40° deflection of the three flap segments. These data had been corrected for atmospheric absorption only. This nozzle mixed the core and fan exhaust streams and discharged the partially mixed flow through a convergent conical nozzle. Acoustic data were measured with nine microphones mounted in an arc of 30.5 m (100 ft) radius on posts 2.74 m (9 ft) above the paved ground and with three microphones mounted flush with the ground at the same radius. For wavelengths larger than twice the microphone diameter, these flush-mounted microphones should have measured complete reflection of acoustic waves. Their outputs should be 6 dB above free field at all frequencies of practical interest. These microphones thus provided spectra that should require a constant correction independent of frequency. Because downward-radiated noise is reflected by the ground, data from post-mounted microphones are a sum of directly radiated noise and reflected noise. These two types of noise had approximately equal path lengths so their acoustic intensities at the microphone posts should have been equal. At frequencies where these acoustic signals had the same phase, reflection should have reinforced the direct radiation and increased the noise to 6 dB above free field. At other frequencies where the two signals had opposite phase, cancellation should have reduced the noise below free field. For frequency bands wide enough to contain random phasing of the two signals, reflection should double the acoustic intensity and therefore would have increased the noise to 3 dB above free field. The required correction data from post-mounted microphones can be obtained by subtracting their measured spectra from those from flush microphones at the same measurement direction and test condition.

This correction was evaluated from the tabulated data for 70° , 90° , and 110° direction angles and five exhaust velocities. No systematic trend with direction or velocity was observed. Average values for this correction in each one-third-octave band are plotted as circle symbols in figure 57. The brackets denote the range of data for the five velocities at 90° direction. This correction for post-mounted microphones in the flyover plane was arbitrarily approximated by four straight lines as shown in the figure and tabulated below.

<u>1/3 Octave Center Frequency, Hz</u>	<u>Correction, dB</u>	<u>1/3 Octave Center Frequency, Hz</u>	<u>Correction, dB</u>
100 or less	-6	400	0
125	-5	500	+1
160	-4	630	0
200	-3	800 to 2000	-1.5
250	-2	2500 or more	-3
315	-1		

The average correction required for frequencies of 2500 Hz or larger was -2.8 dB, in good agreement with the expected -3 dB.

Sideline noise was measured with microphones on overhead booms. The nominal wingtip sideline position was 17.6 m (57.6 ft) from the nozzle centerline. Reinforcement and cancellation effects should be unimportant for this position. Noise generated at the centerline and reflected from the ground to this microphone had a path length roughly 1.3 times that for directly radiated noise. Because of this longer path length, reflected intensity was about 50% lower than the direct signal. The sum of these two signals would cause measured noise to be about 2.0 dB above free field.

Most previous data, including those which had been utilized to determine the empirical constants in the prediction methods of references 3 and 21, were not corrected in this manner. For small-scale data, OASPL generally was dominated by the portion of the spectrum above 800 Hz. Those indicated levels may be 1.5 to 3 dB too high. The prediction method of reference 16 had used large-scale data with OASPL adjusted for a smoothed prediction of ground reflections, comprising nearly 3 dB decrease, to compensate for this effect. However, corrected OASPL's measured with the flush-mounted microphones for this one full-scale configuration averaged 4.3 dB less than those measured with post-mounted microphones. This large correction occurred for full-scale configurations because considerable acoustic energy was radiated at low frequencies where output from post-mounted microphones was 6 dB above background.

Most sideline data were obtained in a measurement plane oriented perpendicular to the engine centerline. Surface-radiated noise would be expected to vary with $\sin^2\phi$ where ϕ is the angle below the wingtip. Thus the sideline variation of surface-radiated noise is easily obtained from its calculated level in the flyover plane ($\phi=90^\circ$) at this measurement angle (direction = 90°). In contrast, quadrupole noise is assumed to be axisymmetric relative to the deflected jet centerline, but the angle between that centerline and the measurement direction is a function of sideline angle. In this measurement plane, the angle relative to the deflected exhaust jet's upstream direction is given by

$$180^\circ - \cos^{-1}(\sin \delta \sin \phi)$$

where δ is the jet deflection below the nozzle inlet. As sideline angle is varied from 90° (flyover) to 0° (wingtip), the measurement angle relative to the deflected jet's upstream direction decreases from $180^\circ - \delta$ to 90° . Thus the quadrupole noise should change its amplitude and spectrum shape with sideline angle.

EBF Noise Prediction Methods

Methods for predicting noise beneath EBF configurations range from empirical correlations to representations of several types of noise components. Several openly available methods, their general type, and their range of data base are tabulated below and then described in greater detail.

Methods for Predicting EBF Noise

<u>Method</u>	<u>Ref.</u>	<u>Directivity</u>	<u>Velocity Law</u>	<u>Data Base</u>
ANOPP	16	empirical	$V_J^{6.7}$	NASA large models
GELAC	17	empirical	V_J^6	NASA, GELAC small models
Noise Component	3,5	analytical for each component	several, V_{local}	NASA small models

ANOPP Method

In this method, described in reference 16, OASPL directly below an EBF (zero azimuth angle, 90° polar angle) was approximated by a variation with impingement velocity to the sixth power. Impingement velocity for an UTW installation is defined as the maximum velocity in an isolated jet at the axial distance where the extended nozzle centerline intersects the deflected flaps. Most of the UTW models for which data were used had impingement distances of $7\frac{1}{4}$ to $7\frac{1}{2}$ diameters, which is greater than the length of the jet potential core. Impingement velocity therefore was less than the nozzle exhaust velocity; the ratio of impingement velocity V_i to jet exhaust velocity V_J would be expected to increase as exhaust Mach number was increased. For high subsonic exhaust Mach numbers and these impingement distances, V_i^6 is equivalent to $V_J^{6.7}$. Therefore, in practice the ANOPP empirical velocity dependence for UTW, $V_J^{6.7}$, is an easily calculated approximation for dipole noise based upon local velocity, V_i^6 . The velocity dependence is taken as V_J^6 for USB. Noise ampli-

tude is scaled directly with nozzle diameter squared and inversely with far-field distance squared. Separate equations are given to represent the variation of UTW and USB noise amplitude with flap deflection.

Calculated OASPL for one measurement position is extended to all other polar and azimuth angles by use of normalized directivity curves for each flap deflection. Normalized spectrum curves (referenced to OASPL) are then utilized to calculate spectrum and the spectrum-weighted noise levels. These normalized spectra are independent of polar angle; they vary with flap deflection in the flyover plane but not in the sideline plane.

It should be noted that OASPL amplitudes calculated by this method are 2 to 3 dB smaller than those given by an earlier version (reference 21) of that method. Constants for the earlier method had been obtained using data for large-scale models uncorrected for ground reflection.

GELAC Method

This method (reference 17) exists in two forms, a hand calculation procedure and a computer program. The hand calculation procedure is similar in its usage to the ANOPP Method in that noise is scaled with nozzle exit area, and empirical curves provide directivity and spectra. It differs from the ANOPP Procedure by including a Lockheed-Georgia Co. (GELAC) data base for which nozzle position was extensively varied relative to the wing and flaps. Also, both UTW and USB noise are assumed to vary with exhaust velocity to the sixth power. Azimuthal variation is given only for 90° polar angle. All of the data base was affected by ground reflection.

The computer program includes a representation of these empirical curves plus trailing edge noise and quadrupole noise components as with the noise component method described below. An updated version of this method has been prepared (reference 6) but was not available for this evaluation.

Noise Component Method

This general class of methods represents the total noise as a sum of several components which are acoustically but not aerodynamically independent. Each component has the analytic functional dependence of noise radiation from a simple geometry. If the spatial distributions of mean velocity and turbulence properties were known for an EBF deflected exhaust jet, each of these noise components could be calculated precisely. However, differences probably would exist between noise radiation calculated for a simple geometry and measured for the complex EBF geometry. Furthermore, the spatial variations of velocity and turbulence near each flap segment have not been measured in adequate detail. Empirical constants therefore are used within each component

to represent a combination of both the unknown jet exhaust properties (turbulence levels and ratios of turbulence scale lengths to nozzle diameter) and the unknown interactions between adjacent flap segments or noise components. Specializations of the general noise component method have been used successfully by many investigators (e.g., references 3, 6, 22-25) to describe noise from complex geometries.

The specific noise component method given in reference 3 and used herein regards both UTW and USB EBF noise as a sum of fluctuating lift noise, trailing edge noise, and quadrupole noise. An earlier version of that method had been given in reference 24. Directivity shapes and velocity exponents for these separate components are shown in figure 58. Fluctuating lift noise, also called scrubbing noise or inflow noise, is dominant for UTW. It has the directivity of a lift dipole perpendicular to each wing and flap chord. From crosscorrelation of surface and far-field pressures (reference 2), it was concluded that these dipoles were fluctuating lift noise similar to that from an isolated airfoil with incident turbulence. For each flap segment, calculated (reference 3) noise varies with local velocity to the sixth power and product of nozzle diameter and segment chord. It also depends on the flap location relative to the exhaust jet. Resulting predictions should be valid for a large range of flap geometries and positions.

Trailing edge noise was included as a noise component to explain the observed forward-radiated noise in directions where lift dipoles associated with wing and flap panels have negligible strength. As shown analytically in reference 9 and experimentally in reference 25, trailing edge noise is one limiting case of fluctuating lift noise as the ratio of chord to acoustic wavelength approaches infinity. For comparisons with free-field data, the numerical constants given in reference 3 for calculating fluctuating lift noise and trailing edge noise were halved.

Finally, UTW quadrupole noise is generated by two regions: the deflected distorted jet and the usually smaller contribution from the initial undistorted jet. The increase of quadrupole noise above that for an isolated jet was taken as that for deflecting the jet with a large solid surface (reference 26). This increase was approximated semi-empirically.

To these fundamental components, one must add the noise caused by feedback tones and flow attachment devices such as jet deflectors, account for changes in local velocities caused by use of mixer nozzles, and account for refraction near the deflected exhaust and reflection and shielding of each source by the wing (and at large azimuth angles by the fuselage).

Another EBF noise component method, developed at NASA (references 5 and 22), presently is limited to UTW configurations. Predictions by that method were not evaluated in the comparison presented here.

Under-the-Wing Mixer Nozzle

Of the various geometric changes tested with the half-scale UTW model, the only one that reduced the measured OASPL at constant exhaust velocity and approach flap deflection was a mixer nozzle. Acoustic and exhaust-velocity data for this configuration are given in references 27 and 28. Lift effectiveness was not reduced by this device. Because NASA's interim method for predicting EBF noise (reference 16) does not include the effects of a mixer nozzle, the method of reference 3 was applied to predicting these data. Noise beneath a UTW installation with a mixer nozzle is calculated by that method as a sum of four types of noise. These are (1) quadrupole noise of the isolated mixer nozzle, increased 3 dB to account for reflection from the wing, (2) quadrupole noise of the deflected mixed exhaust jet, calculated from the measured mixer nozzle noise, ratio of measured impingement velocity to exhaust velocity, and trailing flap deflection angle, (3) lift-dipole scrubbing noise, and (4) trailing edge noise. The last two types of noise were calculated by the methods given in reference 3 but with a specified rather than calculated impingement velocity ratio. They were then arbitrarily increased 3 dB as was found necessary in reference 3 to obtain better agreement with data for a model tested with a mixer nozzle. This increase of surface-radiated noise can be attributed to the increased turbulence level caused by the mixer nozzle.

The mixer nozzle used in the tests described in references 27 and 28 had eight lobes of which the lobe closest to the wing was blocked off. Exit area of the seven unobstructed lobes was 1255 cm^2 (195 in.^2) corresponding to a 40 cm (15.75 in.) equivalent diameter. The nozzle was tested with unheated air, and acoustic data were obtained at 15.24 m (50 ft) radius in the flyover plane. The nozzle was tested alone and with a wing having 2.08 m (82 in.) retracted-flap chord and a two-segment trailing-edge flap.

Unpublished tests at NASA Lewis Research Center have established that significant ground-reflection effects exist in the data tabulated in reference 28. Besides cancellation and reinforcement which causes wavyness in the spectra at low and mid-frequencies, there is an approximately constant increase at higher frequencies. The tabulated spectra data are believed to be approximately free-field between 200 and 1250 Hz frequencies. At higher frequencies they are believed to be roughly 2.6 dB above free field. Spectra measured with these mixer nozzles were relatively flat, with major contributions to OASPL at frequencies from 200 to 5000 Hz. As a crude approximation, roughly half the major contribution to OASPL was free-field and the remainder was 2.6 dB too large. Resulting tabulations of OASPL would then be about 1.1

dB above the free field. This correction has not been applied to the measured OASPL plotted here. However, all measured 1/3 octave spectra presented in this report include the detailed correction supply by NASA Lewis Research Center.

Measured overall sound pressure level (OASPL) directivity for the nozzle alone, and with the wing and retracted flaps, is given in figure 59 for four subsonic pressure ratios. Also shown are directivities calculated for the area-equivalent conical nozzle and for the nozzle plus wing. Directivity data for the mixer nozzle alone had been shown in references 27 and 28 to be in good agreement with data for a conical nozzle. These data can be seen in figure 59 to be predicted within about ± 2 dB by the method of reference 11. To facilitate the calculation of noise for the mixer nozzle and wing, these calculated nozzle OASPL directivities were used rather than the irregularly varying data.

Calculated directivities for the nozzle plus wing with retracted flaps were in good agreement with data taken directly below the wing. These calculations used the peak local velocity at the axial location of the trailing edge, as measured in the exhaust without a wing. At moderate and small angles below the nozzle exit, measured levels for the nozzle plus wing were only about 1 dB above those for the nozzle alone. These measured levels were overestimated by the calculations which assumed that noise in these directions was the sum of direct and reflected jet mixing noise. Quadrupole noise above the wing and attributed to the velocity-decayed exhaust jet downstream of the trailing edge was underestimated. Noise in the upper forward quadrant, which is predicted to be dominated by trailing edge noise, was overestimated by 3 to 5 dB. This error probably was caused by lower turbulence levels near the trailing edge of the retracted flap, relative to those which occur when the flap is deflected into the exhaust.

Measured and calculated spectra for the nozzle and wing with retracted flap are compared in figure 60 for pressure ratios of 1.3 and 1.7. Spectra are shown for two directions, one nearly beneath the wing and the other at maximum intensity near the exhaust jet. Spectra were calculated as the sum of the measured nozzle-alone spectra increased 3 dB to account for reflection (shown as dash lines), plus calculated spectra for scrubbing and trailing-edge noise. Calculated spectrum levels at low frequencies near 50 Hz were dominated by trailing edge noise and generally agreed with data. A measured local minimum occurred in all spectra at 100 Hz frequency for all pressure ratios and was not predicted by the calculations. At frequencies above 500 Hz which have large contributions to perceived noise level, calculated surface-radiated noise was unimportant relative to measured nozzle-alone exhaust noise. Spectra measured directly below the wing were predicted within about ± 2 dB, except for frequencies near 100 Hz, by assuming that all noise from the nozzle alone was reflected by the wing. Closer to the exhaust direction, measured spectra were overestimated by about 3 dB as would occur if this noise was not reflected.

Measured and calculated directivities are shown in figure 61 for 10° vane and 20° flap deflection. In the UTW mixer nozzle calculations given in reference 3, the directivity pattern of direct and reflected noise radiation from the mixer nozzle exhaust jet had been assumed to be unaffected by the flap. Only the impingement noise (impact noise) caused by deflection of the velocity-decayed jet was rotated through flap angle. When this was tried for this large mixer nozzle installation, the measured noise levels directly beneath the wing were underpredicted and the shape of the calculated directivity was in poor agreement with data. The calculated curves shown in figure 61 were obtained by rotating all quadrupole noise directivities through the flap deflection angle. Resulting predictions generally are in good agreement with data. Predictions are too high at the larger pressure ratios for directions near the deflected exhaust jet, as with the similar overprediction for the wing with retracted flap. Calculated levels were too low above and behind the wing, where nozzle exhaust noise and impingement noise could radiate through the flap slots rather than being shielded.

Measured and calculated spectra for this flap deflection and pressure ratios of 1.3 and 1.7 are given in figure 62 for two directions. The spectra were reasonably predicted beneath the wing but were underestimated at high frequencies at the 125° maximum-intensity direction. Also, spectra beneath the wing were systematically underestimated by 3 or 4 dB between about 200 and 630 Hz frequencies.

Measured and calculated directivities for 30° vane and 60° flap deflection are given in figure 63. The measured shape beneath the wing resembles that for a lift dipole oriented normal to the vane. Amplitude of this noise was underestimated by the calculations. Quadrupole noise near the deflected jet was overestimated, as with the smaller flap deflections. Measured and calculated spectra for this configuration at pressure ratios of 1.3 and 1.7 are given in figure 64. Directly beneath the wing, where calculated and measured OASPL's were in good agreement, spectra also were in good agreement. In the direction 40° below the nozzle inlet, where measured OASPL's were underestimated 2 to 3 dB, measured spectra were underestimated 6 to 7 dB in the 125 to 1250 Hz frequency range. Surface-radiated noise scaled to the hydraulic diameter of one mixer-nozzle lobe would be likely to have peak amplitude in this frequency range.

An alternate method for predicting noise of this mixer nozzle installation would be to scale the available data from the small-scale model of reference 29. That configuration had linear dimensions 0.15 times those of the large model. Data from the small model were scaled by use of equation (10) of reference 16 as recommended for UTW installations. Acoustic intensity thus was assumed to vary directly with nozzle exit area, inversely with far-field radius

squared, and directly with exit velocity to the 6.7 power. The resulting comparison for 30° vane and 60° flap deflection, at pressure ratios of 1.3 and 1.7, is given in figure 65. As shown in the upper part of this figure, OASPL directivity obtained from the small model had the same general shape as that for the large model but was 2 to 3 dB low. Spectra measured in the direction 80° beneath the small model and scaled to the large model were 4 to 6 dB low. For this direction, calculated spectra obtained from the isolated large mixer nozzle's measured spectra and measured velocity decay were in much better agreement with large-model data.

Noise reduction for this wing position and flap deflection with a mixer nozzle, relative to that for a conical nozzle, had been reported in references 27 and 28. This reduction in perceived noise level (PNL) is explained by the decrease of calculated surface-radiated OASPL and quadrupole impact-noise OASPL associated with decreased impingement velocity. The decrease of PNL was less than the decrease of OASPL because, at these relatively low exhaust velocities, the mixer nozzle shifts quadrupole noise from low frequencies into the high-annoyance mid-frequency range. At smaller flap deflections where surface-radiated noise and impact noise was relatively less, the decrease of PNL caused by reduced impingement velocity was nearly compensated by the nozzle-alone increase. Calculated spectra for directions that were reported in reference 4 to yield peak PNL and maximum flyover PNL were dominated by quadrupole noise. This predicted importance of quadrupole noise is verified by the measured variations of PNL with nozzle exhaust velocity to the eighth and ninth power as shown in figures 22 and 23 of reference 28.

Under-the-Wing Three-Flap Model

The under-the-wing installation tested with the noise-suppressed TF-34 engine and described in references 30 and 31 is shown in figure 66(a). Nozzle configurations included the coannular nozzle sketched, plus decayer and mixer-decayer nozzles. (In this notation, a mixer nozzle mixes the core and fan exhaust jets while a decayer nozzle mixes the outer air with the engine exhaust.) These nozzles were tested with a 25° sweptback wing having 3.9 m (12.75 ft) chord at the engine centerline with the flaps retracted. The three-segment trailing-edge flap was tested retracted and with 0° - 20° - 40° and 15° - 35° - 55° deflection. Data were obtained at 30.5 m (100 ft) radius in the flyover plane beneath the nozzle. Acoustic data were corrected by NASA for atmospheric absorption.

To evaluate the basic concepts of the noise prediction method for a wing tested in an unmixed engine exhaust rather than with unheated compressed air, some comparisons were made for tests that used the simple coannular nozzle. Maximum PNL during a simulated 152 m (500 ft) flyover was shown in figure 19(a) of reference 30 for the engine alone with this nozzle and for the engine and nozzle with the wing at all three flap deflections. These data are reproduced here as figure 66(b). They have not been corrected for ground reflection because relative differences between these curves, rather than absolute levels, are examined. For the wing with retracted flaps, directly radiated plus reflected engine-alone noise should dominate the portion of the frequency spectrum that is heavily weighted in calculating PNL. Maximum flyover PNL would then be expected to be that for the engine alone plus 3 dB for reflection from the wing surface. As shown in the figure, this simple estimate is within 1.5 PNdB of data.

Maximum flyover PNL for this nozzle and 40° trailing flap deflection was shown in figure 22(d) of reference 30 to occur at a measurement direction 40° closer to the inlet than that for the engine alone. Both of these maxima thus occurred at roughly the same direction relative to the deflected exhaust jet. Velocity decay of the exhaust jet at the flap leading-edge axial location was shown in figure 8 of reference 30 to be negligible with this exhaust nozzle. Again assuming that PNL is dominated by quadrupole noise, this noise would be predicted to be increased over that for the engine alone by $3 + 10 \log(1 + 12 \sin^2 \delta)$ dB. The jet deflection angle δ was taken as the angle between the nozzle centerline and the trailing flap. Resulting calculated increases of 11.5 dB at 40° flap angle (45° jet deflection) and 13.0 dB at 55° flap angle (60° jet deflection) are shown in figure 66(b) to be in good agreement with data.

Tabulated uncorrected spectra were supplied by NASA Lewis Research Center for 40° aft flap deflection. Before evaluating the variation of measured OASPL with direction angle, it is useful to examine corrected spectra measured at 90° azimuth direction in (or nearly in) the flyover plane. These spectra are given in figure 67 for three mass-averaged exhaust velocities and two types of measurements. The circle symbols are for microphones mounted on posts; spectra were corrected for ground reflections by the frequency-dependent empirical correction shown in figure 57. The triangle points were measured with microphones flush-mounted in a hard surface along the ground in an azimuthal plane 10° away from the flyover plane. Acoustic pressures measured with the flush-mounted microphones were decreased 6 dB to correct for in-phase reflection of sound waves at all frequencies. Corrected spectra obtained by these two methods generally were in good agreement, with largest differences at the lowest velocity.

More important, note the variations of spectrum shape with velocity. The spectra measured at 230 m/sec were relatively smooth and resembled those from small-scale models. Maximum amplitude occurred within a broad peak extending between about 100 to 400 Hz frequencies. In contrast, at 167 m/sec a relatively sharp peak centered at 80 Hz protruded above the smooth shape. Roughly half of the OASPL measured between 50 and 20,000 Hz was caused by this peak region between 50 and 100 Hz. Clearly, OASPL at this velocity would be about 3 dB larger than what should be attributed to the externally blown flap. Decreasing the exhaust velocity to 122 and (not shown here) 108 m/sec shifted this peak to the 50 Hz one-third-octave band. This additional low-frequency noise decreased less rapidly with exhaust velocity than did the smooth peak, and it dominated the measured OASPL. Because of the large contribution of this sharp peak and the relatively large contributions to OASPL expected from portions of the smoothed spectrum below 50 Hz, corrected OASPL's were not calculated for 122 m/sec and lower exhaust velocities. For 167 m/sec they were calculated excluding the 50, 63, and 83 Hz bands, while for 230 m/sec they were calculated using all of the measured frequency range. These spectra also contain a high-frequency hump between 6300 and 10,000 Hz at the lower exhaust velocities. This high-frequency noise probably was engine turbine tones. It had almost disappeared within the smooth spectrum at 167 m/sec exhaust velocity.

Corrected OASPL directivities in the flyover plane for 167 and 230 m/sec exhaust velocities are compared in figure 68 with predictions by several methods. Corrected levels measured with post-mounted and with flush-mounted microphones generally agreed within ± 1 dB. The NASA ANOPP method of reference 16 and the method evaluated in this report were in good agreement with these data. Good agreement had been expected for the ANOPP method because these specific data for 90° azimuth angle were used in developing that method. The calculated directivity curve shown in figure 68 for this method was obtained by interpolating between the curves given in figure 13 of reference 16 for 20° and 60° flap angle. The predicted minimum near 120° does not match the data and was caused by the large minimum near this direction for 60° flap angle. The GEIAC method of reference 17 overestimates these data by about 10 dB.

Measured and calculated variations of corrected OASPL with sideline angle, in the azimuthal plane perpendicular to the nozzle centerline, are given in figure 69. All three methods predict the measured trend; the ANOPP method and the method of this report predict the measured levels. For surface-radiated noise varying with sine squared of the angle from the sideline plane, decreases of 4, 7, and 14.5 dB below the levels measured in the flyover plane would be expected at the three measurement angles near the sideline plane. The 4 dB decrease predicted for 38.8° angle did occur, but only about 7 dB total decrease occurred at the angle closest to the sideline plane. The method evaluated in this report predicts that noise at shallow angles from the

sideline plane is dominated by quadrupole noise from the deflected jet as viewed from the side. Surface-radiated noise is predicted to decrease below this quadrupole noise floor.

Corrected spectra for three sideline angles and three exhaust velocities are compared in figure 70 with predictions by the NASA ANOPP method and by the method of this report. Spectra calculated by the ANOPP method are shown only for 100° and 10.9° angle relative to the sideline plane because normalized spectra are given in figure 15 of reference 16 for only 90° and 0° angles. At 122 and 167 m/sec exhaust velocities shown in figure 70(a) and (b), the high-frequency portions of spectra calculated by the two methods approximately agree. However, measured one-third-octave spectrum levels often were about 5 dB larger than the predictions. Predicted spectra were calculated by use of generalized spectra normalized relative to OASPL. For this full-scale configuration at low exhaust velocities, an appreciable contribution to OASPL was predicted by the method examined in this report to occur at frequencies below 50 Hz. However, measured OASPL was determined only for the measurement range above that frequency. Thus it was possible to have good agreement between measured corrected OASPL and the predictions but relatively poor agreement between measured and predicted spectra. At 230 m/sec exhaust velocity (figure 70(c)), spectra calculated by the ANOPP method were about 3 dB larger than those for the method of this report. The spectrum measured near the flyover plane was in good agreement with calculations by the ANOPP method; the empirical normalized spectrum for 40° flap deflection had been drawn through these data. Spectra measured at directions closer to the sideline plane had a less rapid decay than was predicted by either method. One weakness of the noise component method examined in this report is that the spectrum shape of quadrupole noise from a deflected exhaust jet is assumed to be independent of sideline angle. This incorrect assumption causes poor predictions of spectrum shape at small angles from the sideline plane.

A comparison between calculated and measured directivities and spectra for a small-scale model of this three-flap UTW configuration is given in reference 32. The small-scale model was tested at a smaller (18° - 20° - 25°) and a larger (8° - 55° - 65°) deflection than for the data just presented. At the smaller deflection, the last flap segment extended further into the exhaust jet than did the last segment of two-flap models which form the data base for the ANOPP method (reference 16) or the GELAC method (reference 17). Measured OASPL directly beneath the wing, at this flap deflection, was underestimated about 4 dB by the method of this report but was underestimated about 10 dB by the other two methods. All methods generally matched the data for the larger flap deflection. Spectra for this small model, scaled in frequency and amplitude, closely matched the spectra measured with a half-scale cold-jet model.

Surface pressure fluctuation spectra had been measured on the lower surface of these flaps tested with the TF-34 engine (reference 33). As in the small-scale tests described in reference 1, maximum overall intensity occurred roughly where a line parallel to the exhaust centerline, and extended from the nozzle upper lip, would intersect the flap surface. This position moved upstream from the second flap segment to the first segment as flap deflection was increased from takeoff (0° - 20° - 40°) to landing (15° - 35° - 55°). Near the trailing edge, maximum surface pressure fluctuations occurred roughly one nozzle radius to the side of the centerline plane. This behavior had been interpreted in reference 1 as caused by pressure fluctuations generated by the jet mixing process, impressed against the flaps, and damped by convection along the solid-surface flaps.

Measured pressure fluctuations of about 165 dB for both flap deflections at 235 m/sec (770 ft/sec) exhaust velocity were reported in reference 33. These were stated to correspond to an rms static pressure fluctuation of 0.2 times the exhaust dynamic pressure, which is twice the maximum level generally reported for flaps tested with cold jets. Taking the viewpoint that the fluctuations are caused by mixing between the outer air and the fan exhaust stream, the relevant dynamic pressure should not be the 1880 kg/m^2 (385 lb/ft^2) average value for the partially mixed hot core and cooler fan exhaust at the nozzle exit. The larger value of 3450 kg/m^2 (706 lb/ft^2) corresponding to average jet velocity and ambient air density would be a more appropriate dynamic pressure. A pressure fluctuation 10% of this quantity would be 164.6 dB, in agreement with measured maximum levels along the centerline. Further aft, maximum measured levels of about 161 dB at 1.3 nozzle radii to the side of the centerline correspond to 0.065 times the revised dynamic pressure. This ratio is a typical maximum level in the mixing region of an isolated exhaust jet. Measured eddy convection speeds of 0.5 to 0.9 times the exhaust velocity were reported in reference 28 for the full-scale flaps and TF-34 engine exhaust. These agree with the convection speed ratio of 0.8 reported in reference 1 for tests with a small unheated jet.

The major result from this comparison is that surface pressure fluctuations on externally blown flaps scrubbed by the exhaust of a turbofan engine can be scaled from data for small unheated jets if dynamic pressure is based on average exhaust velocity and atmospheric density. If this dependence on external air density rather than hot exhaust-gas density is neglected, surface pressure fluctuations would be underestimated by about 6 dB.

Upper Surface Blowing

Noise Radiation Patterns

Upper-surface-blowing installations tested with the noise-suppressed TF-34 engine and described in references 33 and 34 are sketched in figure 71. The engine core exhaust was passed through a twelve lobe mixer nozzle to provide a nominally uniform engine exhaust. Two exit nozzles were used: a circular nozzle with deflector and a 4:1 slot nozzle canted 20° relative to the engine centerline. The slot nozzle had about 15% larger exit area. Each nozzle was tested with the two flap configurations shown in the lower part of figure 71. The short flap was on an unswept wing and provided either 8° , 40° , or 75° deflection of the upper surface at the trailing edge. The long flap was tested on a 25° sweptback wing that would have had the same retracted wing chord and nozzle location. With 40° upper surface deflection at the trailing edge, the distance from the nozzle exit to the flap trailing edge was 5.0 circular-nozzle diameters for the long flap and 3.2 for the short flap. Acoustic data were supplied by NASA for the short flap, slot nozzle and long flap, circular nozzle configurations at 40° flap deflection. Data for the flyover plane were measured with microphones flush with the ground. They were corrected by NASA for ground reflection and atmospheric attenuation.

Noise calculations were conducted by the method of reference 3 for USB configurations with circular nozzles. The effect of wing sweepback on noise was neglected. Quadrupole noise from the canted slot nozzle's exhaust jet downstream of the trailing edge was arbitrarily increased by twelve times the sine squared of the cant angle as for quadrupole impact noise. This change, amounting to a 3.8 dB increase, was found in reference 3 to provide better agreement with data for upper surface blowing with a small 5:1 slot nozzle. Calculations were conducted for the trailing-edge velocity ratios measured at the trailing-edge distance for the actual configurations. For the slot nozzle and short flap, typical measured maximum velocity ratios ranged from 1.01 to 1.02. These are not significantly different from the value of 0.997 calculated for the same axial distance in an isolated jet. The circular nozzle and long flap had measured peak velocity ratios of only about 0.76 as compared with a calculated ratio near 0.98.

Measured noise radiation patterns for the TF-34 engine and circular nozzle with deflector and long flap at 40° deflection are compared with predictions in figure 72. The open symbols are OASPL of the spectra as measured above 50 Hz one-third-octave center frequency. Because the measured spectra of this full-scale configuration had maximum amplitudes near 100 Hz frequencies, it is likely that significant acoustic energy was radiated at frequencies below those for the measurements. The true OASPL was estimated as 1 to

2 dB above these data. Measured radiation patterns were relatively constant in the lower forward quadrant but had a peak in the lower aft quadrant. This peak had maximum amplitude about 20° below the deflected trailing edge and was most prominent at high exhaust velocities. In these directions, amplitude varied approximately with velocity to the eighth power. The directivity shape and velocity dependence are typical of quadrupole noise from a deflected exhaust jet.

Noise radiation patterns were calculated from the model geometry and the measured maximum trailing-edge velocity ratio of 0.76. This ratio caused the calculated surface-radiated noise to be 6 to 7 dB less than would have been obtained with the velocity ratio predicted for an isolated jet. As shown in figure 72(a), measured amplitudes were underestimated about 3 dB directly beneath the wing. The aft quadrupole peak was not predicted, causing up to 9 dB underestimate at 120° direction and the larger velocities.

Noise radiation patterns also were predicted by the NASA ANOPP method of reference 16 and the GELAC method of reference 17, and by scaling the data from small-model tests of references 35 and 36. Although these models had relatively longer flaps than those of the full-scale installations, they were the only ones for which data were openly available. These patterns are compared with the full-scale data in figure 72(b). Directivity shapes and amplitudes in the lower forward quadrant were closely predicted by the ANOPP method. The aft peak was not predicted, and about 5 dB underestimate of amplitude occurred.

Small-model data from references 35 and 36 for 60° and 20° aft flap deflection, respectively, were averaged to provide an estimate of noise radiation for 40° deflection. The ratio of flap length to nozzle diameter for the small models was about 1.4 times that for the full-scale model. As in the method of reference 16, sound intensity was scaled with exhaust velocity to the sixth power, nozzle area to the first power, and far-field radius to the inverse second power. The resulting scaled data are shown in figure 72(b) as solid symbols for the two velocities closest to those for which tabulated small-scale data had been provided by NASA. They are in excellent agreement with ANOPP predictions for all directions and with large-scale data for the lower forward quadrant. As with the two analytical prediction methods, they do not contain the prominent aft peak.

Measured noise radiation patterns for the TF-34 engine with canted 4:1 slot nozzle and short flap at 40° deflection are compared with predictions in figure 73. This configuration was about 4 dB louder than the circular nozzle with deflector and long flap, for which data were given in figure 72. Data also were given in reference 29 for the other two combinations of nozzle shape and flap length. It was shown that increased noise was associated with

the short flap rather than the slot nozzle. Maximum trailing-edge velocity ratio for both short-flap configurations was approximately equal to unity. As shown in figure 73(a), the method of this report closely predicted the measured noise radiation pattern in the lower forward quadrant, except for about 2 dB overestimate at the highest velocity. The aft peak was underestimated by 3 to 6 dB.

Predictions by the NASA ANOPP and GELAC methods, and with scaled small-model data, are shown in figure 73(b). The ANOPP method does not include flap length as a parameter. Its prediction at constant exhaust velocity was 0.6 dB larger than that for the circular nozzle with deflector because the slot nozzle had a larger exhaust area. This prediction agreed with data for the lower forward quadrant and the highest exhaust velocity but underestimated these data at lower velocities. Measured noise, and that calculated by the method of this report, varied approximately with exhaust velocity to the fifth power for this range of direction and velocity. In contrast, a sixth power variation is specified in the NASA ANOPP and GELAC methods.

Small-model data from the aspect ratio 5:1, 20° flap deflection canted slot nozzle configuration of reference 37 were scaled as a reference model for the aspect ratio 4:1, 40° flap deflection full-scale model. The ratio of flap length to nozzle hydraulic diameter was nearly 1.9 times full scale. Thus the small-scale model had a relatively long flap compared with that for the full-scale tests. Scaled data, shown in figure 73(b) for two velocities, agreed with full-scale data directly below the wing but did not reproduce the peak near the deflected jet. Use of these data provided only about 3 dB underestimate of this peak.

Noise radiation patterns were given in reference 34 for full-scale upper surface blowing configurations tested with the noise-suppressed TF-34 engine. Wings having short or long flaps, 8°, 40°, or 75° aft flap deflection, and circular or slot nozzles all had a peak of quadrupole noise located about 30° beneath the deflected jet. This peak did not occur in tests of small-scale models (references 35-37) or nominal half-scale models (reference 38) that used unheated compressed air in the exhaust jet. The cause of this strong quadrupole noise lobe below the engine's deflected exhaust is not known. The engine's turbulence level presumably cannot be blamed because surface-radiated noise in the forward quadrant was adequately predicted. Subsequent unpublished tests have been conducted at NASA Lewis Research Center of a small-scale model that closely reproduced the large model's geometric shape. Results of these tests are believed to match those for the large model.

Spectra in Flyover Plane

Spectra measured at three directions in the flyover plane, with the circular-nozzle and slot-nozzle configurations, are given in figure 74. Data

are plotted for exhaust velocities of 241 and 179 m/sec (792 and 588 ft/sec) for the circular nozzle and 242 and 168 m/sec (795 and 550 ft/sec) for the slot nozzle. These velocities correspond to exhaust pressure ratios near 1.45 and 1.2, respectively. Also plotted are spectra calculated by the method investigated in this report (solid lines) and the NASA ANOPP method of reference 16 (dash lines). Spectra calculated by the NASA ANOPP method have the same normalized shape for all measurement directions in the flyover plane and for all exhaust velocities. Spectra calculated by the method of this report have normalized shapes that depend on the calculated ratio of surface-radiated noise to quadrupole noise for each selected direction and velocity. Spectra obtained by scaling the small-model data from references 35-37 are shown as solid symbols. As with the scaled OASPL, tabulated data for the circular nozzle and both 20° and 60° trailing flap deflection angle were averaged to obtain spectra for 40° deflection. Tabulated data for the slot nozzle and 20° flap deflection were utilized for 40° deflection. Data for both configurations at the same measurement direction are shown on the same page.

Spectra for 60° measurement direction and the circular nozzle with long flap are given in figure 74(a). These spectra were closely predicted (about 2 dB underestimate) by the NASA ANOPP method except for an apparent background noise floor at high frequencies. The method of this investigation underestimated the data by about 6 dB at frequencies near 2000 Hz that are heavily weighted when calculating perceived noise levels. Scaled small-model data from references 35-37 gave a close prediction of full scale data below 400 Hz frequency. However, the scaled small-model data decreased much more rapidly as frequency was increased. Spectra for this measurement direction and the slot nozzle and short flap are given in figure 74(b). The NASA ANOPP method again gave only several dB overestimate, but the method of this study gave a closer prediction for this configuration. Scaled small-model spectra were in worse agreement with full-scale spectra and had too rapid a spectrum decay.

Spectrum comparisons directly below the wing at 90° measurement direction are given in figures 74(c) and (d). Predictions were somewhat worse than at 60°, with the NASA ANOPP method closest for the circular nozzle and long flap and the method of this study closest for the slot nozzle and short flap. Each method was about 7 dB too low for the opposite configuration. Scaled small-model data from references 35-37 decayed too rapidly and would give the worst underestimate of perceived noise level. This discrepancy may have been caused by differences in ratio of flap length to nozzle diameter and in deflector shape between the large and small models.

Spectra for 120° measurement direction and the circular nozzle with long flap are shown in figure 74(e). Quadrupole OASPL beneath the deflected jet had been largest in this direction. This method and the NASA ANOPP method underestimate the data by about 9 and 6 dB, respectively. The 9 dB error corresponds to the decrease of quadrupole noise calculated for the exhaust jet downstream of the trailing edge by use of the measured trailing-edge velocity ratio. That is, spectrum levels at frequencies above roughly 2000 Hz are equal to those for the isolated engine exhaust jet rotated through the flap deflection angle. This result had been indicated in figure 16 of reference 34 where OASPL directivities were plotted for several flap deflections. Maximum OASPL above the deflected exhaust jet but below the horizon, at 75° flap deflection, was approximately equal to that below the exhaust jet at 8° , 40° , and 75° flap deflection. In contrast, nominal half-scale (reference 38) and small-scale (references 35-37) upper surface blowing models with unheated compressed-air exhaust jets were about 10 dB louder at directions above the deflected exhaust than below it. This difference in OASPL directivity is believed to have been caused by the deflector shape used with the full-scale configuration. Data for geometrically similar large and small EBF models with hot or cold exhaust jets tested at NASA Lewis Research Center have been found to scale well.

Spectra for 120° measurement angle and the slot nozzle with short flap are plotted in figure 74(f). They were underestimated about 2 dB over most of the frequency range by the method investigated here. Maximum one-third-octave levels at low frequencies were underestimated by a larger increment. The NASA ANOPP method gave predictions that were about 9 dB too low. Scaled small-model data were about 6 dB low above 500 Hz frequency. Their decay rate was smaller than for directions further upstream and agreed with that for full-scale data.

PAPERS GENERATED DURING CONTRACT YEAR

The following technical papers were generated either directly or indirectly as a result of this contract during this third year of Contract NAS3-17863.

Fink, M. R.: Scrubbing Noise of Externally Blown Flaps. Progress in Astronautics and Aeronautics, Vol. 45, Aeroacoustics: STOL Noise; Airframe and Airfoil Noise, edited by I. R. Schwartz, M.I.T. Press, Cambridge, Mass., 1976, pp 3-25.

Fink, M. R.: Experimental Evaluation of Theories for Trailing Edge and Incidence Fluctuation Noise. AIAA Journal, Vol. 13, No. 11, Nov. 1975, pp 1472-1477.

Fink, M. R. and Olsen, W. A.: Comparison of Predictions and Under-the-Wing EBF Noise Data. Paper 76-501, AIAA, July 1976.

Fink, M. R.: Approximate Prediction of Airframe Noise. Paper 76-526, AIAA, July 1976. To be published in Journal of Aircraft, Vol. 13, No. 11, Nov. 1976.

CONCLUSIONS

1. Externally blown flap noise spectra in forward flight can be calculated from those measured at zero flight speed. For all frequencies at low subsonic exhaust velocities, and for Strouhal numbers less than about one at high subsonic exhaust velocities, the zero-flight-speed spectrum must be decreased in amplitude and shifted to higher frequencies. The adjustment for high Strouhal numbers and high subsonic exhaust velocities is a decrease of amplitude at constant frequency.

2. Directivity and spectra of large-scale externally blown flap models, including an under-the-wing mixer nozzle configuration, are predicted by a noise component method. OASPL directivity generally was predicted within ± 3 dB; $1/3$ octave spectra generally were predicted within 5 dB except for the USB circular nozzle and deflector.

3. Crosscorrelations show that externally blown flap far-field noise is associated with turbulence generated within the exhaust jet, is radiated when this turbulent region approaches the trailing edge, and propagates in all directions including forward along the wing's shielded surface.

REFERENCES

1. Fink, M. R.: Investigation of Scrubbing and Impingement Noise. NASA CR-134762, Feb. 1975.
2. Fink, M. R.: Scrubbing Noise of Externally Blown Flaps. Paper 75-469, AIAA, Mar. 1975. Also, Progress in Aeronautics and Astronautics, Vol. 45, Aeroacoustics: STOL Noise; Airframe and Airfoil Noise, edited by I. R. Schwartz, M.I.T. Press, Cambridge, Mass., 1976, pp 3-25.
3. Fink, M. R.: Prediction of Externally Blown Flap Noise and Turbo-machinery Strut Noise. NASA CR-134883, Aug. 1975.
4. Fink, M. R.: Experimental Evaluation of Theories for Trailing Edge and Incidence Fluctuation Noise. AIAA Journal, Vol. 13, No. 11, Nov. 1975, pp 1472-1477.
5. McKinzie, D. J., Jr., Burns, R. J., and Wagner, J.: Noise Reduction Tests of Large Scale Model Externally Blown Flap Using Trailing Edge Blowing and Partial Flap Slot Covering. NASA TM X-3379, April 1976.
6. Reddy, N. N., Blakney, D. F., Tibbetts, J. G., and Gibson, J. S.: V/STOL Aircraft Noise Prediction. Lockheed-Georgia Co. LG 75ERO054, June 1975. Also, Federal Aviation Administration Report No. FA-RD-75-125, to be published.
7. Siddon, T. E.: Surface Dipole Strength by Cross-Correlation Method. J. Acoust. Soc. Am., Vol. 53, No. 2, Feb. 1973, pp 619-633.
8. Clark, P. J. F. and Ribner, H. S.: Direct Correlation of Fluctuating Lift With Radiated Sound for an Airfoil in Turbulent Flow. J. Acoust. Soc. Am., Vol. 46, No. 3, Pt. 2, Oct. 1969, pp 802-805.
9. Tam, C. K. W. and Yu, J. C.: Trailing Edge Noise. Paper 75-489, AIAA, Mar. 1975.
10. Paterson, R. W., Vogt, P. G., and Foley, W. M.: Design and Development of the United Aircraft Research Laboratories Acoustic Research Tunnel. J. of Aircraft, Vol. 10, No. 7, July 1973, pp 427-433.
11. Stone, J. R.: Interim Prediction Method for Jet Noise. NASA TM X-71618, Dec. 1974.

12. Falarski, M. D., Aiken, T. N., Aoyagi, K., and Koenig, D. G.: Comparison of the Acoustic Characteristics of Large-Scale Models of Several Propulsive-Lift Concepts. J. of Aircraft, Vol. 12, No. 7, July 1975, pp 600-604.
13. Morris, P. J.: Turbulence Measurements in Subsonic and Supersonic Axisymmetric Jets in a Moving Stream. Paper No. 76-25, AIAA, Jan. 1976.
14. Bhat, W. V. and Gallo Rosso, D.: Effect of Forward Speed on Jet Wing/Flap Interaction Noise. Paper 75-475, AIAA, Mar. 1975.
15. Gibson, J. S. and Searle, N.: Characteristics of USB Noise. Paper 15, Powered-Lift Aerodynamics and Acoustics. NASA SP-406, May 1976, pp 227-239.
16. Dorsch, R. G., Clark, B. J., and Reshotko, M.: Interim Prediction Method for Externally Blown Flap Noise. NASA TM X-71768, Aug. 1975.
17. Guinn, W. A., Blakney, D. F., and Gibson, J. S.: V/STOL Noise Prediction and Reduction. FAA-RD-73-145, Aug. 1973.
18. Goodykoontz, J., von Glahn, U., and Dorsch, R.: Forward Velocity Effects on Under-the-Wing Externally Blown Flap Noise. Paper 75-476, AIAA, Mar. 1975.
19. Falarski, M. D., Aoyagi, K., and Koenig, D. G.: Acoustic Characteristics of Large-Scale STOL Models at Forward Speed. NASA TM X-62251, Oct. 1972.
20. Dorsch, R. G., Goodykoontz, J. H., and Sargent, N. B.: Effect of Configuration Variation on Externally Blown Flap Noise. Paper 74-190, AIAA, Jan. 1974.
21. Clark, B., Dorsch, R., and Reshotko, M.: Flap Noise Prediction Method for a Powered Lift System. Progress in Astronautics and Aeronautics, Vol. 38, Aeroacoustics, edited by H. T. Nagamatsu, M.I.T. Press, Cambridge, Mass., 1975, pp 99-112.
22. McKinzie, D. J., Jr. and Burns, R. J.: Analysis of Noise Produced by Jet Impingement Near the Trailing Edge of a Flat and a Curved Plate. NASA TM X-3171, Jan. 1975.
23. Olsen, W. A. and Karchmer, A.: Lip Noise Generated by Flow Separation From Nozzle Surfaces. Paper 76-3, AIAA, Jan. 1976.

24. Fink, M. R.: Mechanisms of Externally Blown Flap Noise. Progress in Astronautics and Aeronautics, Vol. 38, Aeroacoustics, edited by H. T. Nagamatsu, M.I.T. Press, Cambridge, Mass., 1975, pp 113-128.
25. Olsen, W. A.: Noise Generated by Impingement of a Turbulent Jet on Isolated Airfoils of Varying Chord, Cylinders, and Other Flow Obstructions. Paper 76-505, AIAA, July 1976.
26. Olson, W. A., Miles, J. H., and Dorsch, R. G.: Noise Generated by Impingement of a Jet Upon a Large Flat Board. NASA TN D-7075, Dec. 1972.
27. Goodykoontz, J. H., Dorsch, R. G., and Wagner, J. M.: Acoustic Characteristics of Externally Blown Flap Systems With Mixer Nozzles. Paper 74-192, AIAA, Jan. 1974.
28. Goodykoontz, J. H., Dorsch, R. G., and Groesbeck, D. E.: Noise Tests of a Mixer Nozzle-Externally Blown Flap System. NASA TN D-7236, May 1973.
29. Goodykoontz, J. H., Olsen, W. A., and Dorsch, R. G.: Small-Scale Tests of the Mixer Nozzle Concept for Reducing Blown-Flap Noise. NASA TM X-2638, Nov. 1972.
30. Samanich, N. E., Heidelberg, L. J., and Jones, W. L.: Effect of Exhaust Nozzle Configuration on Aerodynamic and Acoustic Performance of an Externally Blown Flap System With a Quiet 6:1 Bypass Ratio Engine. NASA TM X-71466, Nov. 1973. Also, Paper 73-1217, AIAA, Nov. 1973.
31. Jones, W. L. and Heidelberg, L. J.: Investigation of Noise From Full-Scale High Bypass Engine and Blown Flap System. NASA TM X-71539, April 1974. Also, SAE Paper 740467, April 1974.
32. Fink, M. R. and Olsen, W. A.: Comparison of Predictions and Under-the-Wing EBF Noise Data. Paper 76-501, AIAA, July 1976.
33. Schoenster, J. A.: Acoustic Loads on an Externally Blown Flap System Due to Impingement of a TF-34 Jet Engine Exhaust. NASA TM X-71950, April 1974.
34. Heidelberg, L. J., Homyak, L., and Jones, W. L.: Full-Scale Upper-Surface-Blown Flap Noise. NASA TM X-71708, May 1975. Also, SAE Paper 750609, May 1975.

35. Reshotko, M., Olsen, W. A., and Dorsch, R. G.: Preliminary Noise Tests of the Engine-Over-The-Wing Concept, I. 30° - 60° Flap Position. NASA TM X-68032, Mar. 1972.
36. Reshotko, M., Olsen, W. A., and Dorsch, R. G.: Preliminary Noise Tests of the Engine-Over-The-Wing Concept, II. 10° - 20° Flap Position. NASA TM X-68104, June 1972.
37. Dorsch, R. G., Reshotko, M., and Olsen, W. A.: Flap Noise Measurements for STOL Configurations Using External Upper Surface Blowing. Paper 72-1203, AIAA, Dec. 1972.
38. Reshotko, M., Goodykoontz, J. H., and Dorsch, R. G.: Engine-Over-The-Wing Noise Research. NASA TM X-68246, July 1973. Also, Paper 73-631, AIAA, July 1973.

MICROPHONE LOCATIONS AT 5, 15, 30, 38, 50, 62, 70 AND 80% CHORD

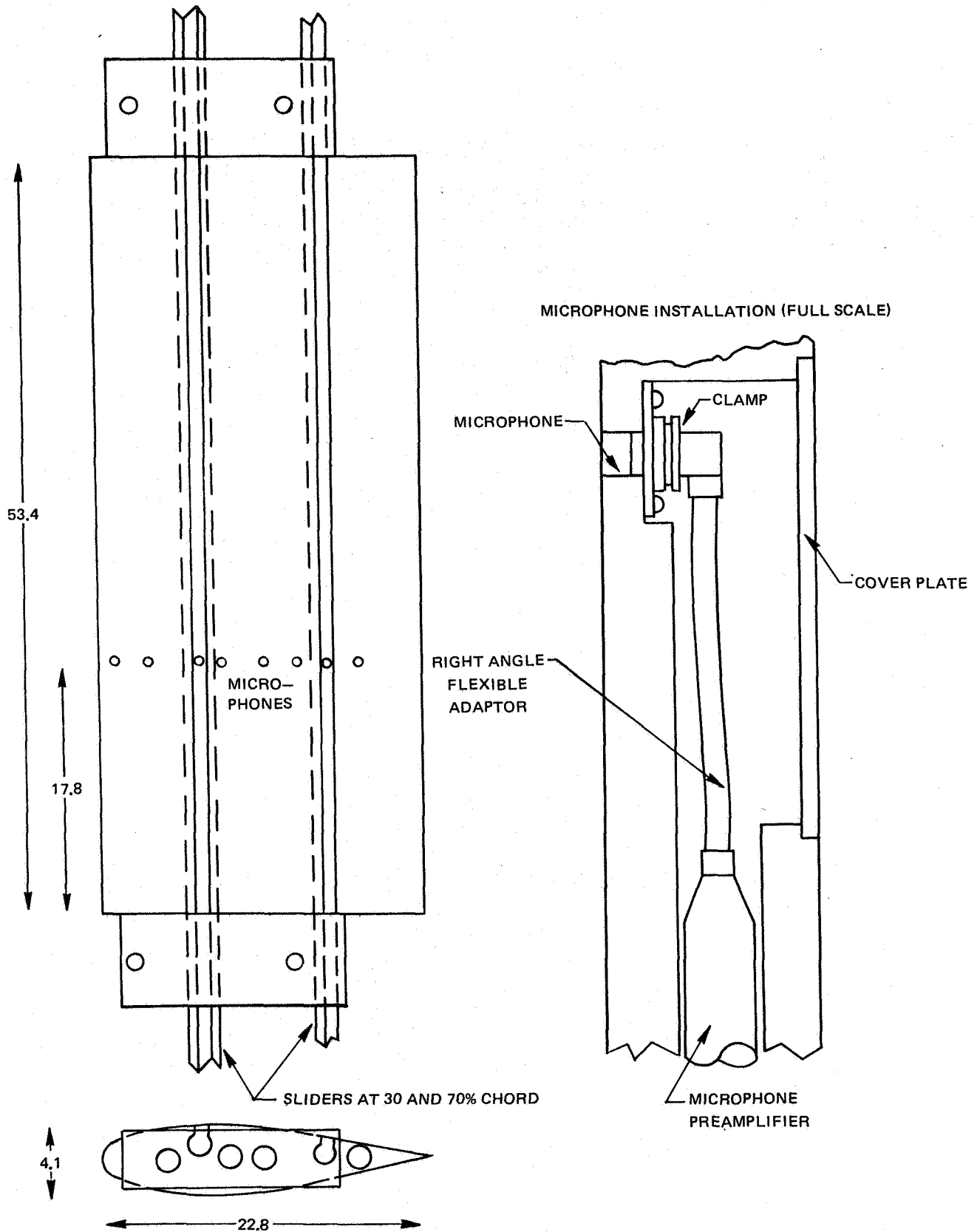
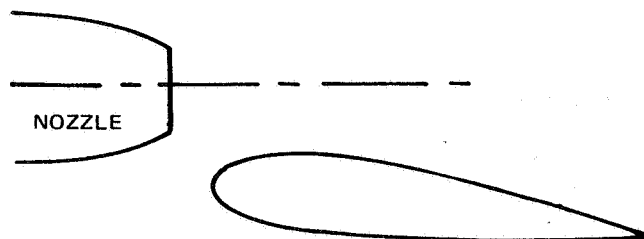
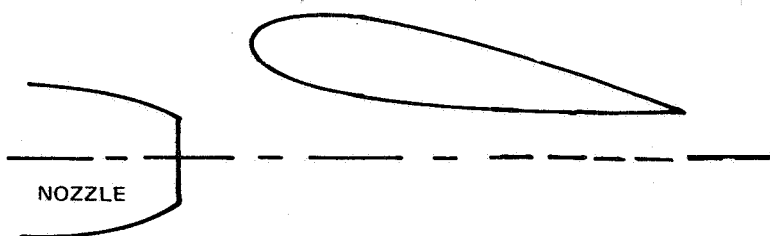


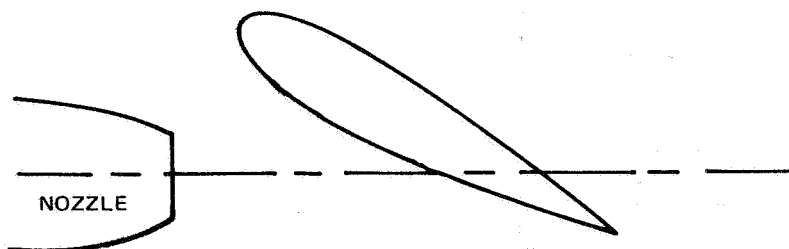
FIGURE 1 - NACA 0018 AIRFOIL. ONE-QUARTER SCALE, ALL DIMENSIONS IN CENTIMETERS.



(a) UPPER SURFACE BLOWING, 90° DEFLECTION

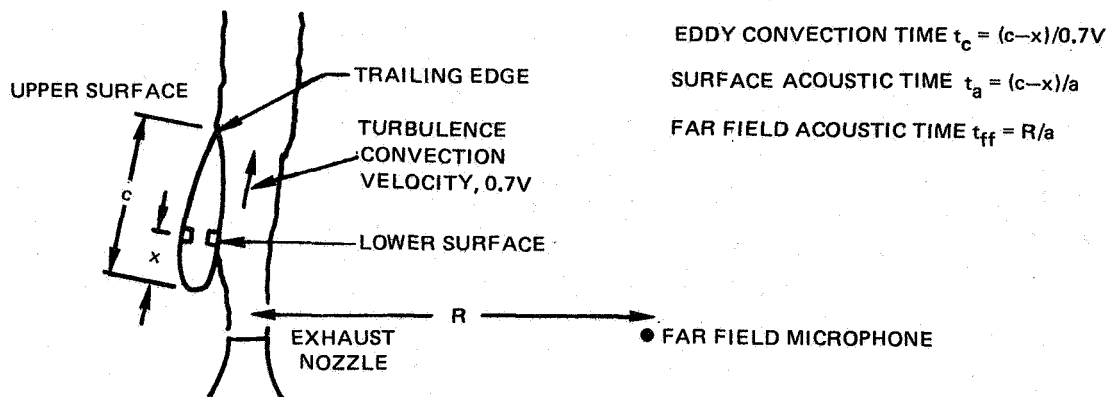


(b) UNDER THE WING, 90° DEFLECTION

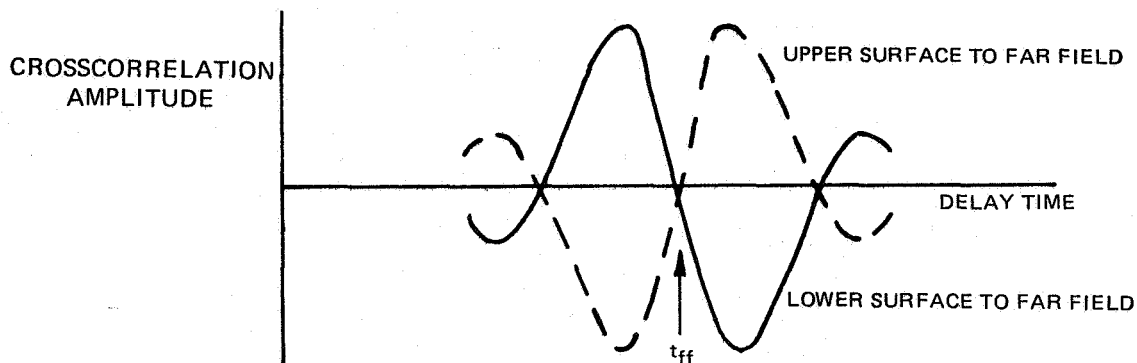


(c) UNDER THE WING, 30° DEFLECTION

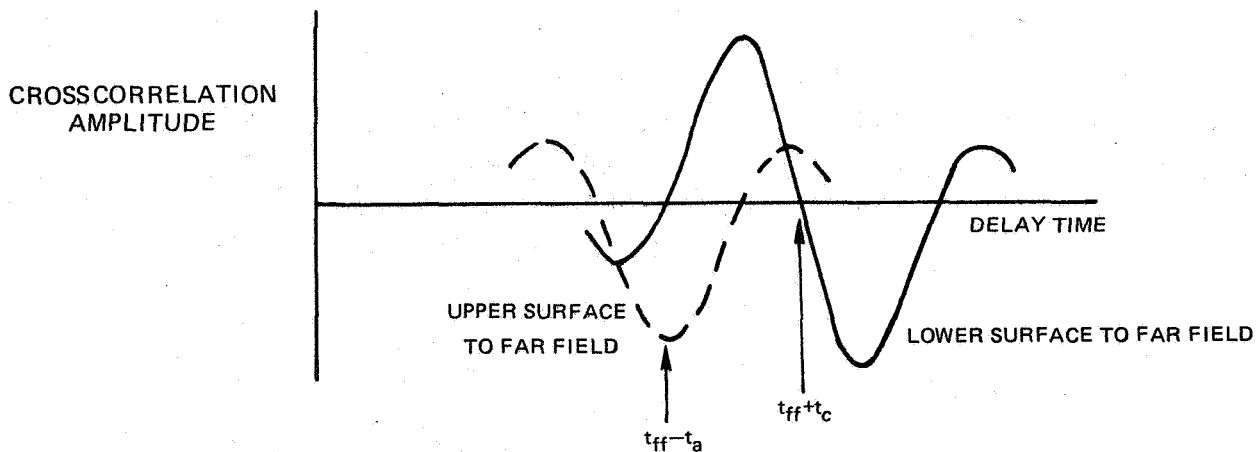
**FIGURE 2— NOZZLE AND DEFLECTED NACA 0018 AIRFOIL POSITIONS
SIMULATING EXTERNALLY BLOWN FLAPS. ¼ SCALE**



DEFINITION OF TIMES FOR EVALUATING CROSSCORRELATIONS



NOISE CAUSED BY FLUCTUATION OF AIRFOIL LIFT



NOISE RADIATED FROM TRAILING EDGE DUE TO TURBULENCE CONVECTED ALONG LOWER SURFACE

FIGURE 3— INTERPRETATION OF CROSSCORRELATIONS BETWEEN EXTERNALLY BLOWN FLAP SURFACE PRESSURES AND FAR FIELD ACOUSTIC PRESSURES

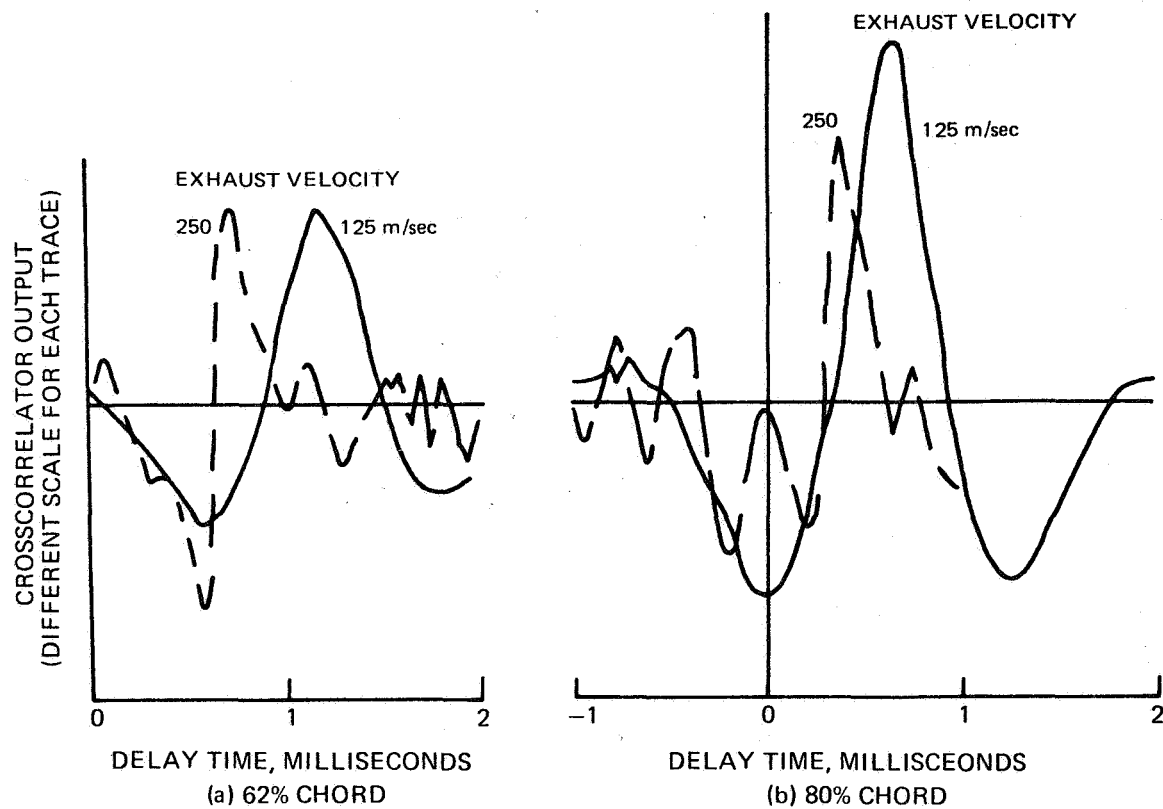


FIGURE 4 – CROSSCORRELATIONS OF AIRFOIL UPPER AND LOWER SURFACE PRESSURE SIGNALS AT CONSTANT CHORD FOR UNDER-THE-WING, 90° DEFLECTION. LOWER SURFACE DELAYED RELATIVE TO UPPER SURFACE

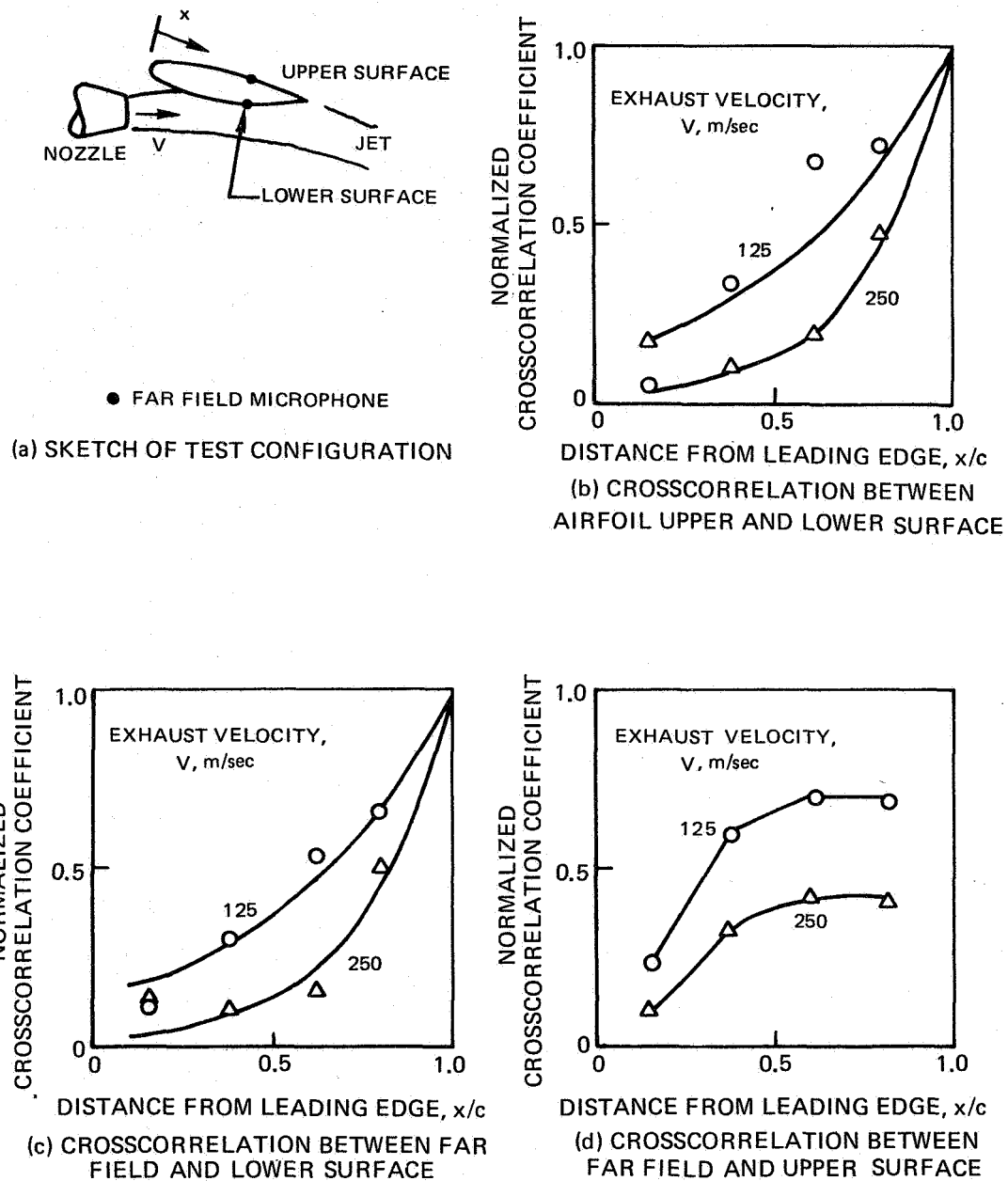
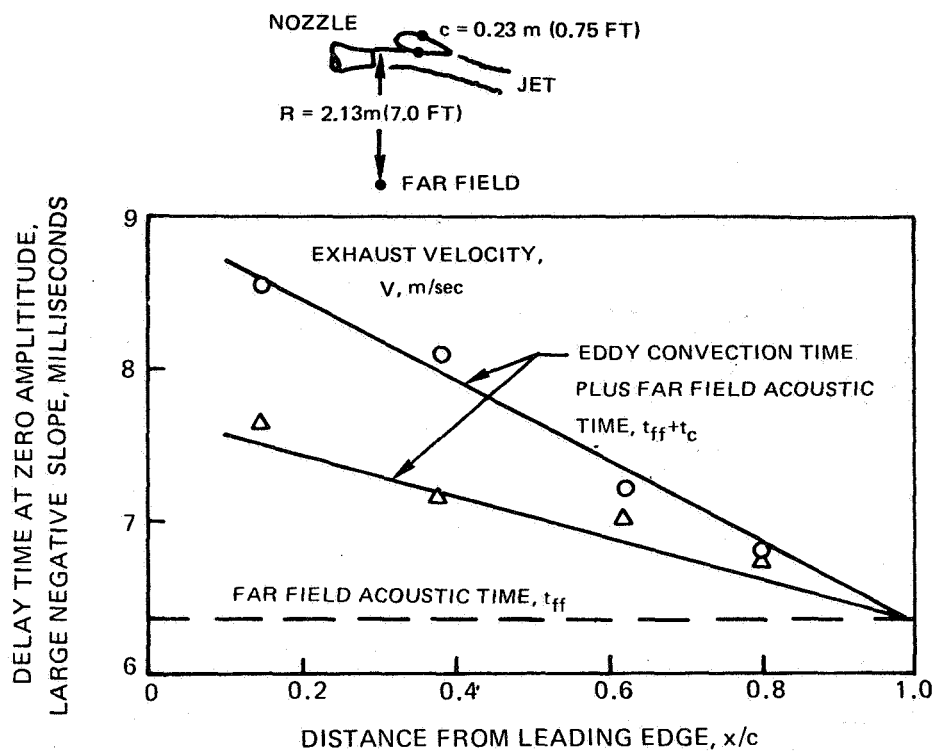
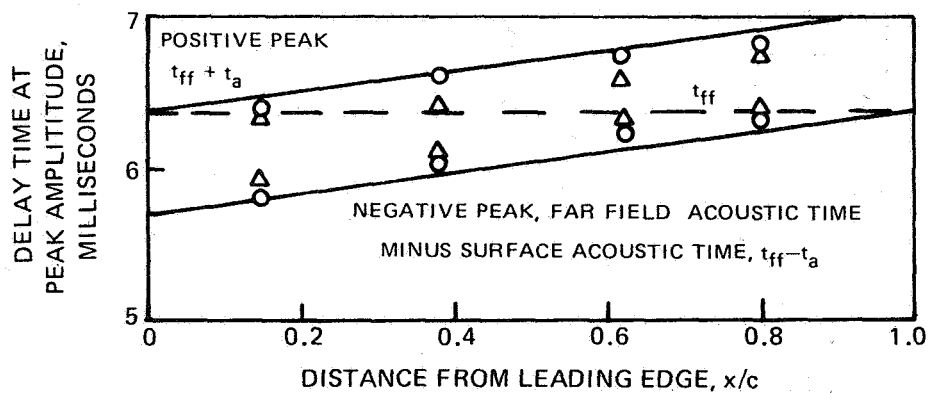


FIGURE 5 – CROSSCORRELATION COEFFICIENTS FOR UNDER-THE-WING CONFIGURATION AT 90° DEFLECTION



(a) CROSSCORRELATION DELAY TIME BETWEEN AIRFOIL LOWER SURFACE AND FAR FIELD



(b) CROSSCORRELATION DELAY TIME BETWEEN AIRFOIL UPPER SURFACE AND FAR FIELD

FIGURE 6— DELAY TIMES FOR SIGNIFICANT EVENTS IN CROSSCORRELATIONS BETWEEN FAR FIELD AND UNDER-THE-WING 90° DEFLECTION AIRFOIL SURFACES

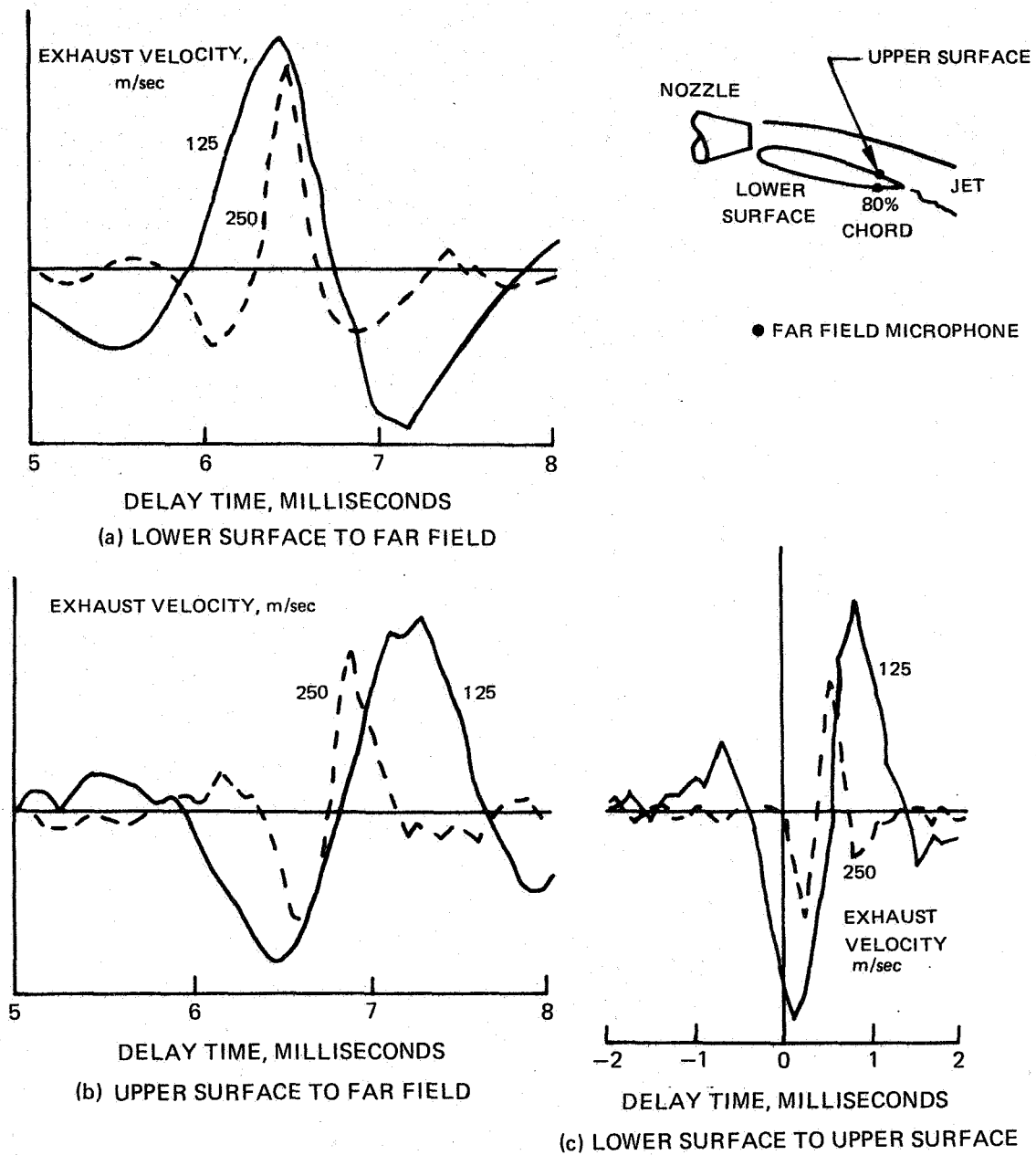


FIGURE 7 — CROSSCORRELATIONS BETWEEN AIRFOIL UPPER AND LOWER SURFACES AT 80% CHORD AND FAR FIELD FOR UPPER SURFACE BLOWING

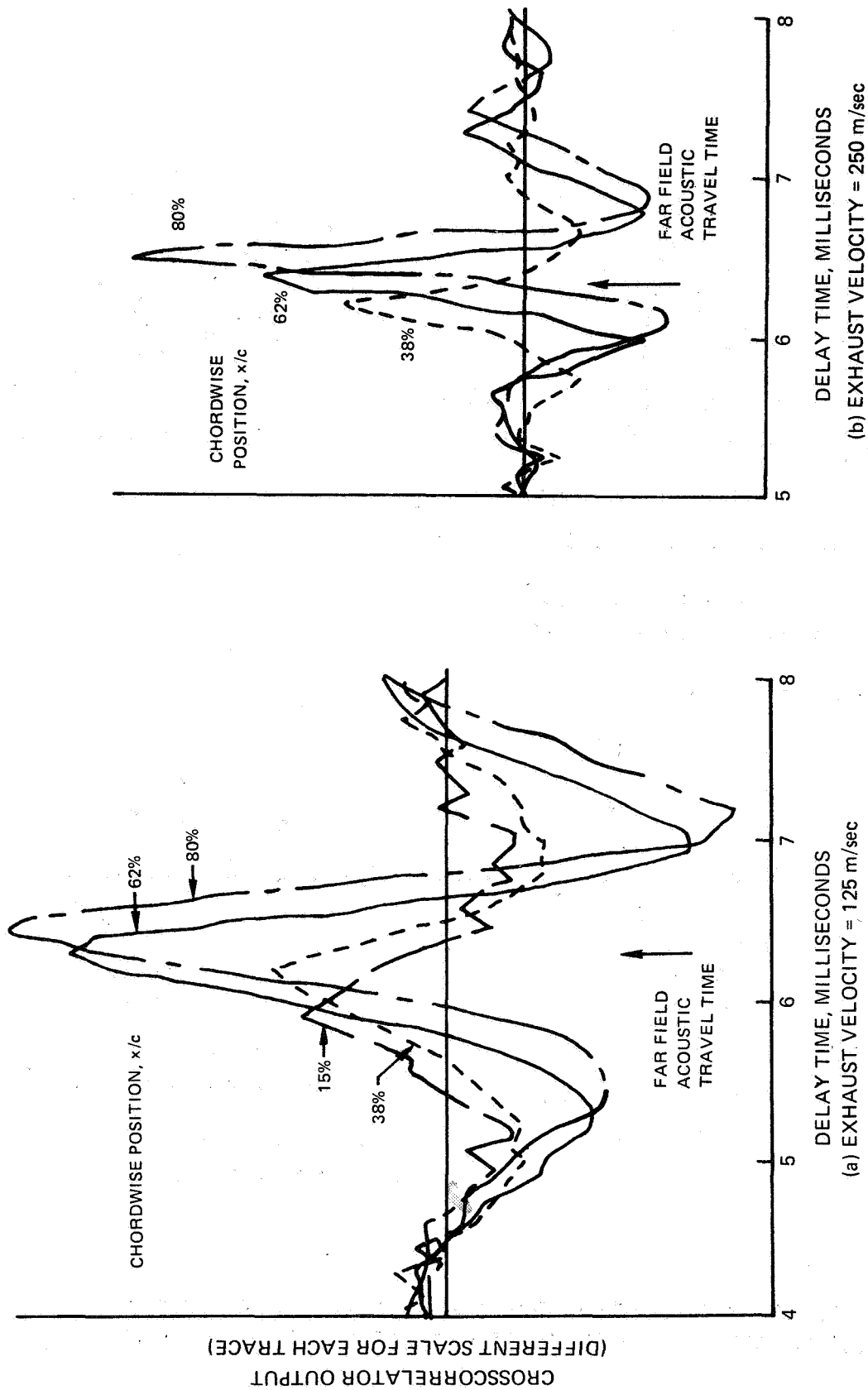


FIGURE 8—CROSSCORRELATIONS BETWEEN AIRFOIL LOWER SURFACE AND FAR FIELD FOR UPPER SURFACE BLOWING

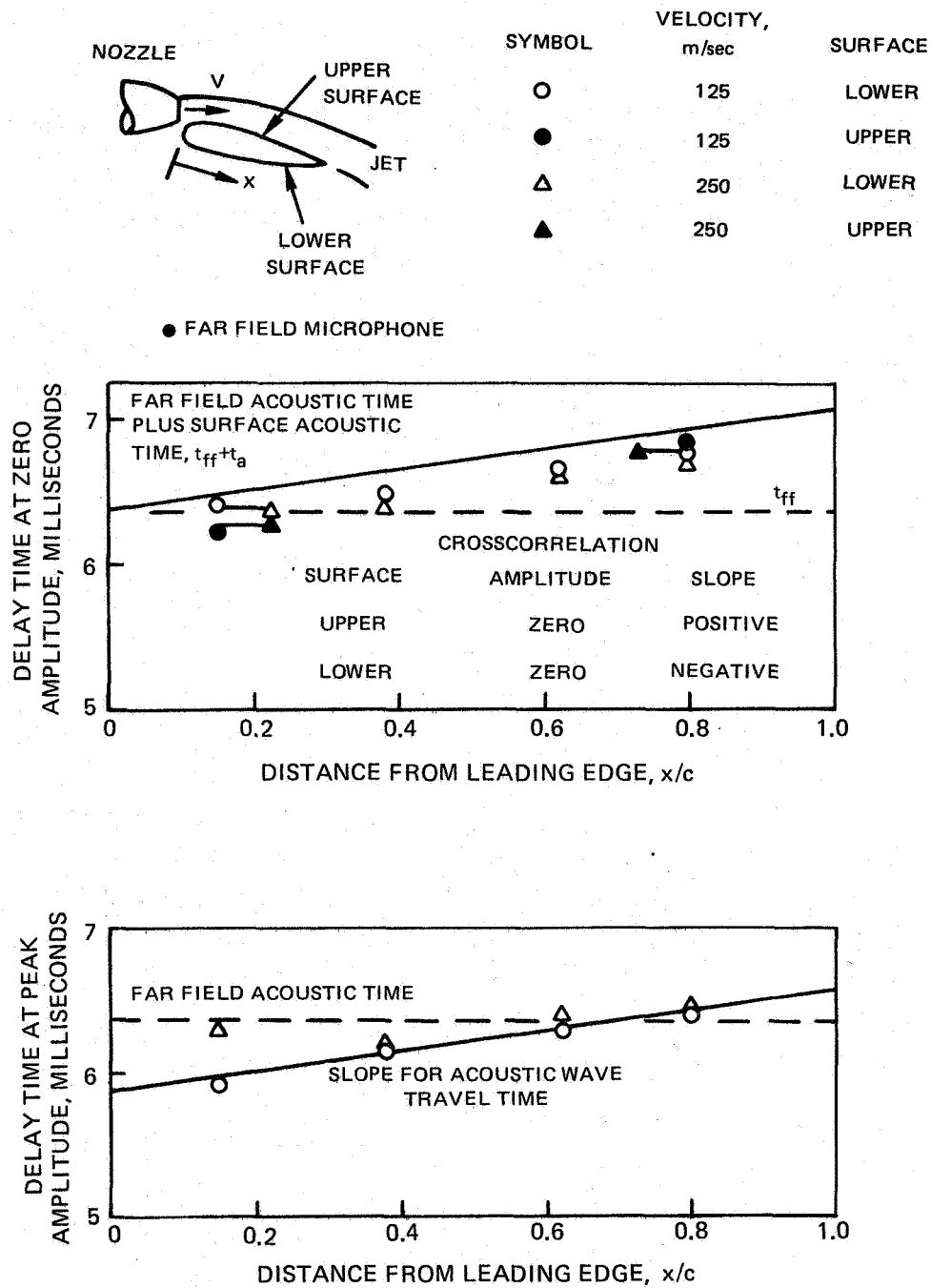
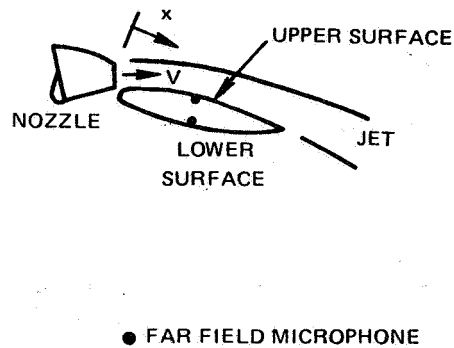
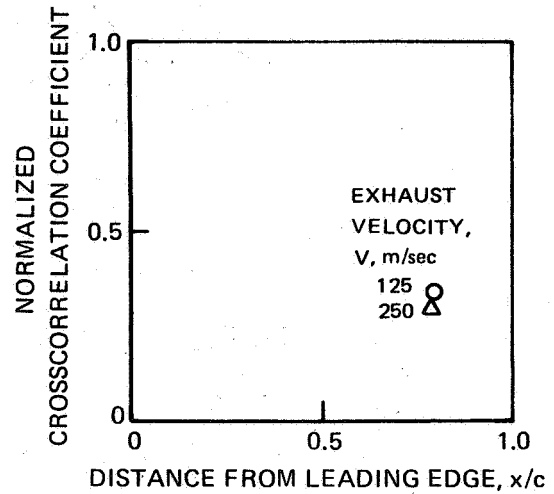


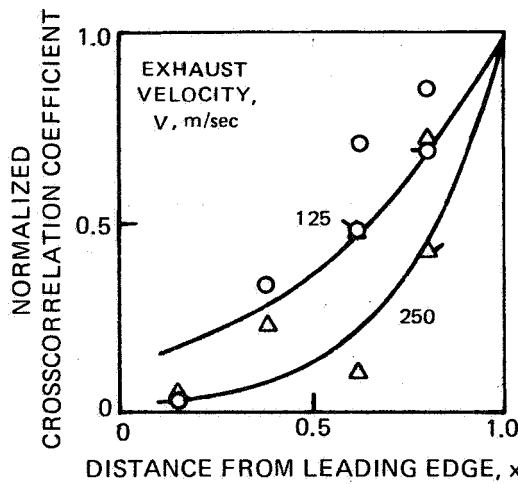
FIGURE 9 — DELAY TIMES FOR SIGNIFICANT EVENTS IN CROSSCORRELATIONS BETWEEN FAR FIELD AND SURFACES OF UPPER SURFACE BLOWN AIRFOIL



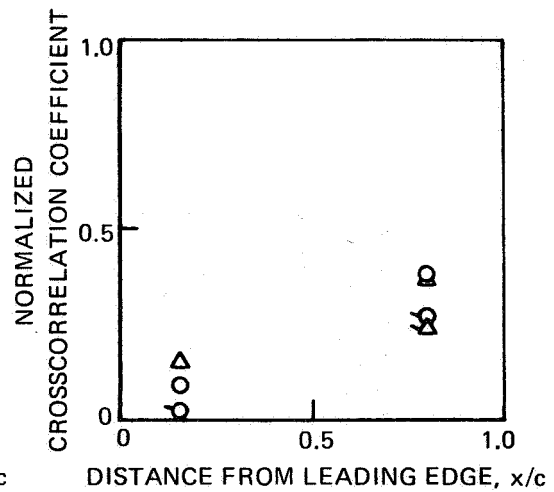
(a) SKETCH OF TEST CONFIGURATION



(b) CROSSCORRELATION BETWEEN AIRFOIL UPPER AND LOWER SURFACES



(c) CROSSCORRELATION BETWEEN FAR FIELD AND LOWER SURFACE



(d) CROSSCORRELATION BETWEEN FAR FIELD AND UPPER SURFACE

FIGURE 10 – CROSSCORRELATION COEFFICIENTS FOR UPPER SURFACE BLOWING CONFIGURATION AT 9° DEFLECTION

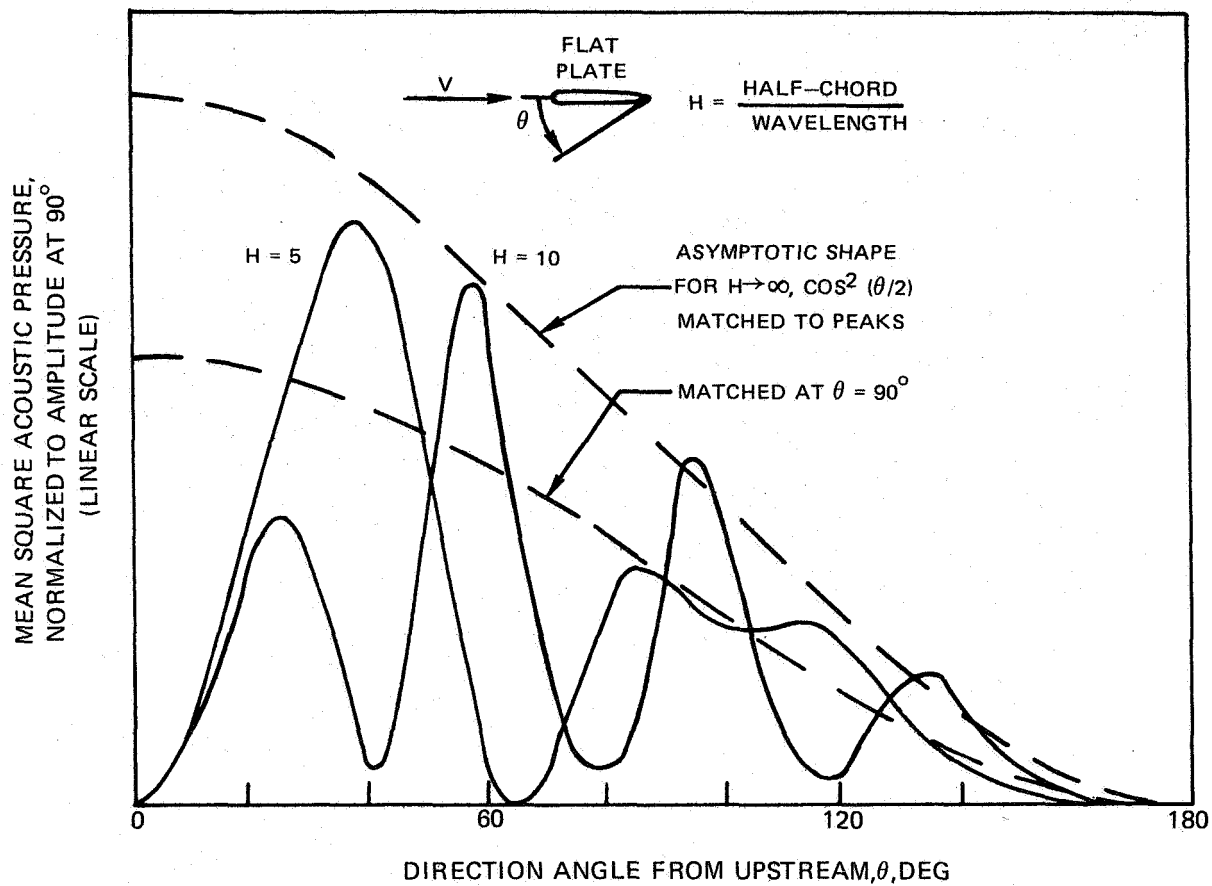
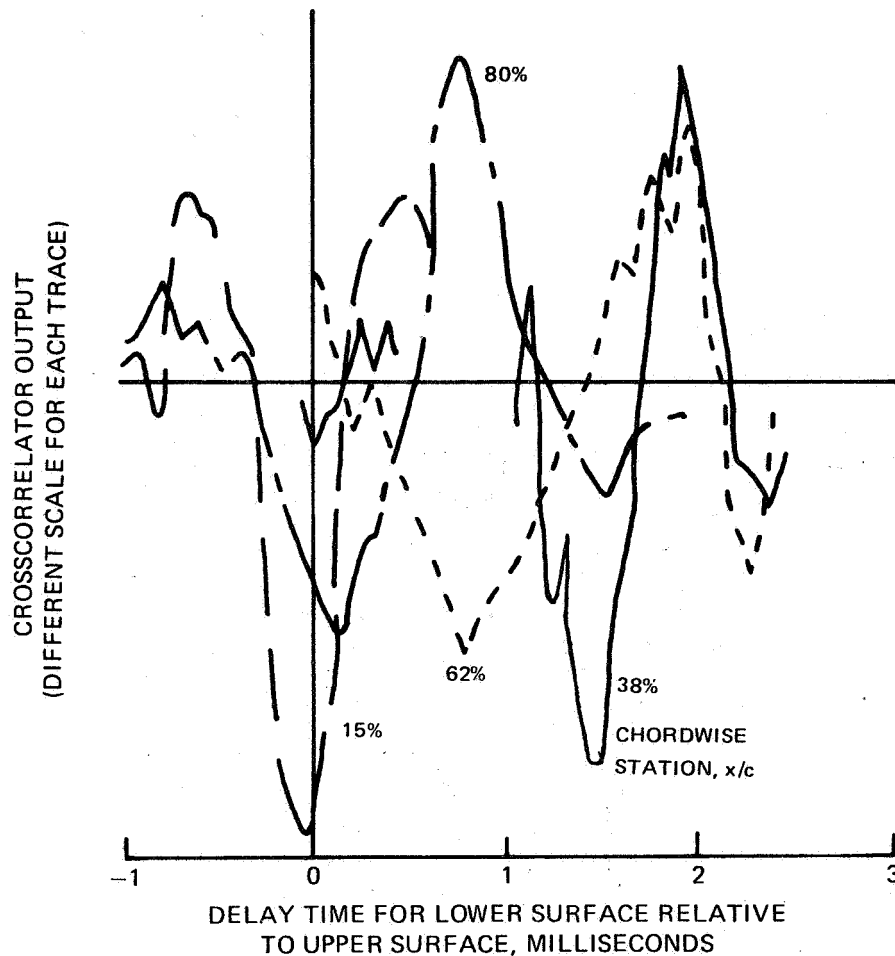
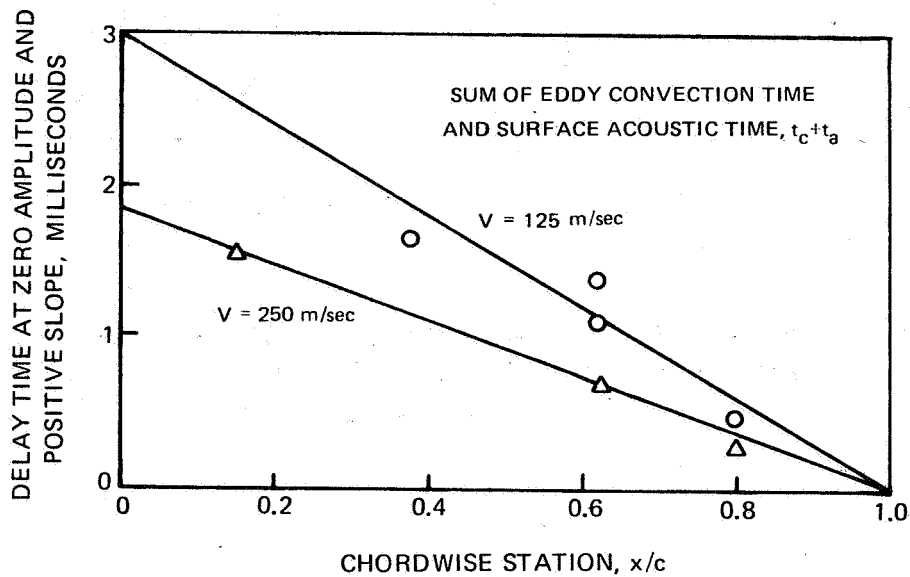


FIGURE 11— COMPARISON OF TAM'S SOLUTION OF TRAILING EDGE NOISE
DIRECTIVITY FOR A FINITE-CHORD FLAT PLATE WITH
DIRECTIVITY SOLUTION FOR A SEMI-INFINITE PLATE



(a) CROSSCORRELATIONS AT 125 m/sec VELOCITY



(b) VARIATION OF DELAY TIME FOR DIPOLE RADIATION

FIGURE 12 – CROSSCORRELATIONS OF AIRFOIL UPPER AND LOWER SURFACE PRESSURE SIGNALS AT CONSTANT CHORD FOR UNDER-THE-WING, 30° DEFLECTION

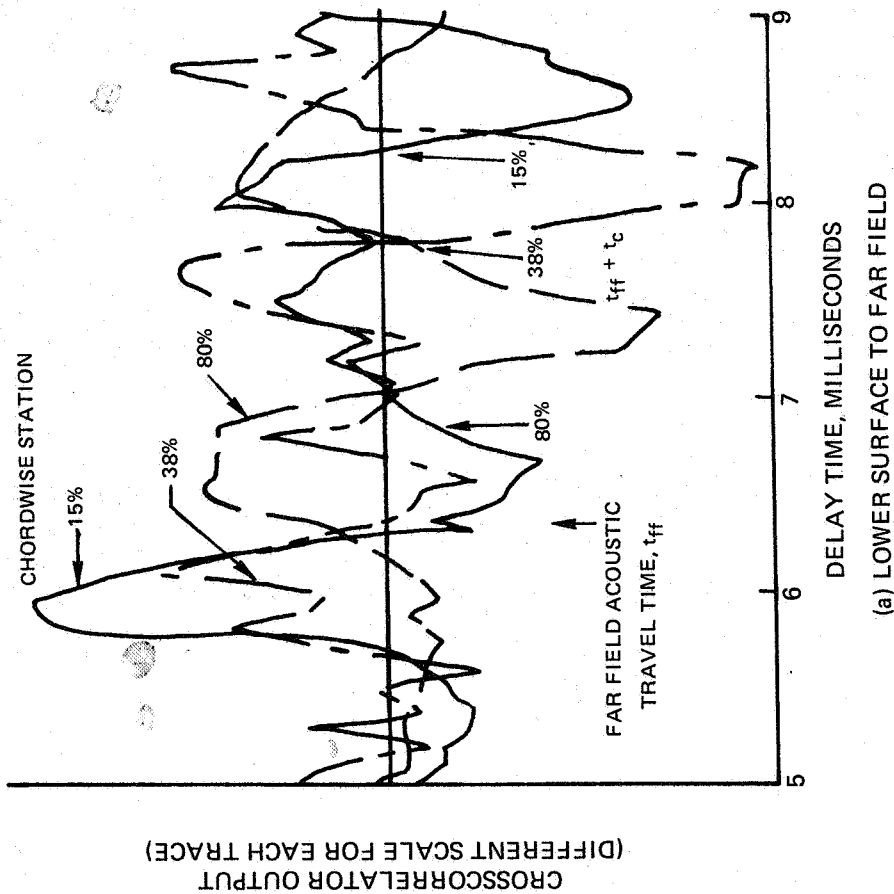
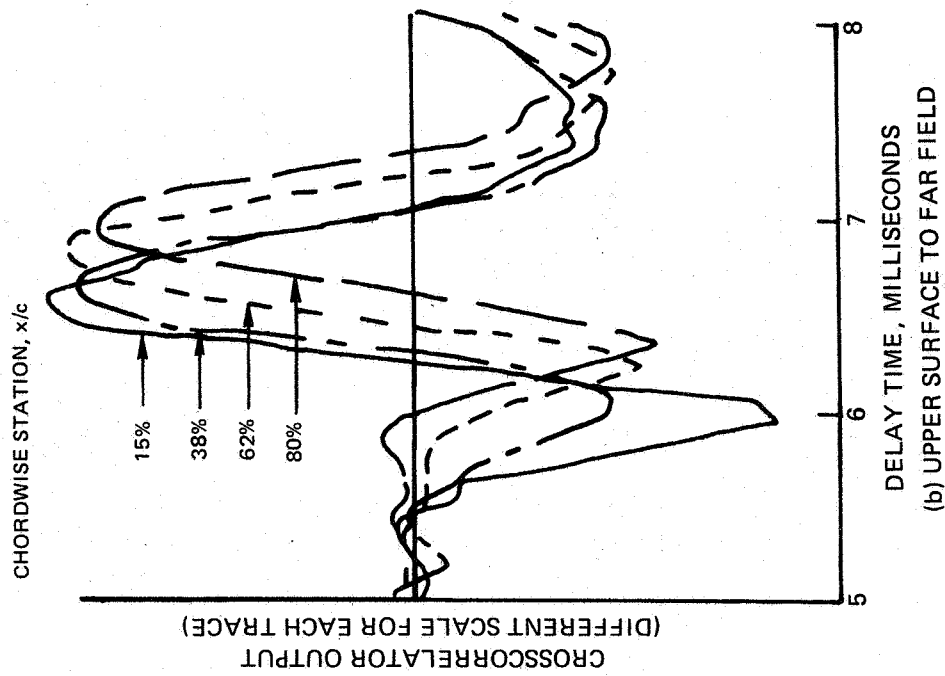
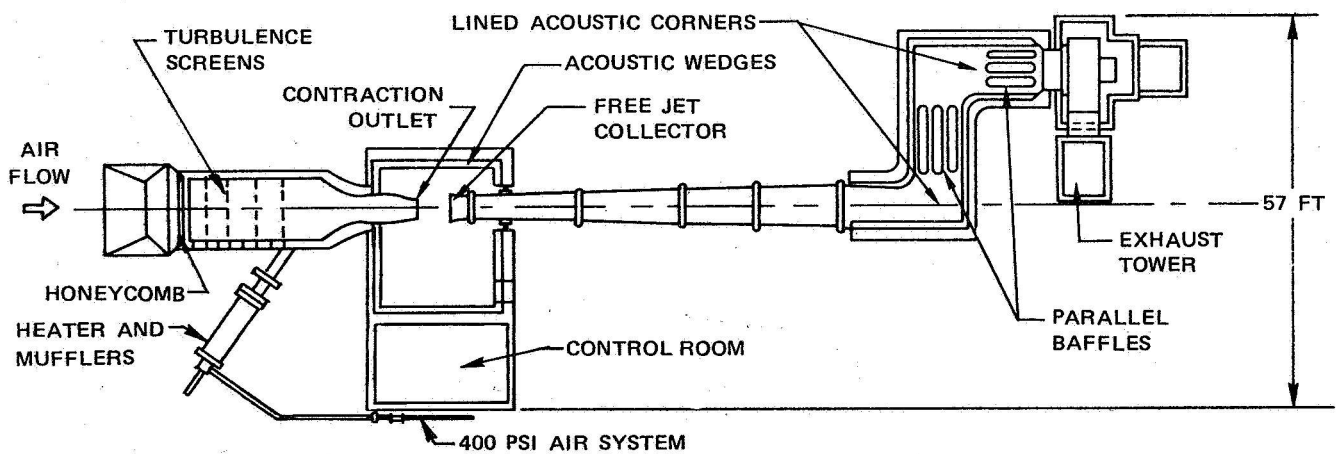
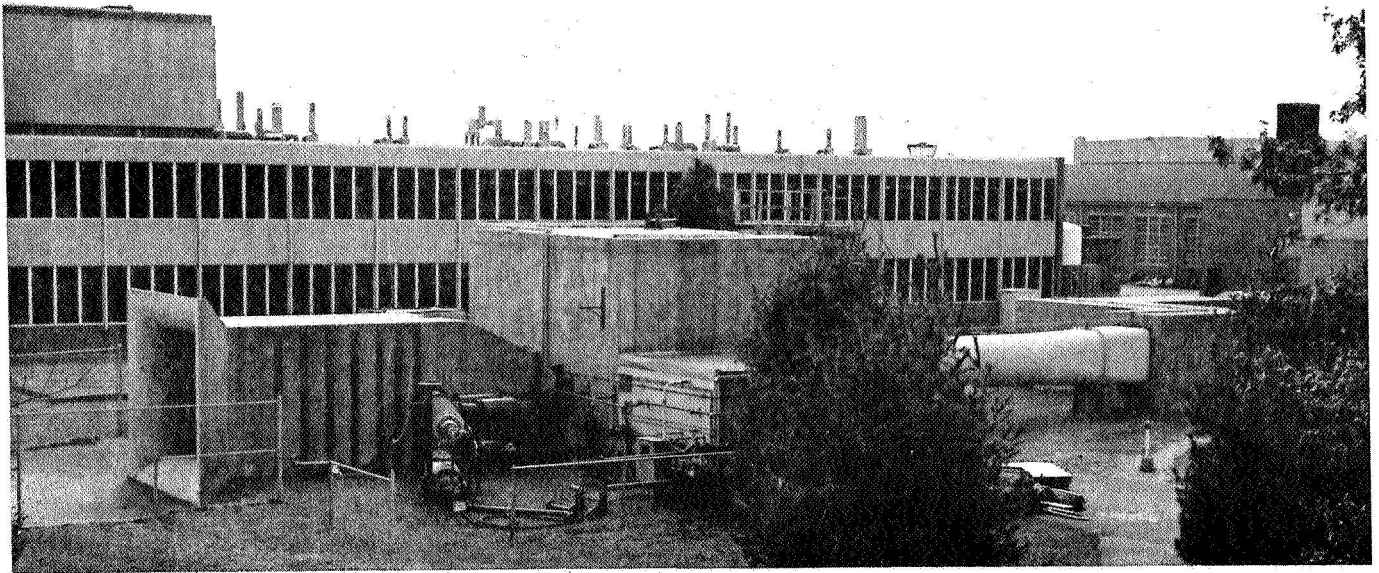
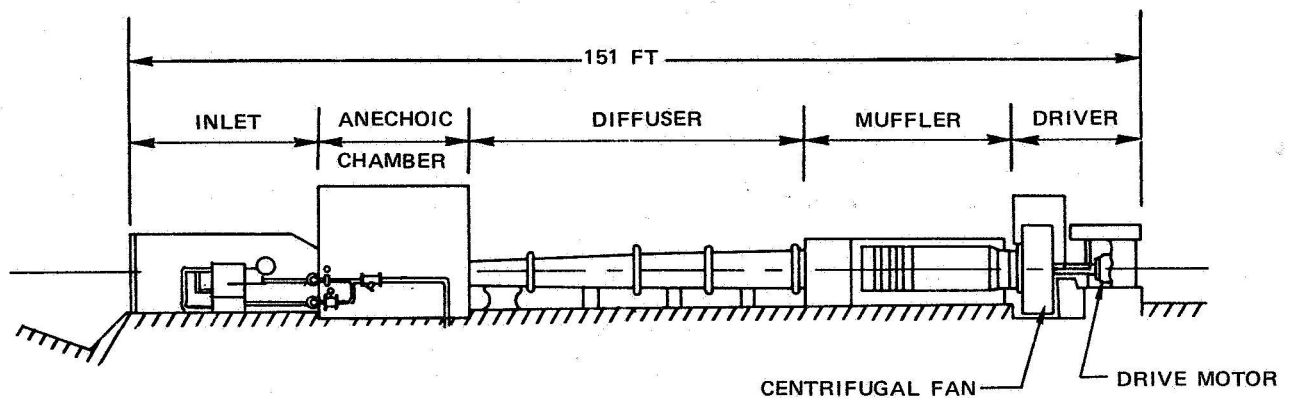


FIGURE 13 — CROSSCORRELATIONS OF AIRFOIL SURFACE PRESSURES AND FAR FIELD ACOUSTIC PRESSURES FOR UNDER-THE-WING, 30° DEFLECTION, 125 m/sec EXHAUST VELOCITY, SURFACE PRESSURES DELAYED RELATIVE TO FAR FIELD



TOP VIEW



SIDE VIEW

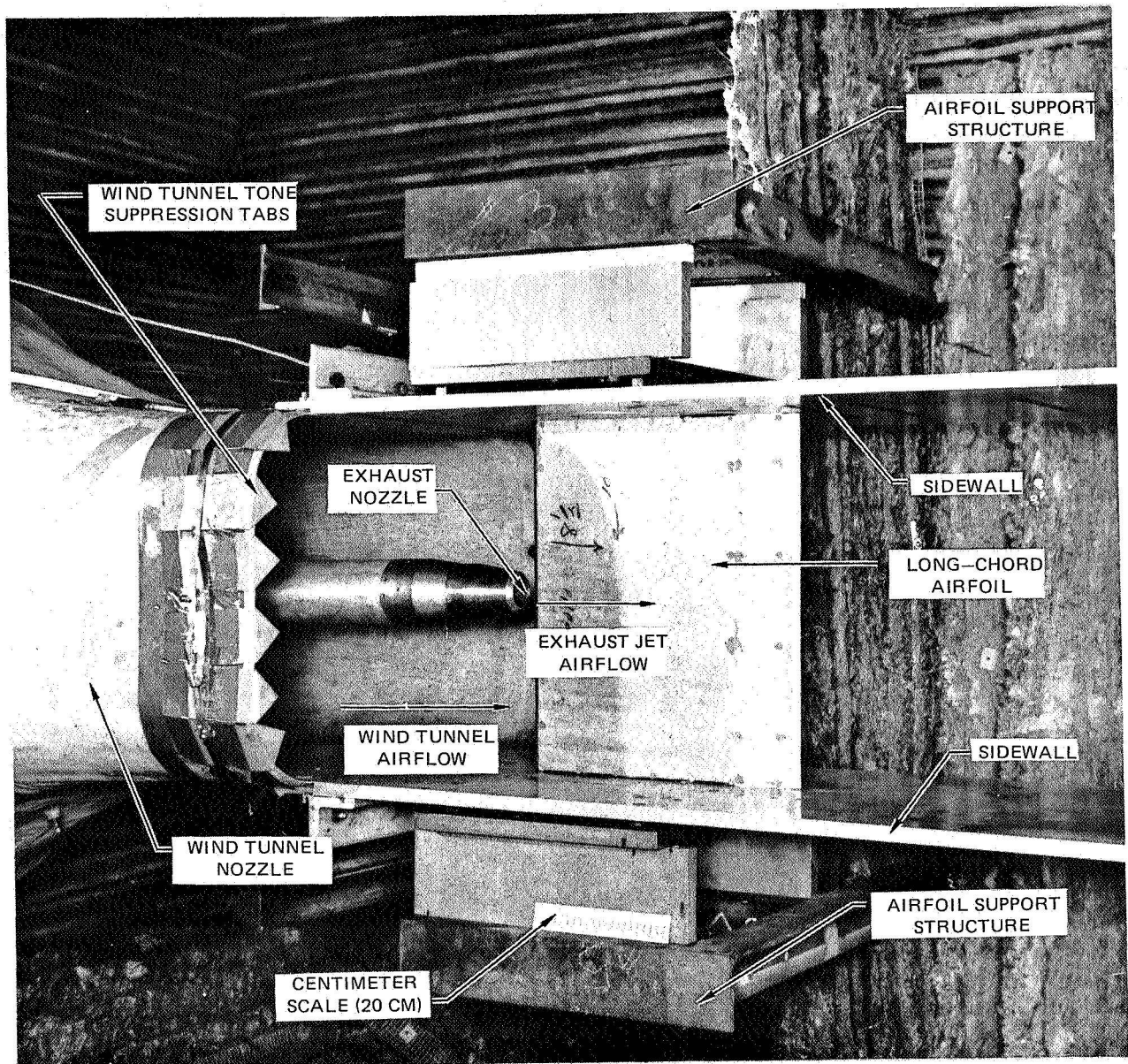


FIGURE 15 — LONG-CHORD UNDER-THE-WING EXTERNALLY BLOWN FLAP INSTALLATION FOR MEASUREMENT OF FORWARD FLIGHT EFFECTS

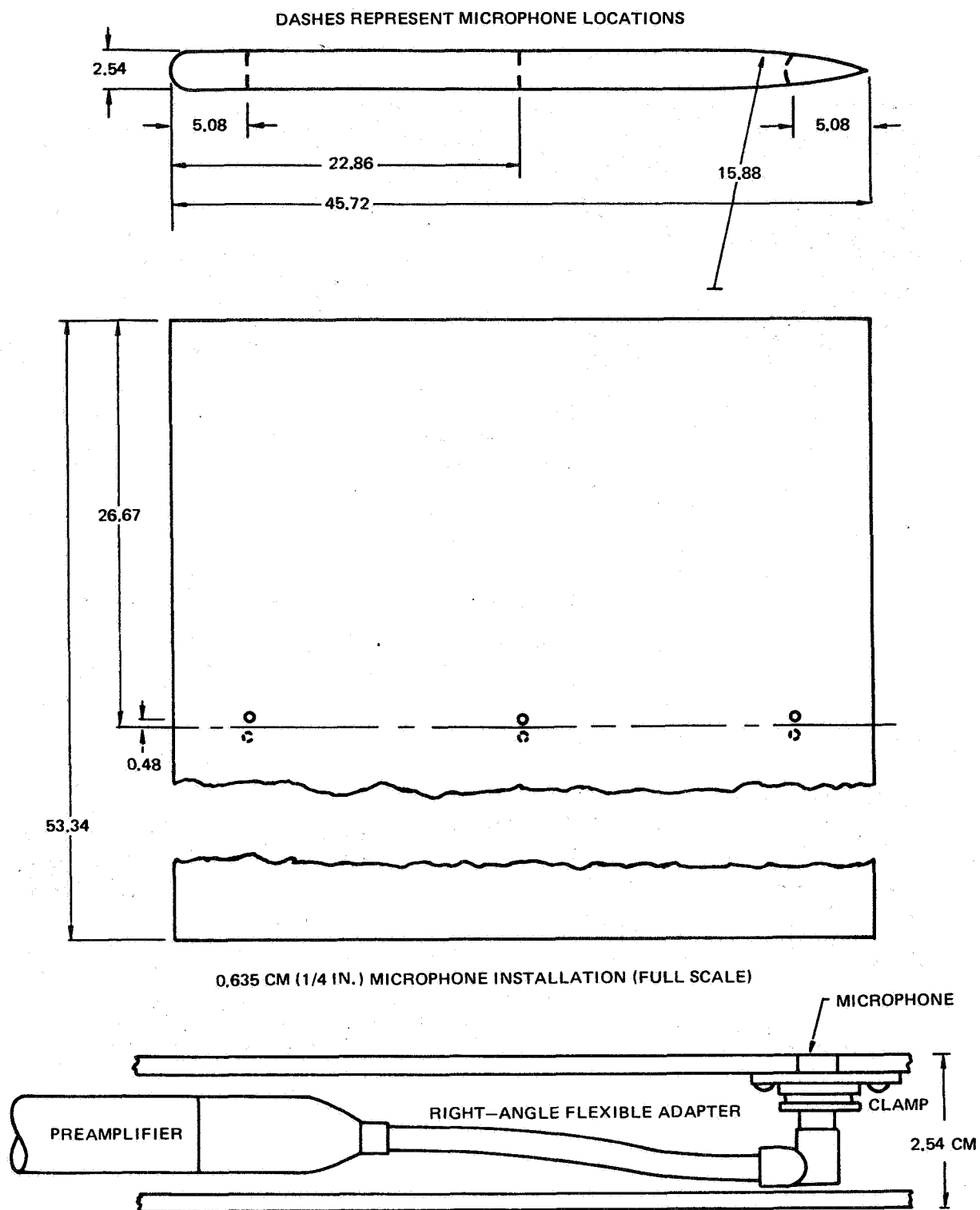
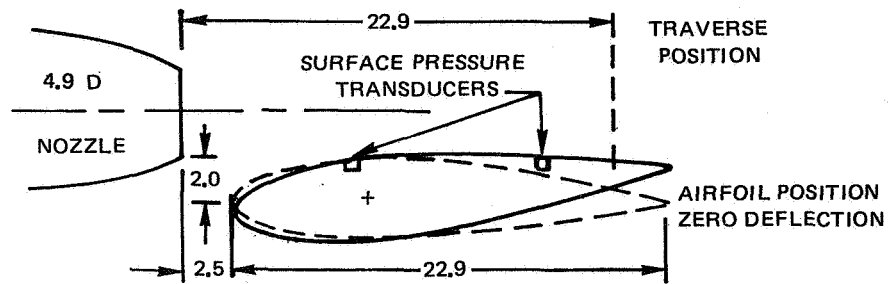
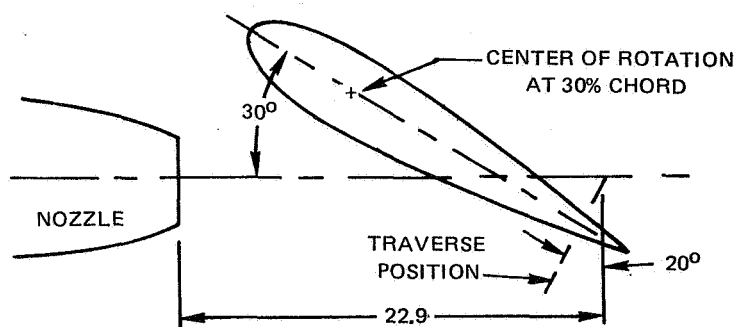


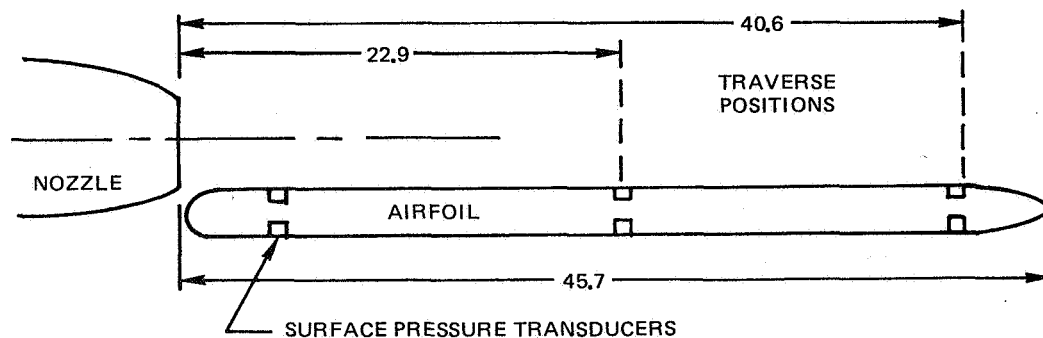
FIGURE 16 – FLAT PLATE AIRFOIL. ONE-QUARTER SCALE EXCEPT WHERE NOTED. ALL DIMENSIONS IN CENTIMETERS



(a) SHORT-CHORD AIRFOIL, 90° DEFLECTION



(b) SHORT-CHORD AIRFOIL, 30° DEFLECTION



(c) LONG-CHORD AIRFOIL

FIGURE 17— AIRFOIL AND NOZZLE CONFIGURATIONS FOR INVESTIGATION OF EBF FORWARD FLIGHT EFFECTS. ¼ SCALE, ALL DIMENSIONS IN CENTIMETERS

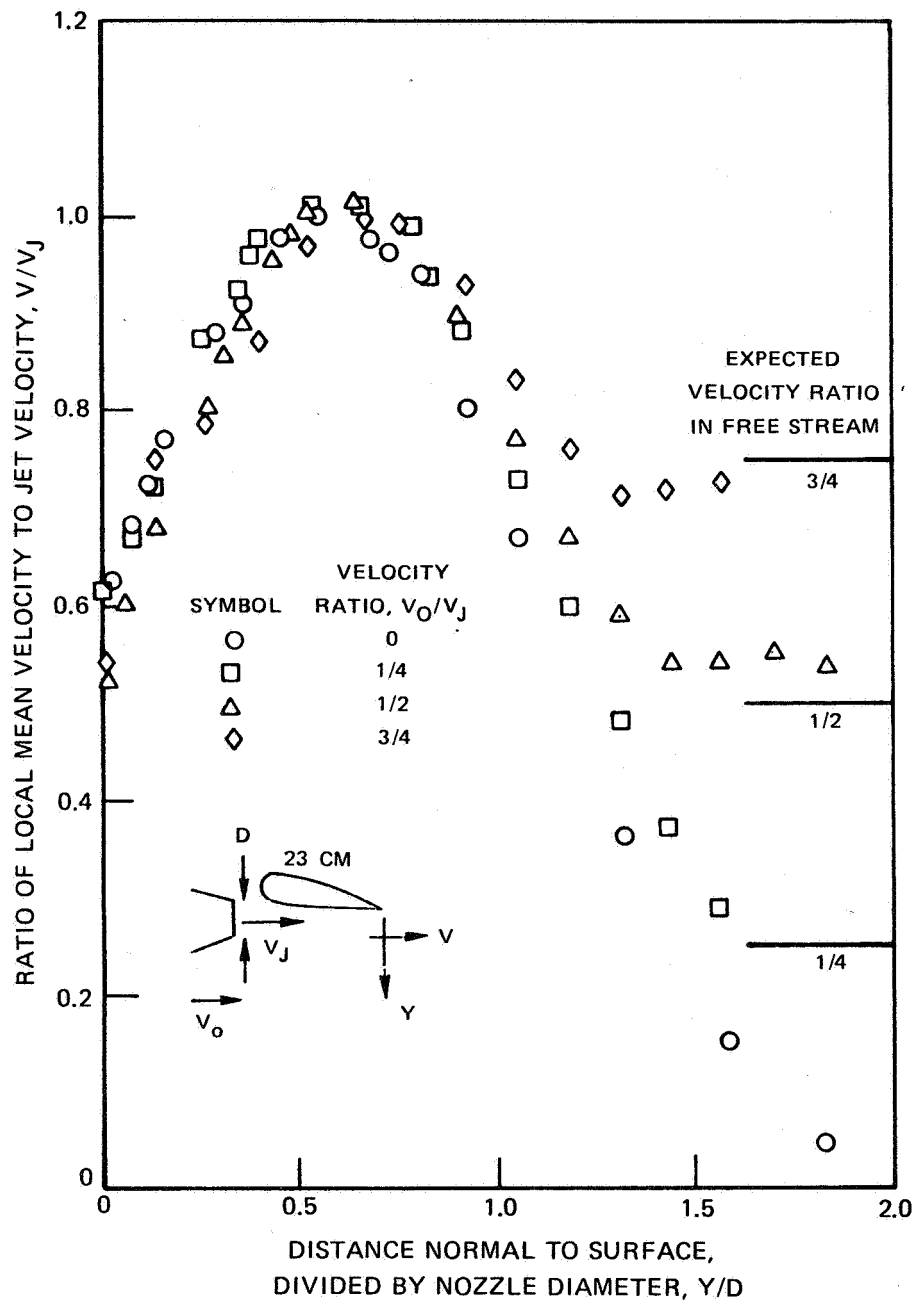


FIGURE 18 — EFFECT OF FLIGHT VELOCITY RATIO ON MEAN VELOCITY PROFILES NEAR TRAILING EDGE OF SHORT-CHORD AIRFOIL, (a) 90° DEFLECTION, 125 M/SEC EXHAUST VELOCITY

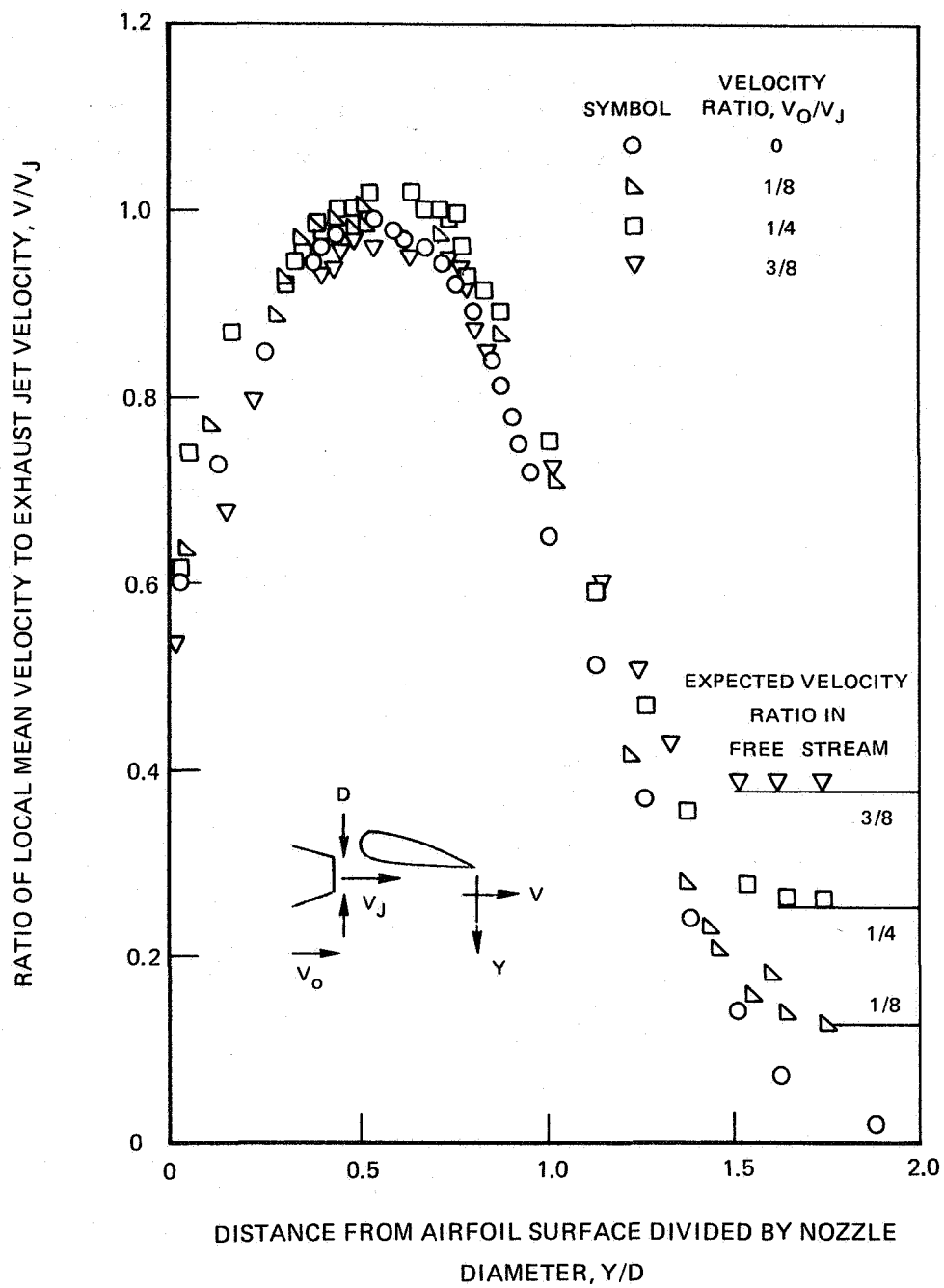


FIGURE 18 – CONTINUED (b) 90° DEFLECTION, 160 m/sec EXHAUST JET VELOCITY

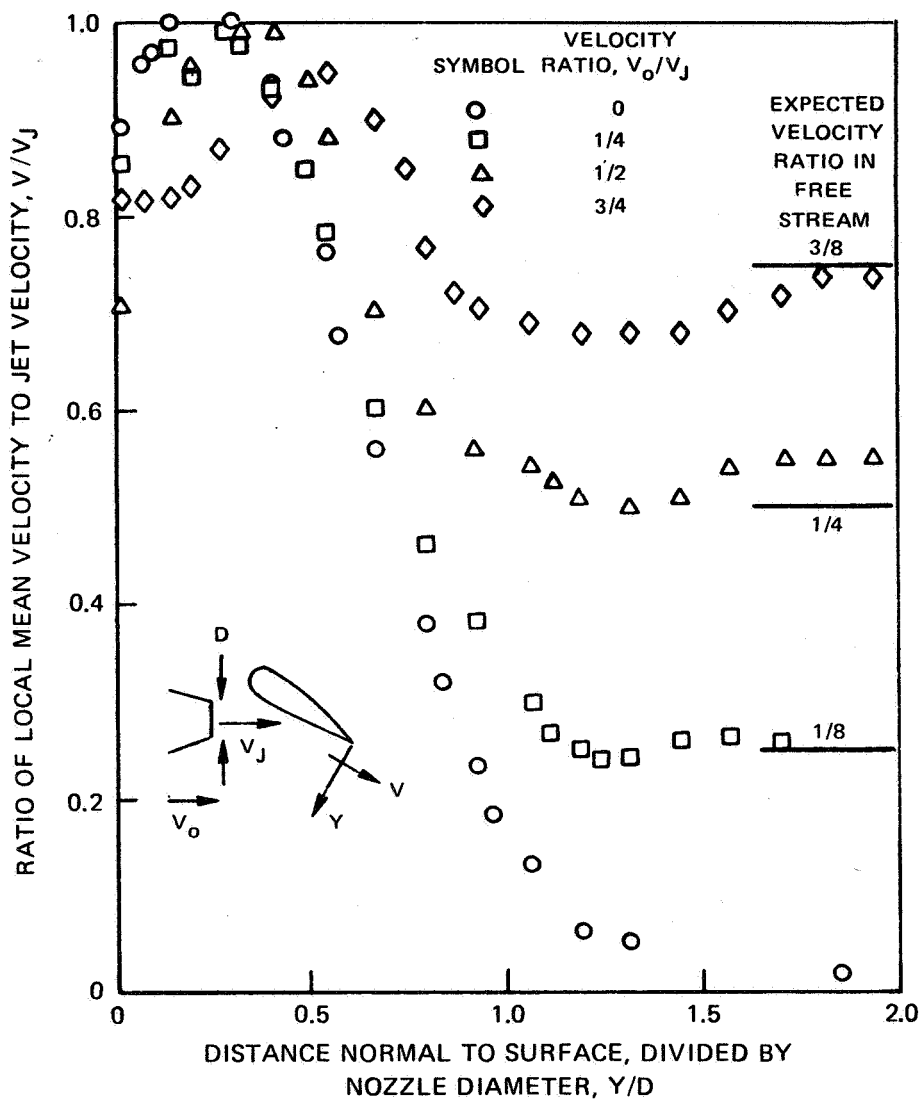


FIGURE 18 – CONTINUED (c) 30° DEFLECTION, 125 M/SEC EXHAUST JET VELOCITY

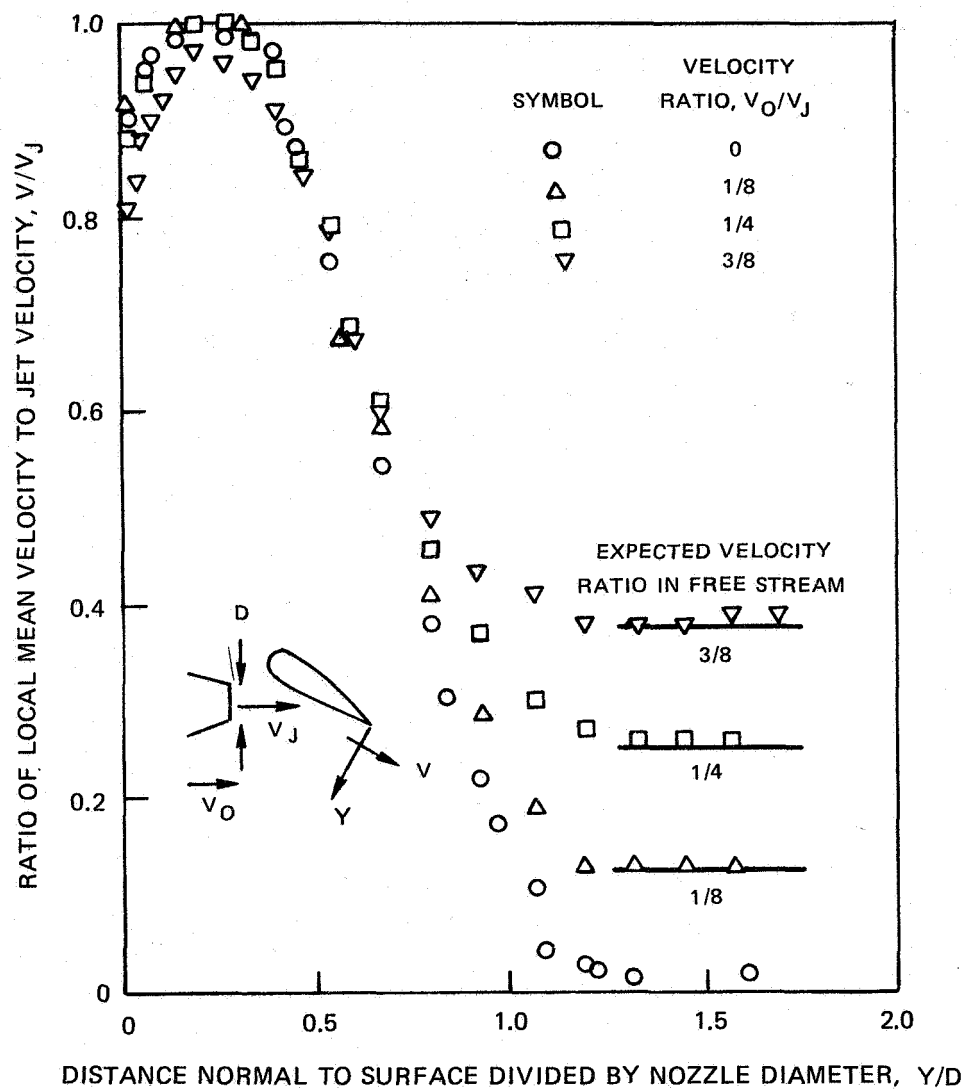


FIGURE 18 – CONCLUDED. (d) 30° DEFLECTION, 160 M/SEC EXHAUST JET VELOCITY

SYMBOL	VELOCITY RATIO, V_0/V_J
○	0
□	1/4
△	1/2
◇	3/4

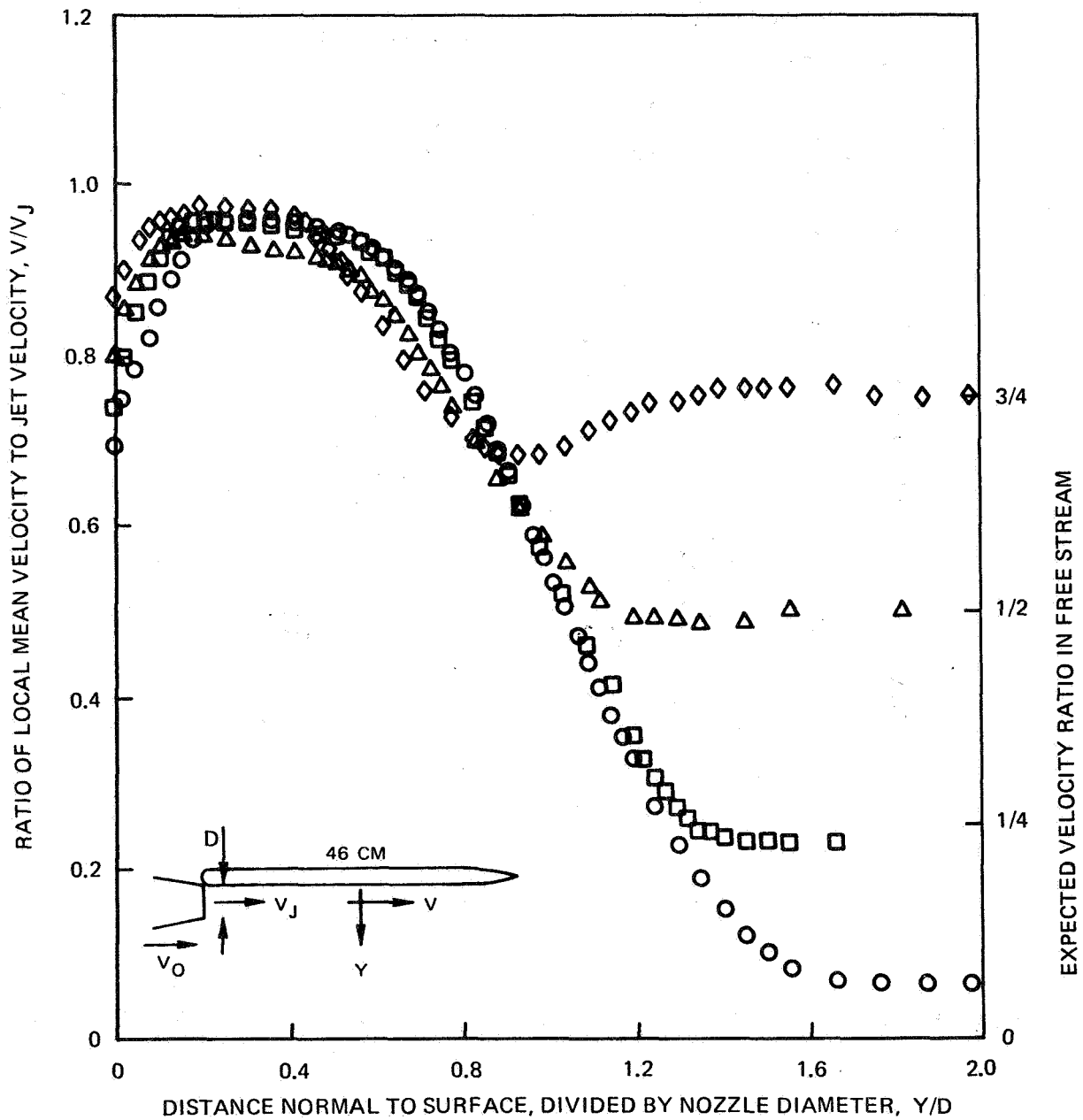


FIGURE 19—EFFECT OF FLIGHT VELOCITY RATIO ON MEAN VELOCITY PROFILES NEAR LONG-CHORD AIRFOIL. (a) MIDCHORD, 125 M/SEC EXHAUST VELOCITY

SYMBOL	VELOCITY RATIO, V_0/V_J
○	0
△	1/8
□	1/4
▽	3/8

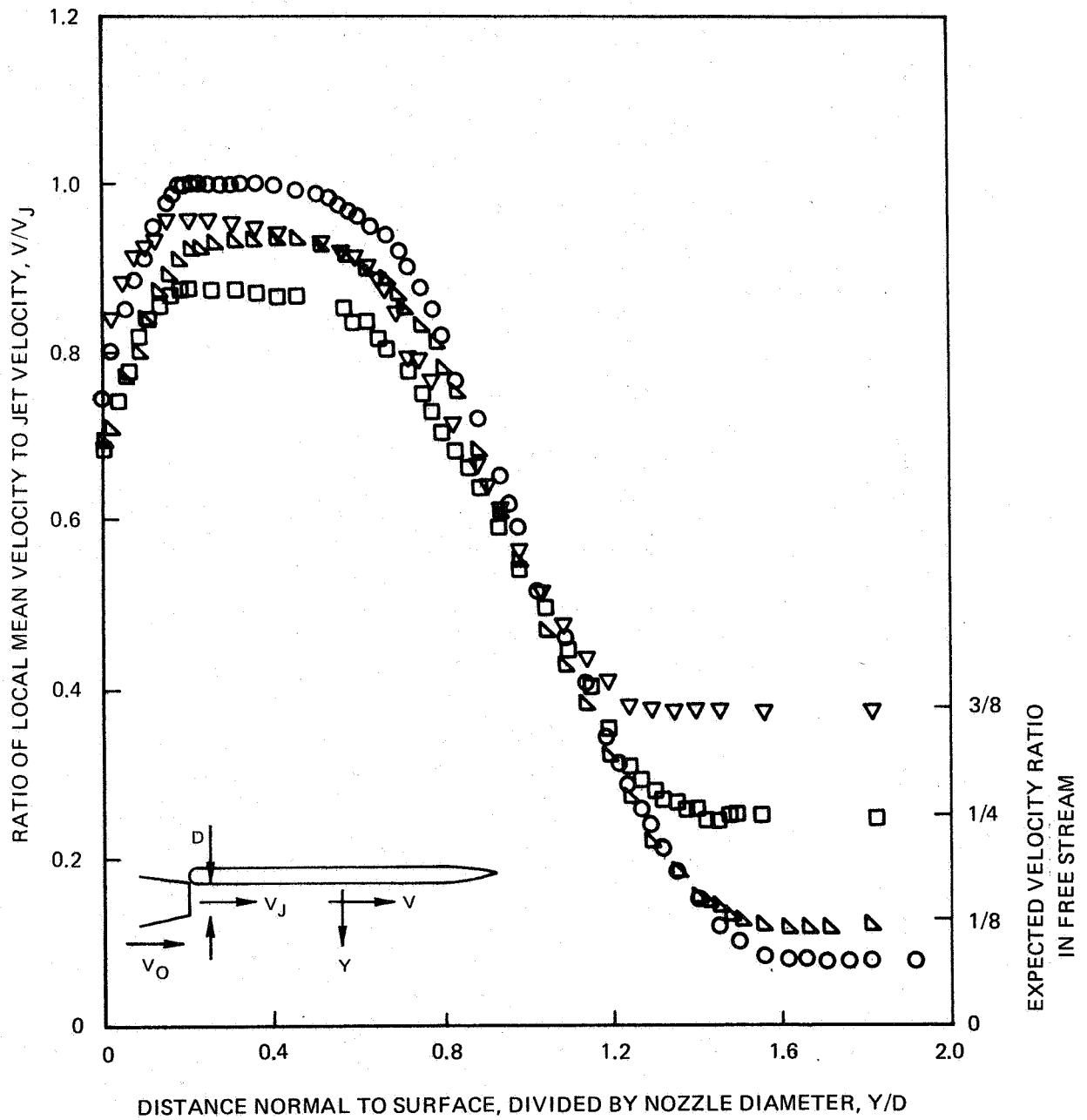


FIGURE 19— CONTINUED. (b) MIDCHORD, 160 M / SEC EXHAUST VELOCITY

SYMBOL	VELOCITY RATIO, V_0/V_J
○	0
□	1/4
△	1/2
◇	3/4

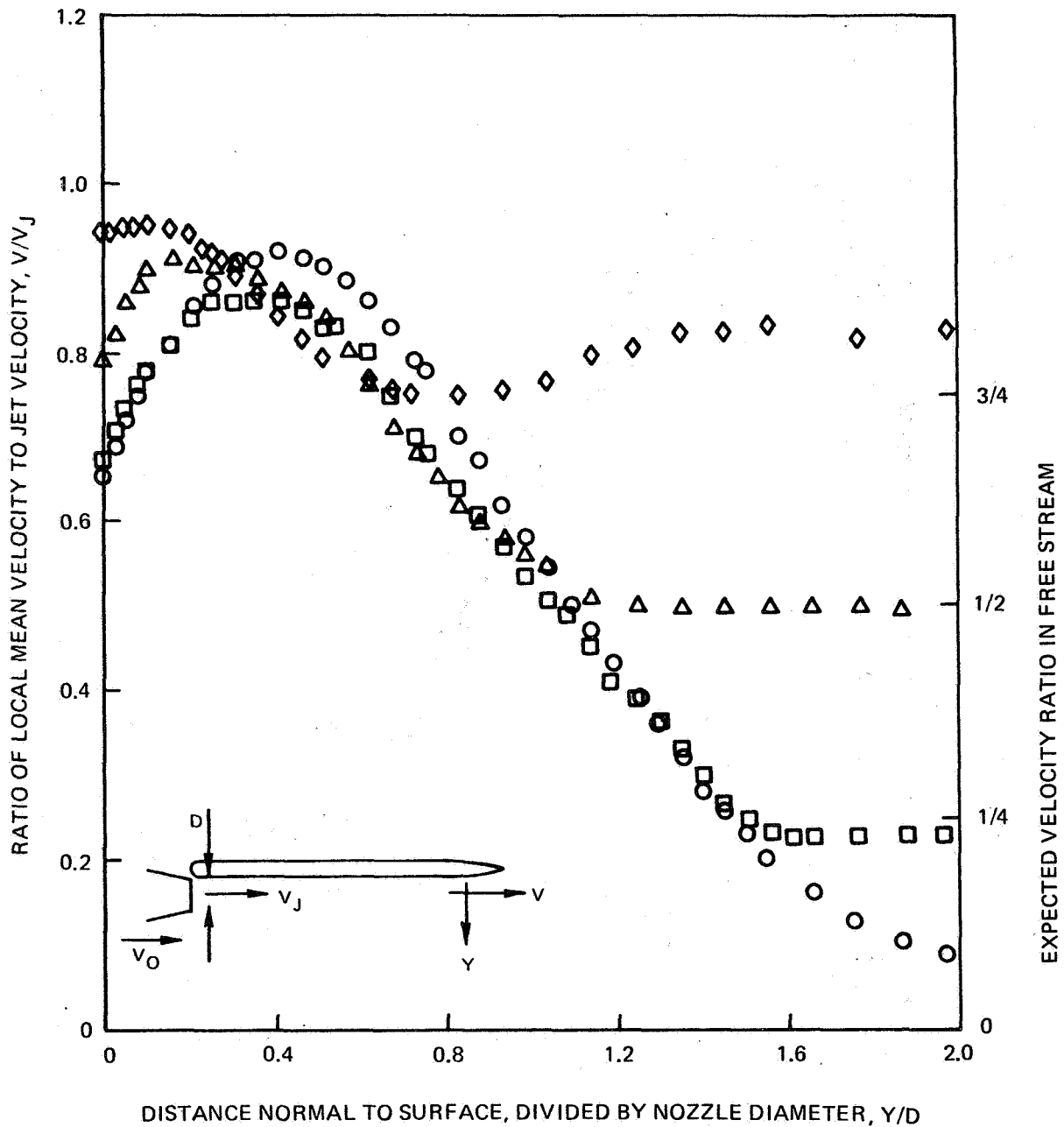


FIGURE 19— CONTINUED. (c) NEAR TRAILING EDGE, 125 M/SEC EXHAUST VELOCITY

SYMBOL	VELOCITY RATIO, V_O/V_J
○	0
△	1/8
□	1/4
▽	3/8

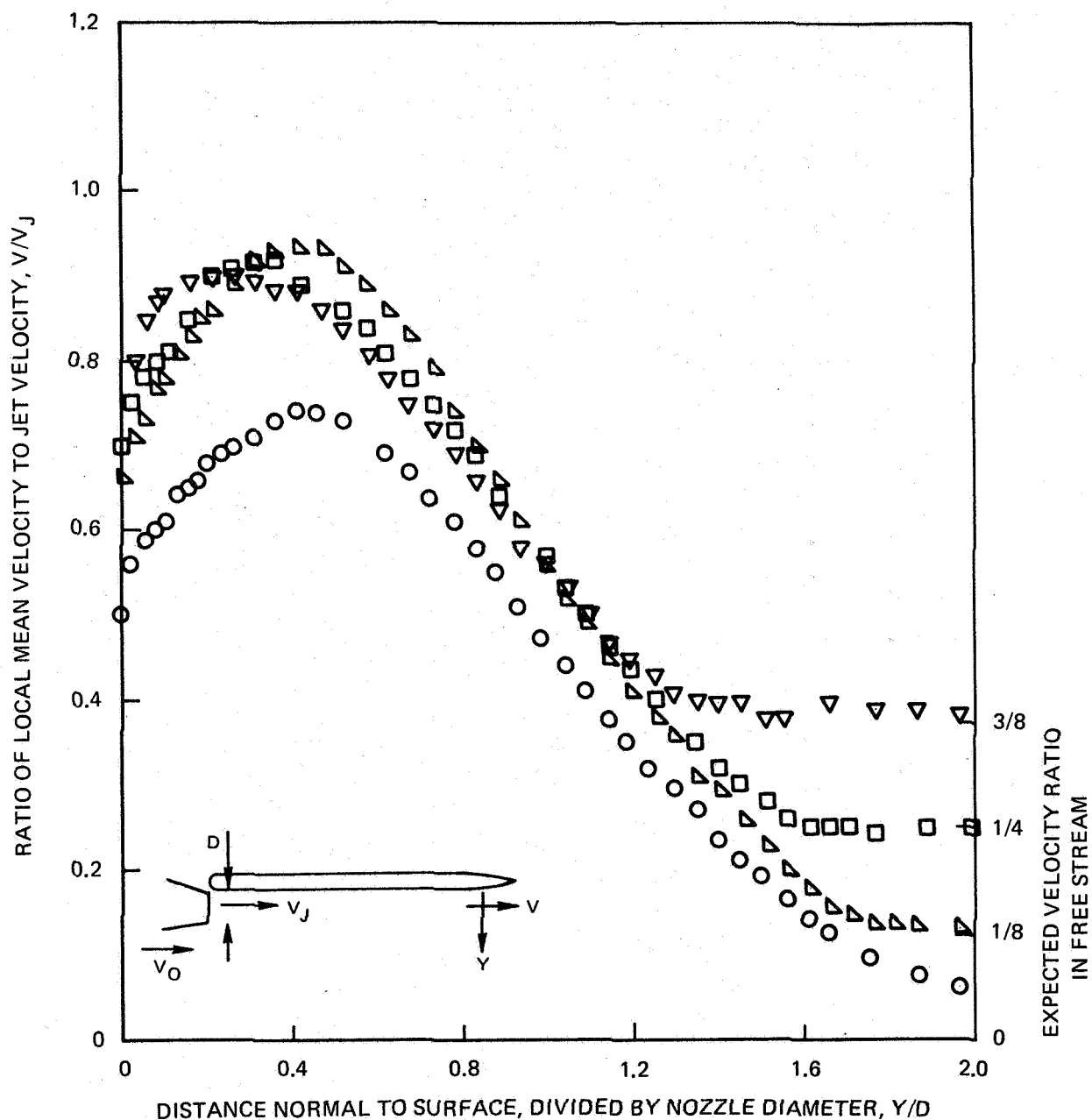


FIGURE 19— CONCLUDED. (d) NEAR TRAILING EDGE, 160 M/SEC EXHAUST VELOCITY

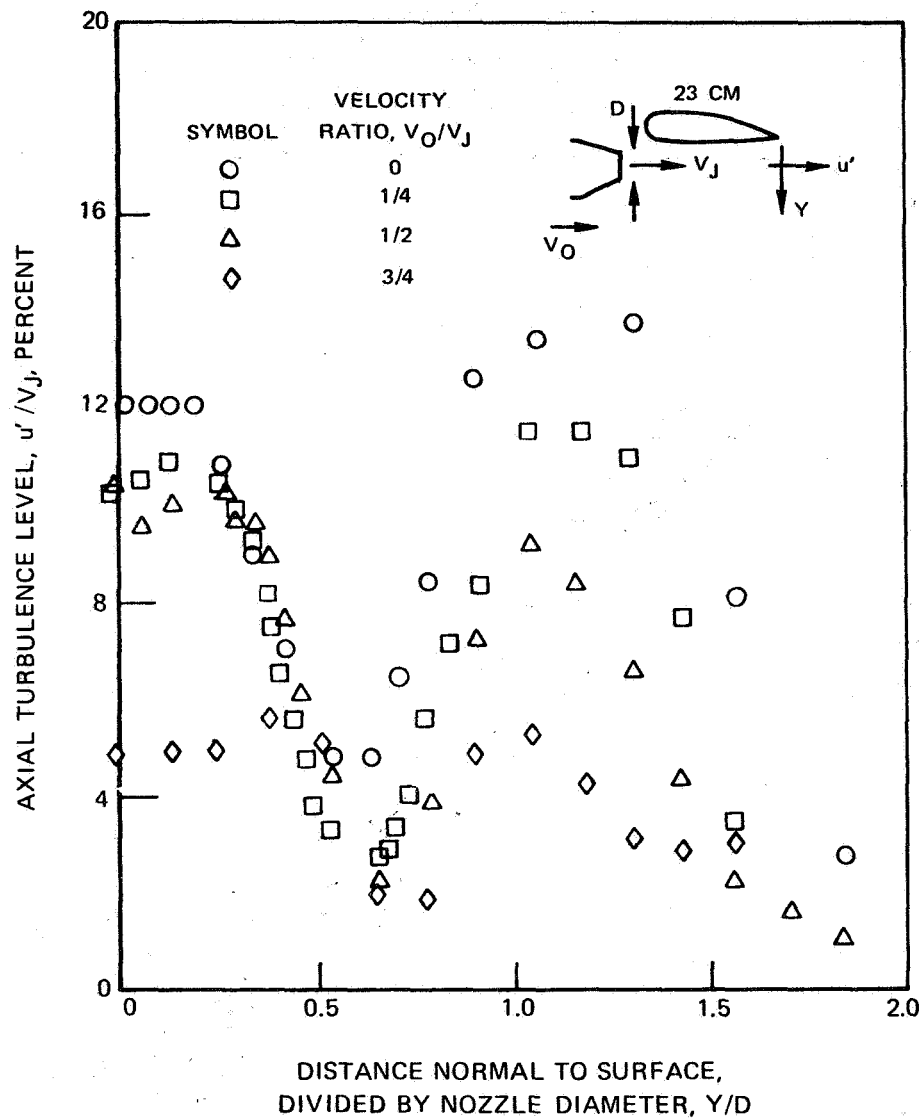


FIGURE 20 — EFFECT OF FLIGHT VELOCITY RATIO ON TURBULENCE PROFILES NEAR TRAILING EDGE OF SHORT-CHORD AIRFOIL (a) 9° DEFLECTION, 125 M/SEC EXHAUST VELOCITY

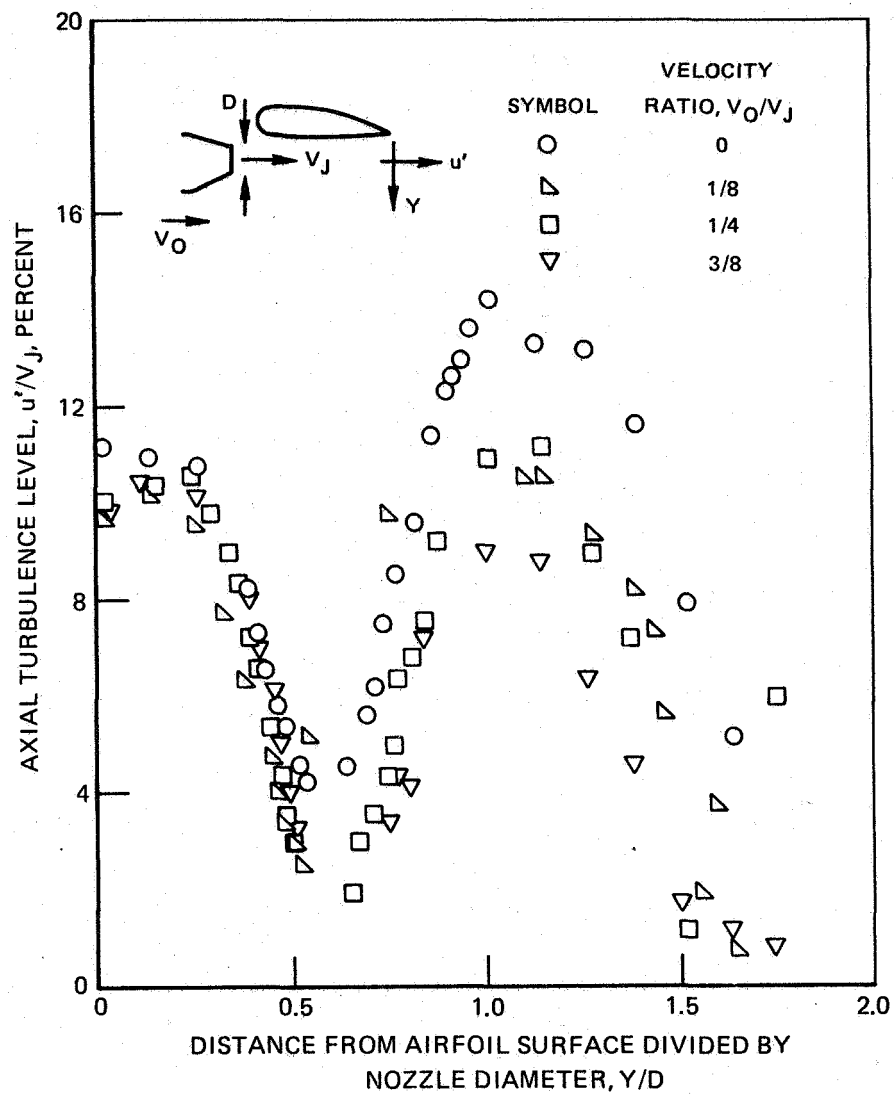


FIGURE 20 — CONTINUED (b) 90° DEFLECTION, 160 m/sec EXHAUST JET VELOCITY

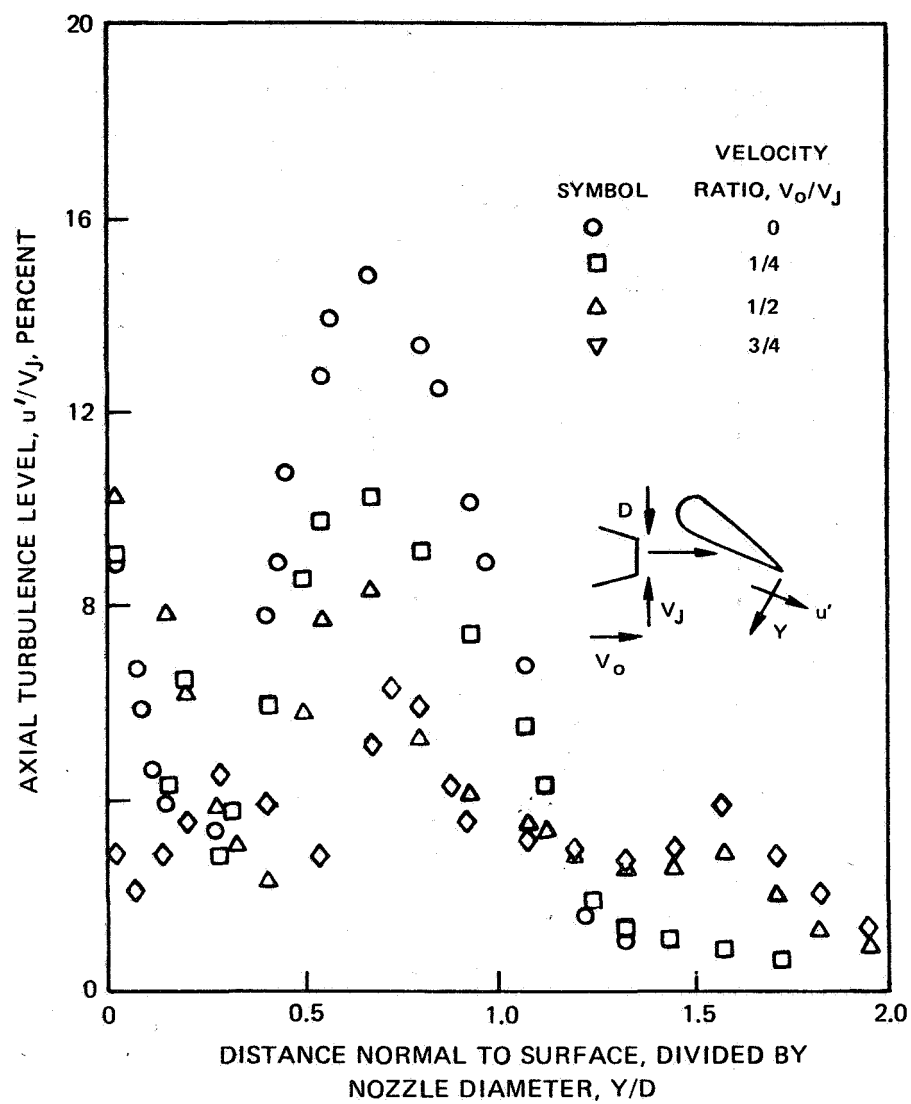


FIGURE 20 – CONTINUED (c) 30° DEFLECTION, 125 M/SEC EXHAUST JET VELOCITY

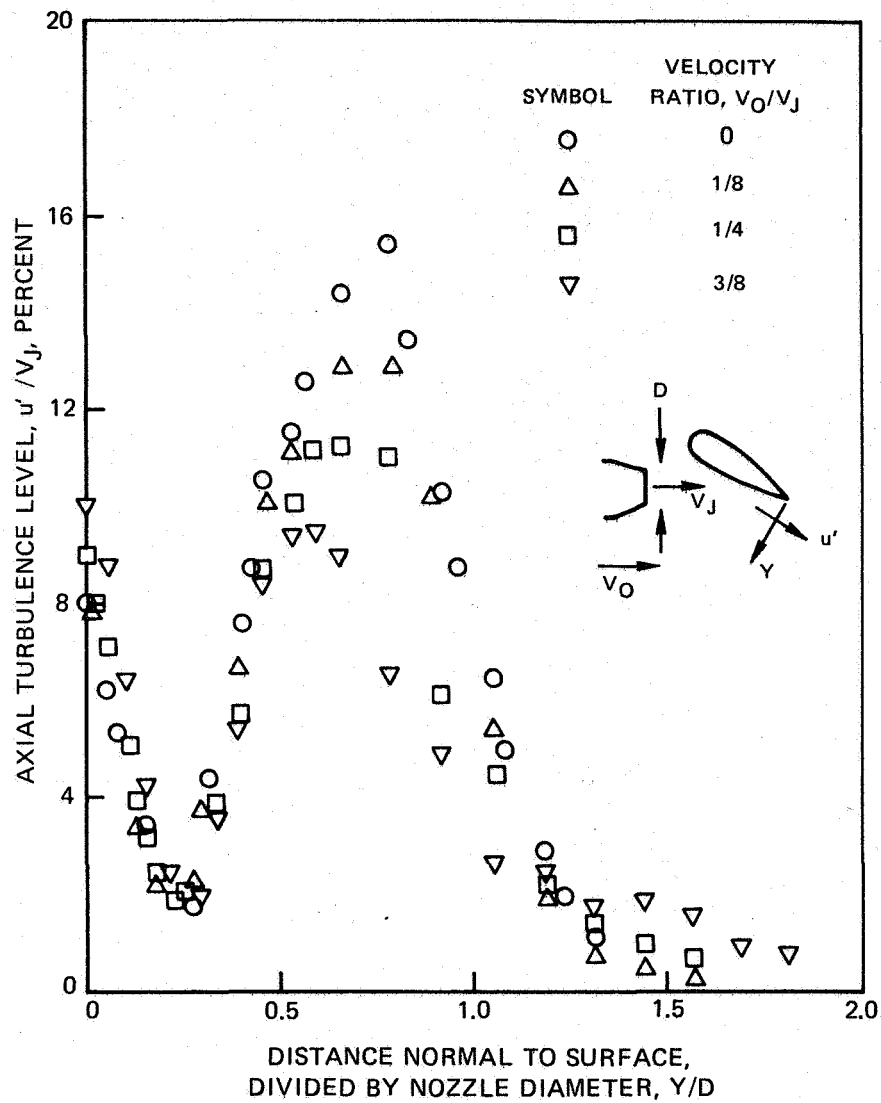


FIGURE 20 – CONCLUDED (d) 30° DEFLECTION, 160 M/SEC EXHAUST JET VELOCITY

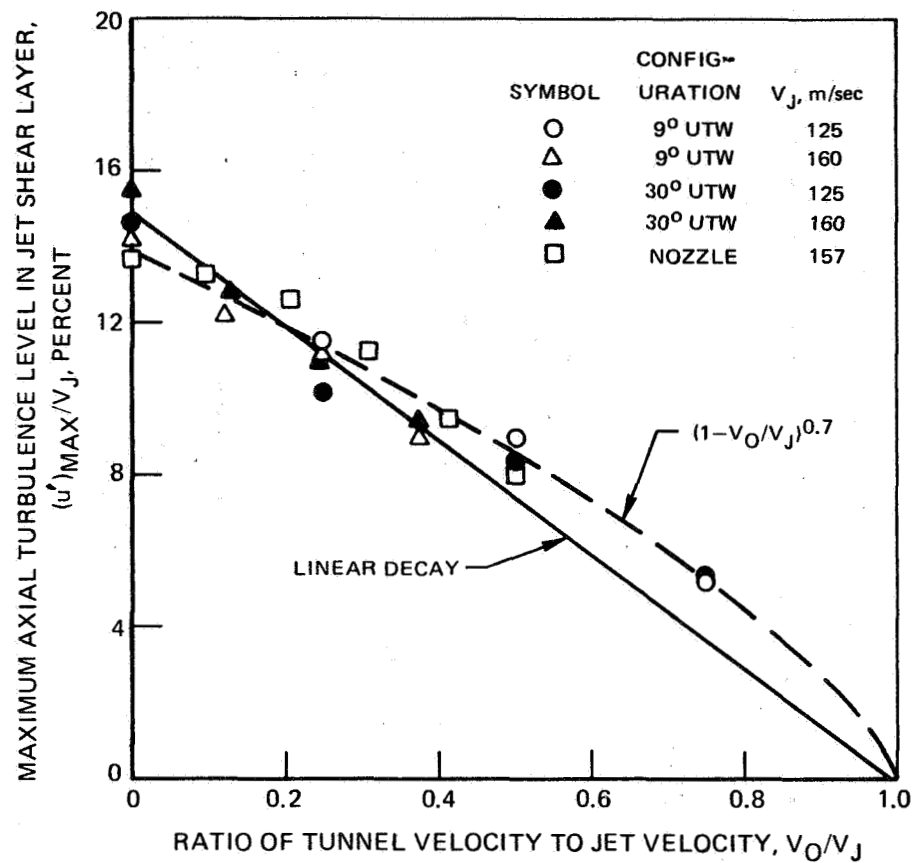


FIGURE 21 — EFFECT OF VELOCITY RATIO ON MAXIMUM MEASURED TURBULENCE LEVEL IN JET SHEAR LAYER FOR SHORT-CHORD AIRFOIL AND ISOLATED NOZZLE

SYMBOL	VELOCITY RATIO, V_0/V_J
○	0
△	1/8
□	1/4
▽	3/8

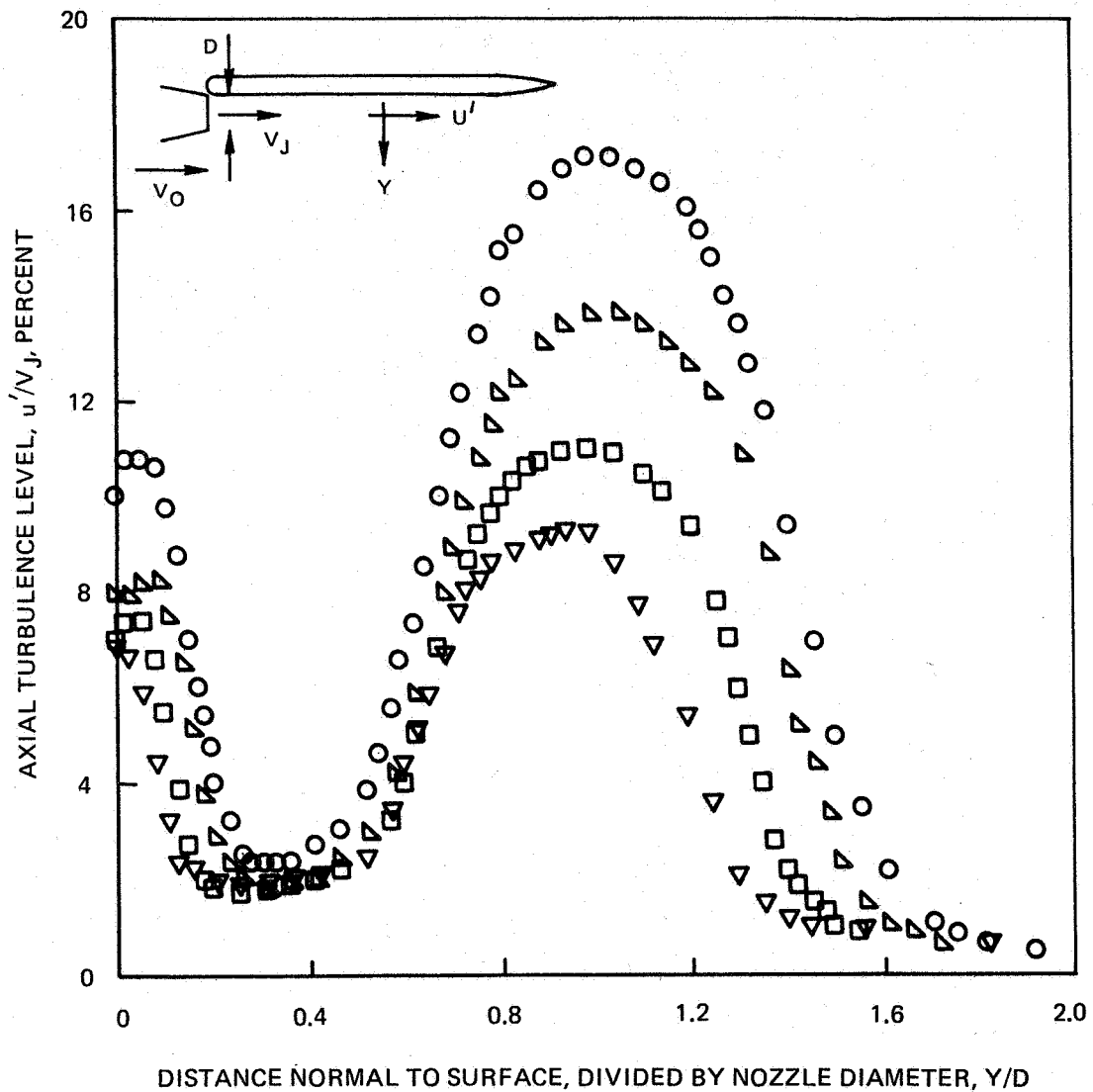


FIGURE 22— CONTINUED. (b) MIDCHORD, 160 M/SEC EXHAUST VELOCITY

SYMBOL	VELOCITY RATIO, V_O/V_J
○	0
□	1/4
△	1/2
◇	3/4

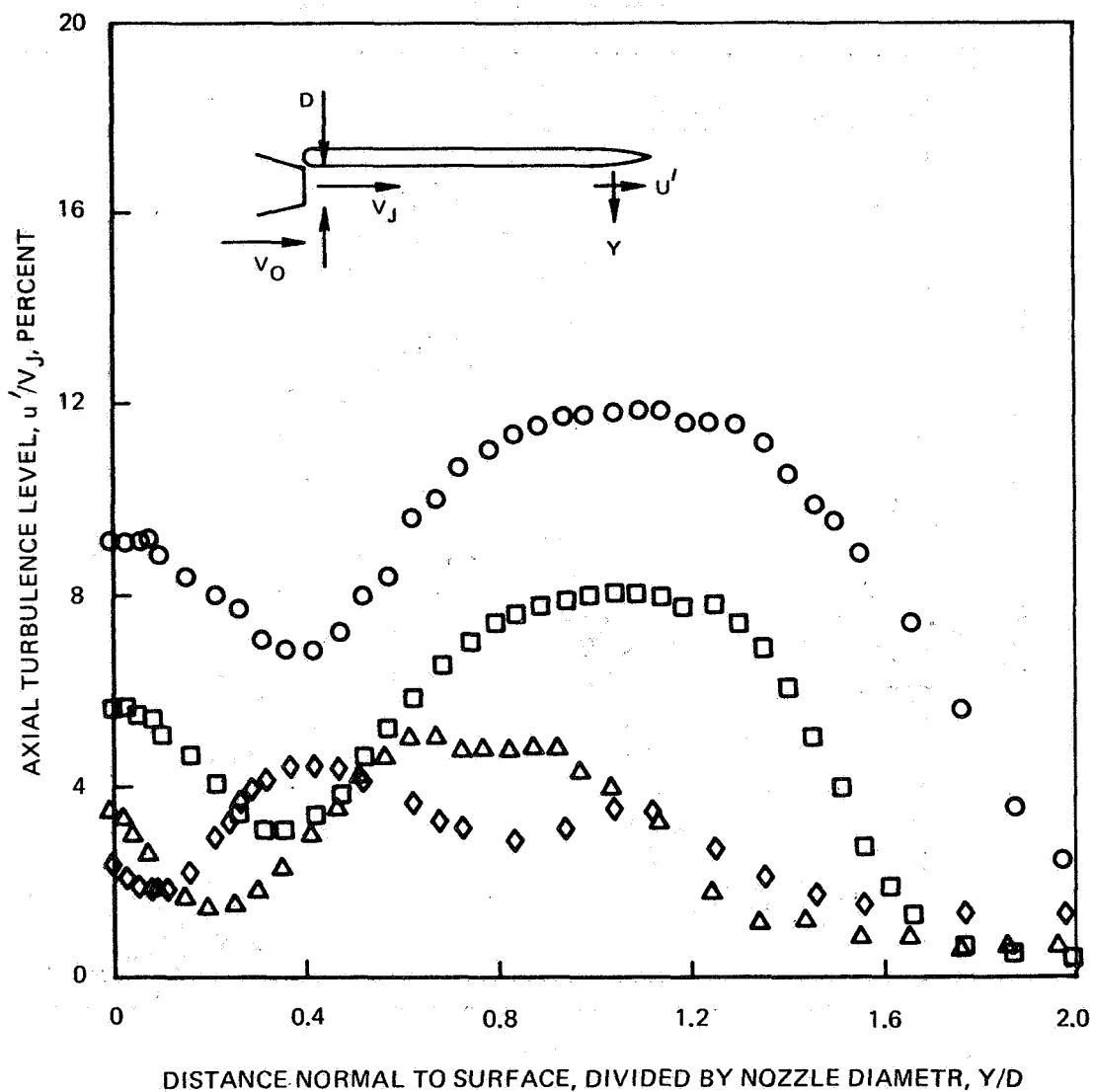


FIGURE 22— CONTINUED. (c) NEAR TRAILING EDGE, 125 M/SEC EXHAUST VELOCITY

SYMBOL	VELOCITY RATIO, V_O/V_J
○	0
△	1/8
□	1/4
▽	3/8

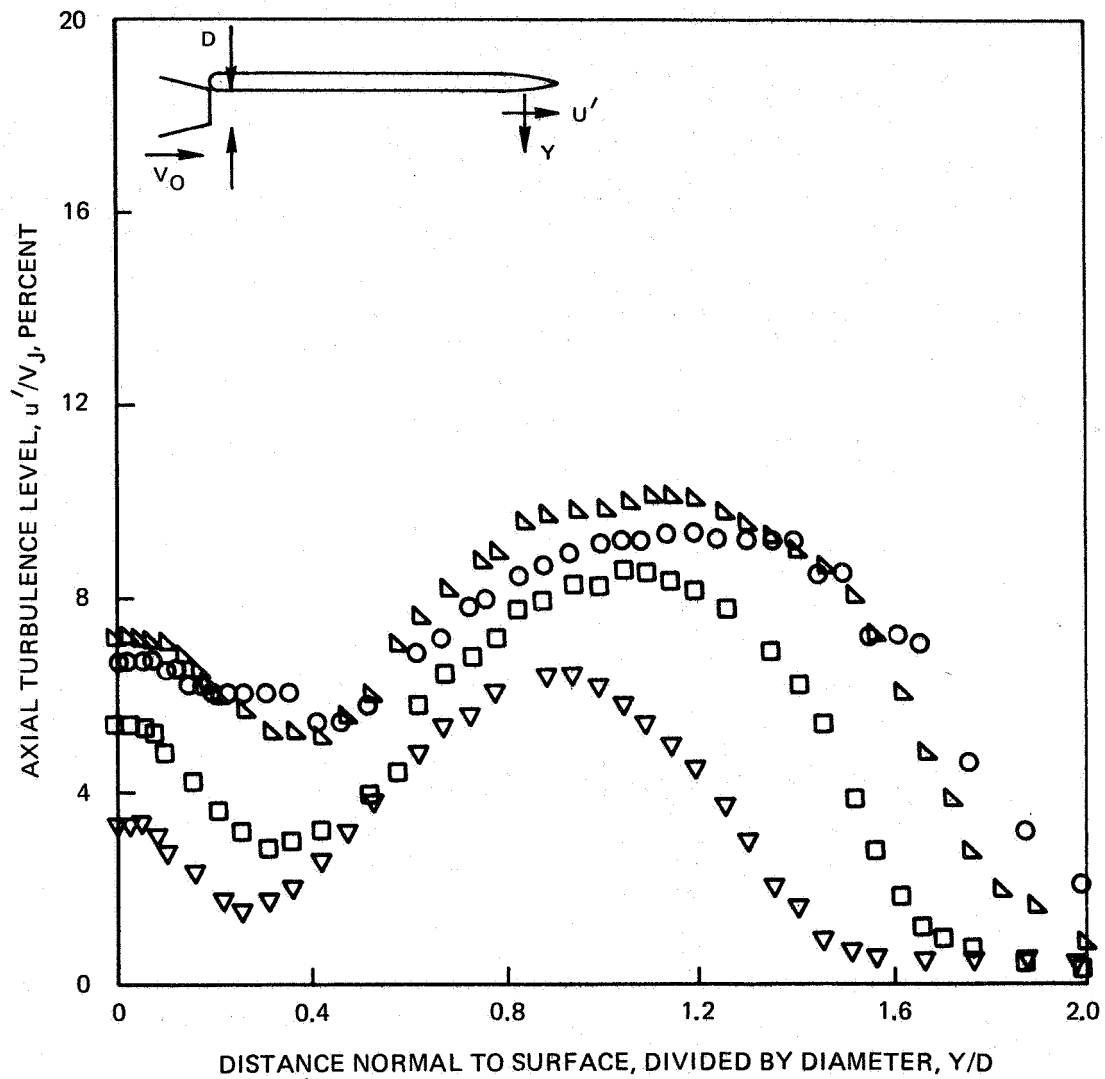


FIGURE 22— CONCLUDED. (d) NEAR TRAILING EDGE, 160 M/SEC EXHAUST VELOCITY

SYMBOL	CONFIGURATION	U_J , M/SEC
○	MIDCHORD	125
△	MIDCHORD	160
●	AFT	125
●	AFT	160
□	NOZZLE	157

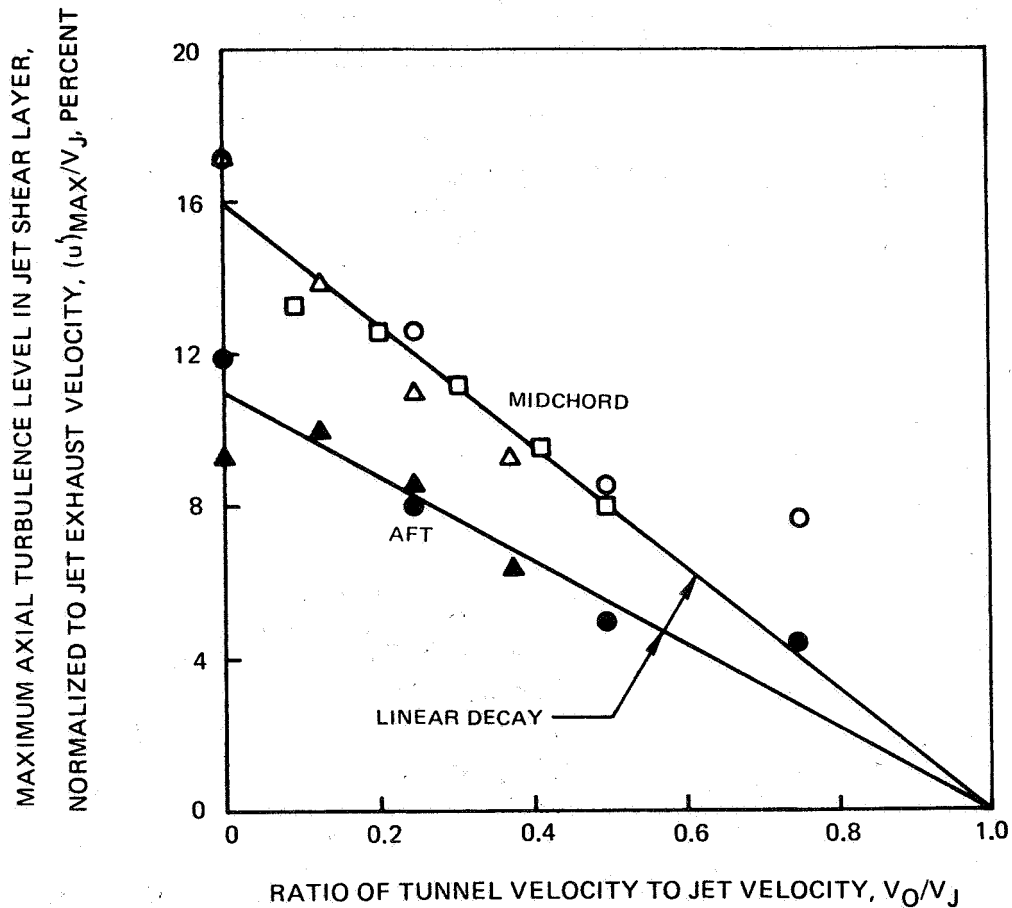


FIGURE 23— EFFECT OF VELOCITY RATIO ON MAXIMUM MEASURED TURBULENCE LEVEL IN JET SHEAR LAYER FOR TWO AXIAL POSITIONS ON LONG-CHORD AIRFOIL

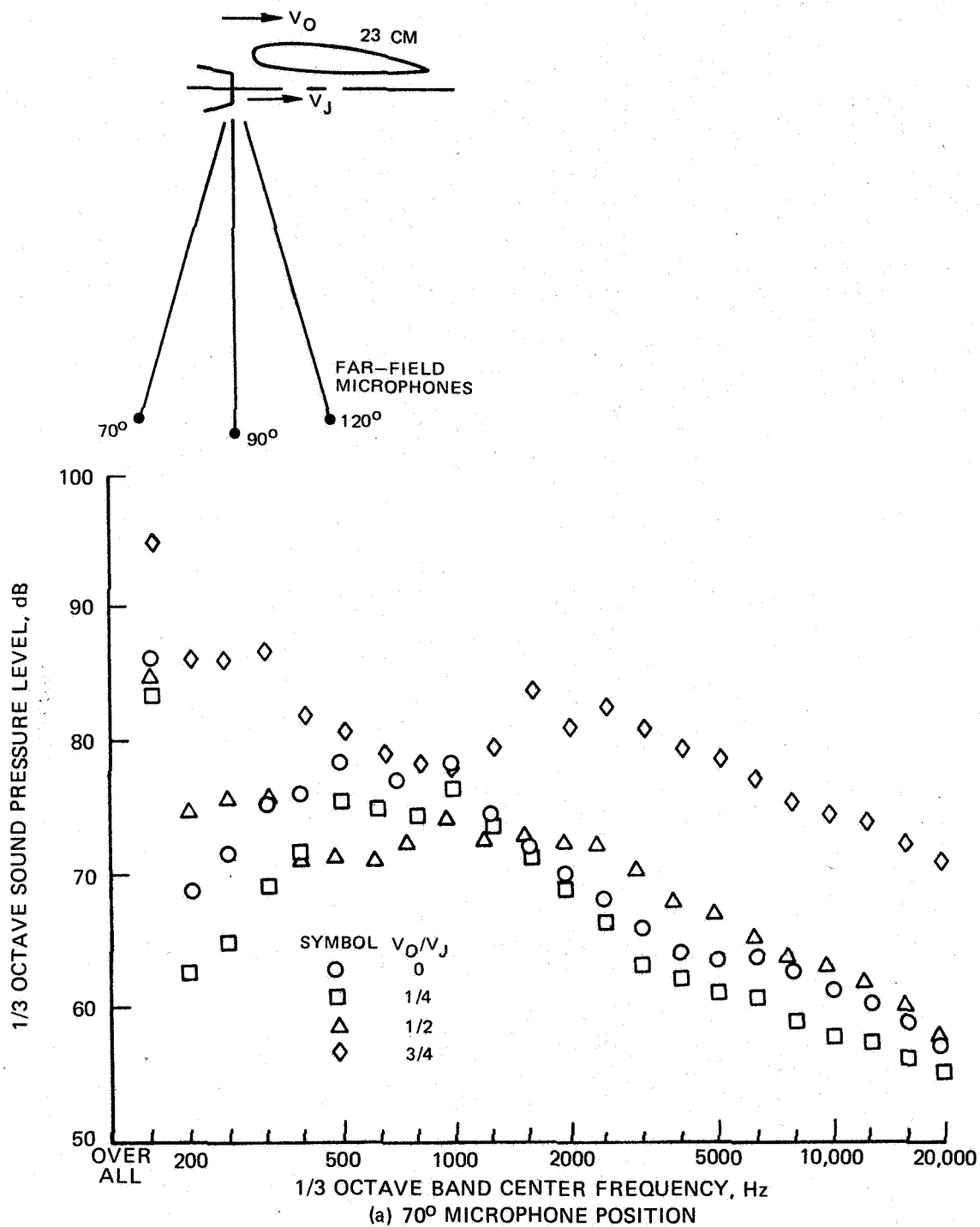


FIGURE 24 — EFFECT OF FLIGHT VELOCITY RATIO ON FAR-FIELD SOUND PRESSURE LEVELS FOR 90° DEFLECTION UNDER-THE-WING EXTERNALLY BLOWN FLAP AND 125 M/SEC EXHAUST VELOCITY

SYMBOL	VELOCITY RATIO, V_0/V_J
○	0
□	1/4
△	1/2
◇	3/4

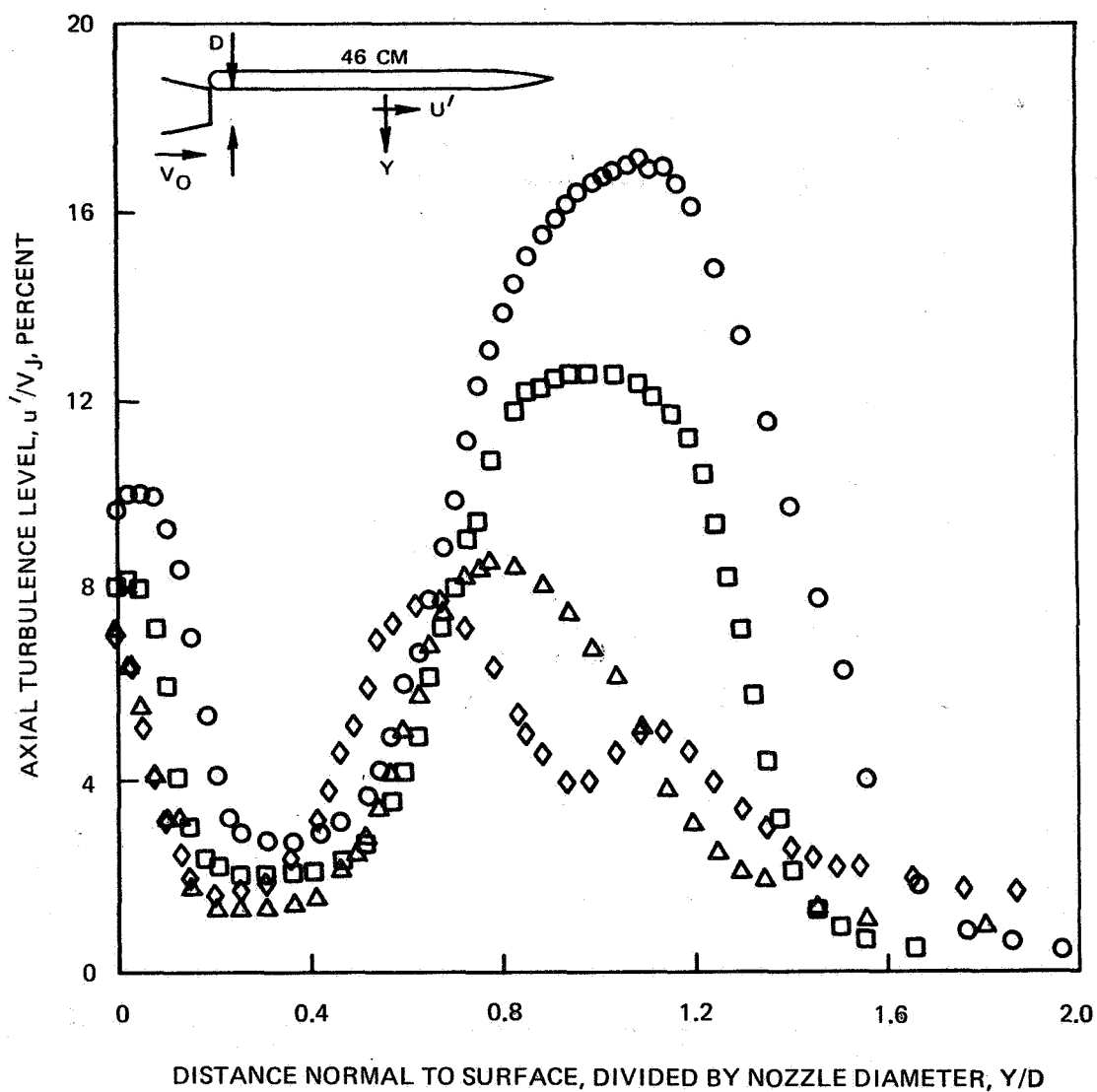


FIGURE 22—EFFECT OF FLIGHT VELOCITY RATIO ON TURBULENCE PROFILES NEAR LONG-CHORD AIRFOIL. (a) MIDCHORD, 125 M/SEC EXHAUST VELOCITY

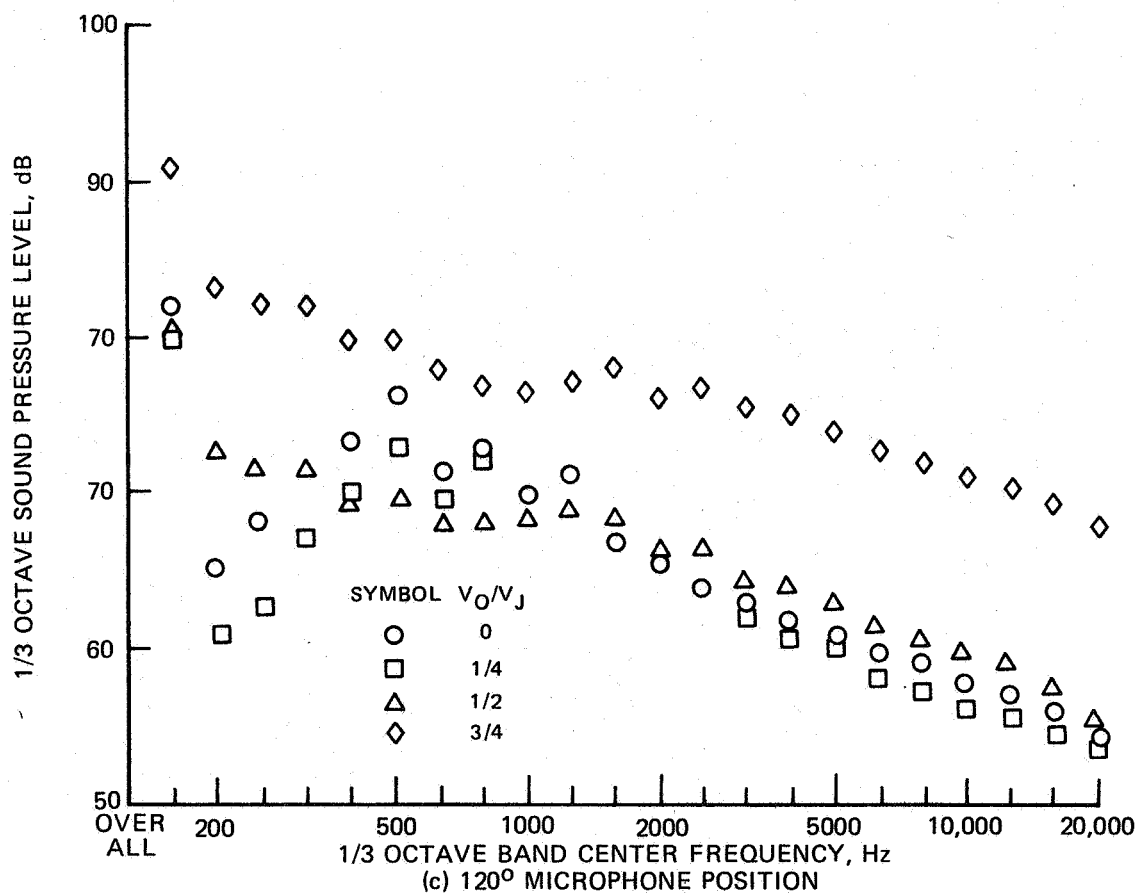
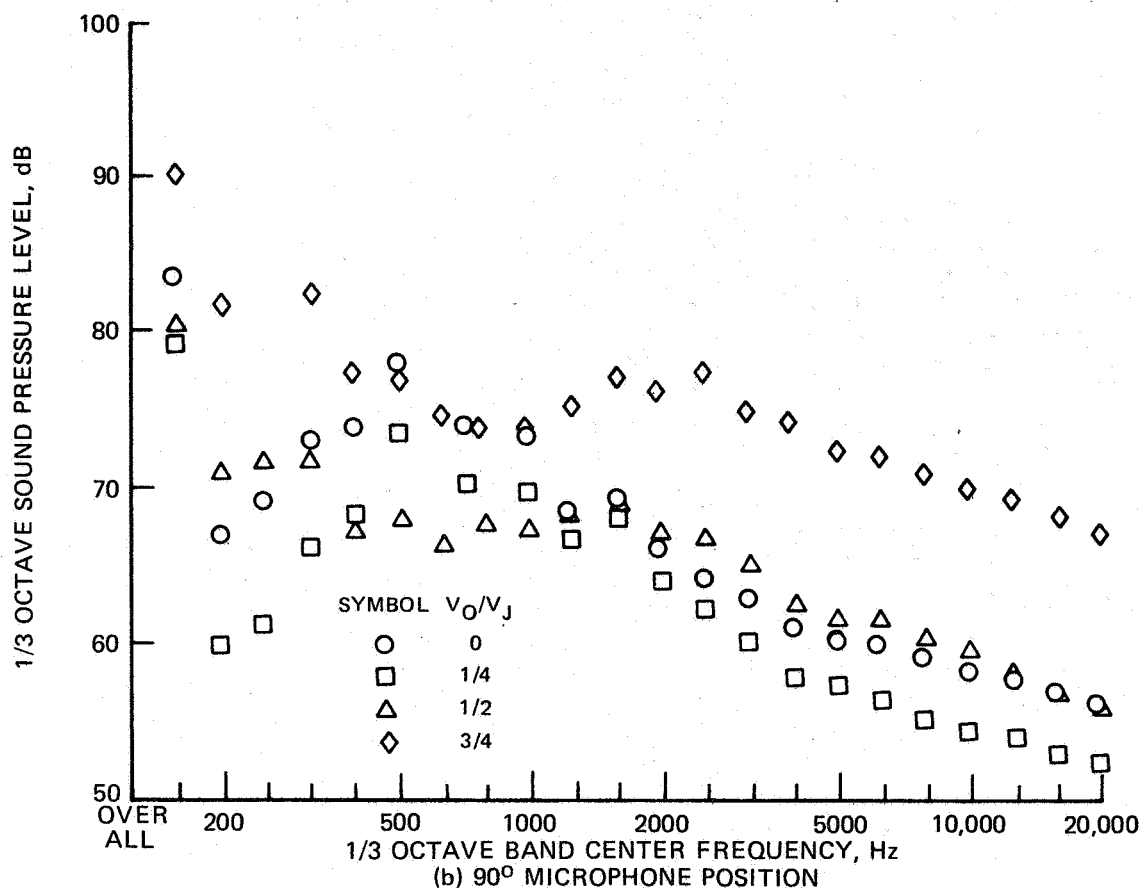


FIGURE 24 - CONCLUDED.

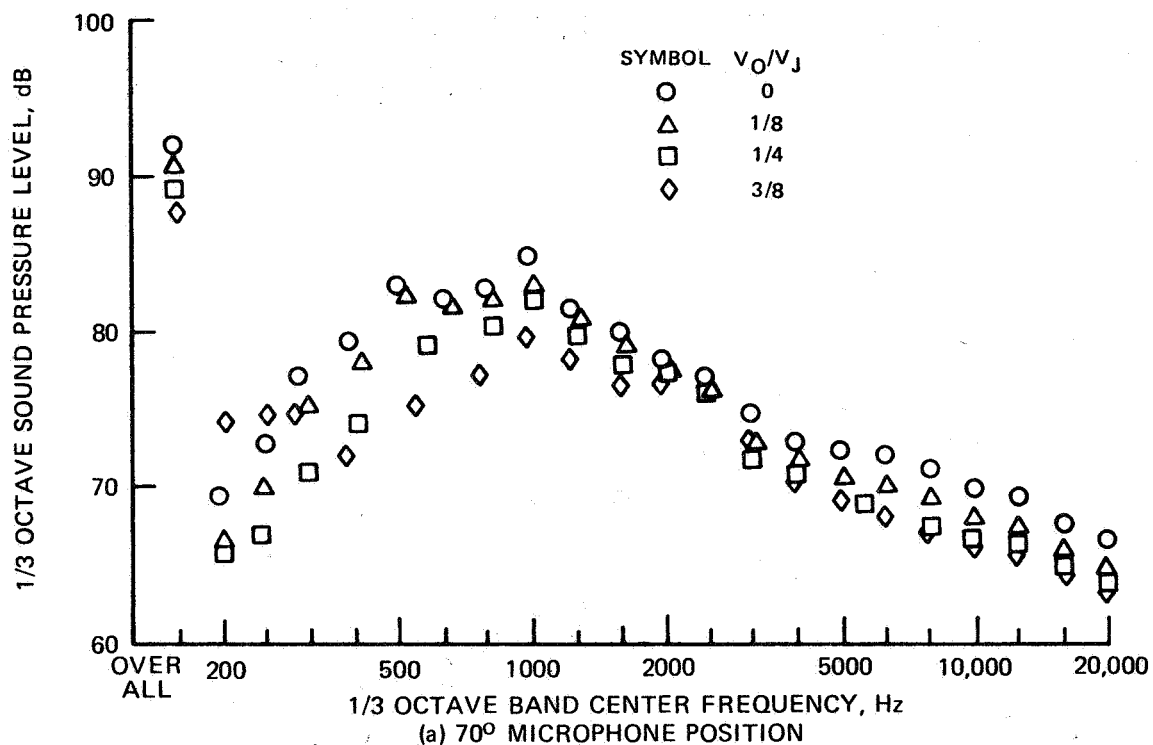
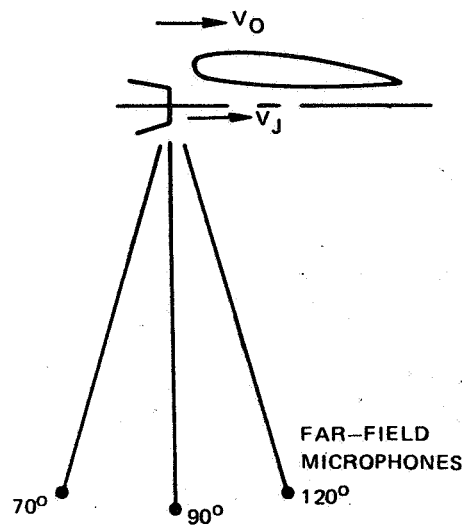


FIGURE 25 – EFFECT OF FLIGHT VELOCITY RATIO ON FAR-FIELD SOUND PRESSURE LEVELS FOR 90° DEFLECTION UNDER-THE-WING EXTERNALLY BLOWN FLAP AND 160 M/SEC EXHAUST VELOCITY

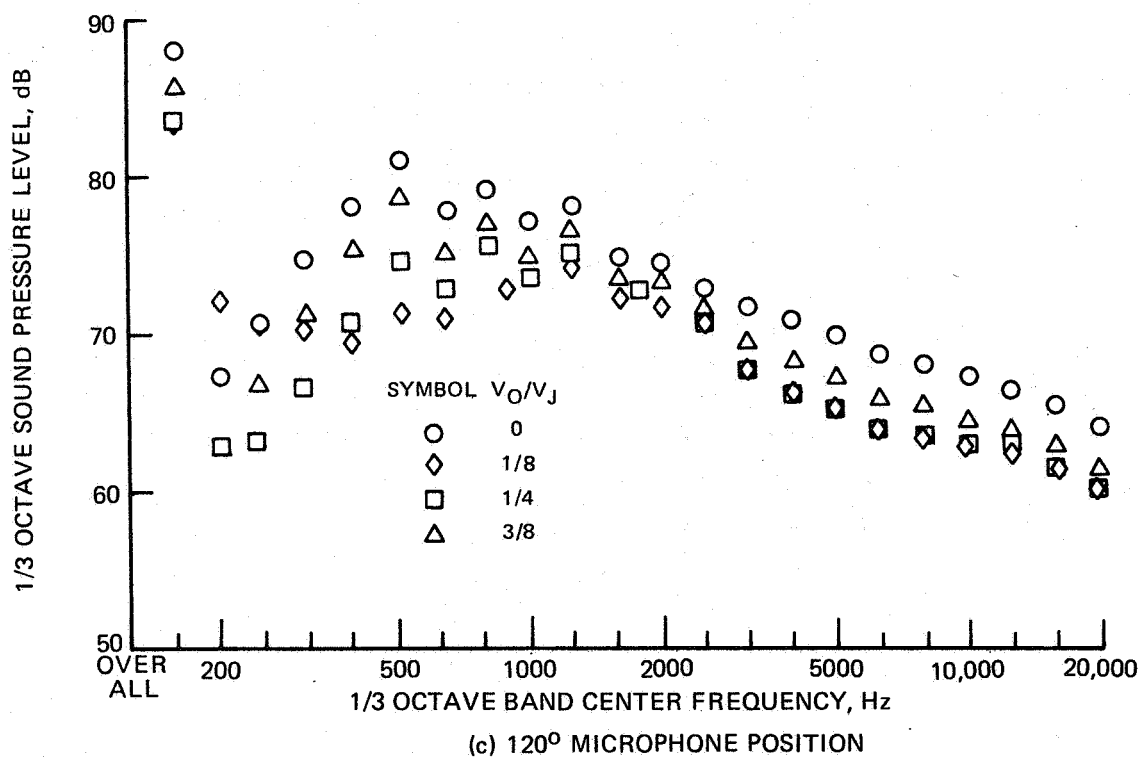
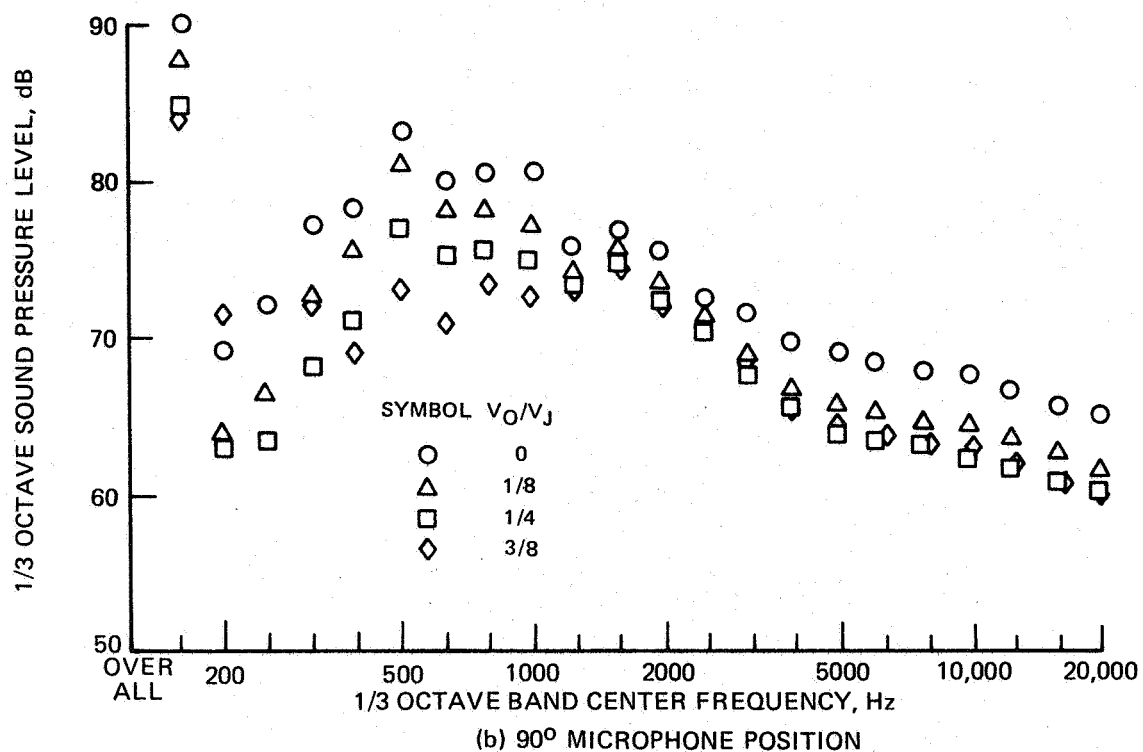


FIGURE 25 – CONCLUDED.

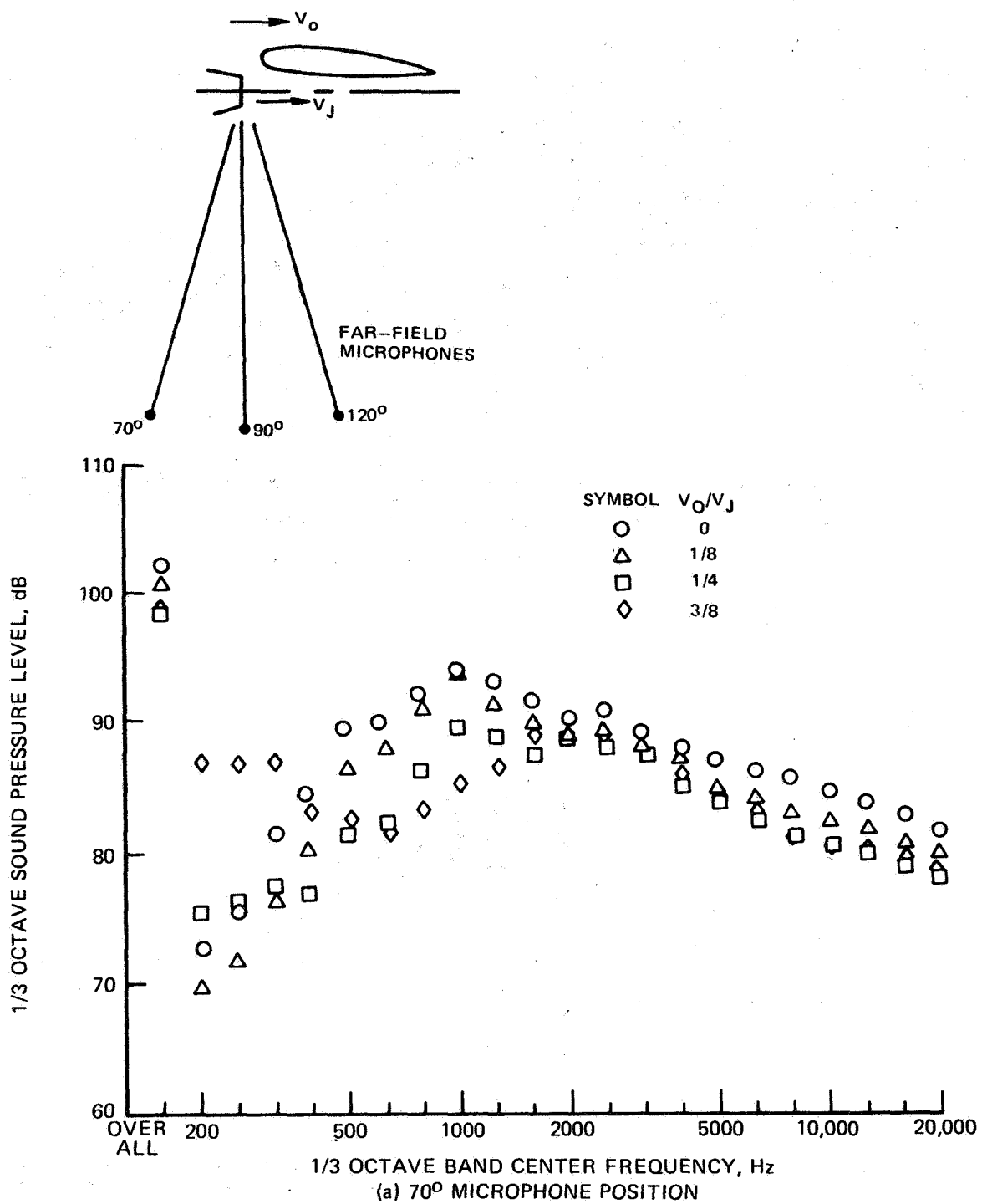


FIGURE 26 — EFFECT OF FLIGHT VELOCITY RATIO ON FAR-FIELD SOUND PRESSURE LEVELS FOR 90° DEFLECTION UNDER-THE-WING EXTERNALLY BLOWN FLAP AND 250 M/SEC EXHAUST VELOCITY

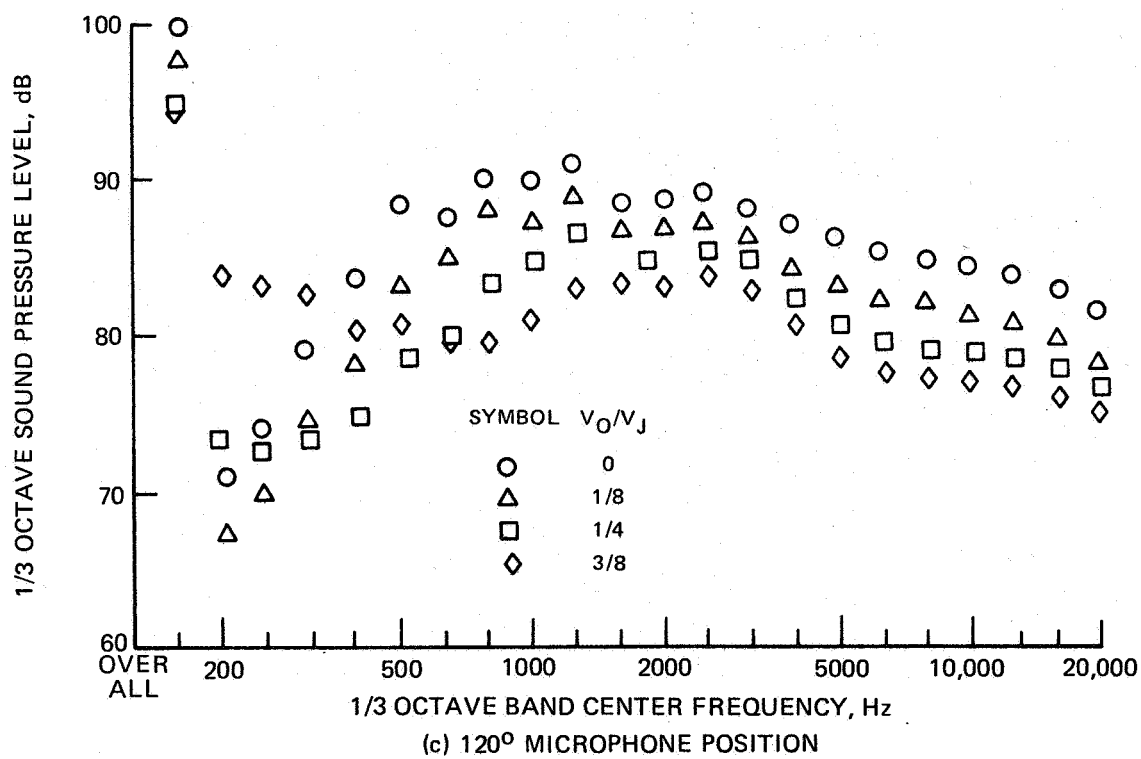
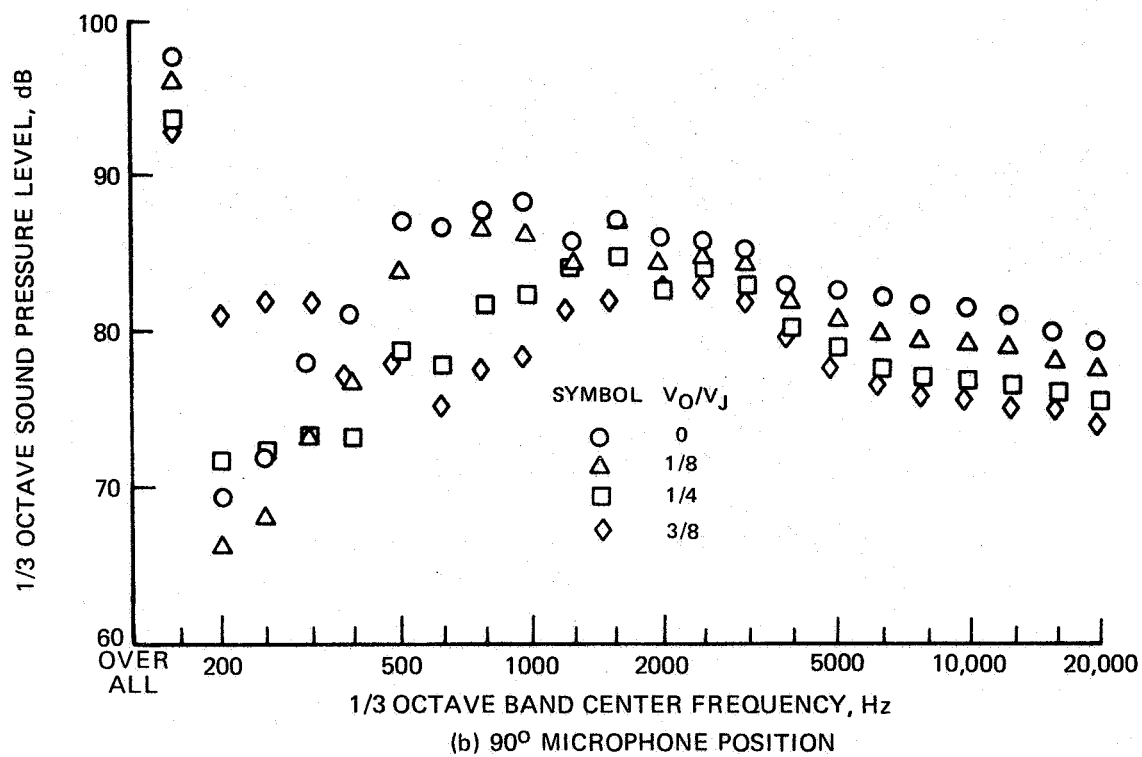
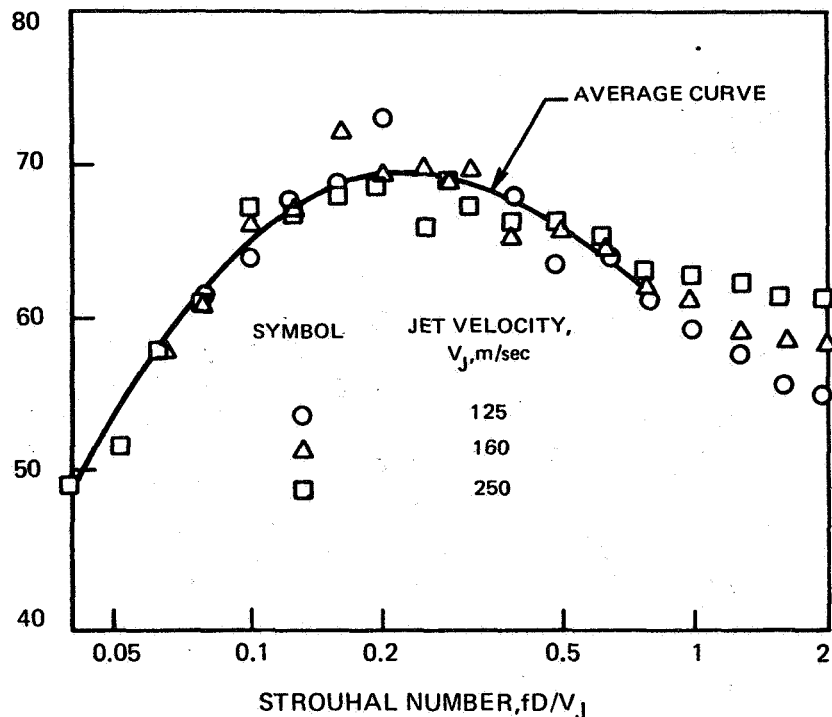


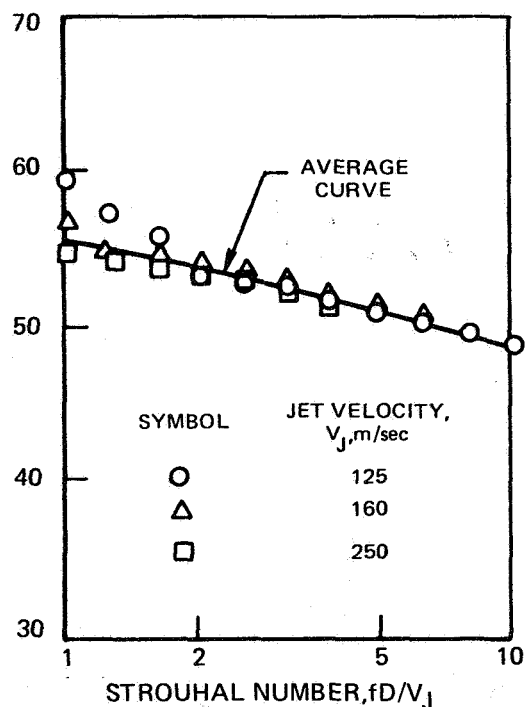
FIGURE 26 — CONCLUDED.

1/3 OCTAVE SOUND PRESSURE LEVEL ADJUSTED TO
100 m/sec JET VELOCITY FOR TRAILING EDGE NOISE,
SPL-50 LOG(V_j/100),dB



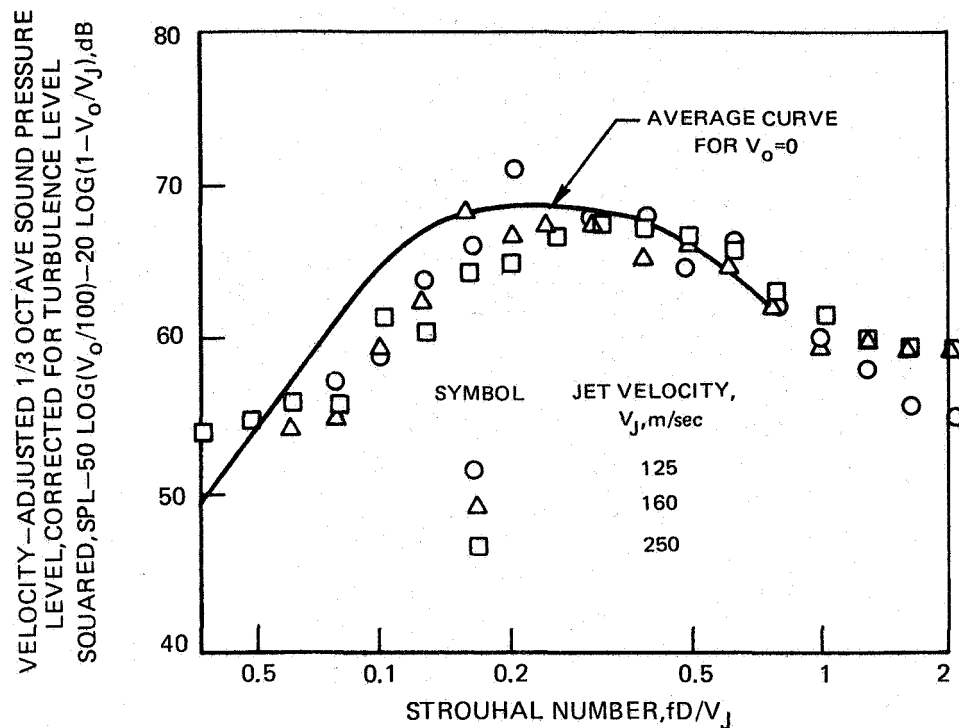
(a) ADJUSTED FOR JET VELOCITY AT LOW STROUHAL NUMBERS
AND ZERO TUNNEL VELOCITY

1/3 OCTAVE SOUND PRESSURE LEVEL ADJUSTED TO
100 m/sec JET VELOCITY FOR SURFACE NOISE AND
QUADRUPOLE NOISE, SPL-50 LOG(V_j/100),dB

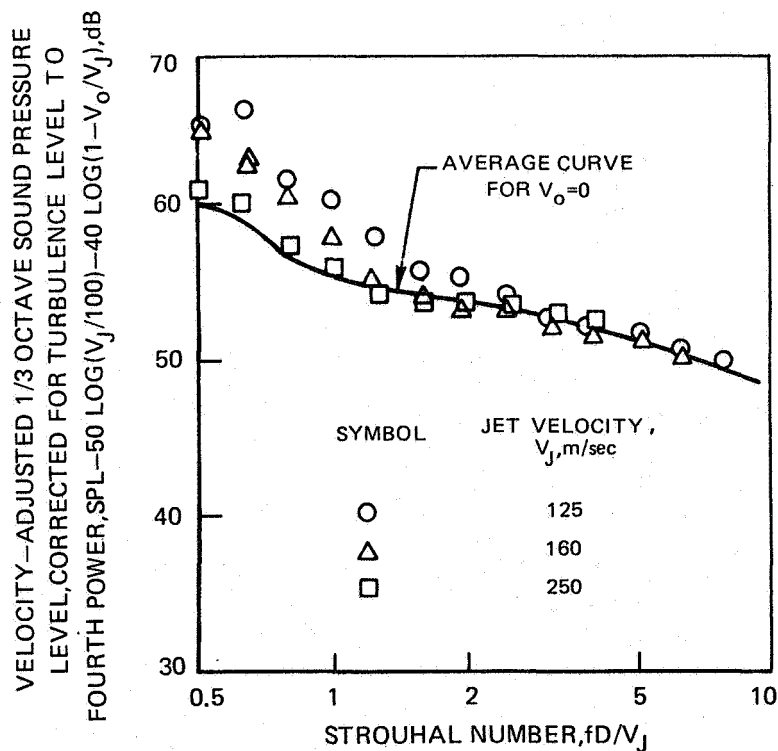


(b) ADJUSTED FOR JET VELOCITY AT HIGH
STROUHAL NUMBERS AND ZERO TUNNEL
VELOCITY

FIGURE 27 -EFFECT OF FLIGHT VELOCITY RATIO AND JET EXHAUST VELOCITY ON
FAR-FIELD ACOUSTIC SPECTRA FOR 9° DEFLECTION UNDER-THE-WING
CONFIGURATION IN DIRECTION 90° FROM NOZZLE INLET



(c) ADJUSTED FOR JET VELOCITY AND TURBULENCE LEVEL
AT LOW STROUHAL NUMBERS AND VELOCITY RATIO
 $V_o/V_j=1/4$



(d) ADJUSTED FOR JET VELOCITY AND TURBULENCE
LEVEL AT HIGH STROUHAL NUMBERS AND VELOCITY
RATIO $V_o/V_j=1/4$

FIGURE 27 - CONCLUDED.

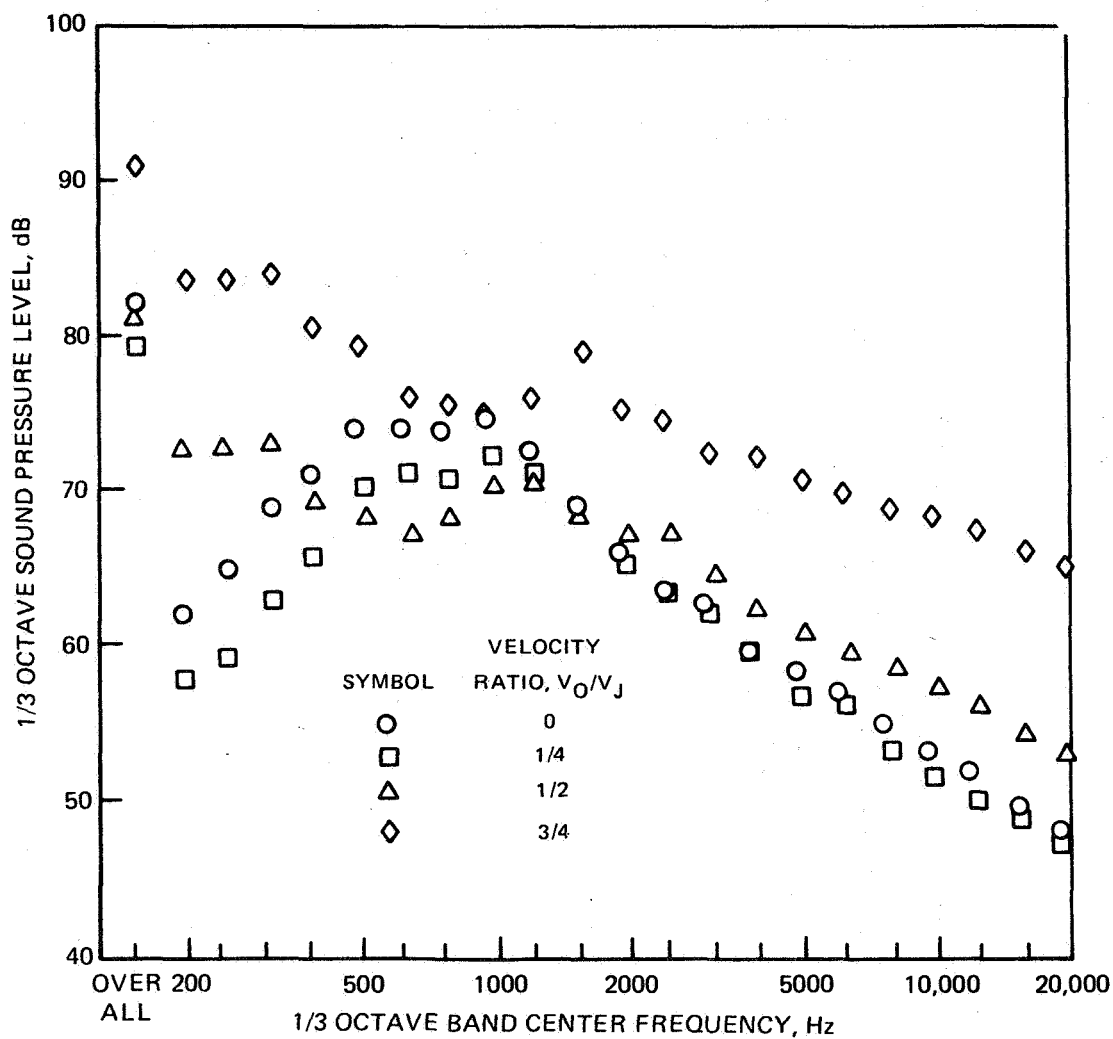
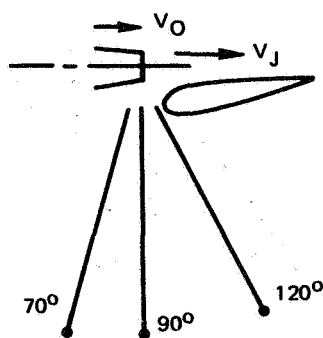


FIGURE 28—EFFECT OF FLIGHT VELOCITY RATIO ON FAR-FIELD SOUND PRESSURE LEVELS FOR SHORT-CHORD UPPER-SURFACE-BLOWING EXTERNALLY BLOWN FLAP AND 125 M/SEC EXHAUST VELOCITY. (a) 70° MICROPHONE POSITION

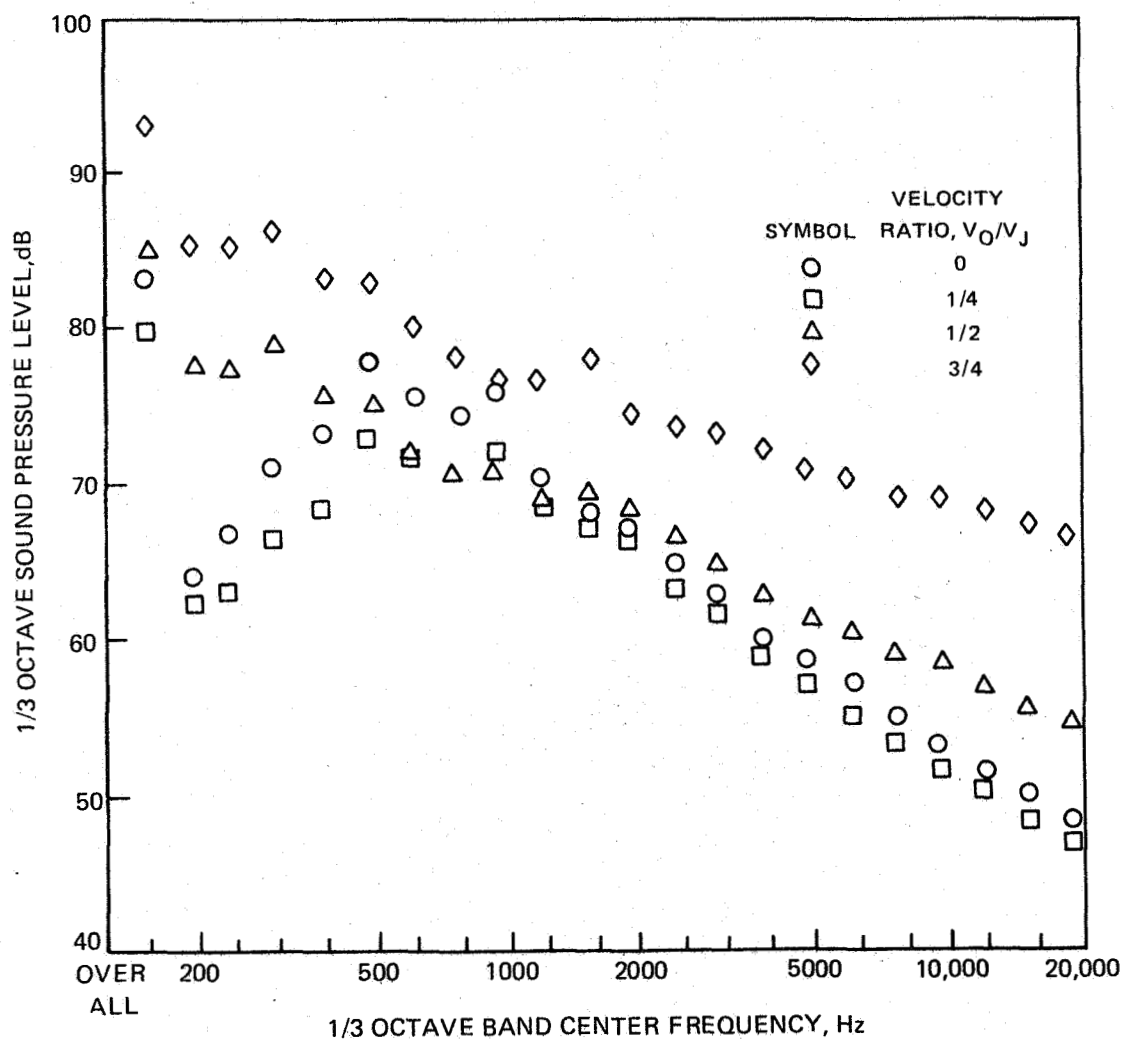
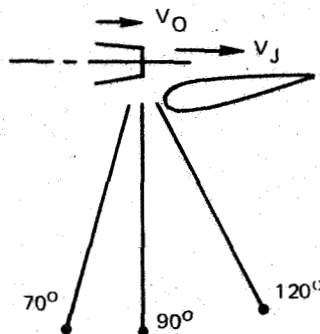


FIGURE 28—EFFECT OF FLIGHT VELOCITY RATIO ON FAR-FIELD SOUND PRESSURE LEVELS FOR SHORT-CHORD UPPER-SURFACE-BLOWING EXTERNALLY BLOWN FLAP AND 125 M/SEC EXHAUST VELOCITY. (b) 90° MICROPHONE POSITION

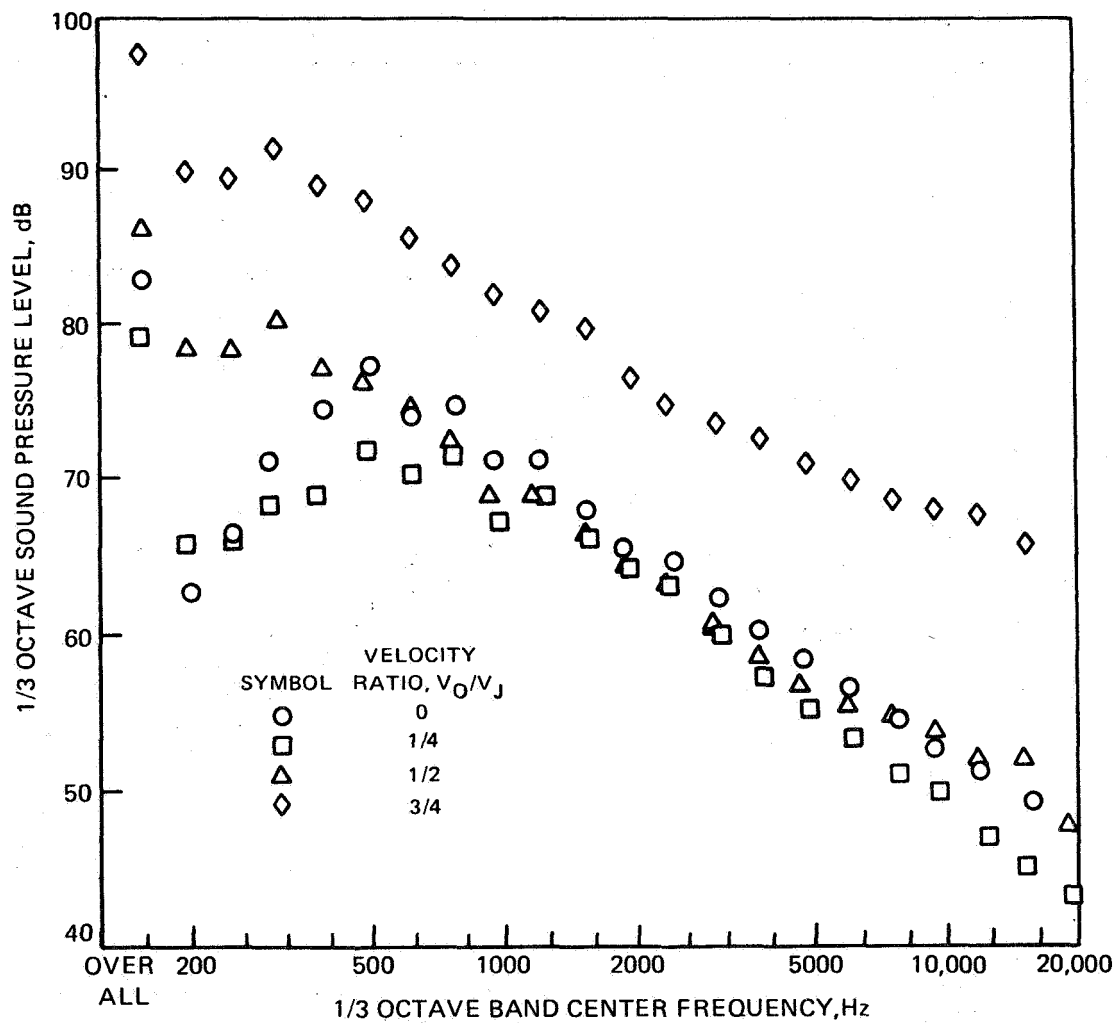
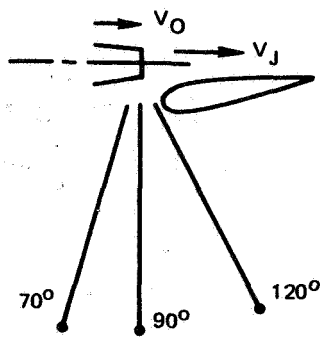


FIGURE 28—EFFECT OF FLIGHT VELOCITY RATIO ON FAR-FIELD SOUND PRESSURE LEVELS FOR SHORT-CHORD UPPER-SURFACE-BLOWING EXTERNALLY BLOWN FLAP AND 125 M/SEC EXHAUST VELOCITY. (c) 120° MICROPHONE POSITION

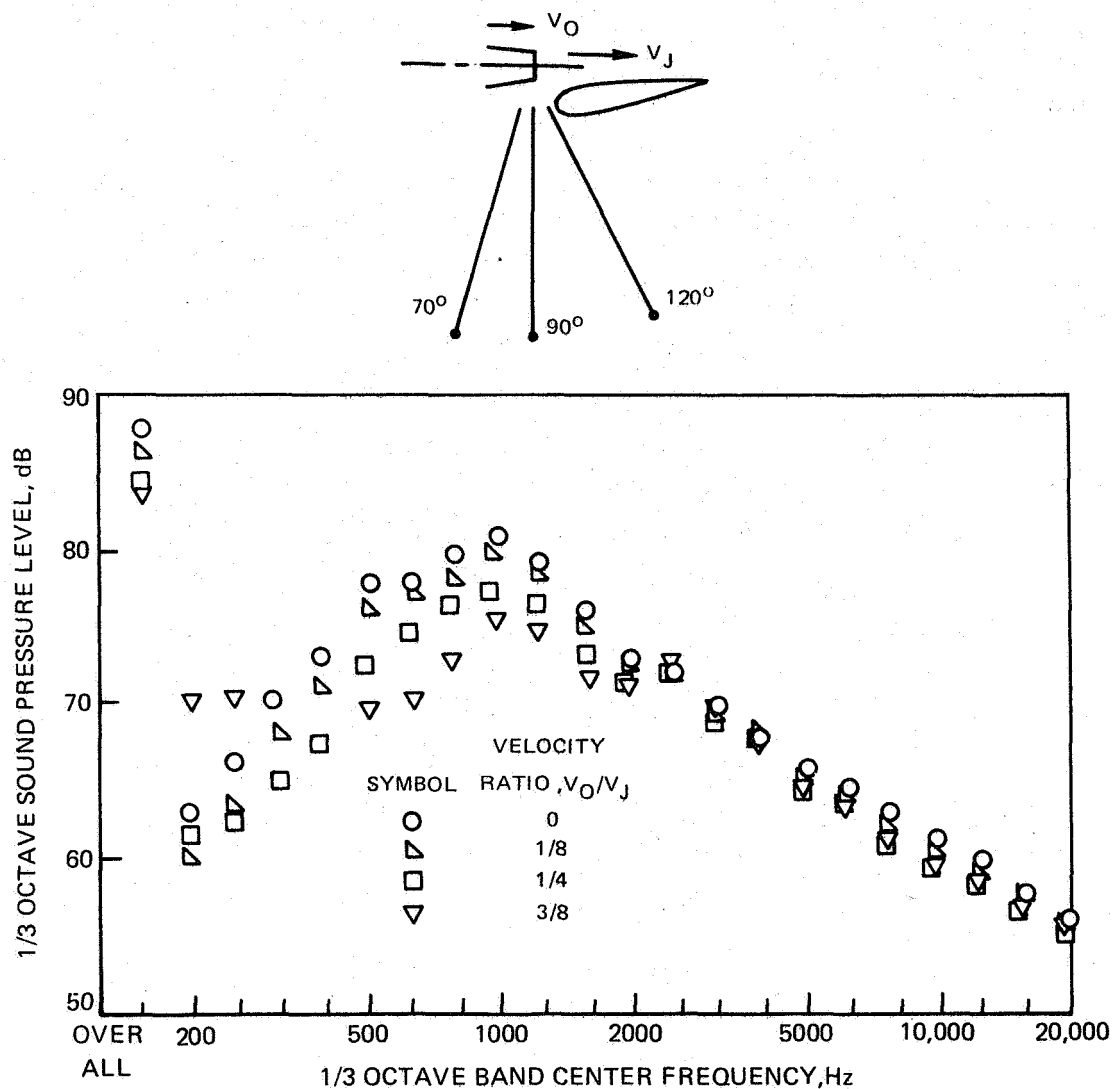


FIGURE 29—EFFECT OF FLIGHT VELOCITY RATIO ON FAR-FIELD SOUND PRESSURE LEVELS FOR SHORT-CHORD UPPER-SURFACE-BLOWING EXTERNALLY BLOWN FLAP AND 160 M/SEC EXHAUST VELOCITY. (a) 70° MICROPHONE POSITION

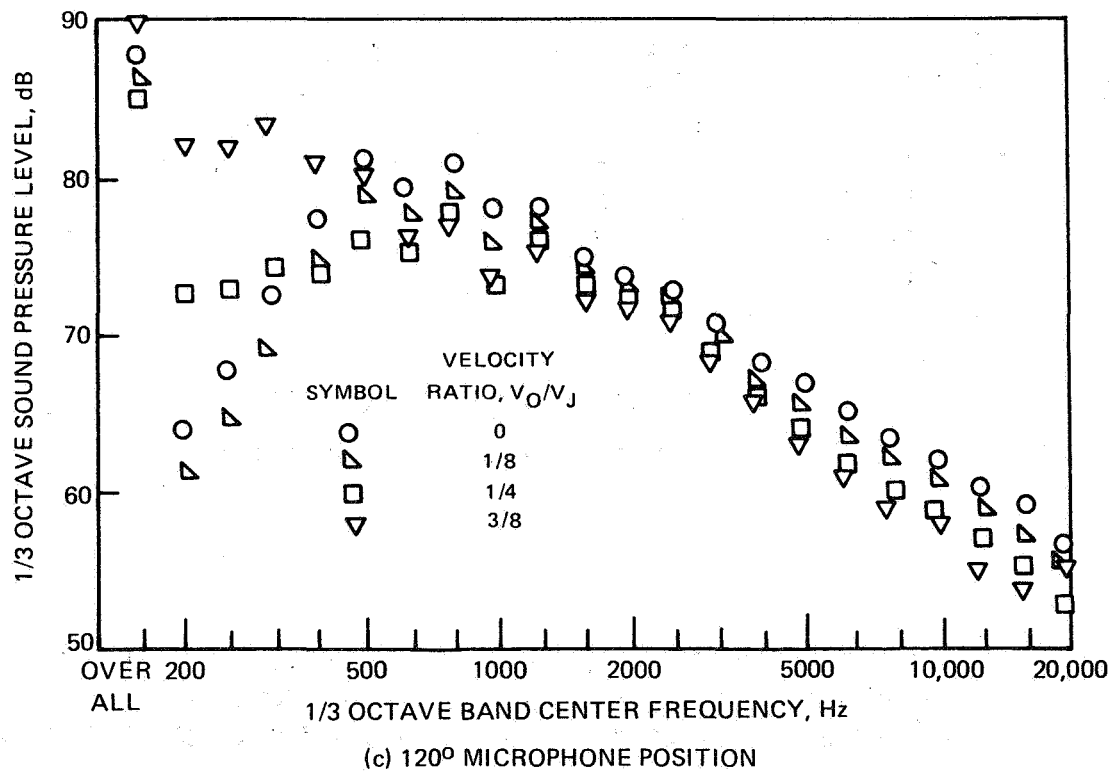
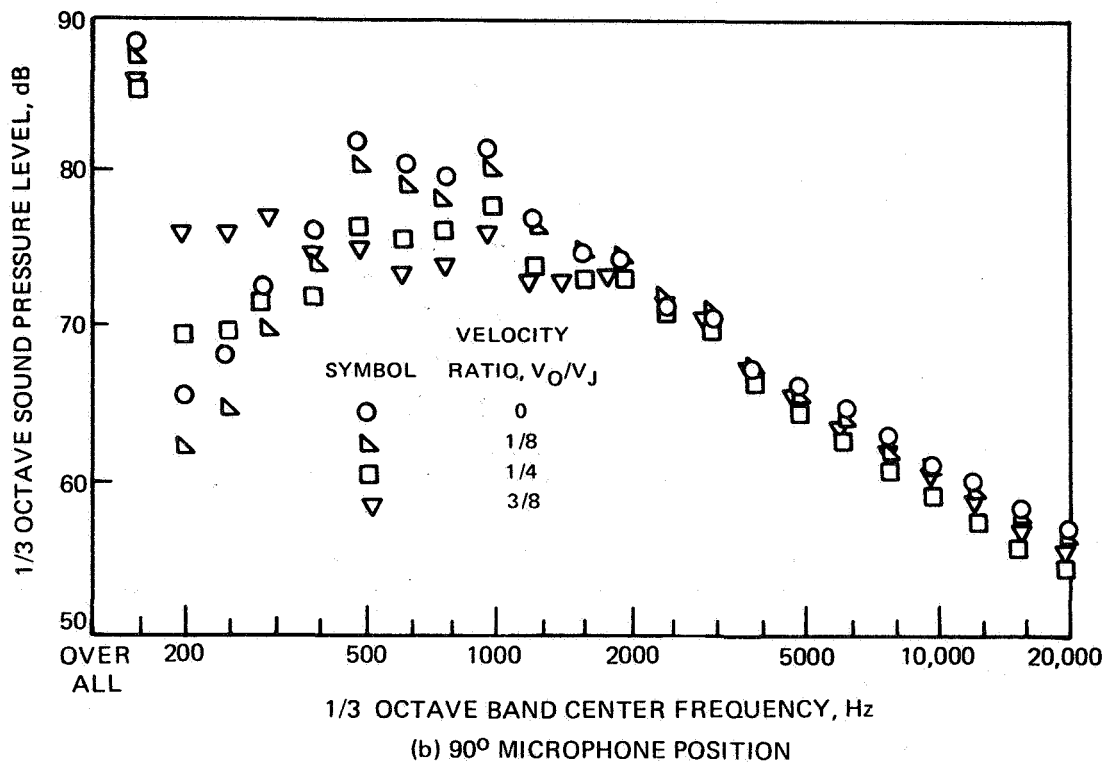


FIGURE 29— CONCLUDED.

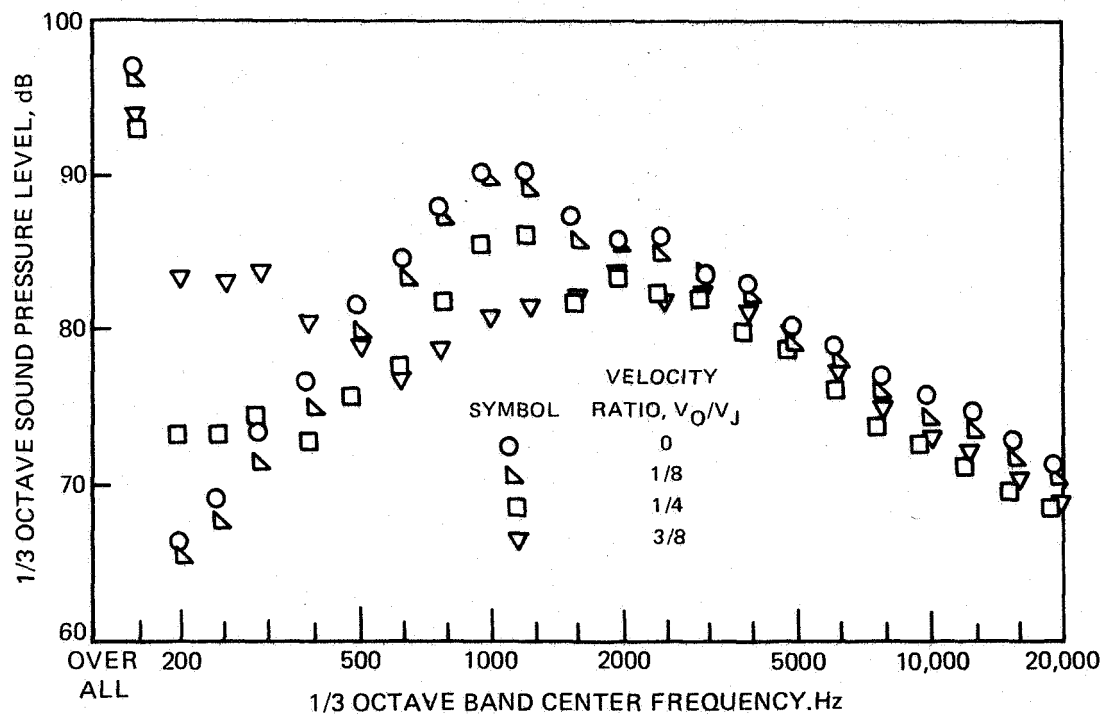
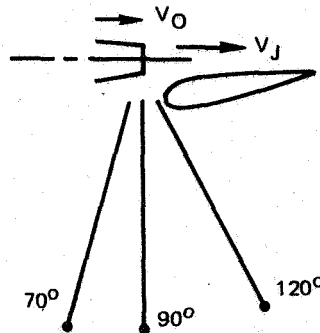


FIGURE 30—EFFECT OF FLIGHT VELOCITY RATIO ON FAR-FIELD SOUND PRESSURE LEVELS FOR SHORT-CHORD UPPER-SURFACE-BLOWING EXTERNALLY BLOWN FLAP AND 250 M/SEC EXHAUST VELOCITY. (a) 70° MICROPHONE POSITION

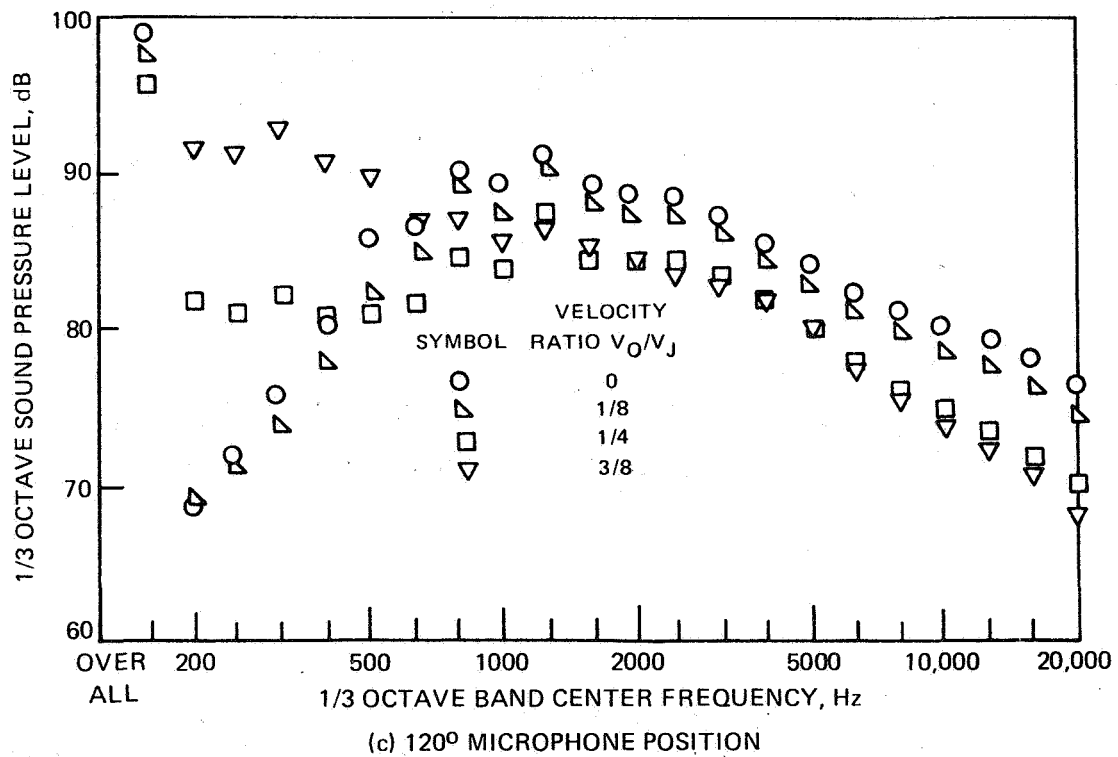
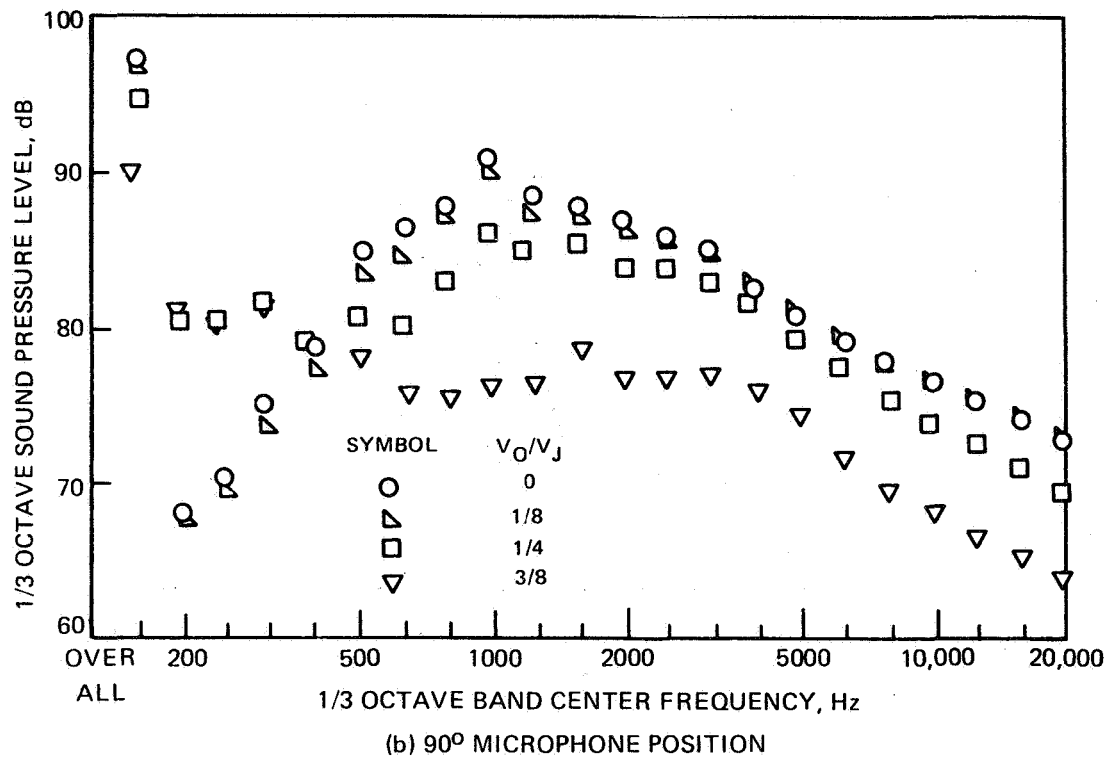
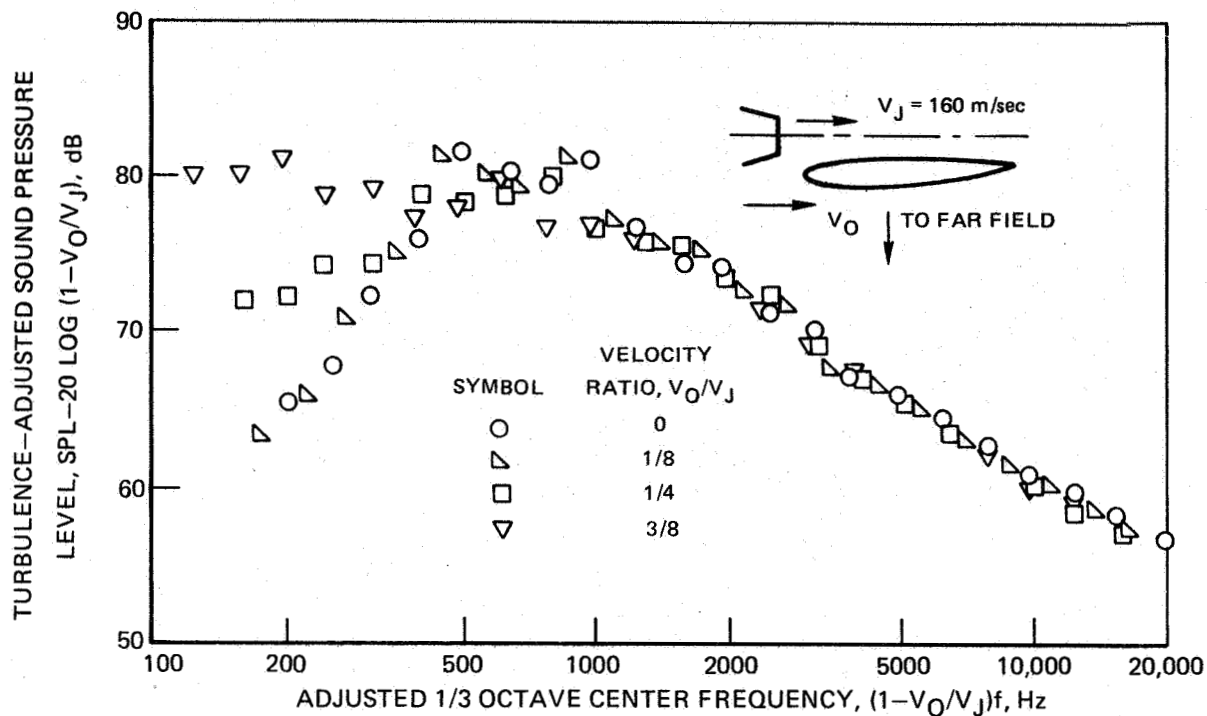
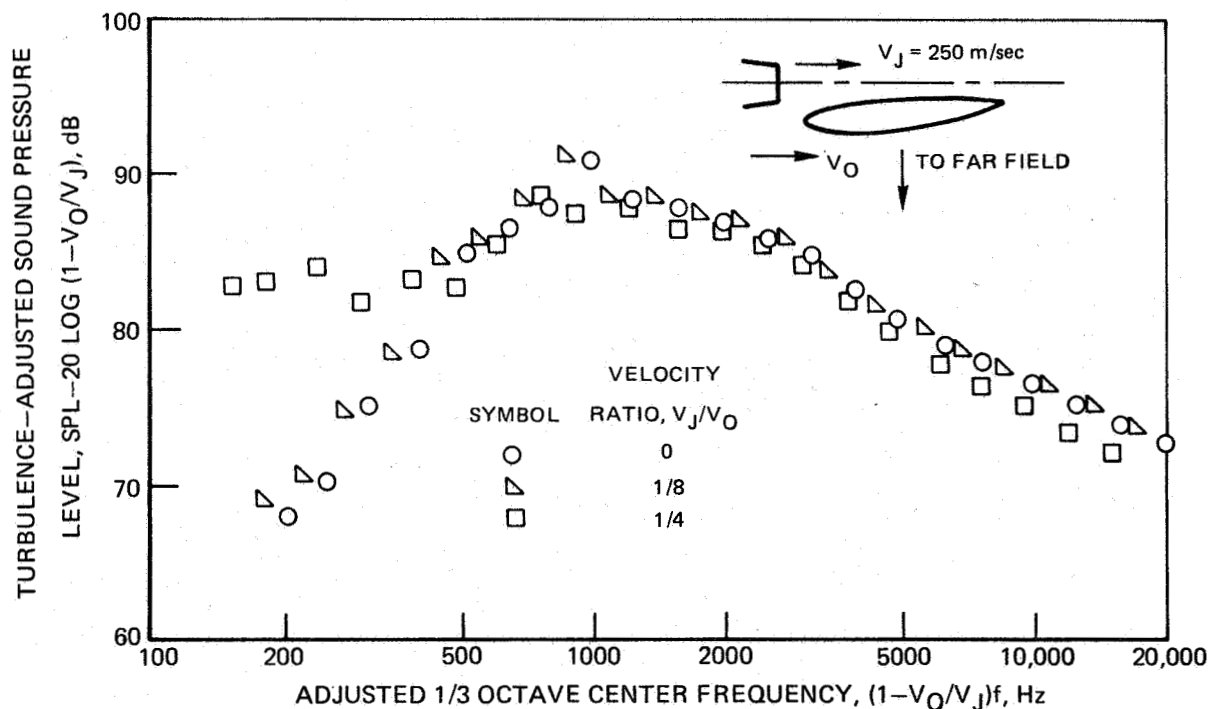


FIGURE 30— CONCLUDED.



(a) 160 m/sec EXHAUST JET VELOCITY



(b) 250 m/sec EXHAUST VELOCITY

FIGURE 31 – ADJUSTED FAR-FIELD SPECTRA AT 90° DIRECTION FROM SHORT-CHORD UPPER SURFACE BLOWING MODEL AT DIFFERENT VELOCITY RATIOS

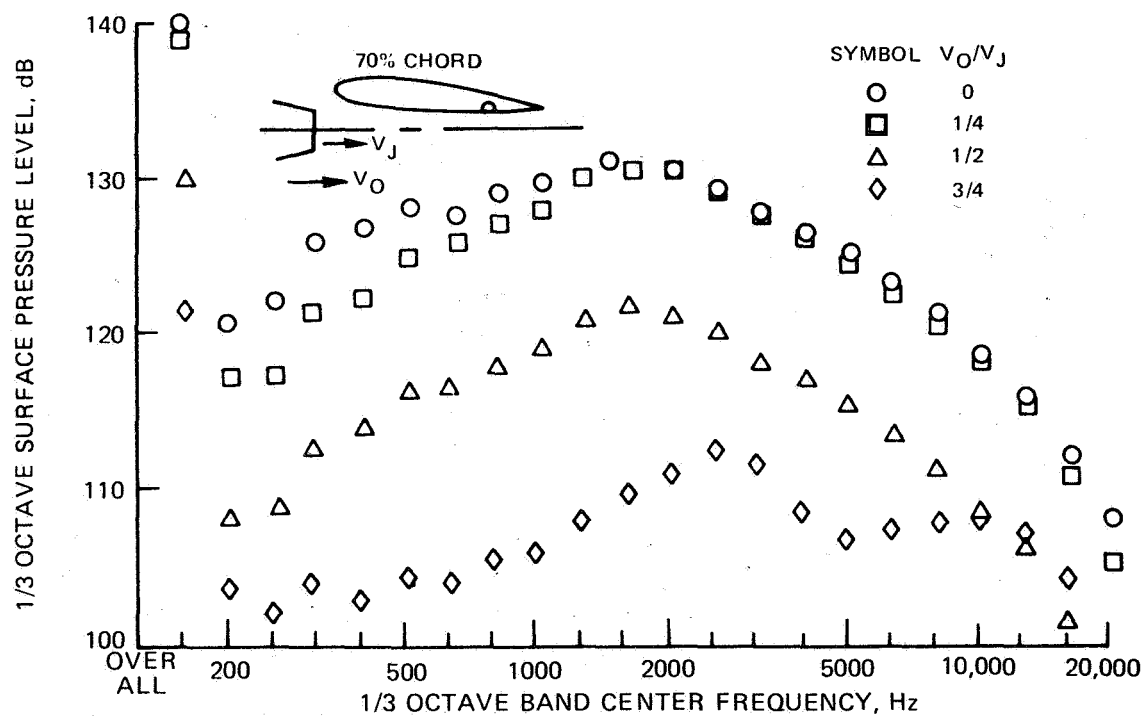
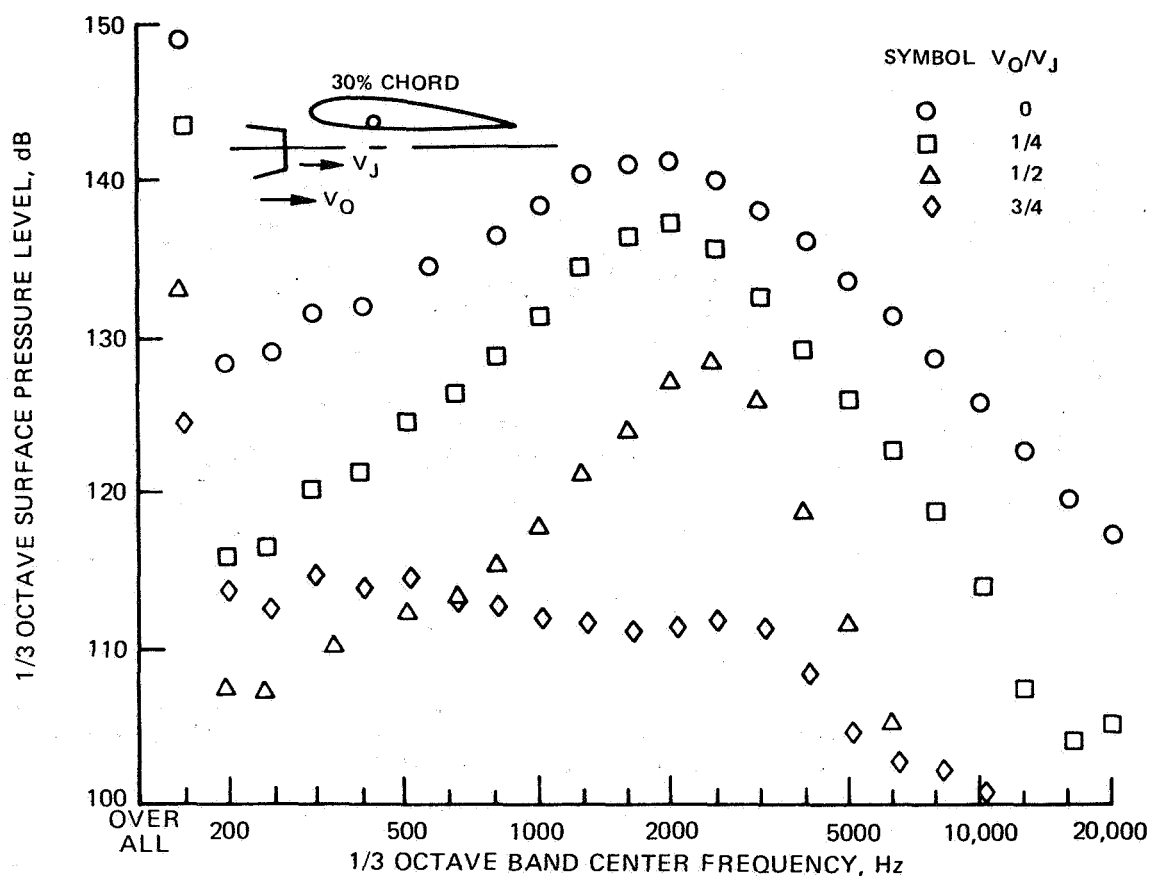


FIGURE 32—EFFECT OF FLIGHT VELOCITY RATIO ON SURFACE PRESSURE SPECTRA FOR 90° DEFLECTION UNDER-THE-WING EXTERNALLY BLOWN FLAP. (a) 125 M/SEC EXHAUST VELOCITY

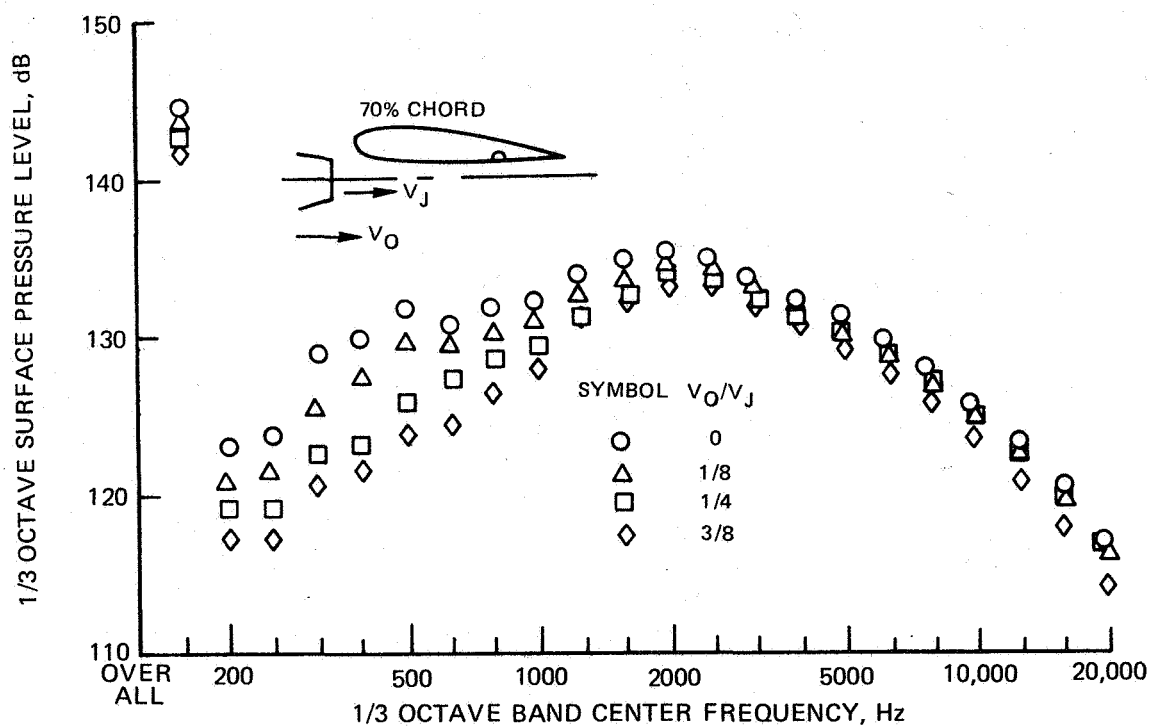
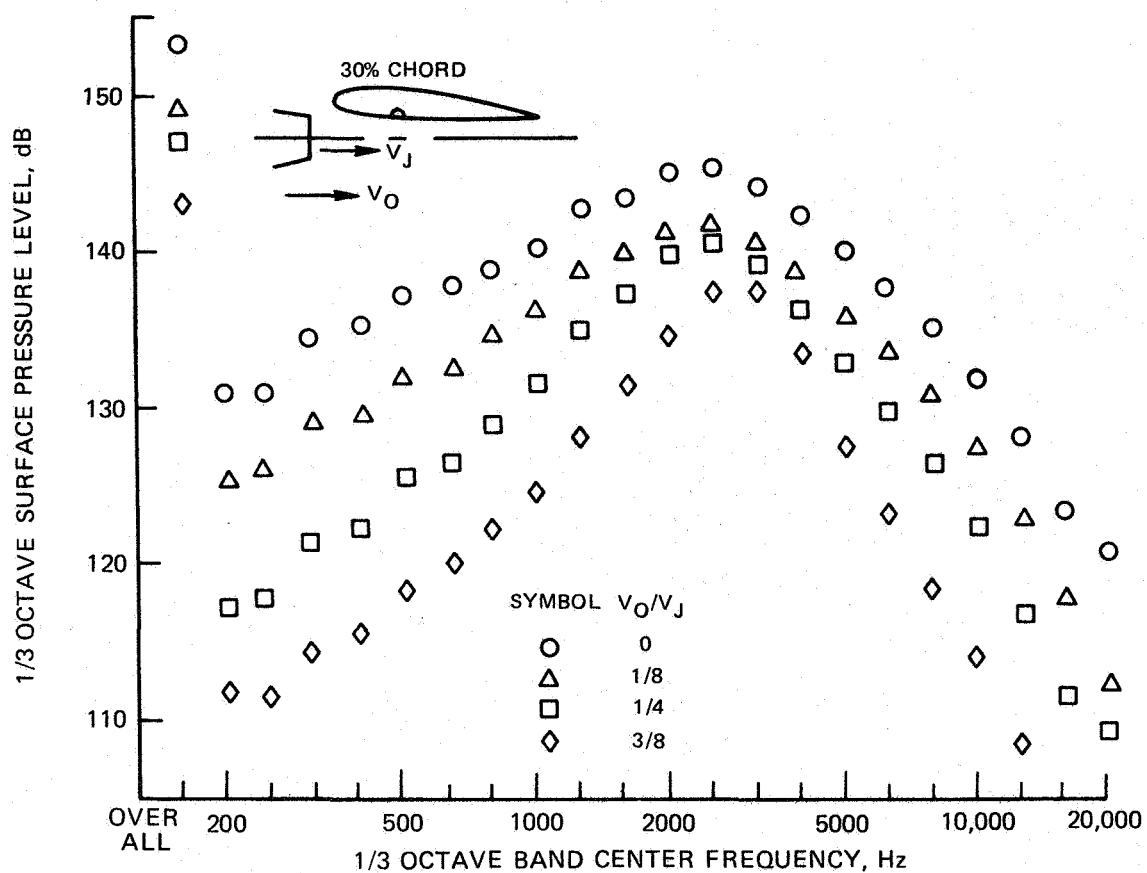


FIGURE 32 —CONTINUED. (b) 160 M/SEC EXHAUST VELOCITY

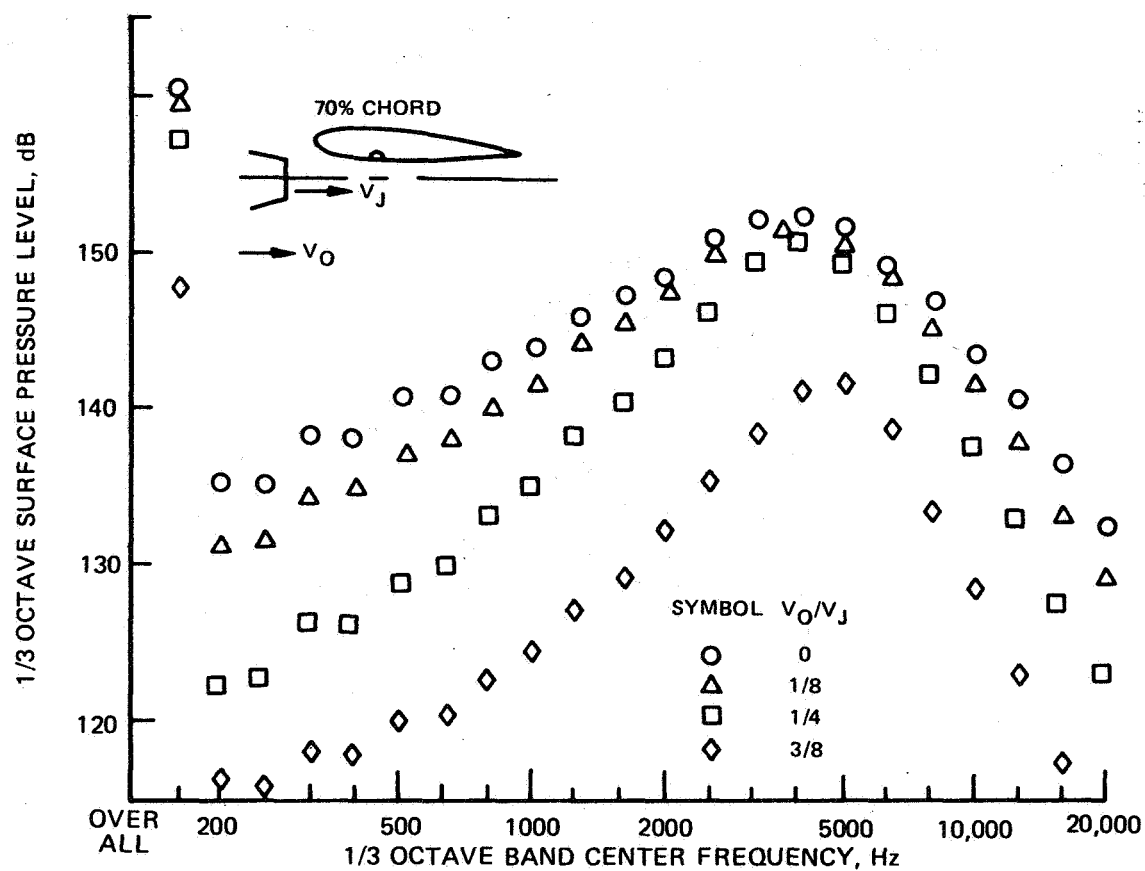
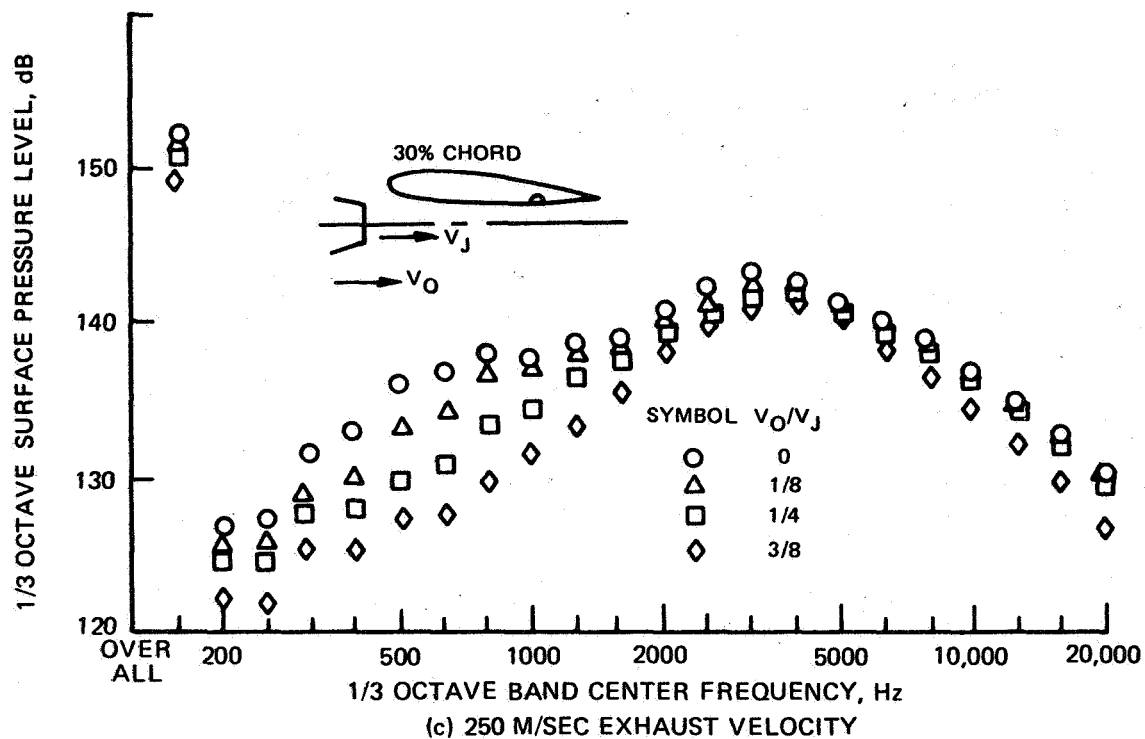
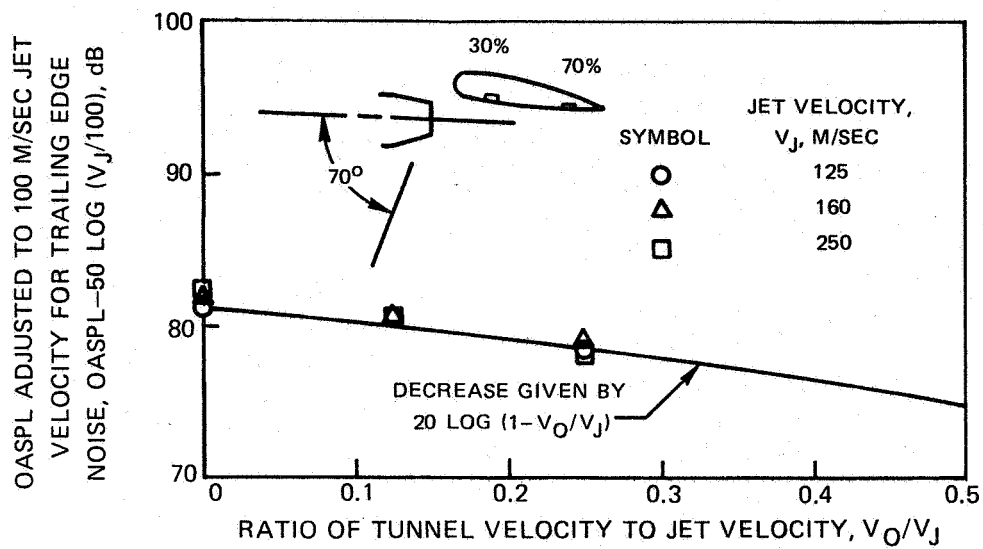
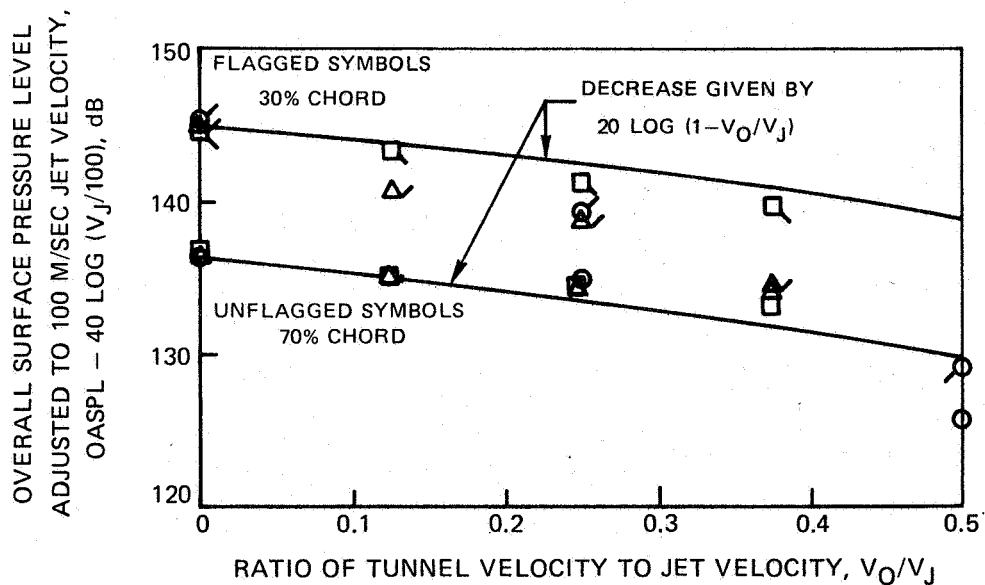


FIGURE 32 – CONCLUDED. (c) 250 M/SEC EXHAUST VELOCITY



(a) EFFECT OF VELOCITY RATIO ON OVERALL SOUND PRESSURE LEVEL IN DIRECTION 70° FROM NOZZLE



(b) EFFECT OF VELOCITY RATIO ON OVERALL SURFACE PRESSURE LEVEL AT 30% AND 70% CHORD

FIGURE 33 — EFFECT OF FLIGHT VELOCITY ON OVERALL SOUND AND SURFACE PRESSURE LEVELS FOR 9° DEFLECTION UNDER-THE-WING CONFIGURATION

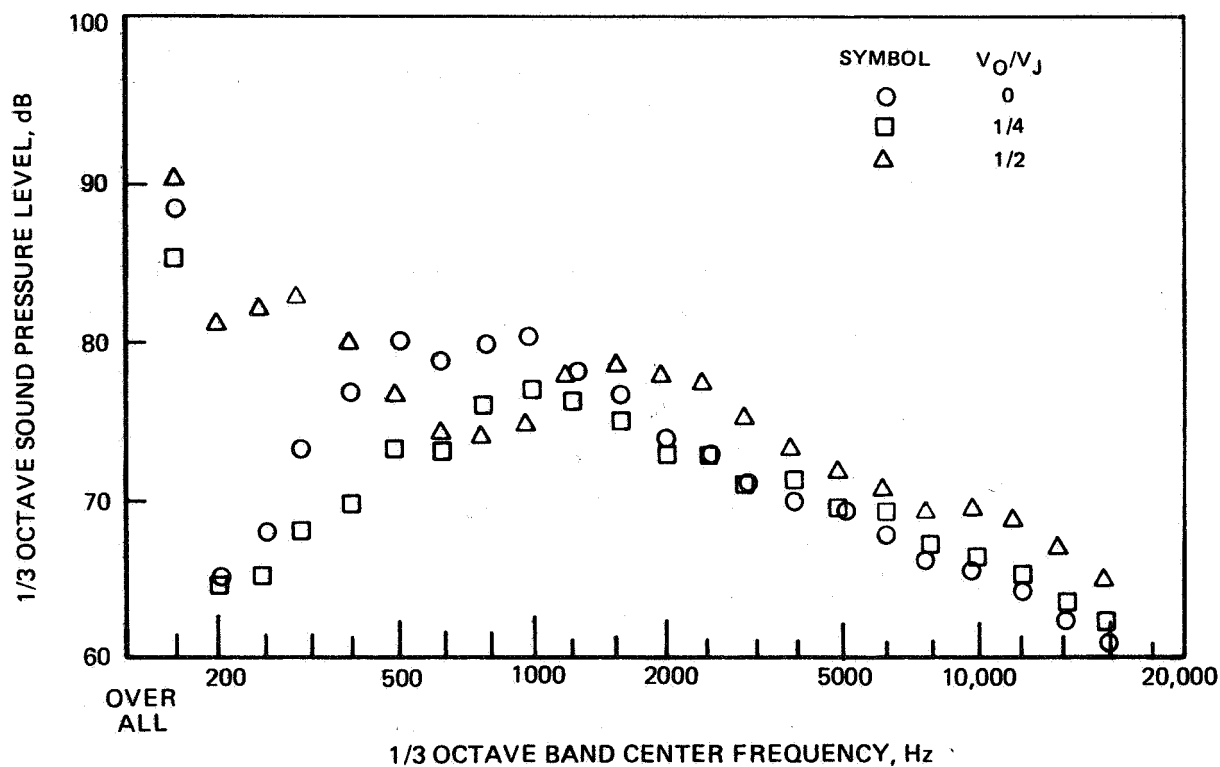
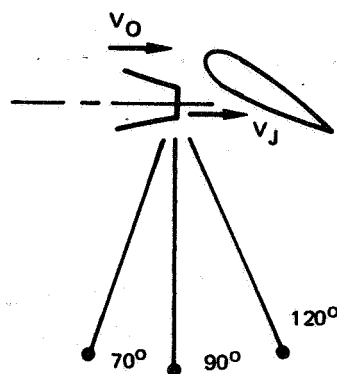


FIGURE 34— EFFECT OF FLIGHT VELOCITY RATIO ON FAR-FIELD SOUND PRESSURE LEVELS FOR 30° DEFLECTION UNDER-THE-WING EXTERNALLY BLOWN FLAP AND 125 M/SEC EXHAUST VELOCITY. (a) 70° MICROPHONE POSITION

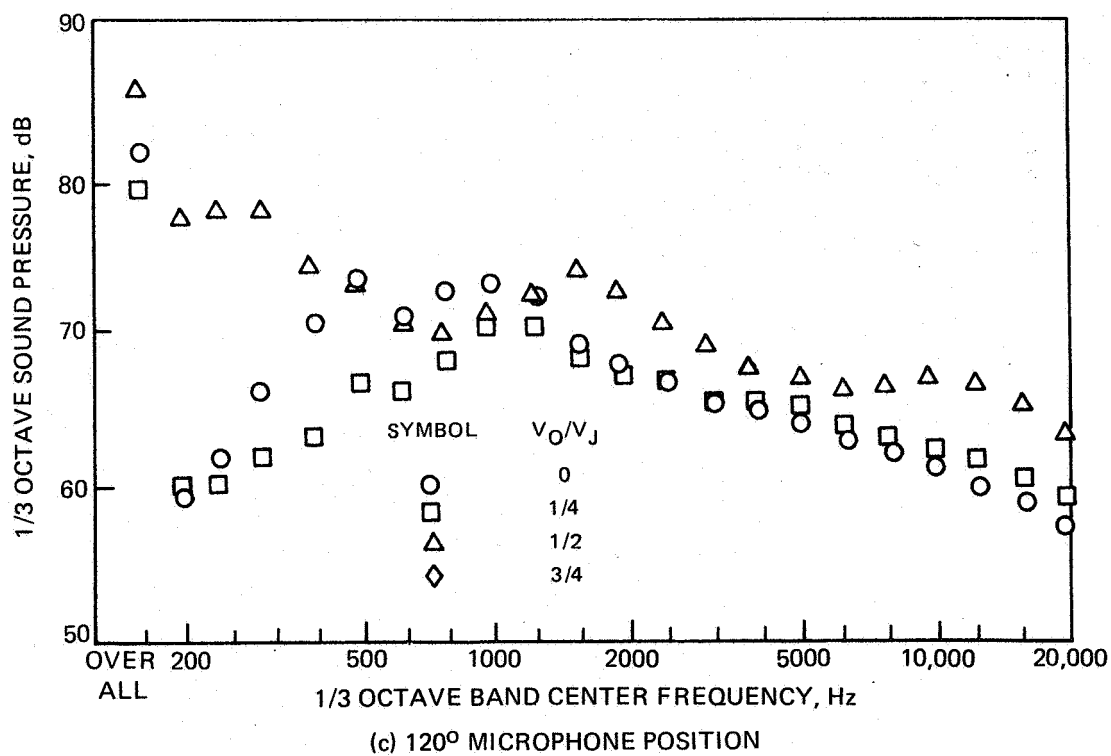
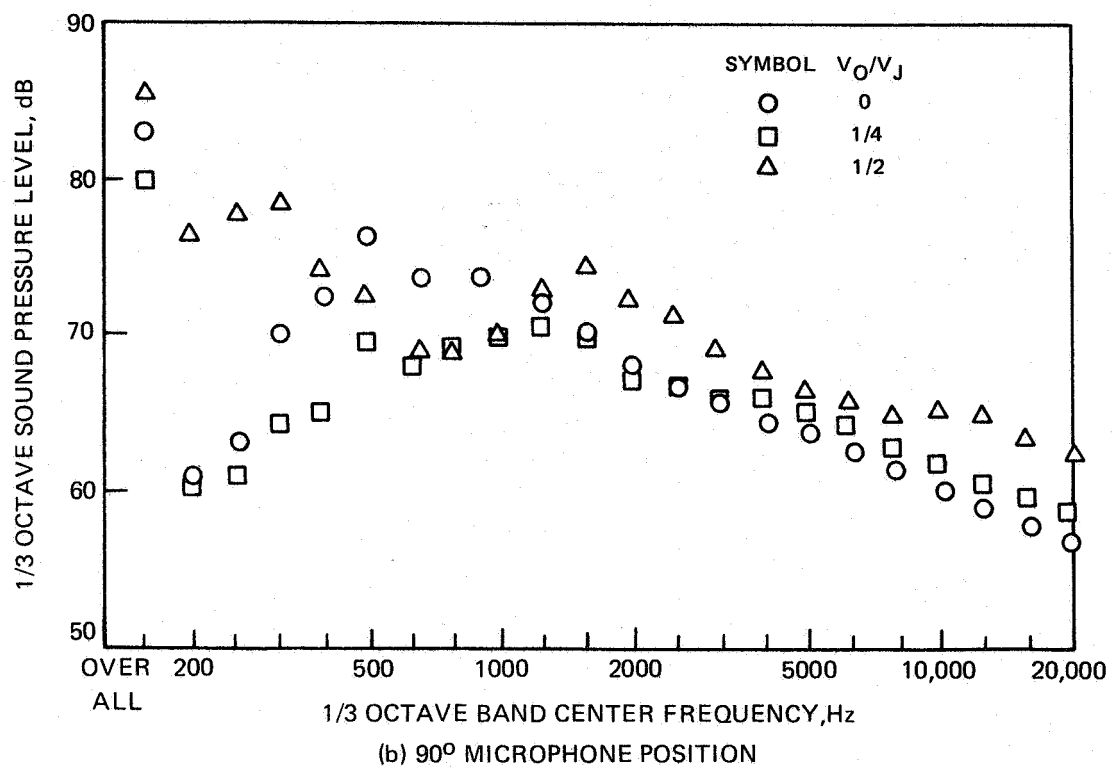


FIGURE 34— CONCLUDED.

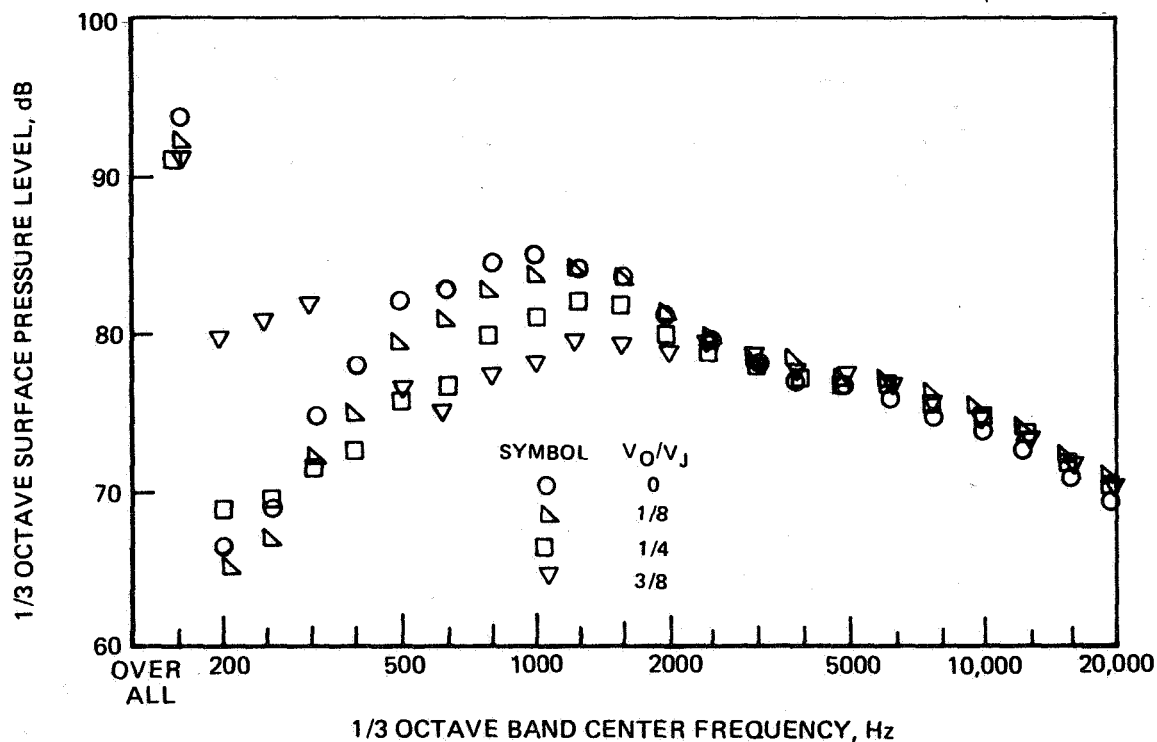
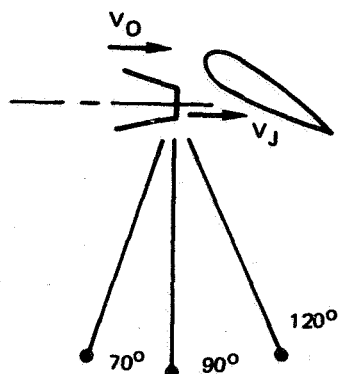


FIGURE 35—EFFECT OF FLIGHT VELOCITY RATIO ON FAR-FIELD SOUND PRESSURE LEVELS FOR 30° DEFLECTION UNDER-THE-WING EXTERNALLY BLOWN FLAP AND 160 M/SEC EXHAUST VELOCITY. (a) 70° MICROPHONE POSITION

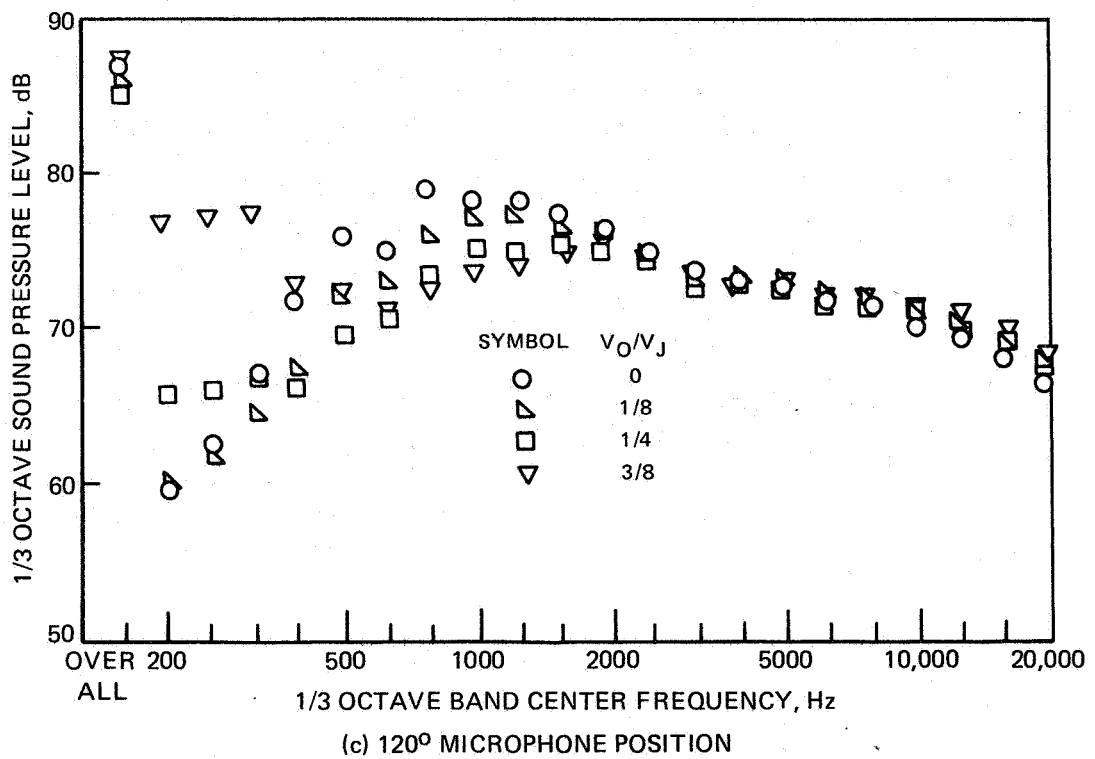
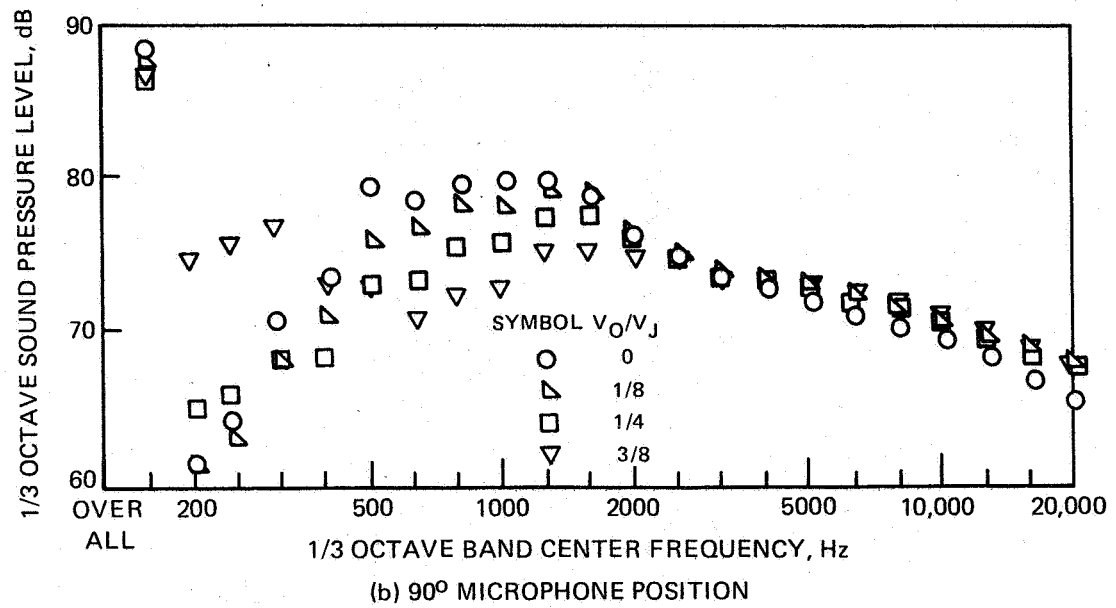


FIGURE 35— CONCLUDED.

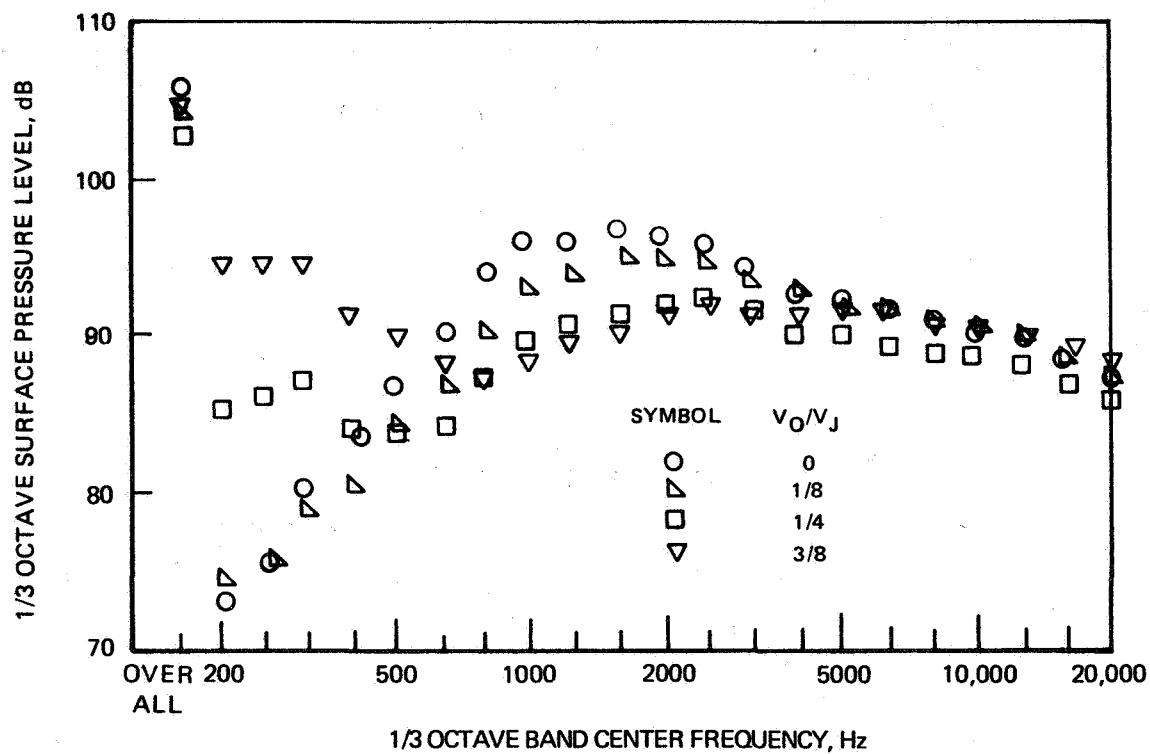
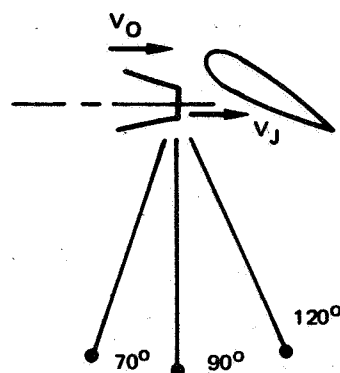


FIGURE 36— EFFECT OF FLIGHT VELOCITY RATIO ON FAR-FIELD SOUND PRESSURE LEVELS FOR 30° DEFLECTION UNDER-THE-WING EXTERNALLY BLOWN FLAP AND 250 M/SEC EXHAUST VELOCITY. (a) 70° MICROPHONE POSITION

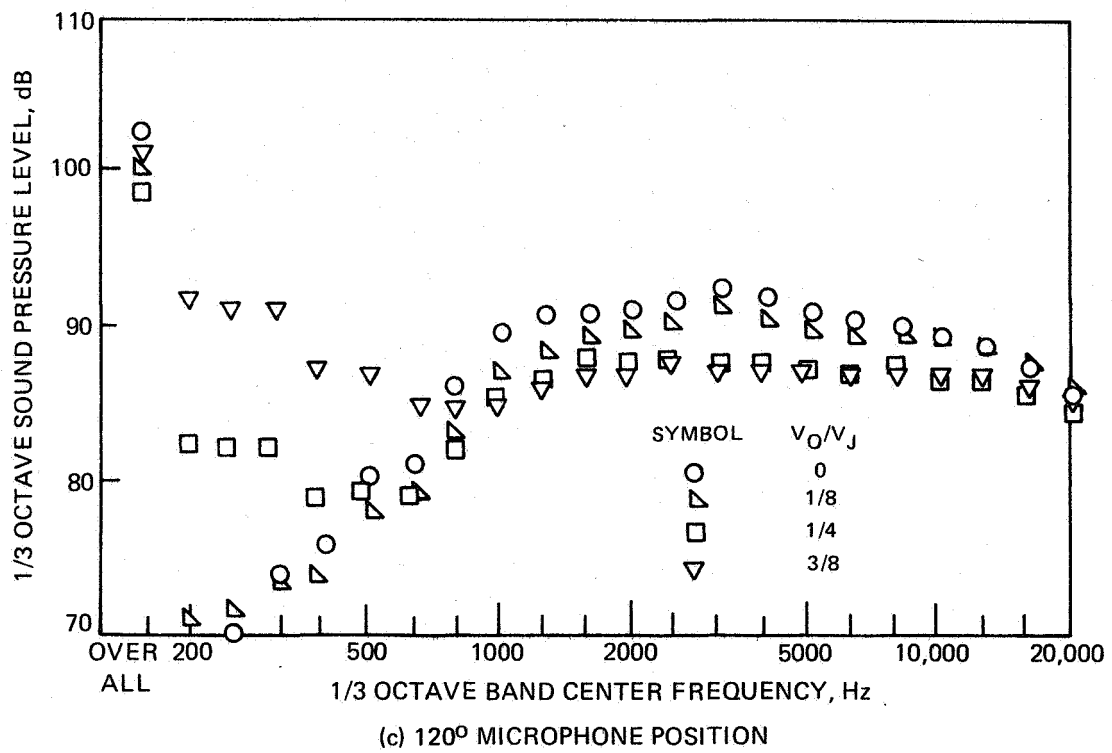
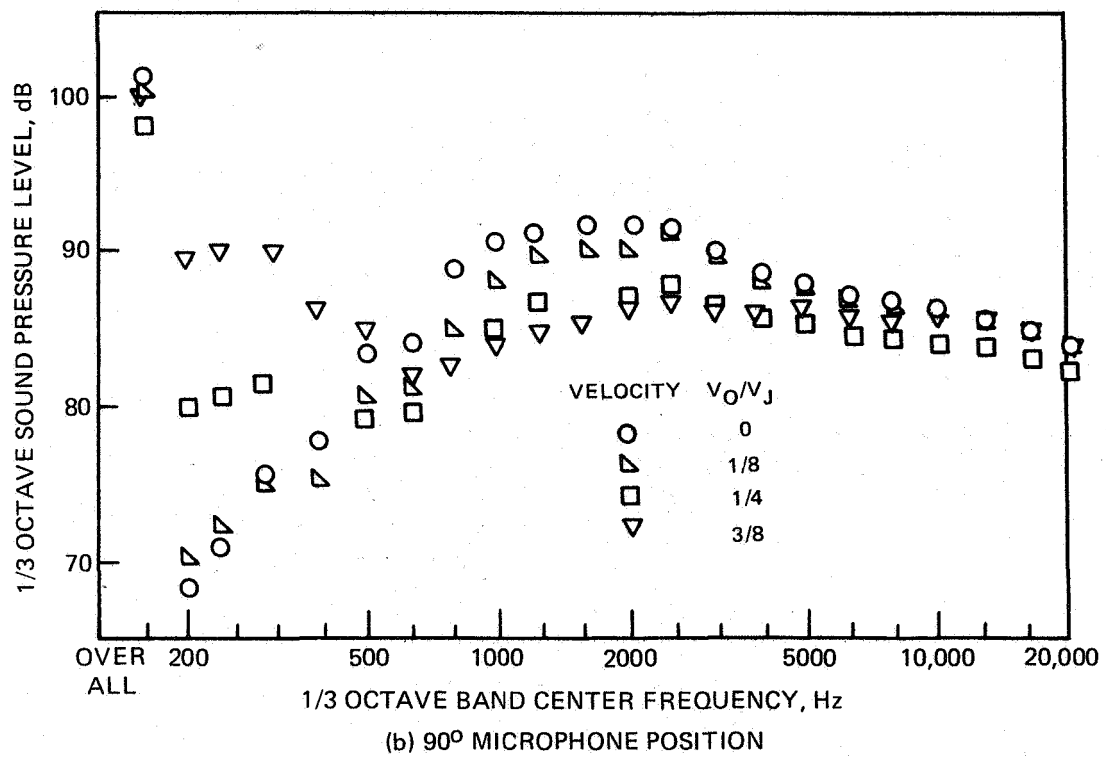
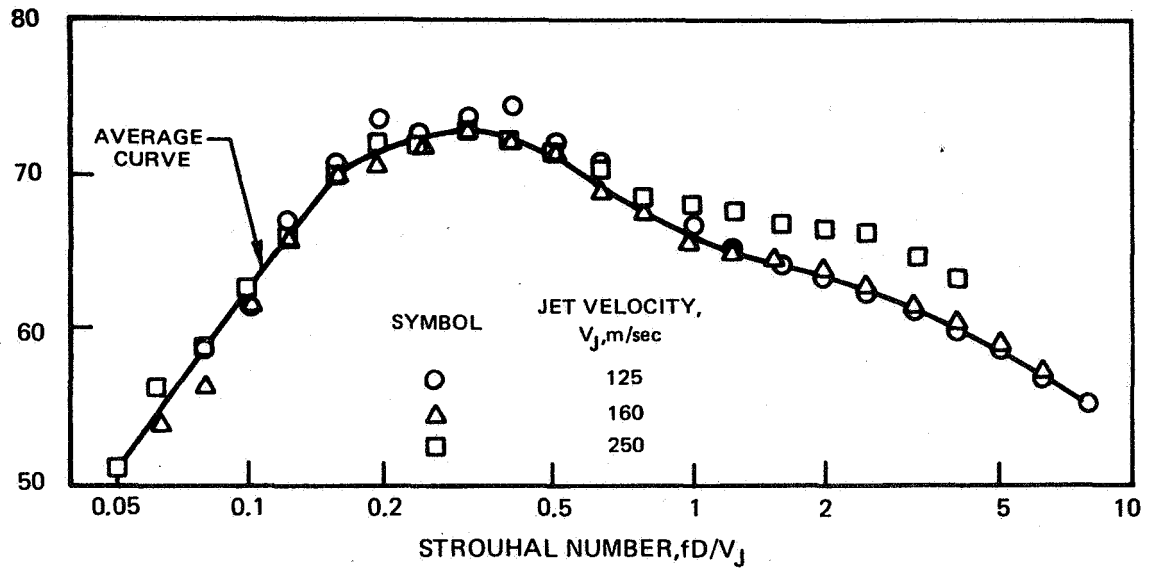
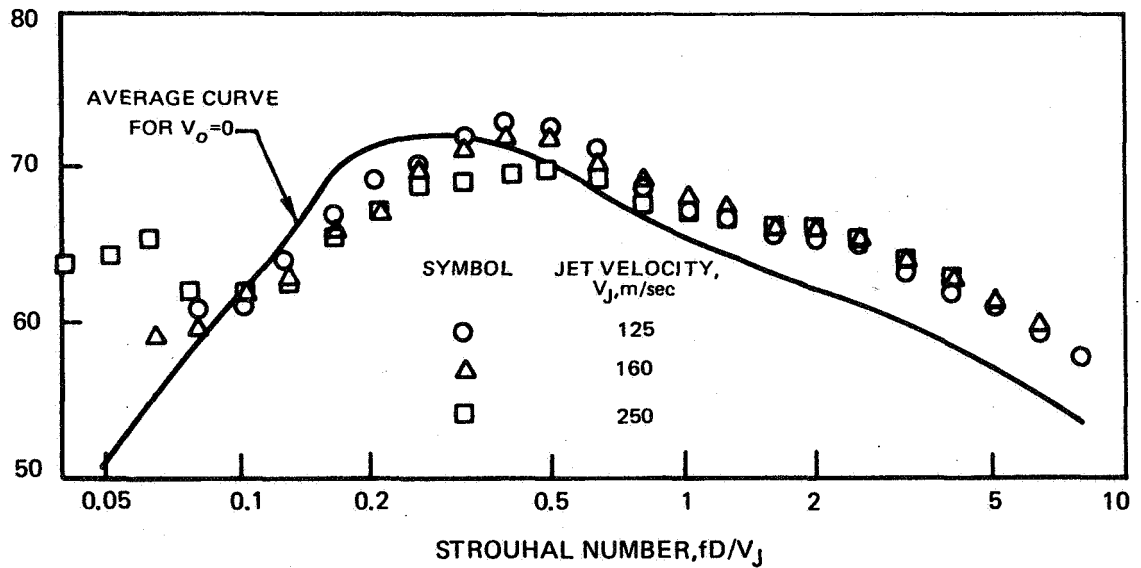


FIGURE 36— CONCLUDED.

1/3 OCTAVE SOUND PRESSURE LEVEL, ADJUSTED TO 100 m/sec JET VELOCITY AND
CORRECTED FOR TURBULENCE LEVEL SQUARED, SPL-50 LOG(V_J/100)-20 LOG
(1-V₀/V_J), dB



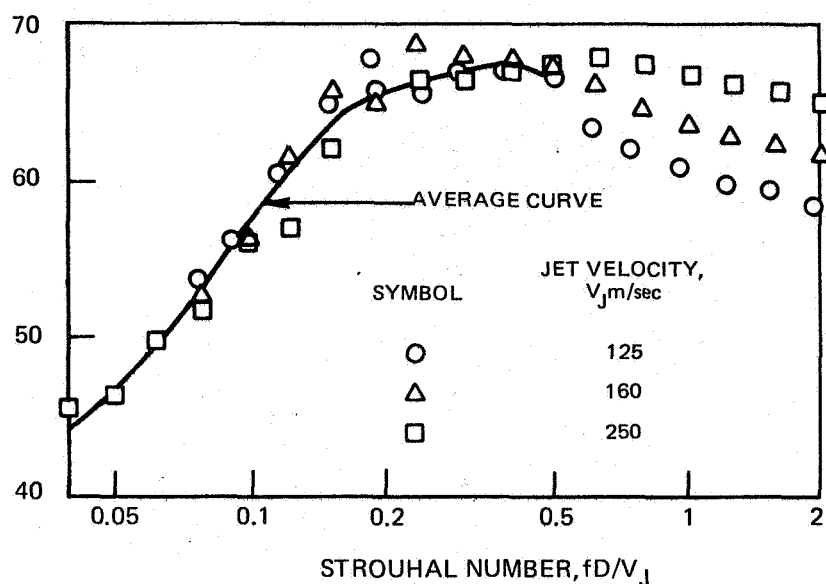
(a) ADJUSTED FOR JET VELOCITY AT ZERO TUNNEL VELOCITY



(b) ADJUSTED FOR JET VELOCITY AND TURBULENCE LEVEL AT VELOCITY RATIO $V_0/V_J = 1/4$

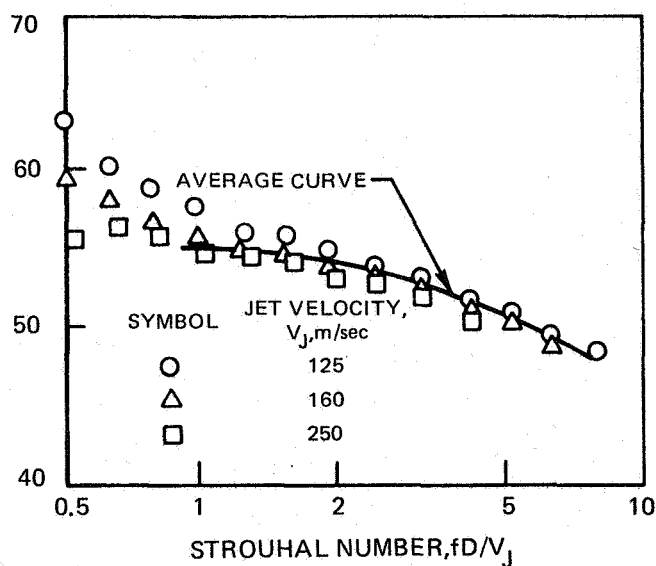
FIGURE 37—EFFECT OF FLIGHT VELOCITY RATIO AND JET EXHAUST VELOCITY ON FAR-FIELD ACOUSTIC SPECTRA FOR 30° DEFLECTION UNDER-THE-WING CONFIGURATION IN DIRECTION 70° FROM NOZZLE INLET

1/3 OCTAVE SOUND PRESSURE LEVEL,
ADJUSTED TO 100 m/sec JET VELOCITY
FOR LIFT DIPOLE NOISE, SPL-60 LOG
($V_j/100$), dB



(a) ADJUSTED FOR JET VELOCITY AT LOW STROUHAL NUMBERS
AND ZERO TUNNEL VELOCITY

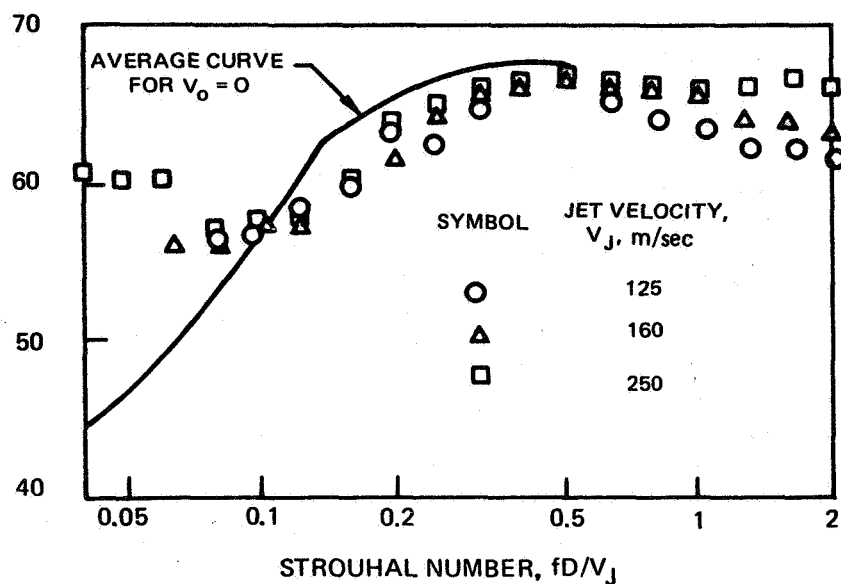
1/3 OCTAVE SOUND PRESSURE LEVEL,
ADJUSTED TO 100 m/sec JET VELOCITY
FOR QUADRUPOLE NOISE, SPL-90 LOG
($V_j/100$), dB



(b) ADJUSTED FOR JET VELOCITY AT HIGH STROUHAL
NUMBERS AND ZERO TUNNEL VELOCITY

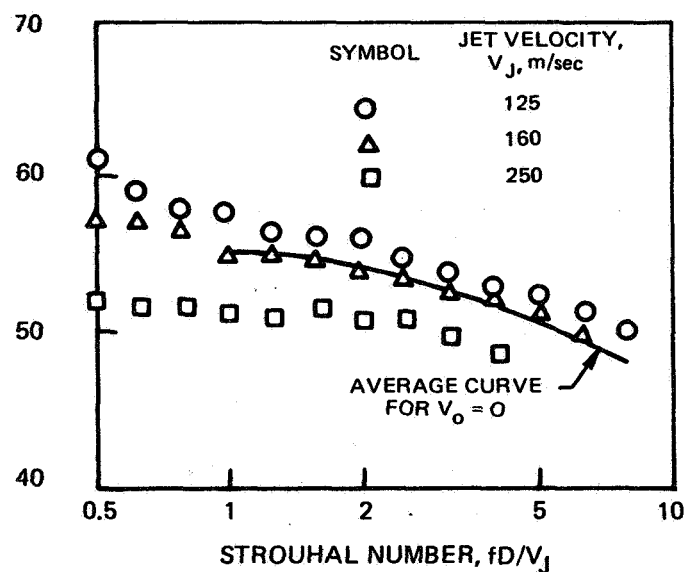
**FIGURE 38—EFFECT OF FLIGHT VELOCITY RATIO AND JET EXHAUST VELOCITY
ON FAR-FIELD ACOUSTIC SPECTRA FOR 30° DEFLECTION UNDER—
THE-WING CONFIGURATION IN DIRECTION 120° FROM NOZZLE INLET**

VELOCITY-ADJUSTED 1/3 OCTAVE SOUND
PRESSURE LEVEL, CORRECTED FOR
TURBULENCE LEVEL, SQUARED, SPL-60
 $\text{LOG}(V_j/100) - 20 \text{ LOG}(1 - V_o/V_j), \text{dB}$



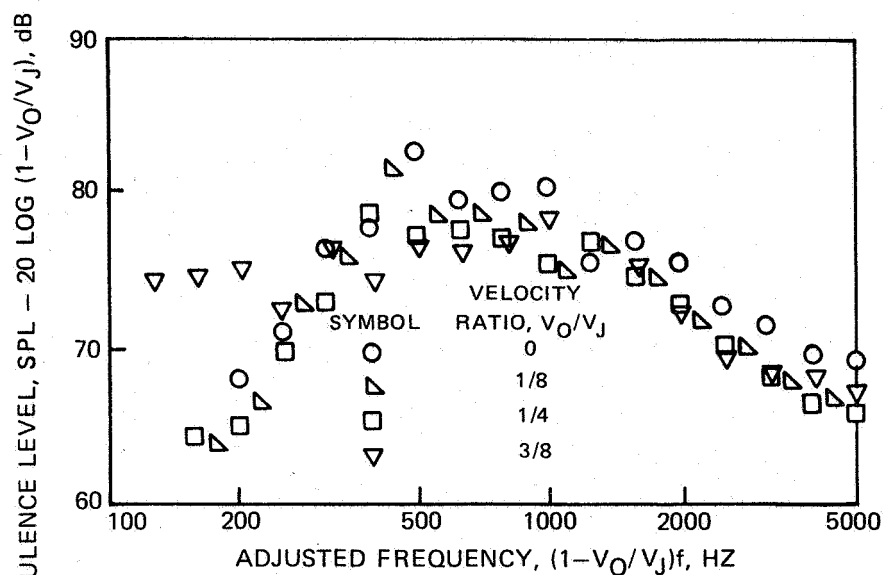
(c) ADJUSTED FOR JET VELOCITY AND TURBULENCE LEVEL
AT LOW STROUHAL NUMBERS AND VELOCITY RATIO
 $V_o/V_j = 1/4$

VELOCITY-ADJUSTED 1/3 OCTAVE SOUND
PRESSURE LEVEL, UNCORRECTED FOR
TURBULENCE LEVEL, SPL-90 $\text{LOG}(V_j/100), \text{dB}$

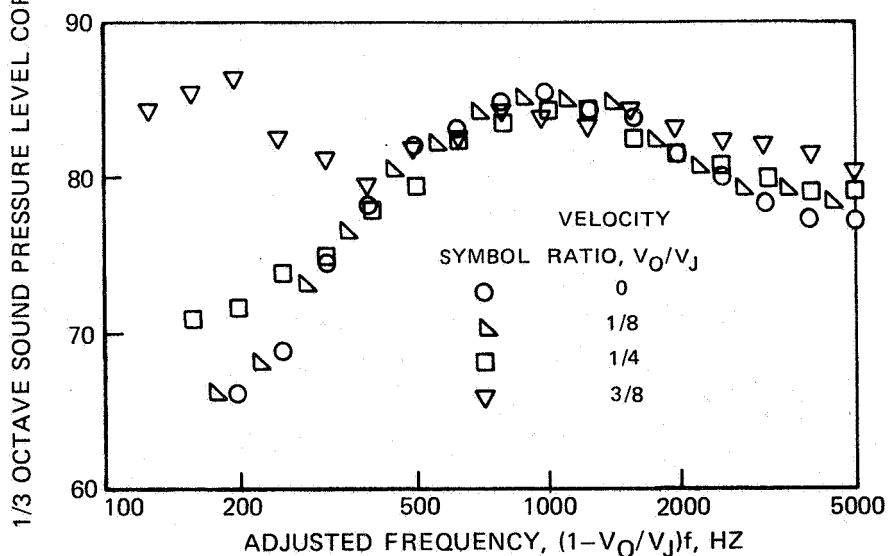


(d) ADJUSTED FOR JET VELOCITY ONLY, AT HIGH STROUHAL
NUMBERS AND VELOCITY RATIO $V_o/V_j = 1/4$

FIGURE 38- CONCLUDED.



(a) 90° DEFLECTION UNDER-THE-WING CONFIGURATION, 90° FROM NOZZLE INLET



(b) 30° DEFLECTION UNDER-THE-WING CONFIGURATION, 70° FROM NOZZLE INLET

FIGURE 39 — USE OF ADJUSTED FREQUENCY FOR CORRELATING THE EFFECT OF FLIGHT VELOCITY RATIO ON FAR-FIELD ACOUSTIC SPECTRA AT 160 M/SEC EXHAUST JET VELOCITY

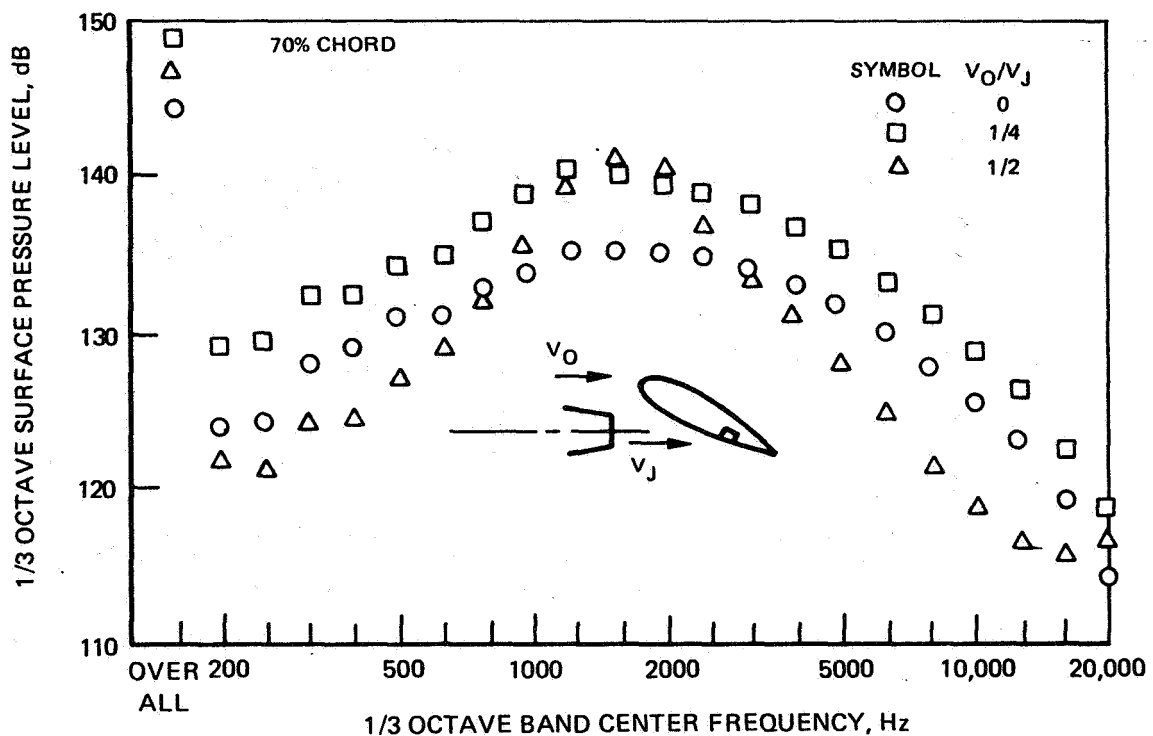
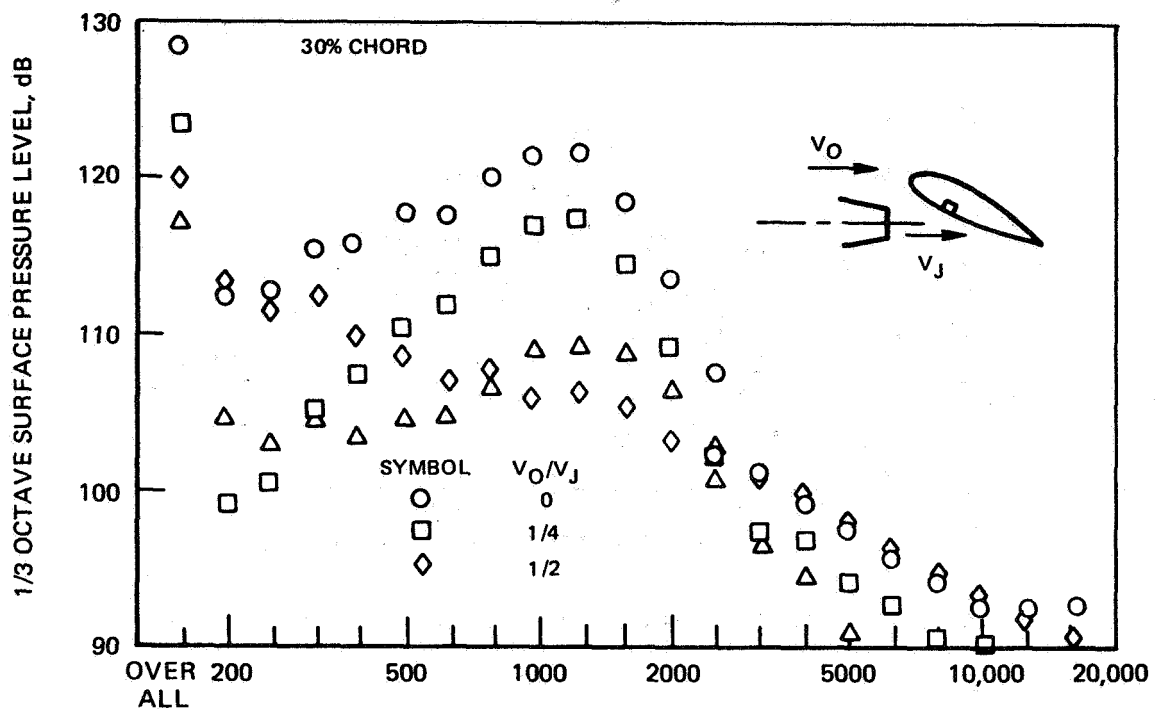


FIGURE 40—EFFECT OF FLIGHT VELOCITY RATIO ON SURFACE PRESSURE SPECTRA FOR 30° DEFLECTION UNDER-THE-WING EXTERNALLY BLOWN FLAP.
(a) 125 M/SEC EXHAUST VELOCITY

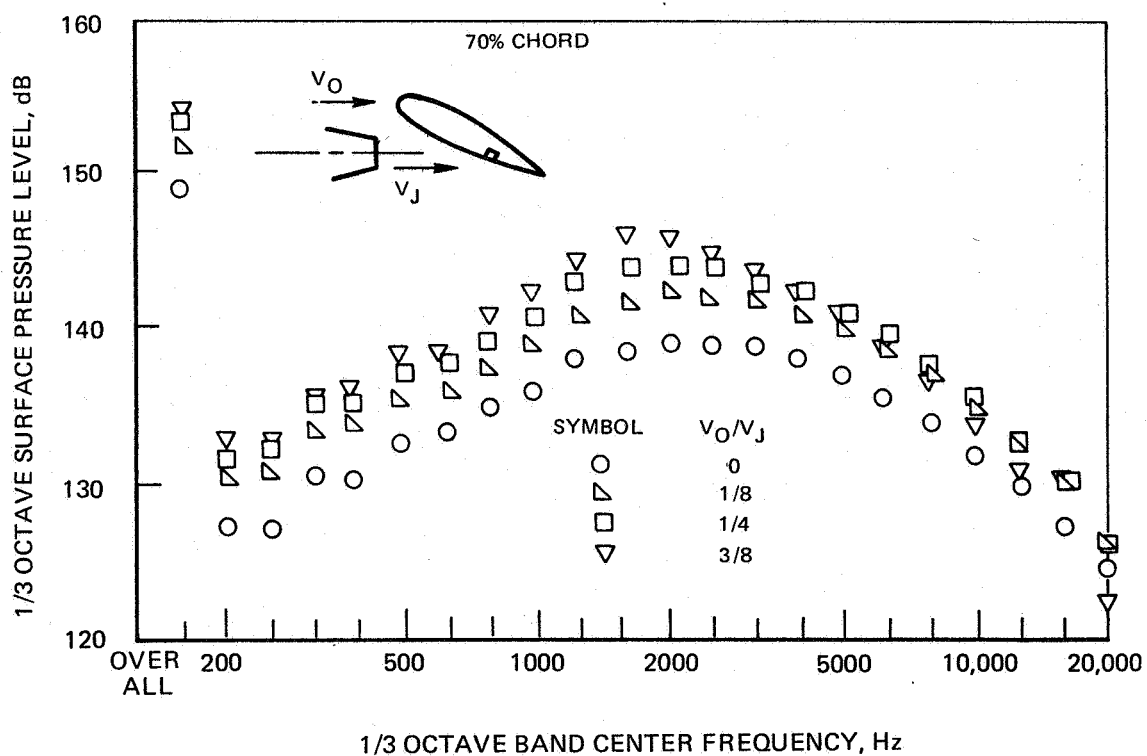
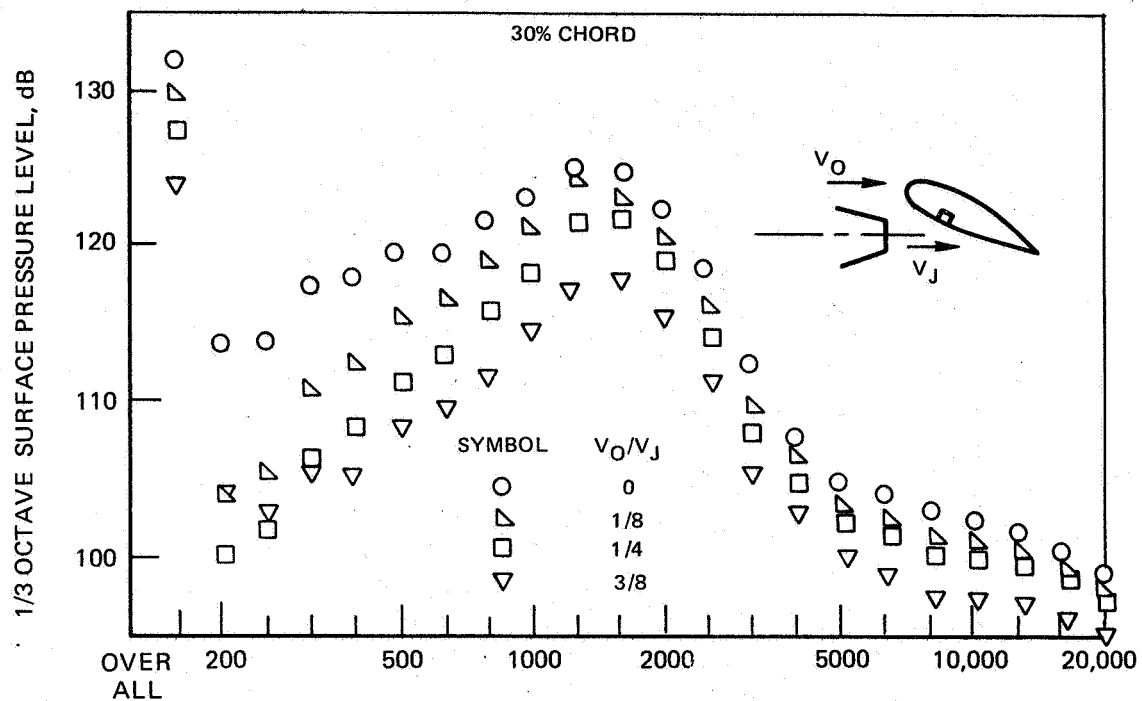


FIGURE 40- CONTINUED. (b) 160 M/SEC EXHAUST VELOCITY

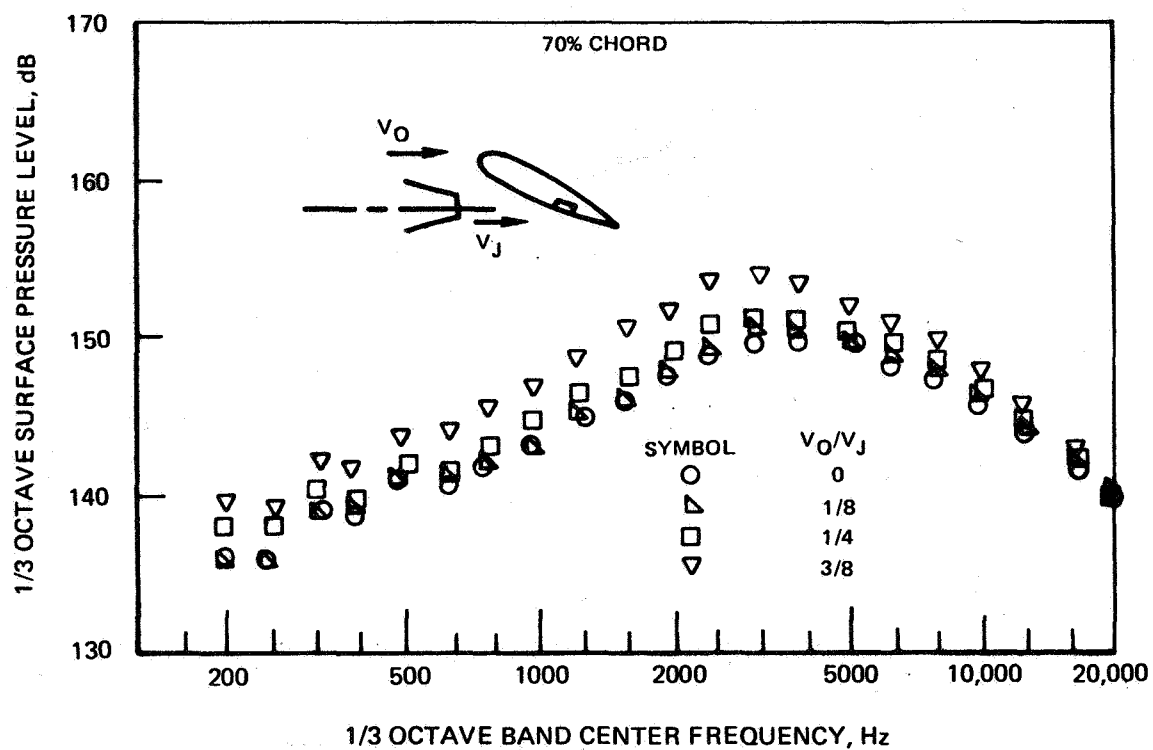
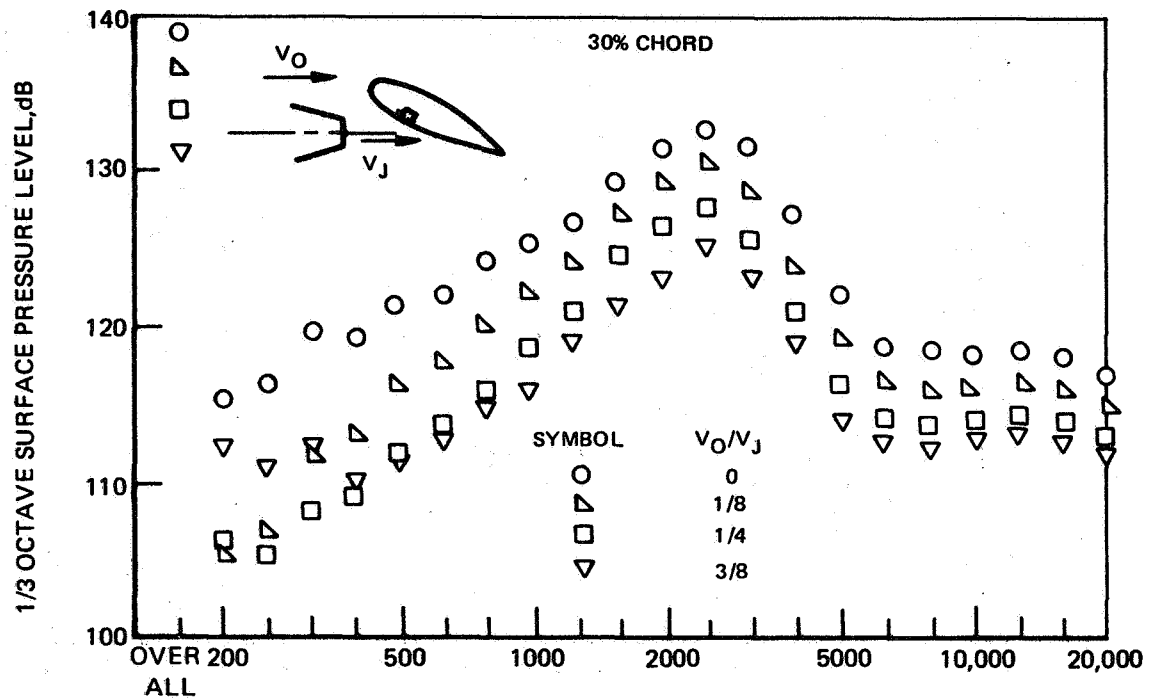
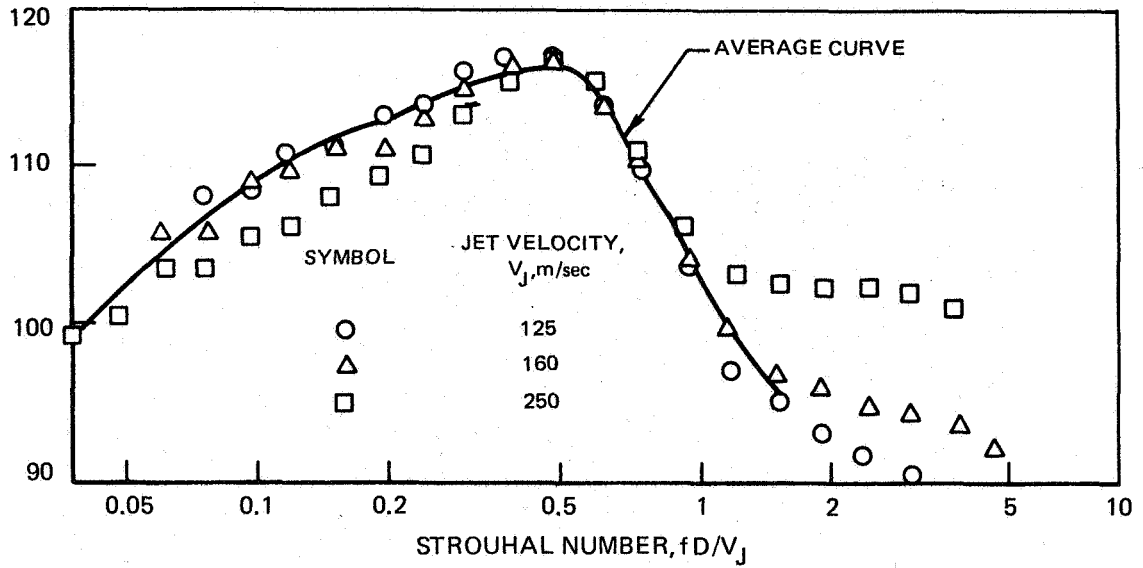
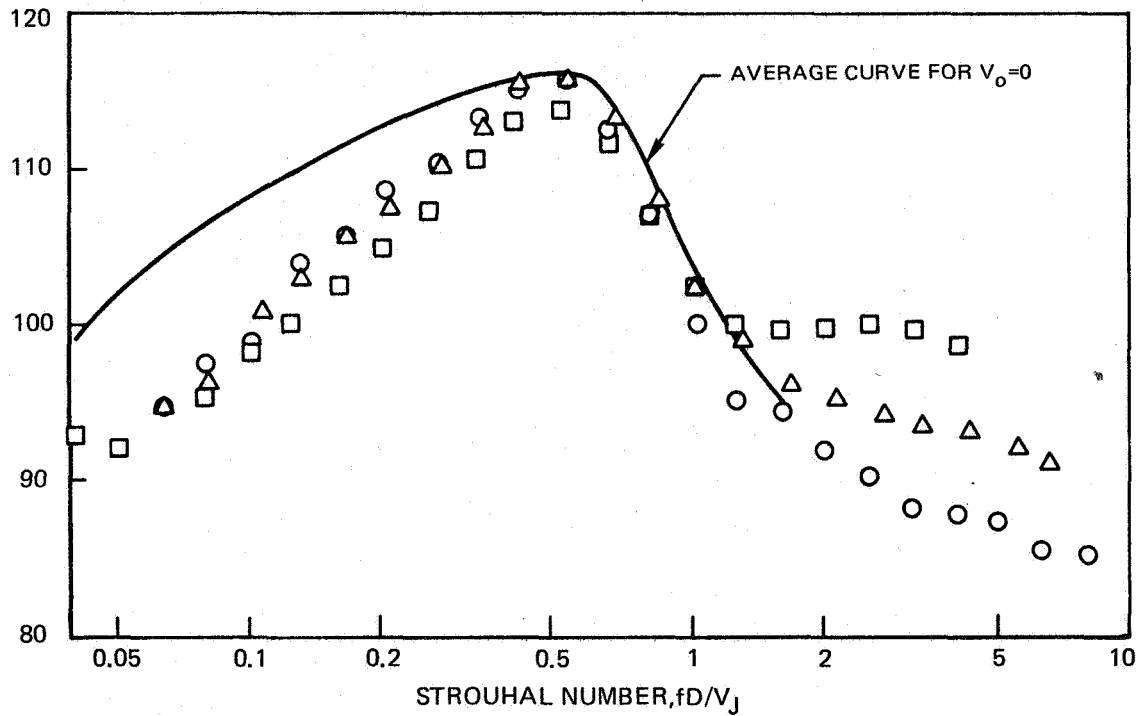


FIGURE 40— CONCLUDED. (c) 250 M/SEC EXHAUST VELOCITY

1/3 OCTAVE SURFACE PRESSURE LEVEL ADJUSTED TO 100 m/sec JET VELOCITY AND CORRECTED
FOR TURBULENCE LEVEL SQUARED, SPL-40 LOG(V_J/100)-20 LOG(1-V₀/V_J), dB



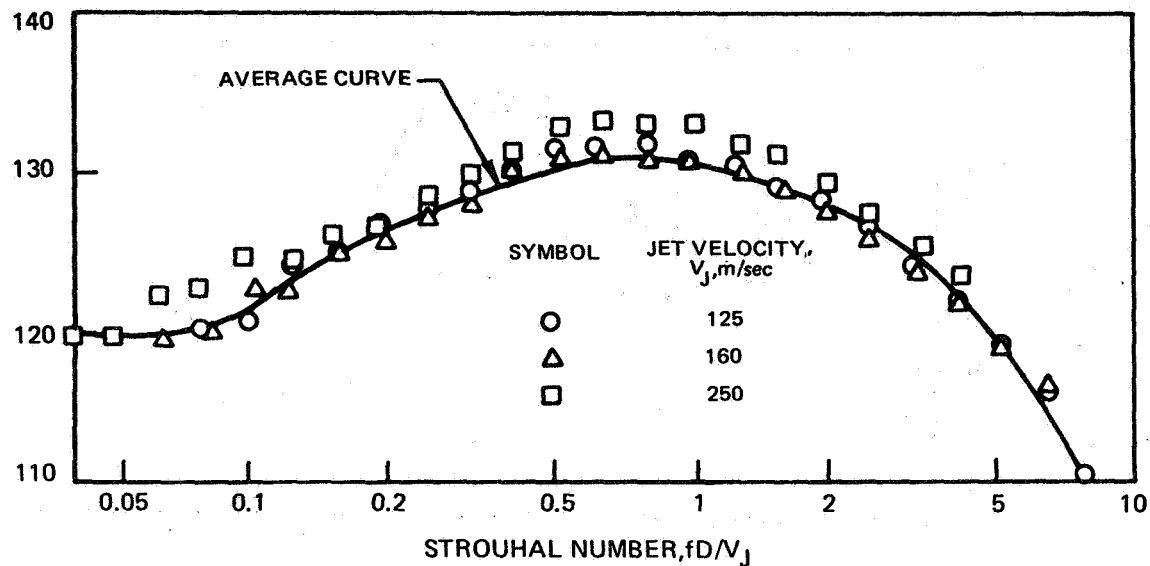
(a) ADJUSTED FOR JET VELOCITY AT ZERO TUNNEL VELOCITY



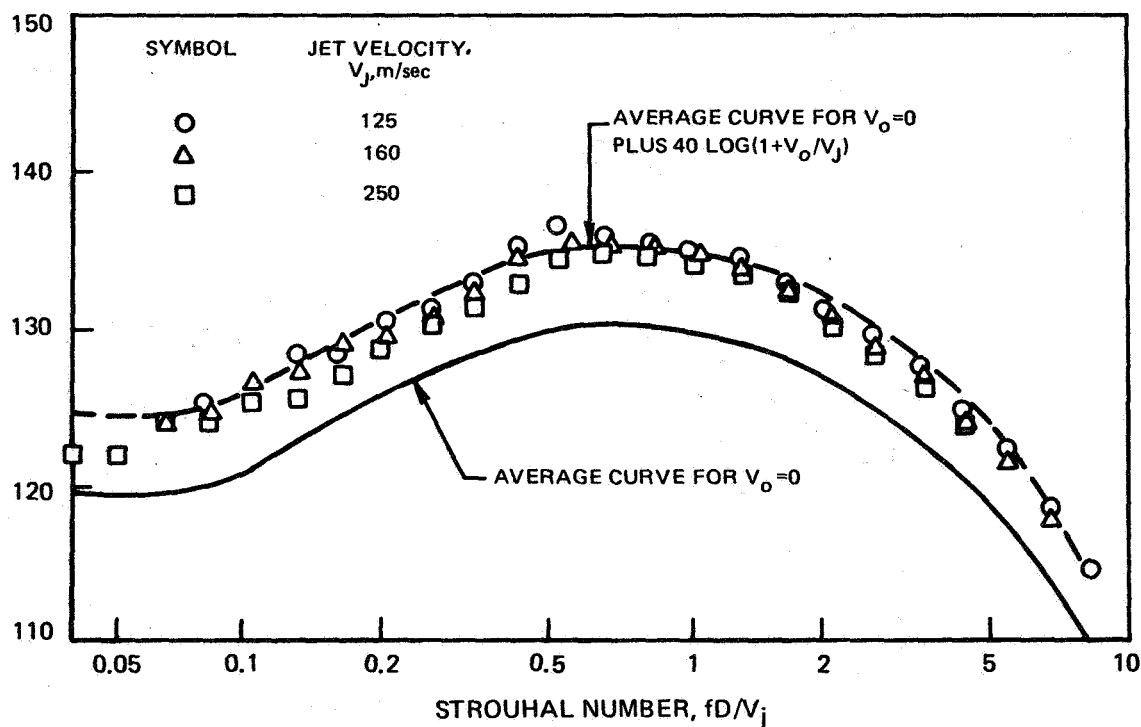
(b) ADJUSTED FOR JET VELOCITY AND TURBULENCE LEVEL AT VELOCITY RATIO $V_0/V_J = 1/4$

FIGURE 41—EFFECT OF FLIGHT VELOCITY RATIO AND JET EXHAUST VELOCITY ON SURFACE PRESSURE SPECTRA AT 30% CHORD FOR 30° DEFLECTION UNDER-THE- WING CONFIGURATION

1/3 OCTAVE SURFACE PRESSURE LEVEL ADJUSTED TO 100m/sec JET VELOCITY,
SPL-40 LOG ($V_j/100$), dB

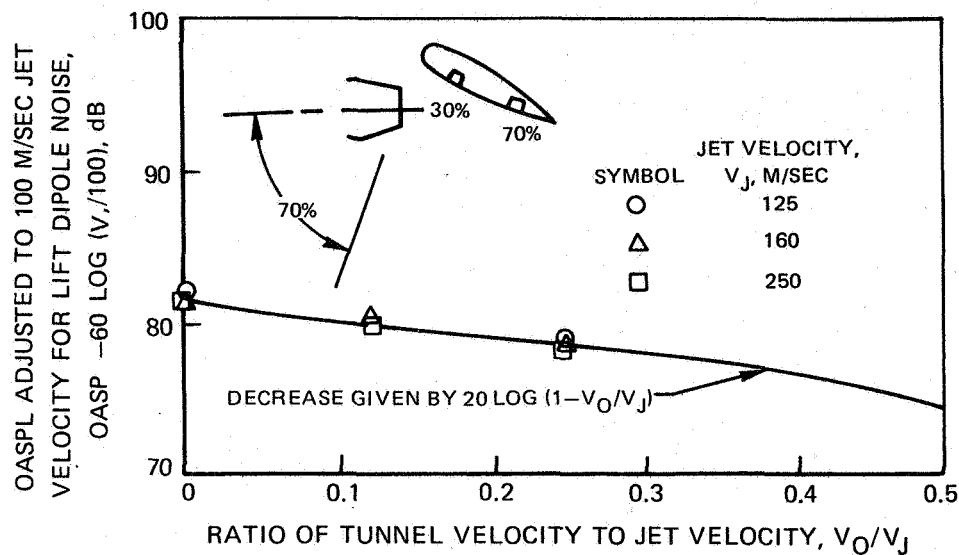


(a) ADJUSTED FOR JET VELOCITY AT ZERO TUNNEL VELOCITY

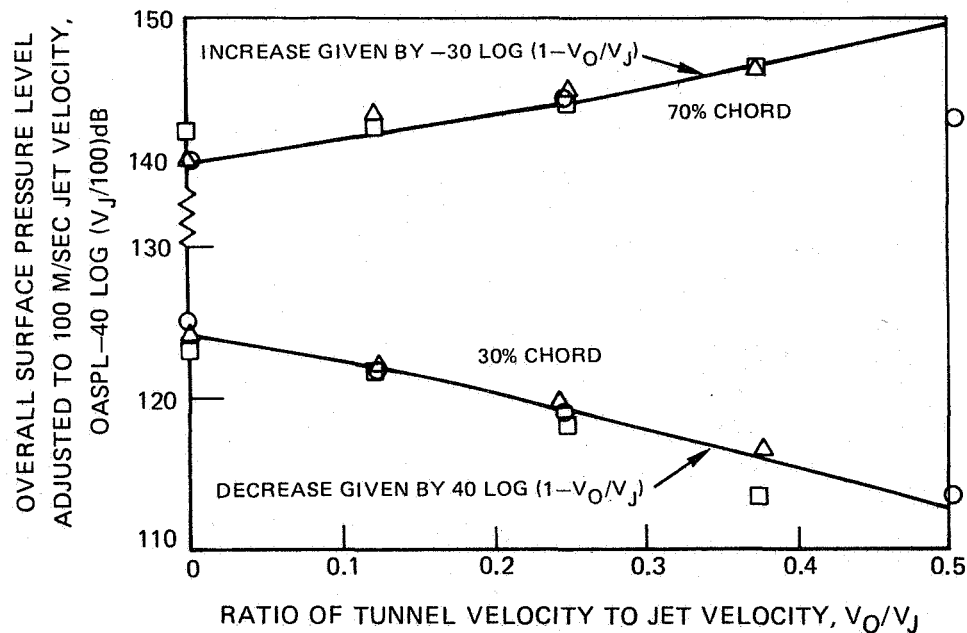


(b) ADJUSTED FOR JET VELOCITY AT VELOCITY RATIO $V_o/V_j = 1/4$

FIGURE 42—EFFECT OF FLIGHT VELOCITY RATIO AND JET EXHAUST VELOCITY ON SURFACE PRESSURE SPECTRA AT 70% CHORD FOR 30° DEFLECTION UNDER-THE-WING CONFIGURATION



(a) EFFECT OF VELOCITY RATIO ON OVERALL SOUND PRESSURE LEVEL IN DIRECTION 70° FROM NOZZLE INLET



(b) EFFECT OF VELOCITY RATIO ON OVERALL SURFACE PRESSURE LEVEL AT 30% AND 70% CHORD

FIGURE 43 — EFFECT OF FLIGHT VELOCITY ON OVERALL SOUND AND SURFACE PRESSURE LEVELS FOR 30° DEFLECTION UNDER-THE-WING CONFIGURATION

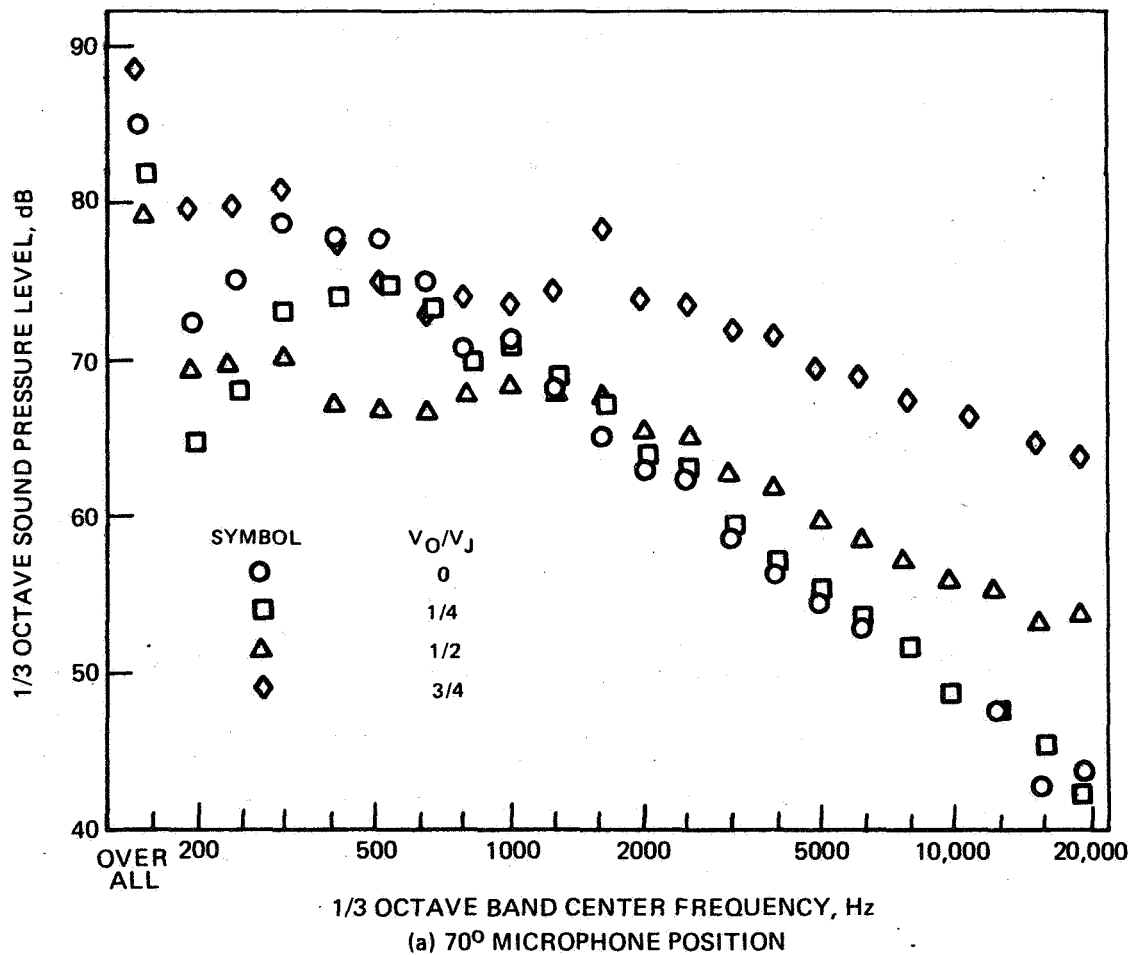
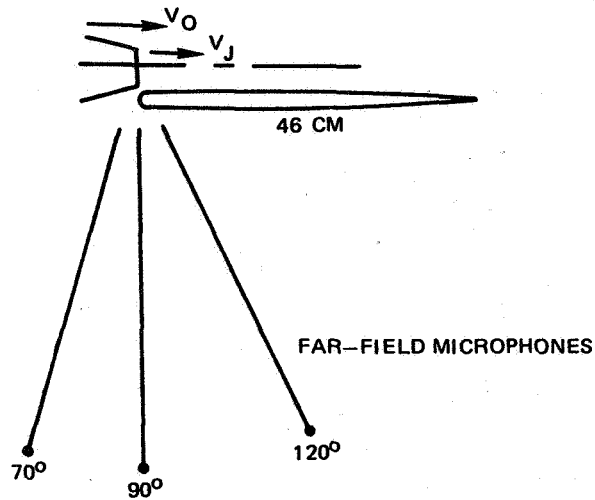


FIGURE 44 – EFFECT OF FLIGHT VELOCITY RATIO ON FAR-FIELD SOUND PRESSURE LEVELS FOR LONG-CHORD UPPER-SURFACE-BLOWING EXTERNALLY BLOWN FLAP AND 125 M/SEC EXHAUST VELOCITY

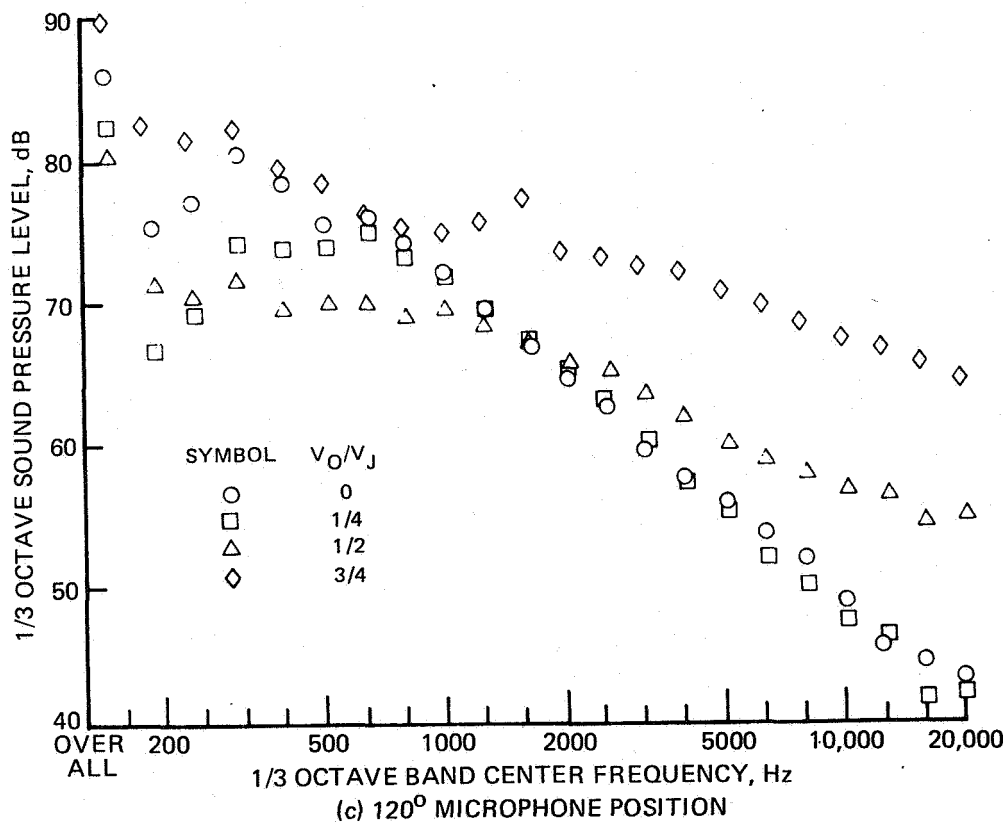
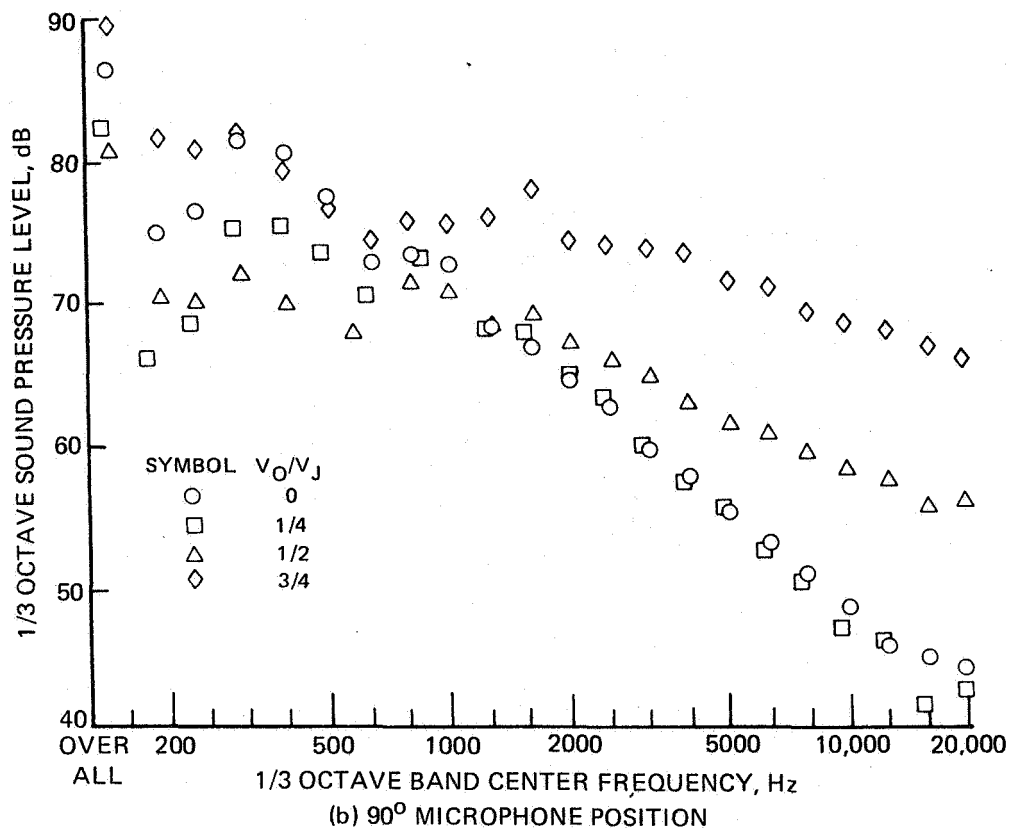


FIGURE 44— CONCLUDED.

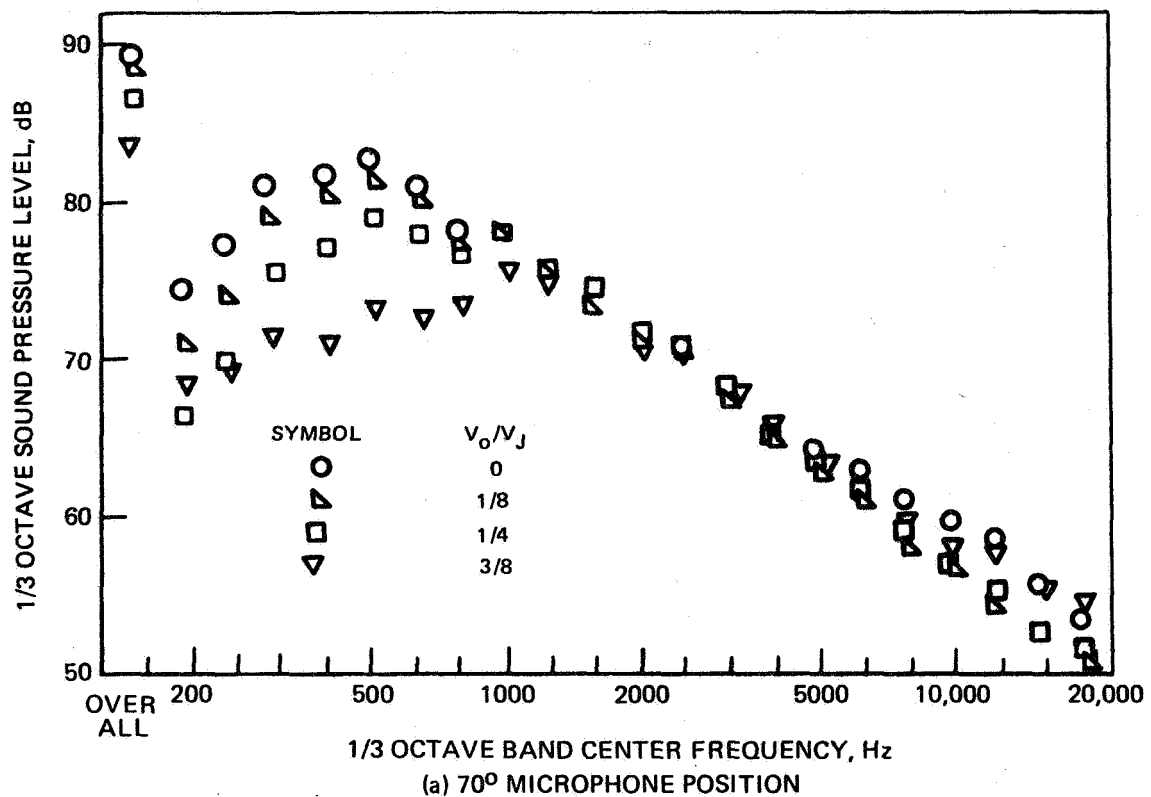
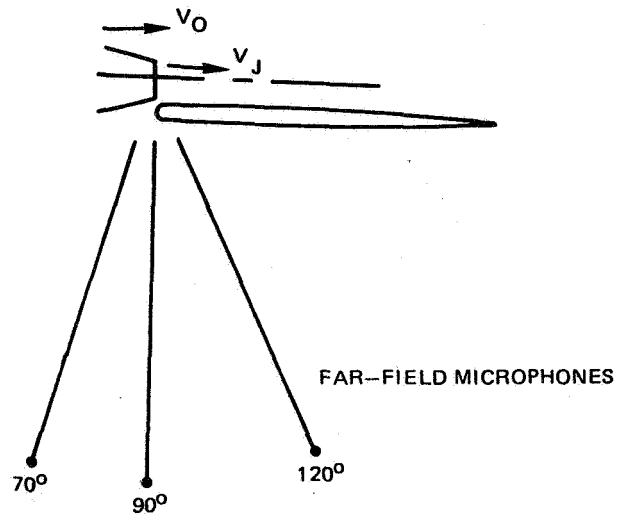


FIGURE 45 — EFFECT OF FLIGHT VELOCITY RATIO ON FAR-FIELD SOUND PRESSURE LEVELS FOR LONG-CHORD UPPER-SURFACE-BLOWING EXTERNALLY BLOWN FLAP AND 160 M/SEC EXHAUST VELOCITY

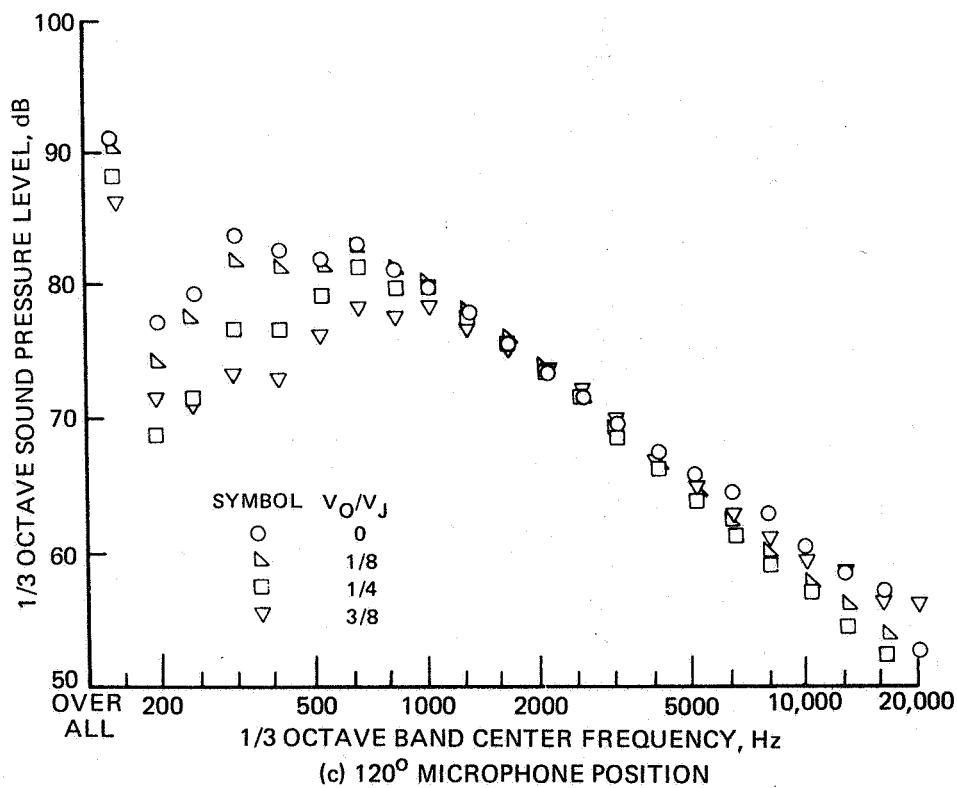
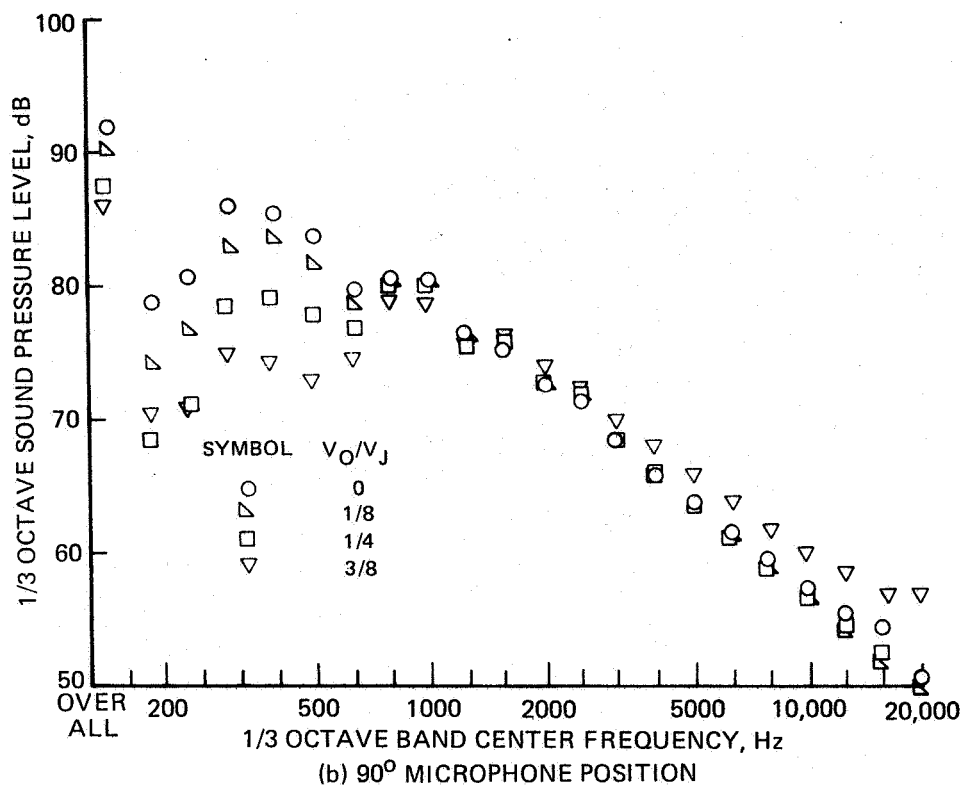


FIGURE 45— CONCLUDED.

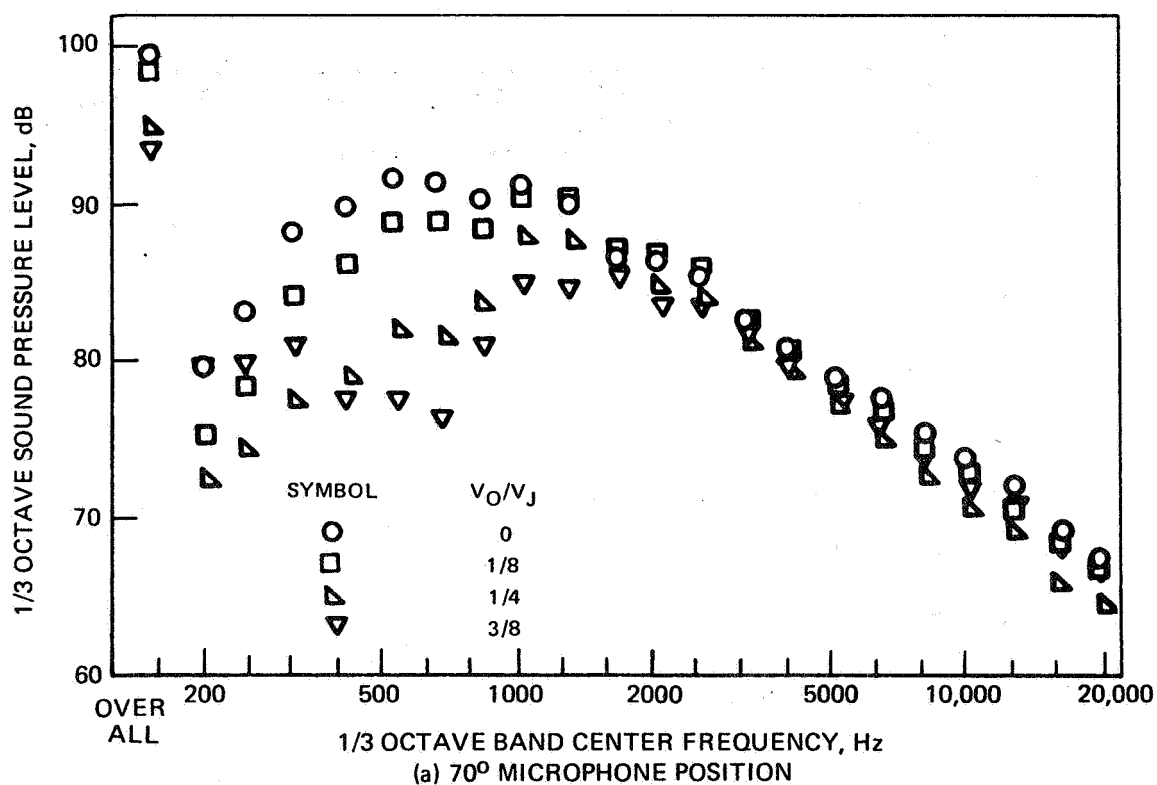
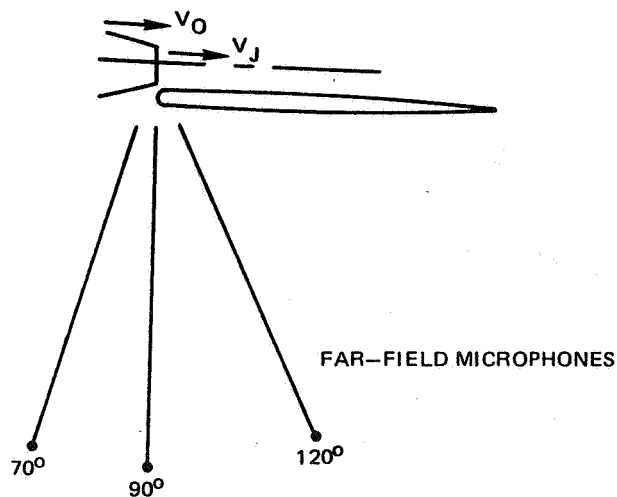


FIGURE 46 — EFFECT OF FLIGHT VELOCITY RATIO ON FAR-FIELD SOUND PRESSURE LEVELS FOR LONG-CHORD UPPER-SURFACE-BLOWING EXTERNALLY BLOWN FLAP AND 250 M/SEC EXHAUST VELOCITY

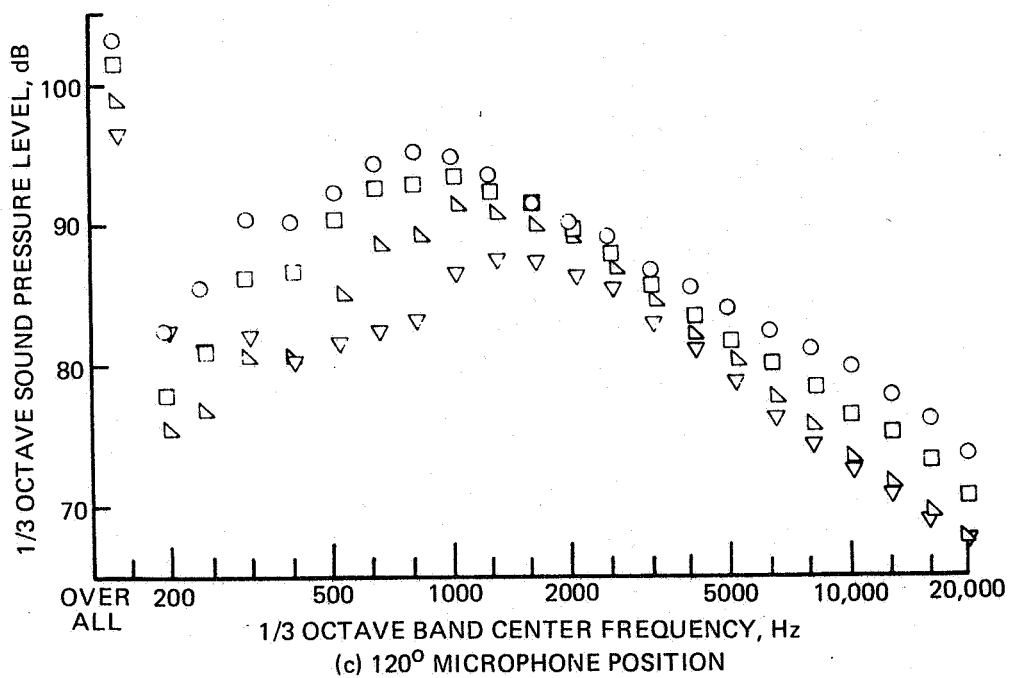
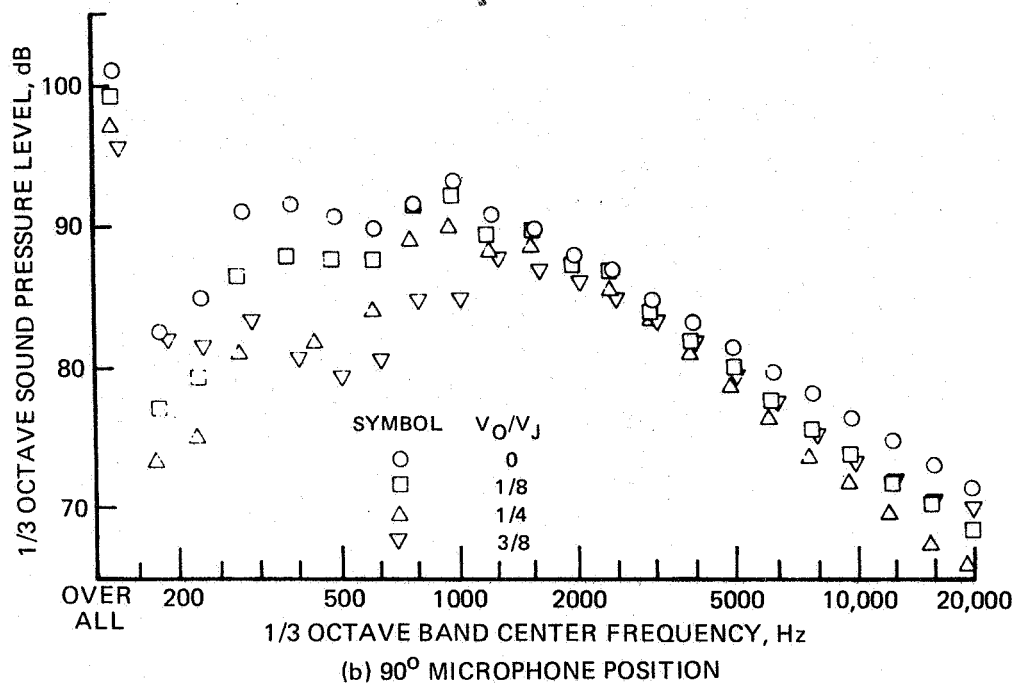


FIGURE 46— CONCLUDED.

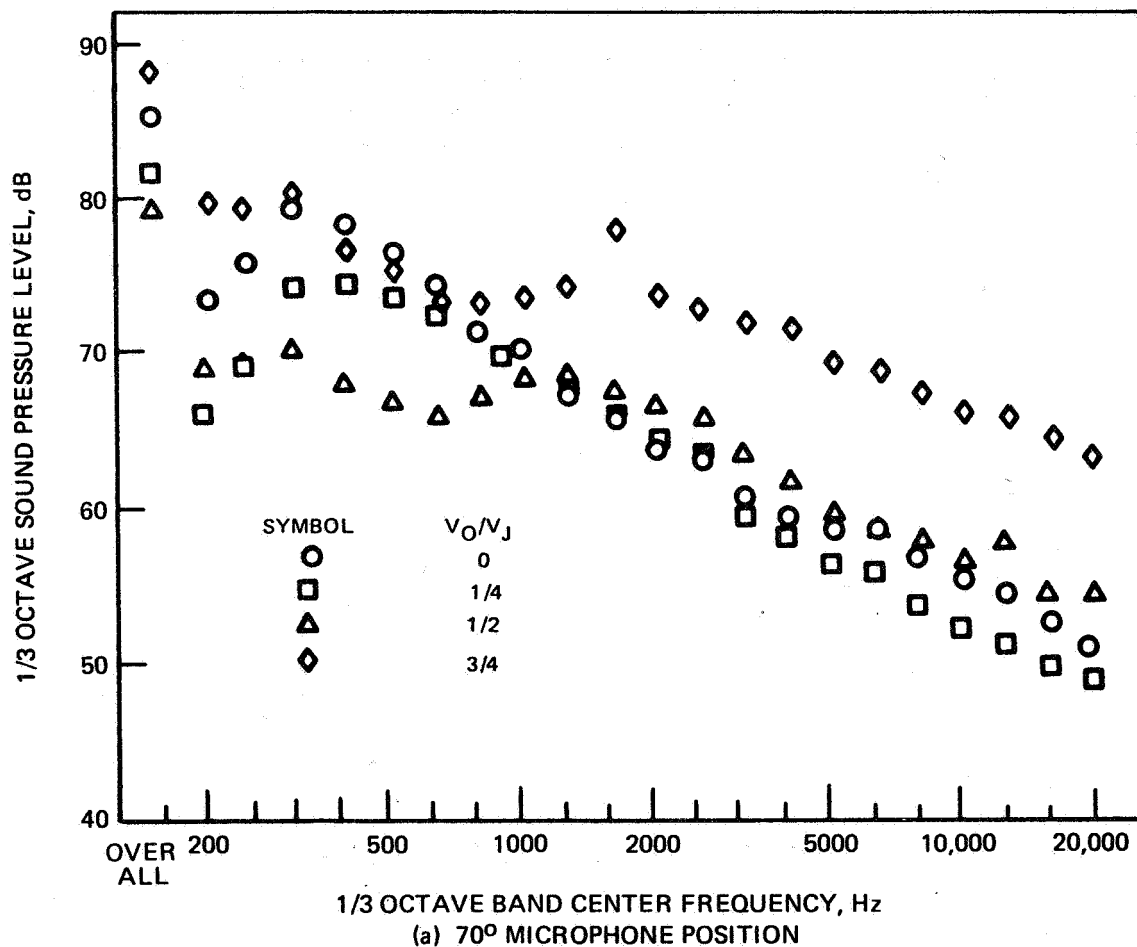
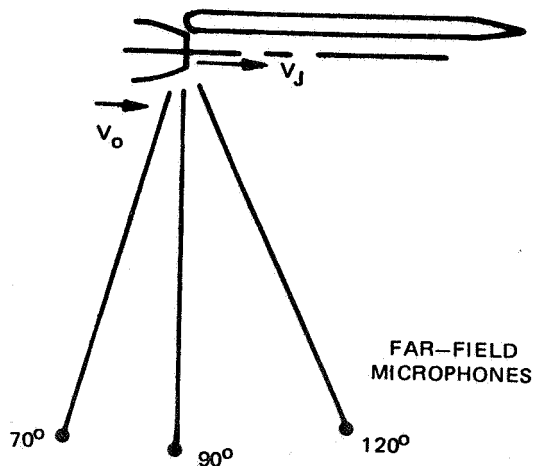


FIGURE 47 —EFFECT OF FLIGHT VELOCITY RATIO ON FAR-FIELD SOUND PRESSURE LEVELS FOR LONG-CHORD UNDER-THE-WING EXTERNALLY BLOWN FLAP AND 125 M/SEC EXHAUST VELOCITY

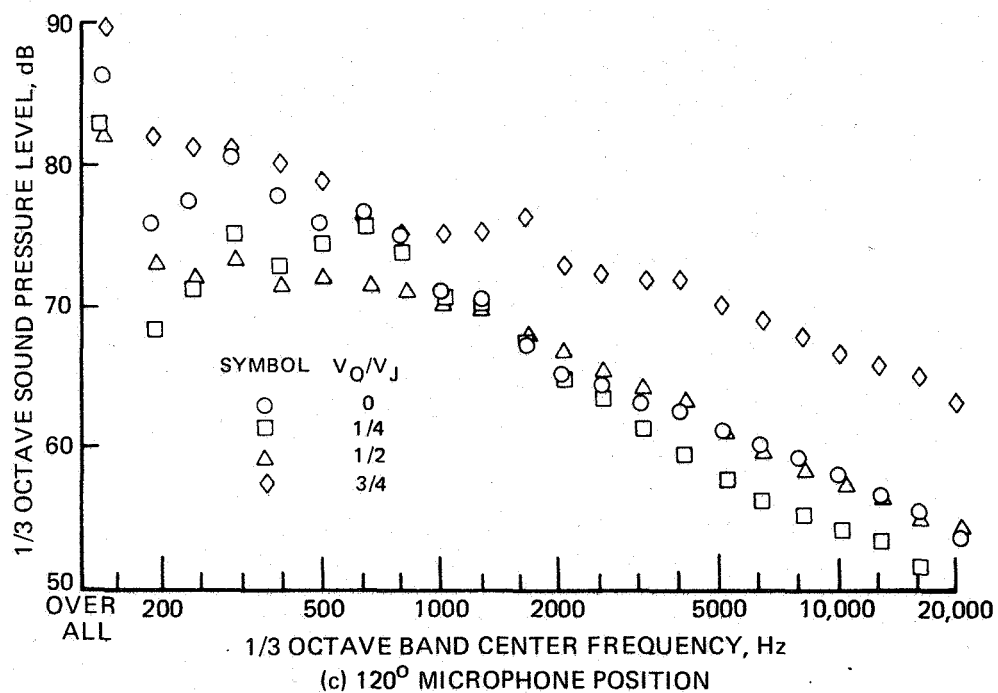
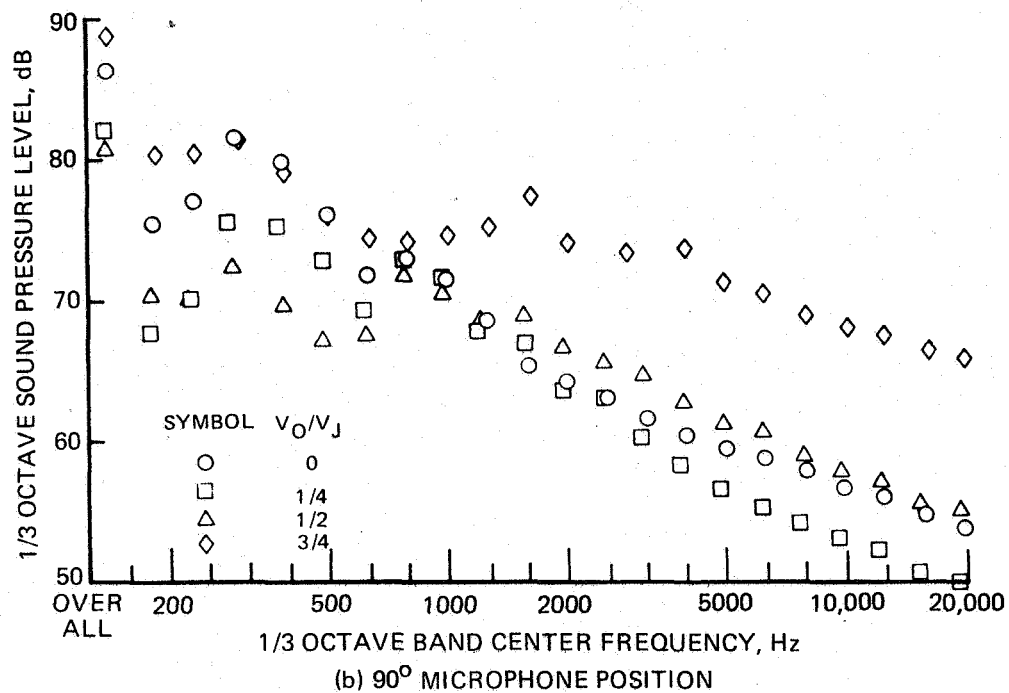


FIGURE 47— CONCLUDED.

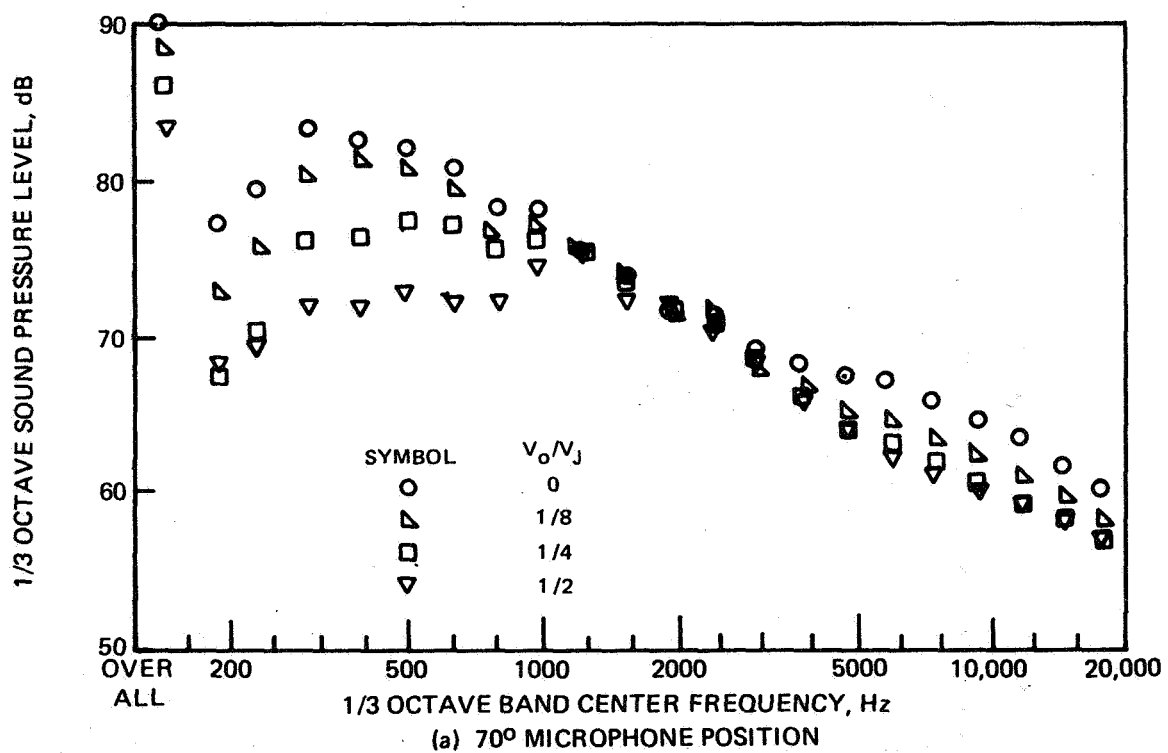
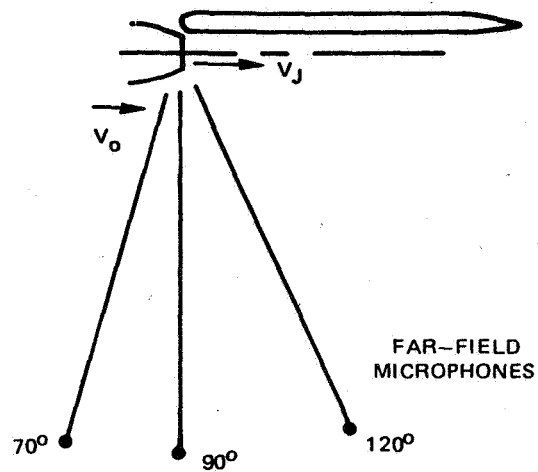


FIGURE 48 — EFFECT OF FLIGHT VELOCITY RATIO ON FAR-FIELD SOUND PRESSURE LEVELS FOR LONG-CHORD UNDER-THE-WING EXTERNALLY BLOWN FLAP AND 160 M/SEC EXHAUST VELOCITY

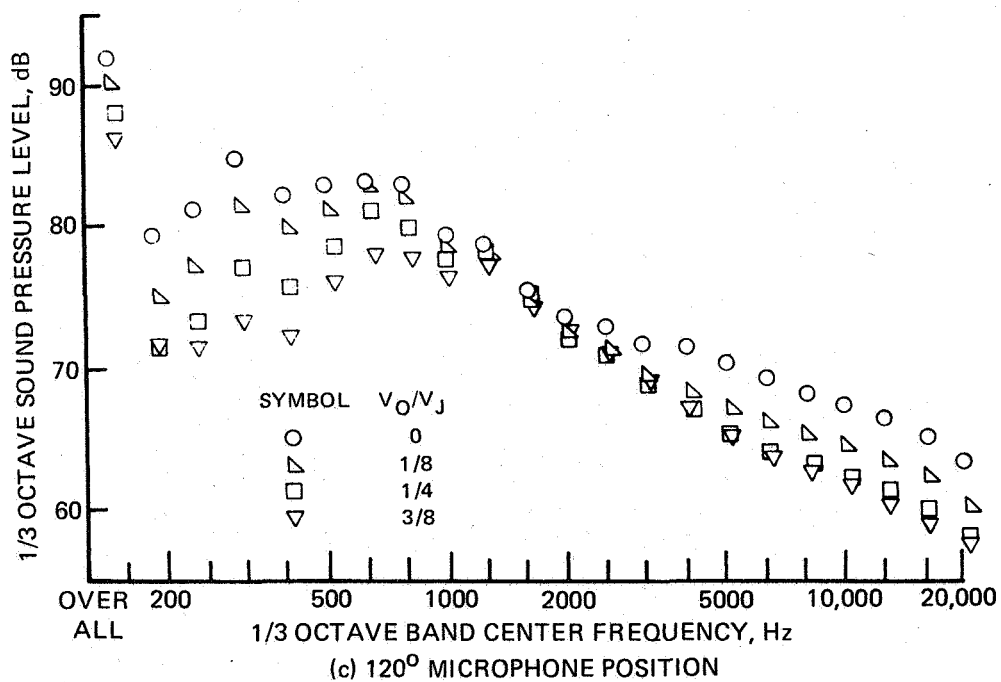
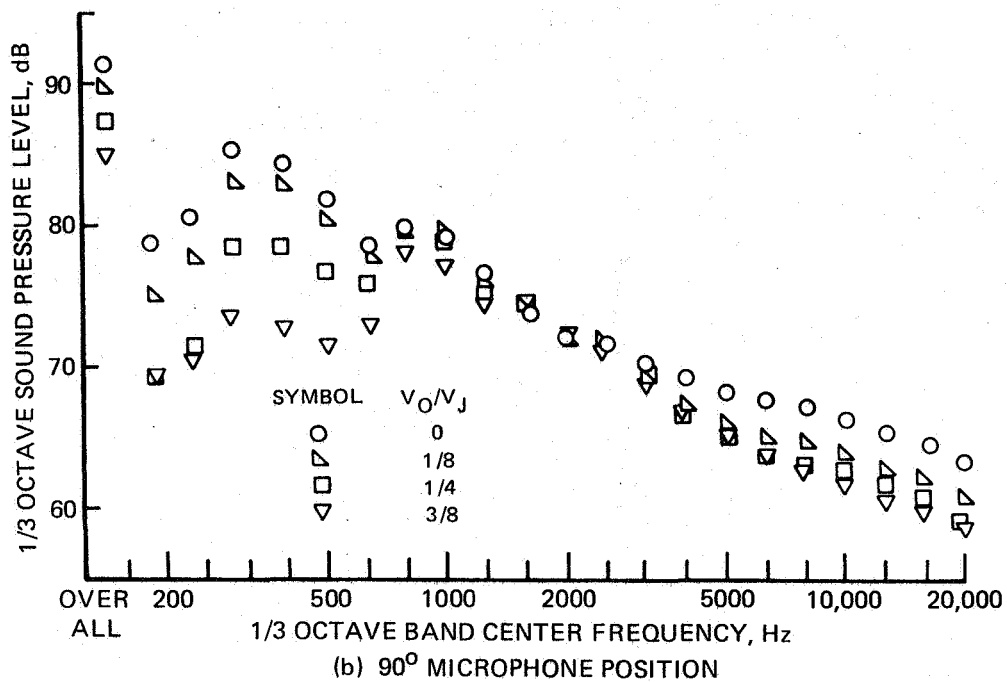


FIGURE 48— CONCLUDED.

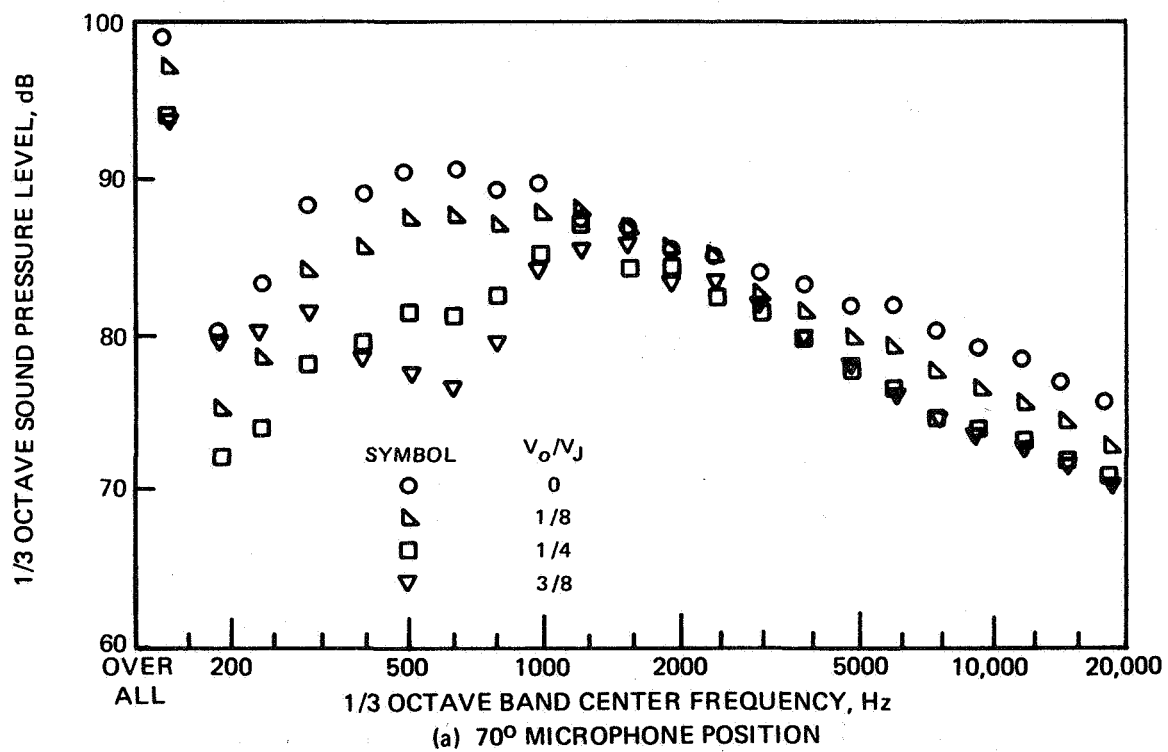
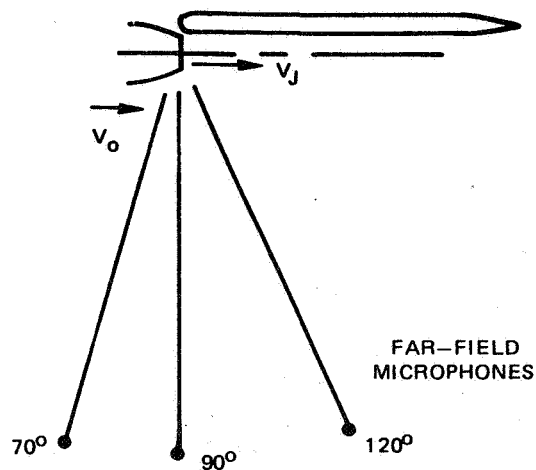


FIGURE 49 – EFFECT OF FLIGHT VELOCITY RATIO ON FAR-FIELD SOUND PRESSURE LEVELS FOR LONG-CHORD UNDER-THE-WING EXTERNALLY BLOWN FLAP AND 250 M/SEC EXHAUST VELOCITY

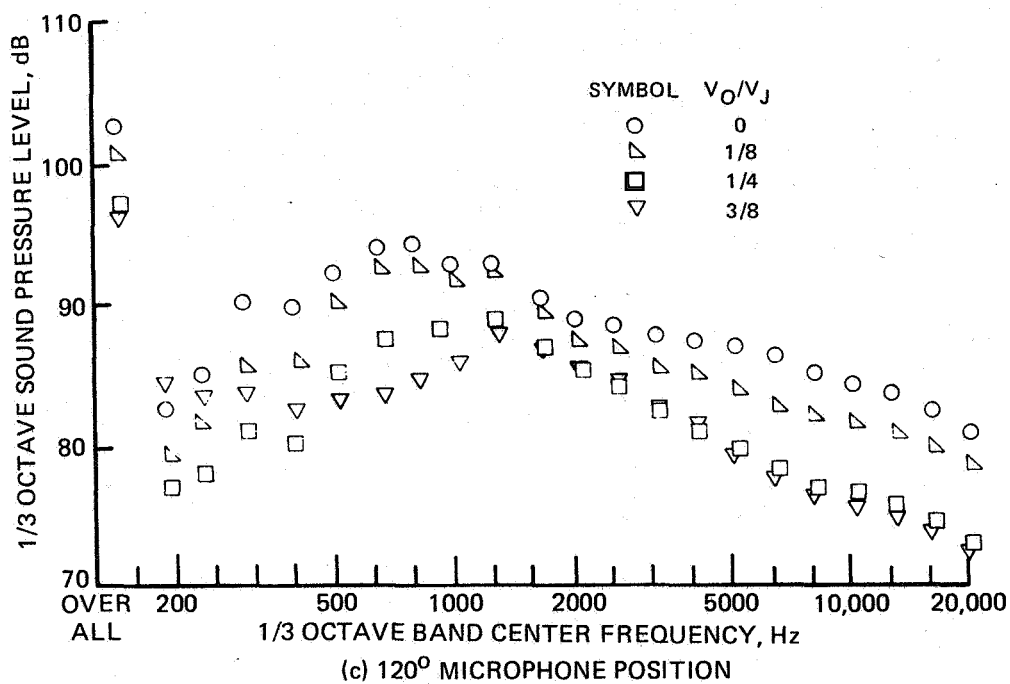
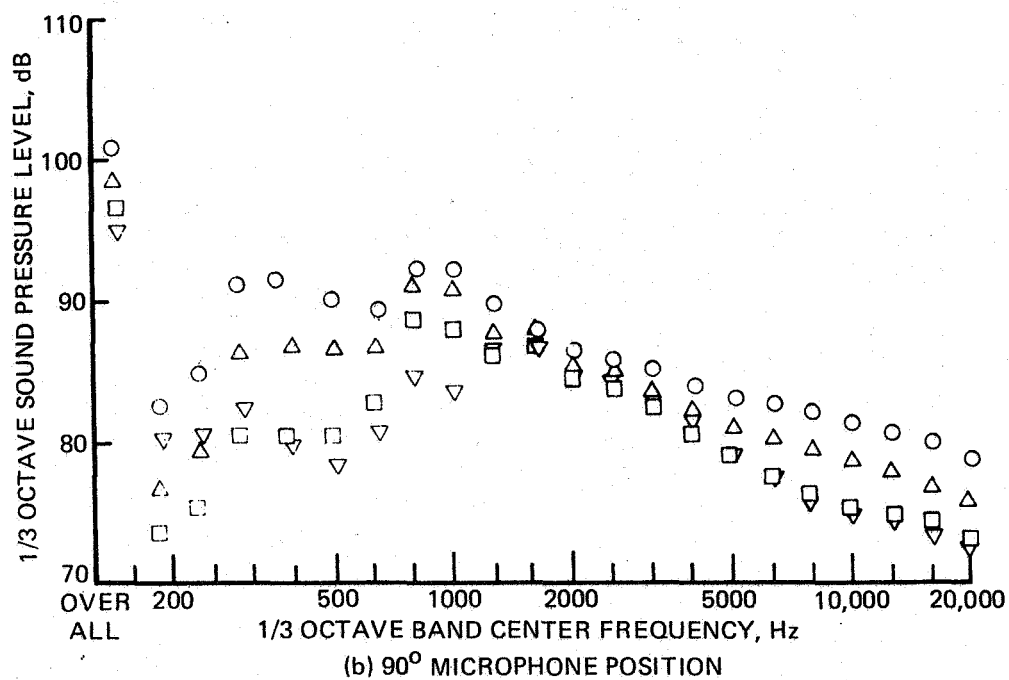


FIGURE 49—CONCLUDED.

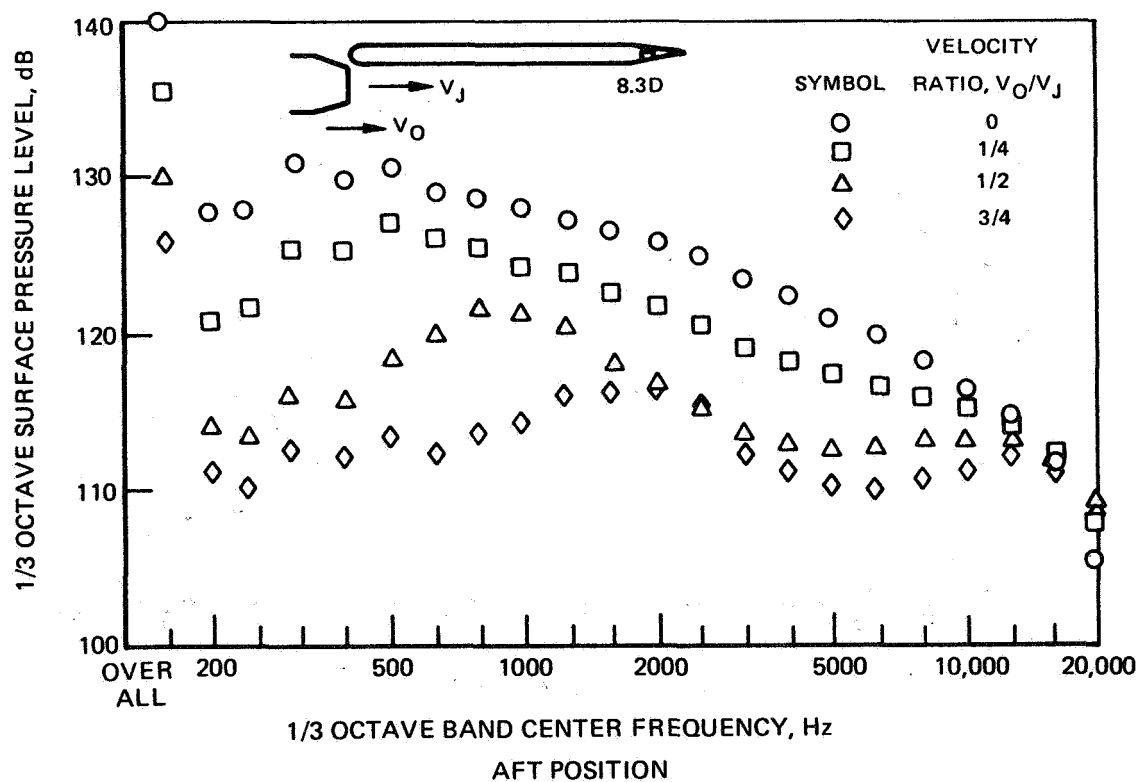
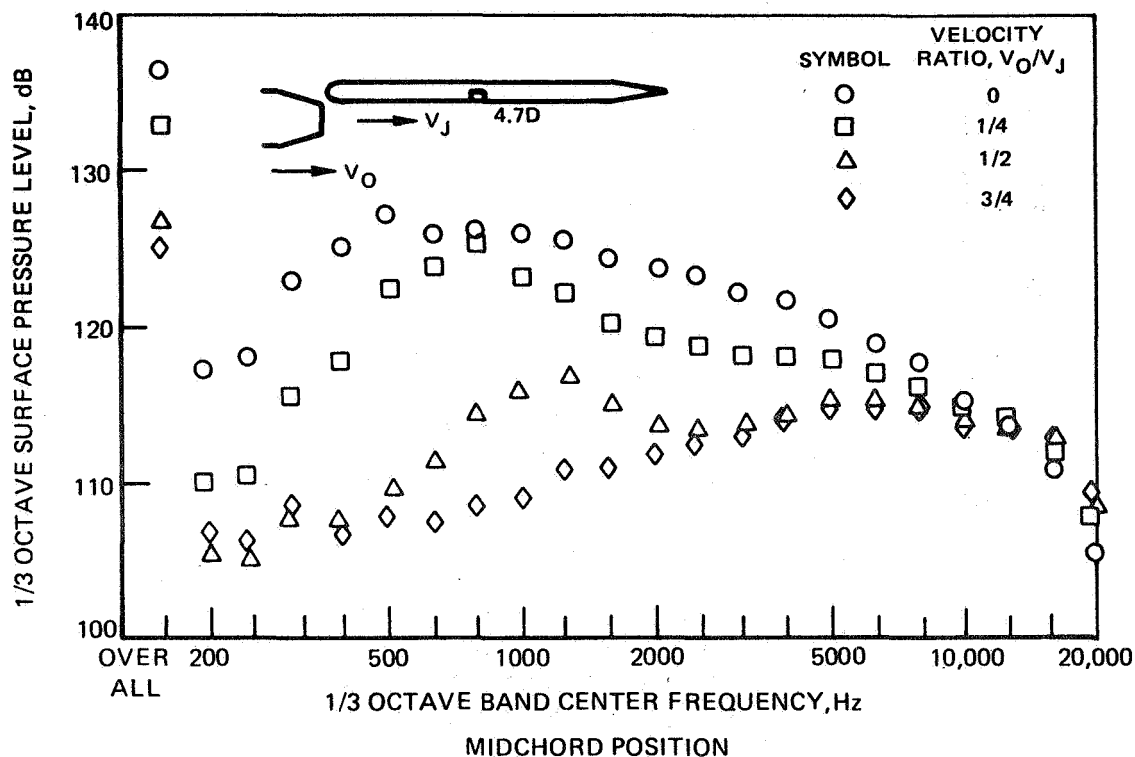


FIGURE 50—EFFECT OF FLIGHT VELOCITY RATIO ON SURFACE PRESSURE SPECTRA
FOR LONG-CHORD UNDEFLECTED EXTERNALLY BLOWN FLAP
(a) 125 M/SEC EXHAUST VELOCITY

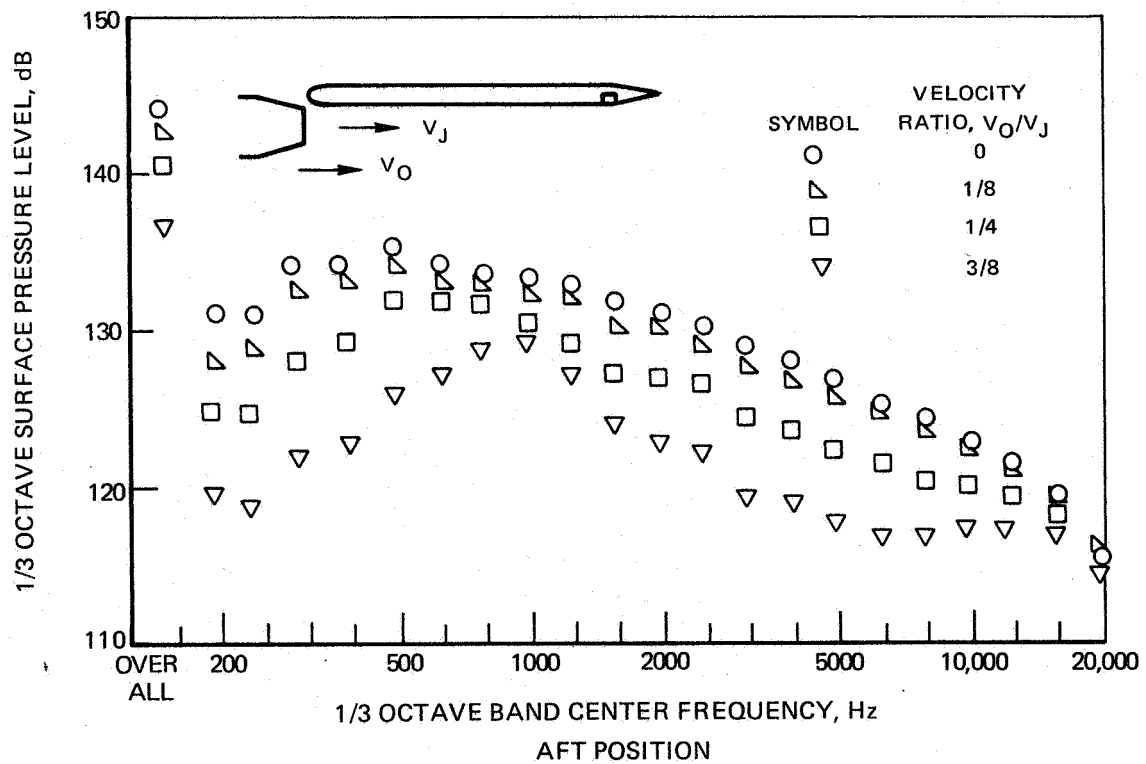
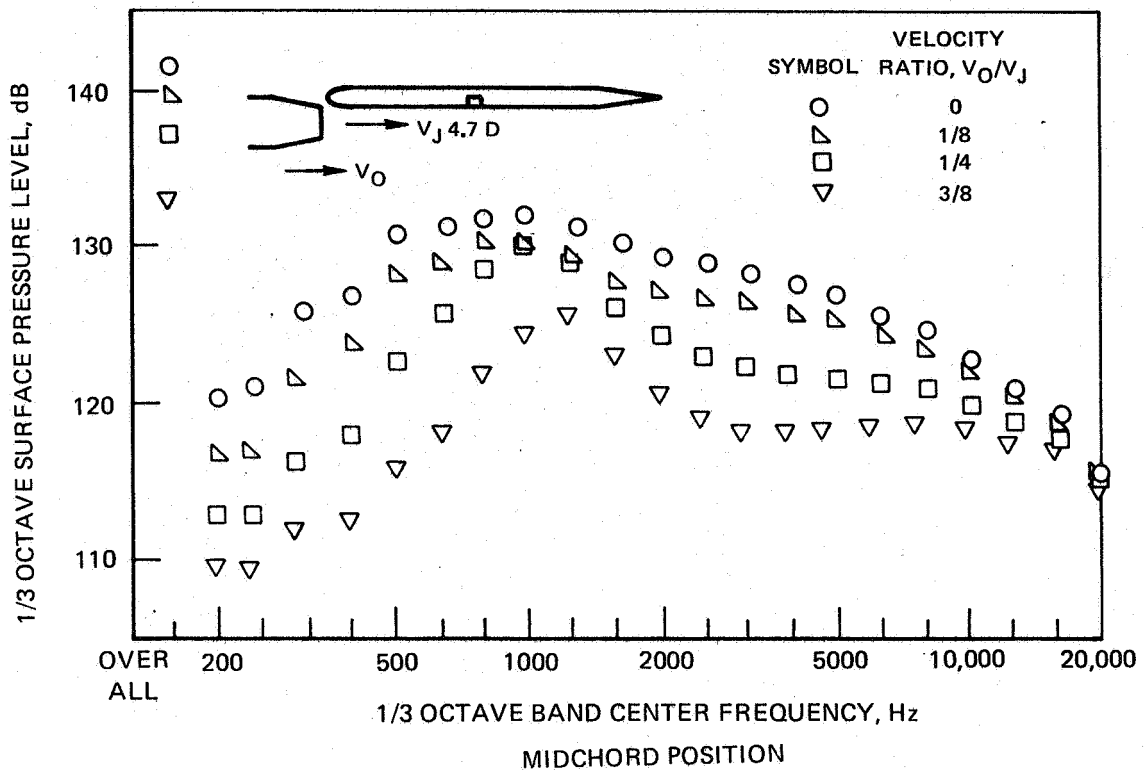


FIGURE 50—CONTINUED. (b) 160 M/SEC EXHAUST VELOCITY

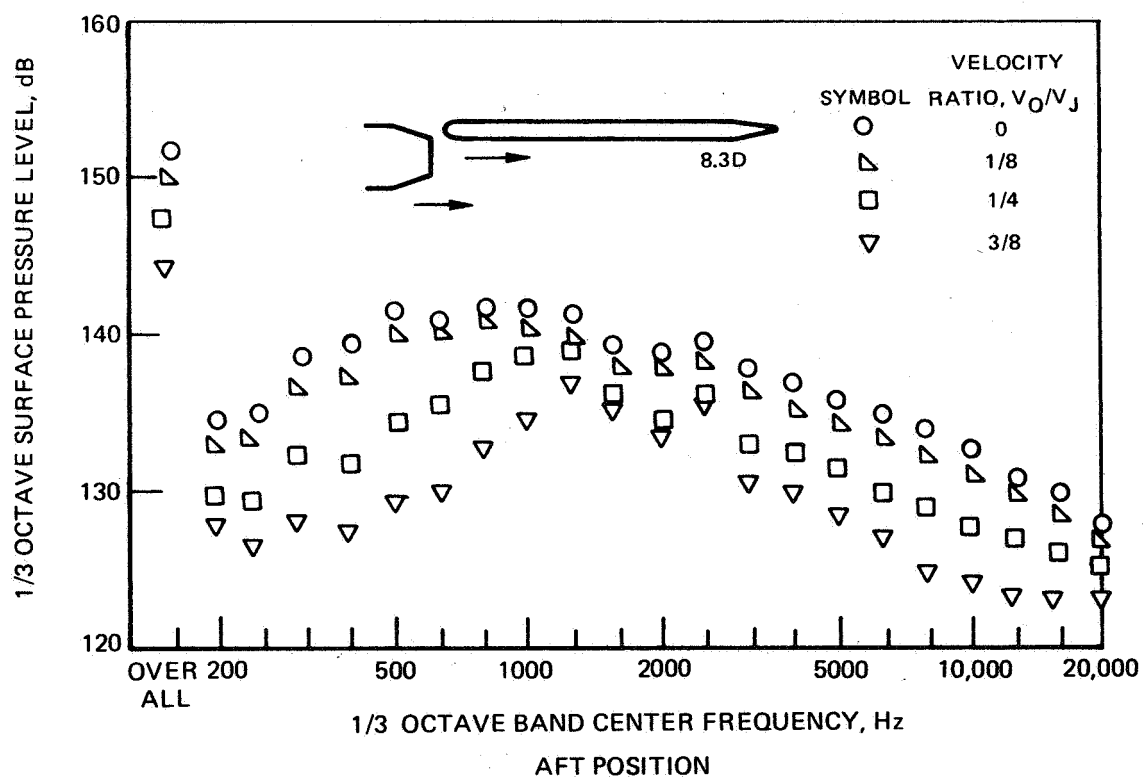
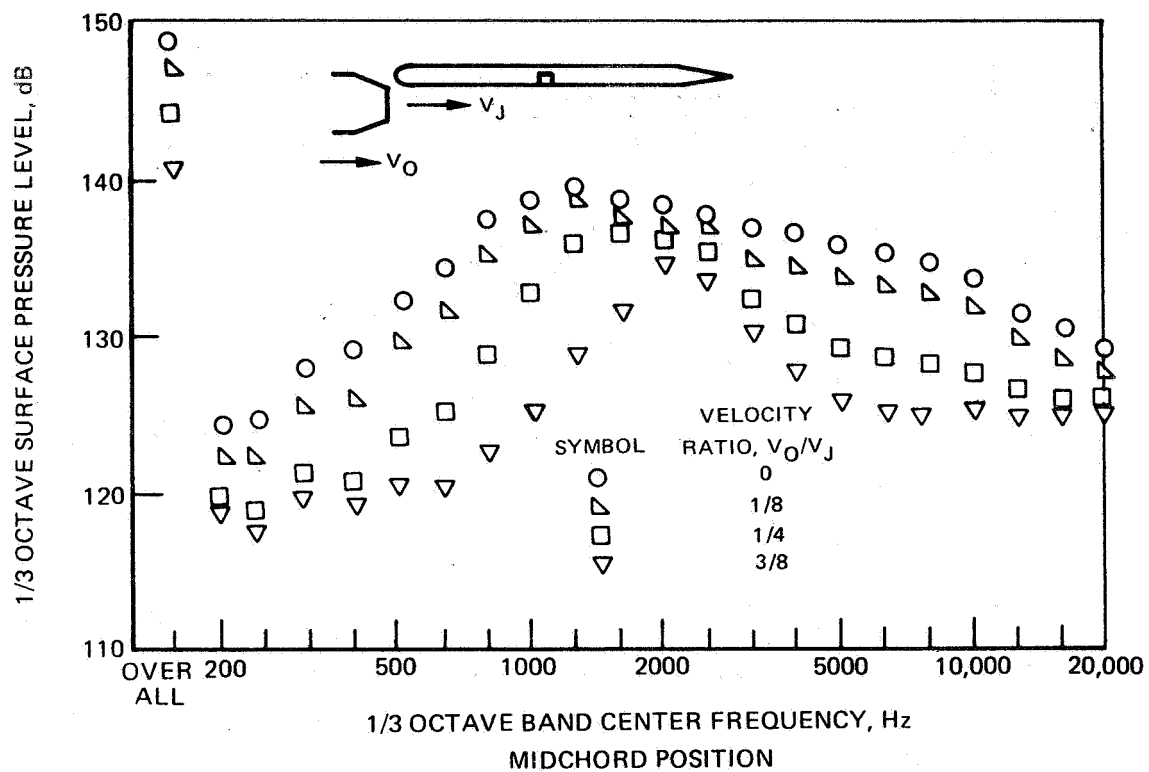


FIGURE 50—CONCLUDED. (c) 250 M/SEC EXHAUST VELOCITY.

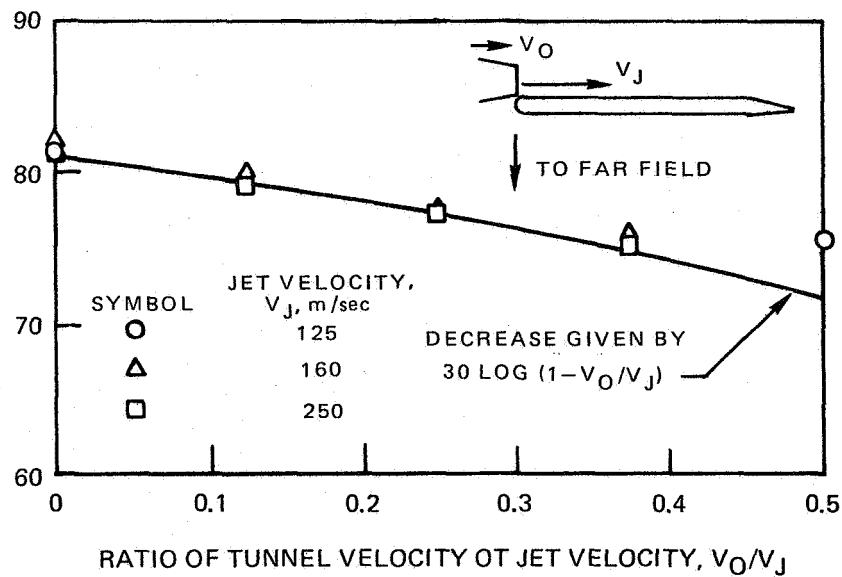
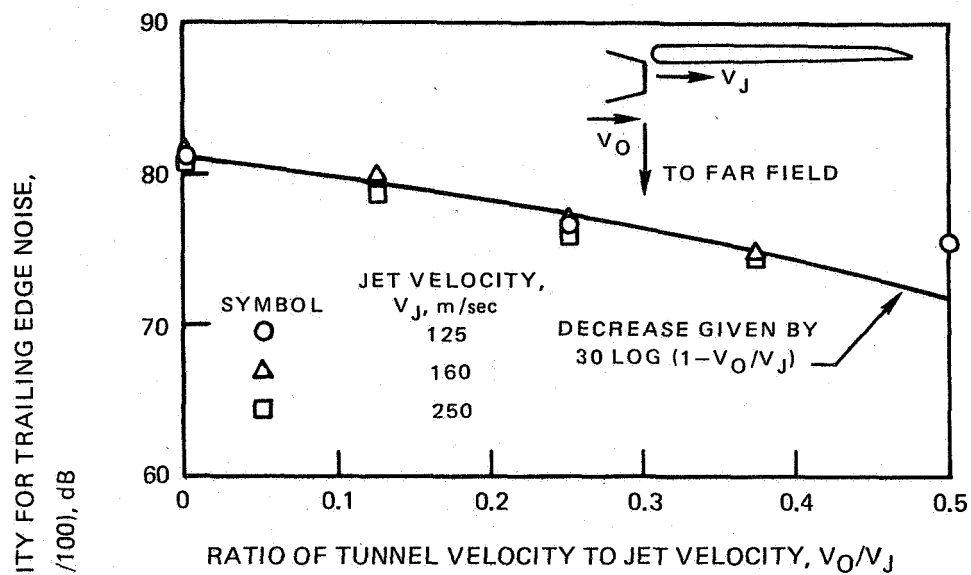


FIGURE 51 —EFFECT OF FLIGHT VELOCITY ON OVERALL SOUND PRESSURE LEVELS DIRECTLY BELOW LONG-CHORD AIRFOIL IN UNDER-THE-WING AND UPPER SURFACE BLOWING CONFIGURATIONS

1/3 OCTAVE SOUND PRESSURE LEVEL ADJUSTED TO 100 M/SEC JET VELOCITY AND
CORRECTED FOR TURBULENCE LEVEL, $SPL - 50 \log (V_J/100) + 20 \log (1 - V_0/V_J)$, dB

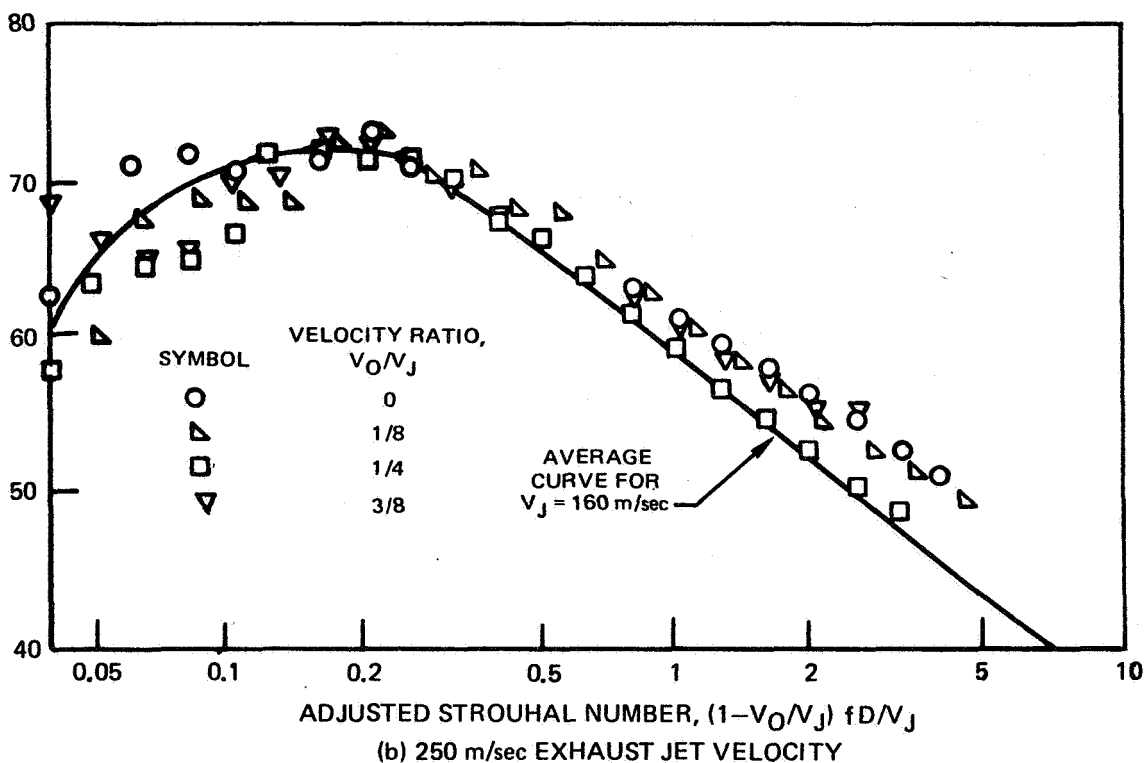
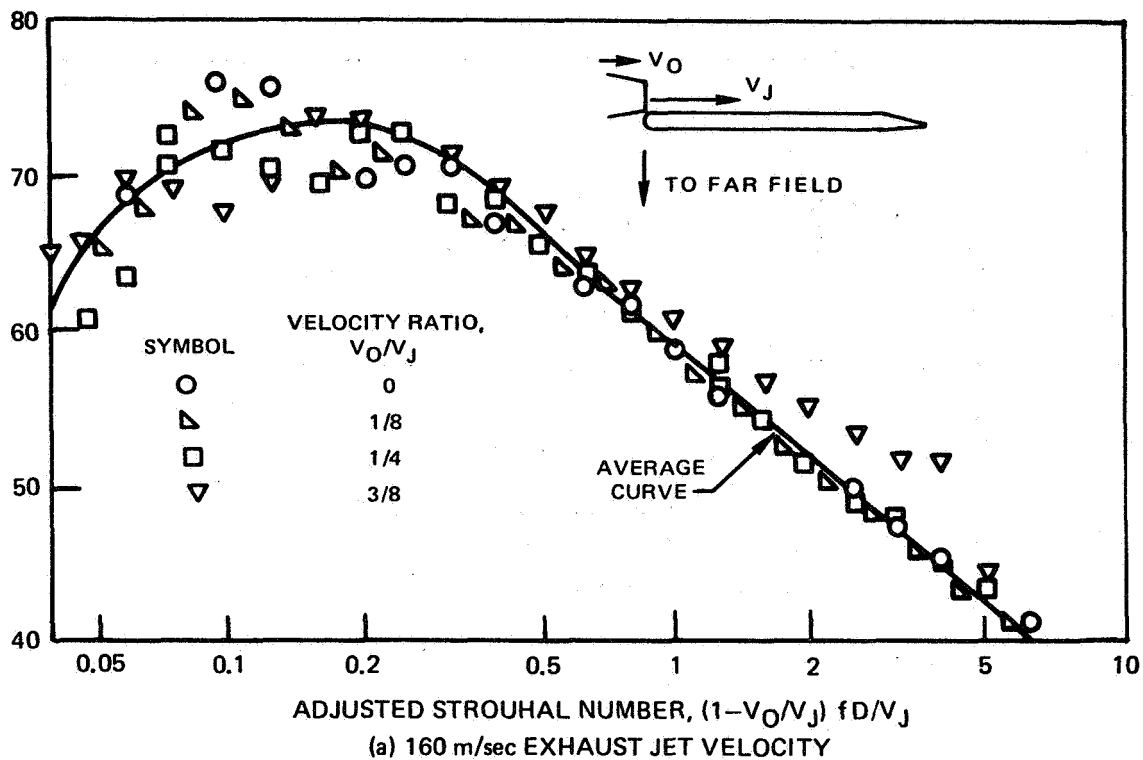


FIGURE 52 —USE OF ADJUSTED FREQUENCY FOR CORRELATING THE EFFECT OF FLIGHT VELOCITY RATIO ON FAR-FIELD SPECTRA OF LONG-CHORD UPPER SURFACE BLOWING CONFIGURATION

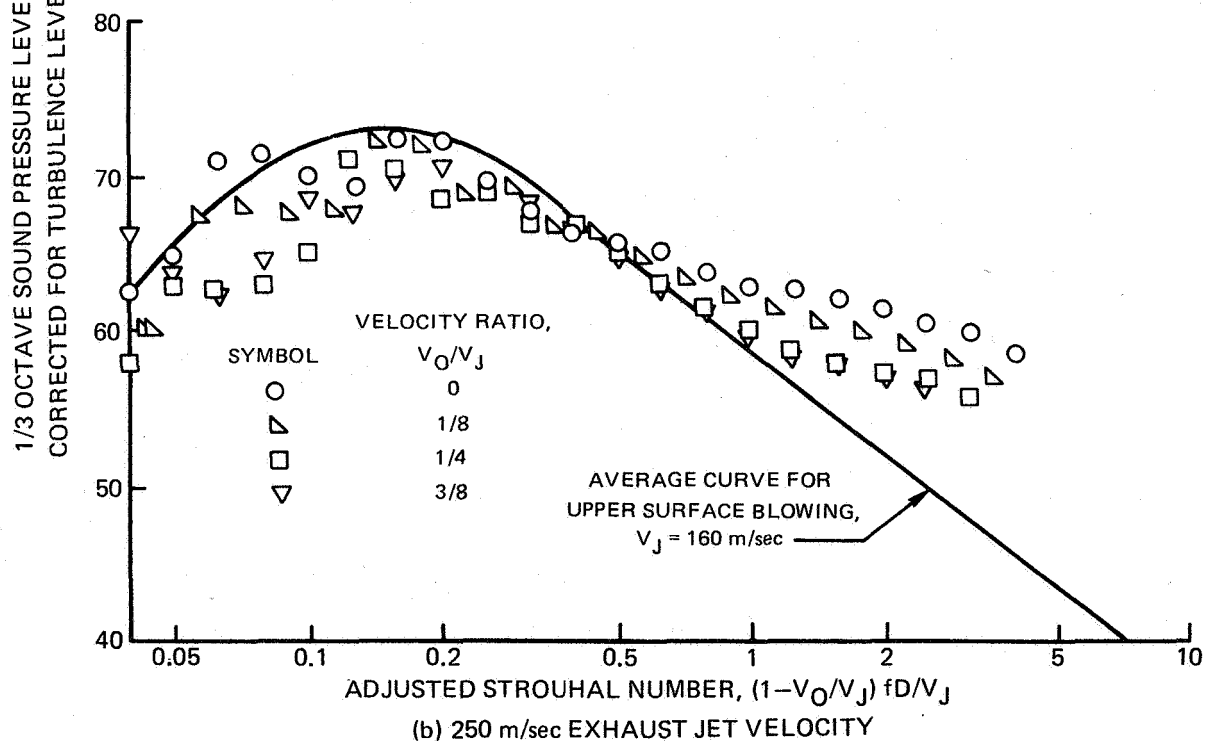
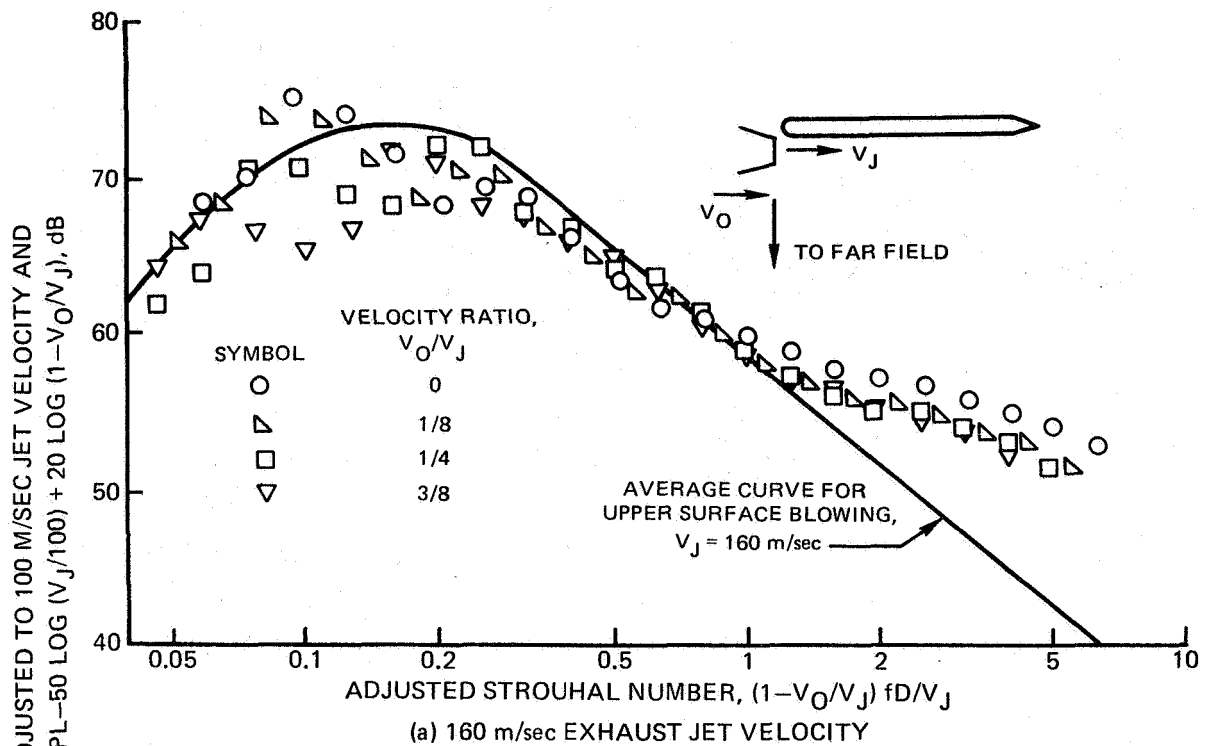
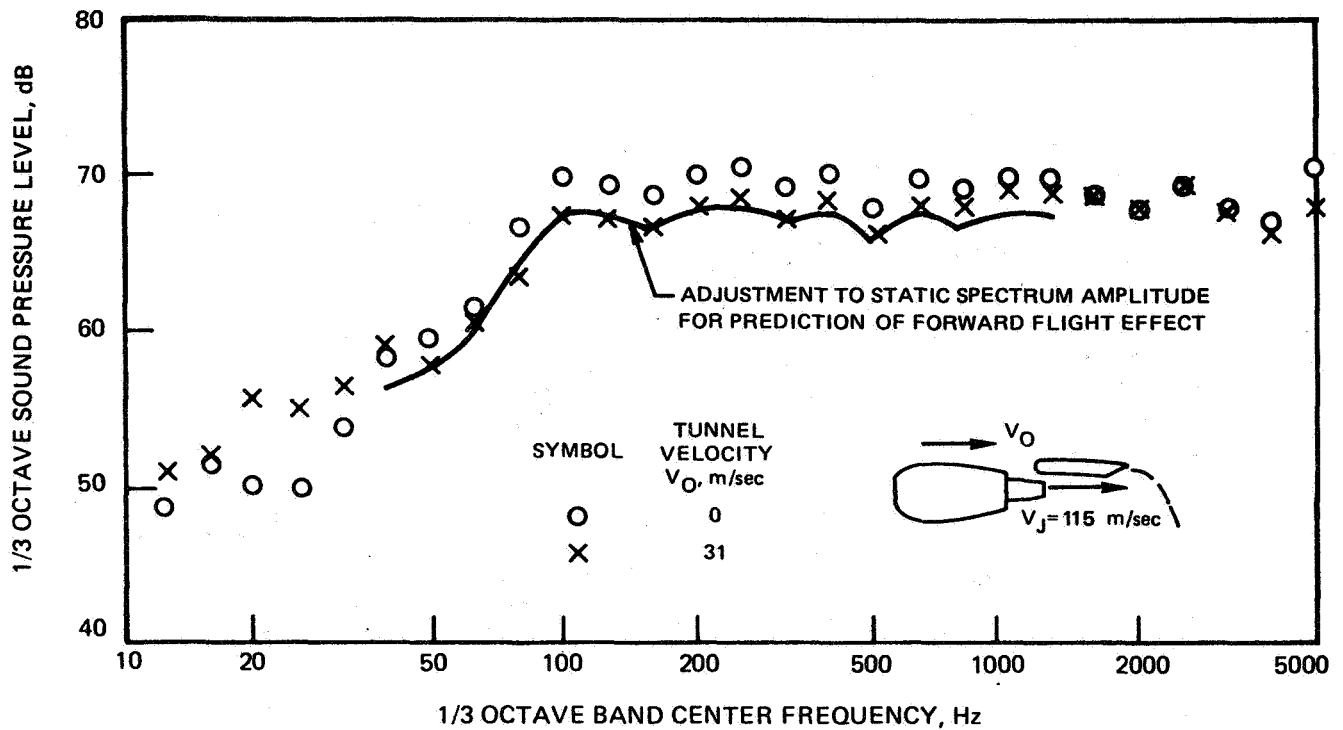
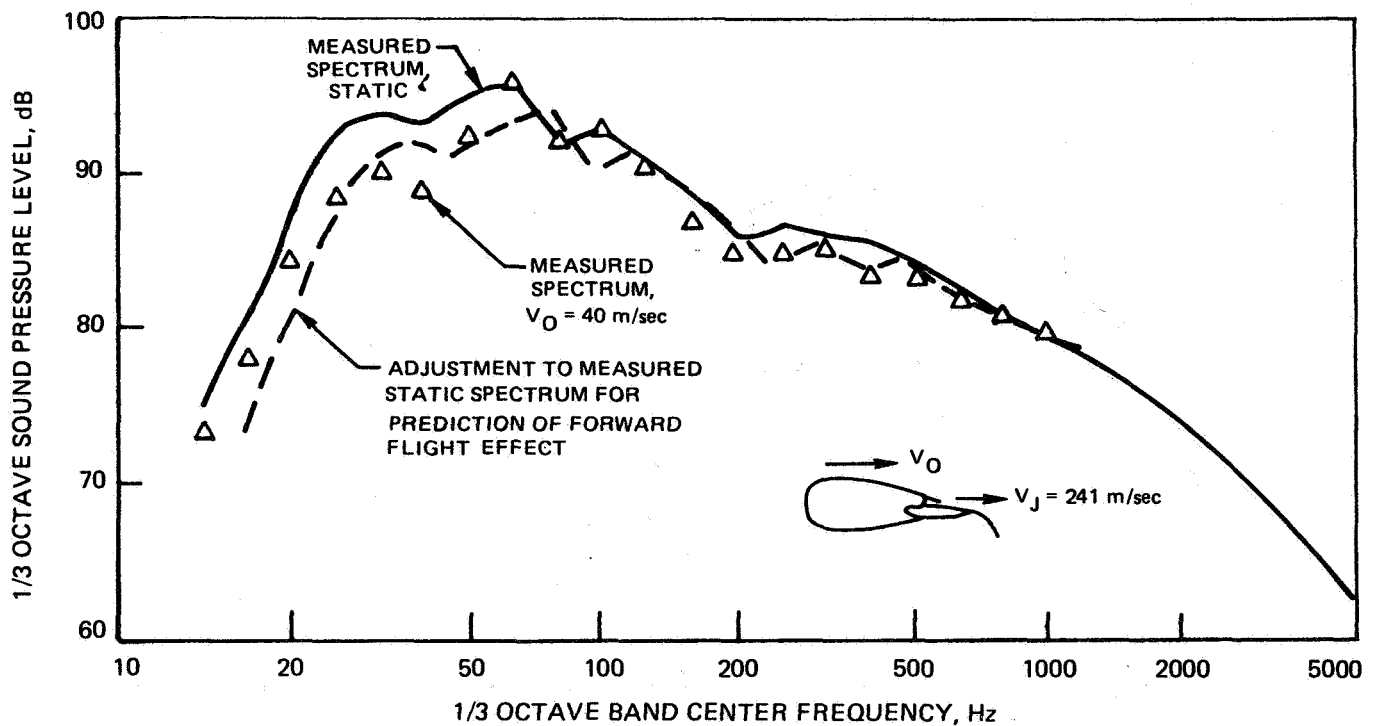


FIGURE 53 — USE OF ADJUSTED FREQUENCY FOR CORRELATING THE EFFECT OF FLIGHT VELOCITY RATIO ON FAR-FIELD SPECTRA OF LONG-CHORD UNDER-THE-WING CONFIGURATION

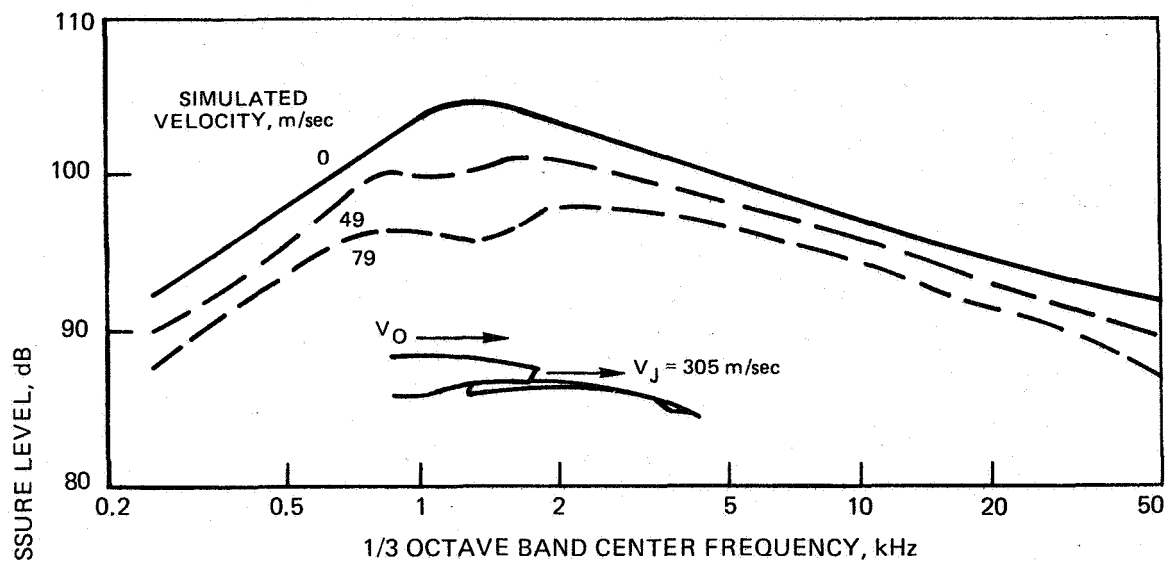


(a) UNDER-THE-WING APPROACH CONFIGURATION, 115 m/sec JET VELOCITY

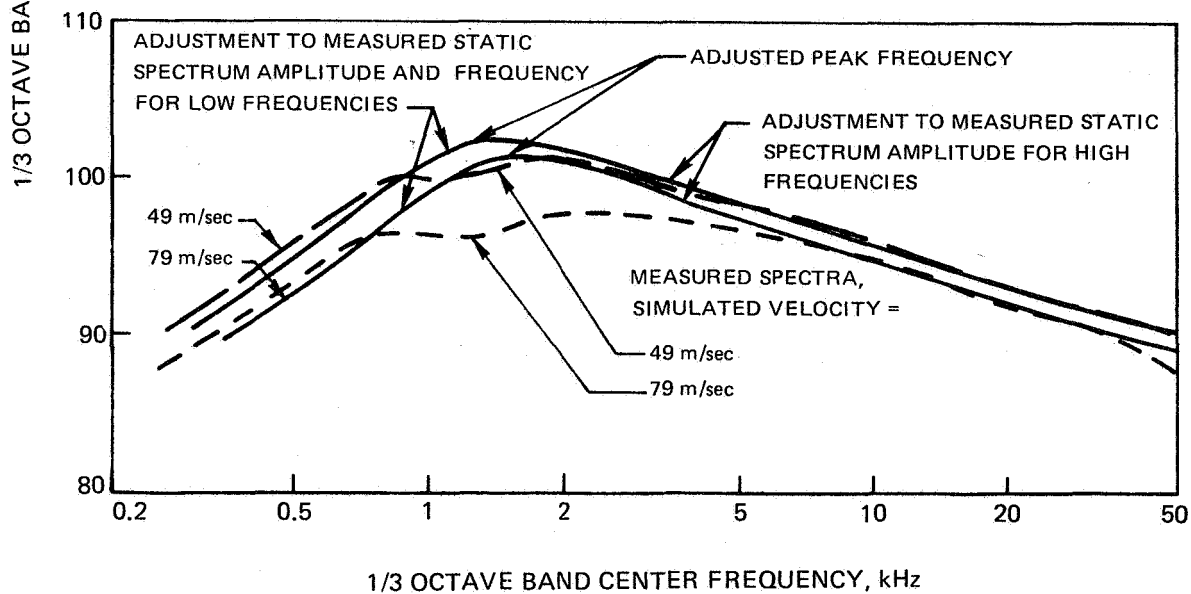


(b) UPPER-SURFACE-BLOWING TAKEOFF CONFIGURATION, 241 m/sec JET VELOCITY

FIGURE 54 — MEASURED AND PREDICTED FORWARD FLIGHT EFFECTS FOR EBF CONFIGURATIONS TESTED IN THE NASA AMES RESEARCH CENTER 40x80 FT WIND TUNNEL



(a) MEASURED FAR-FIELD SPECTRA



(b) PREDICTED EFFECT OF WIND TUNNEL VELOCITY

FIGURE 55— MEASURED AND PREDICTED EFFECT OF SIMULATED FLIGHT VELOCITY ON FAR-FIELD SPECTRA OF BOEING CO. UPPER SURFACE BLOWING CONFIGURATION. 305 m/sec JET VELOCITY

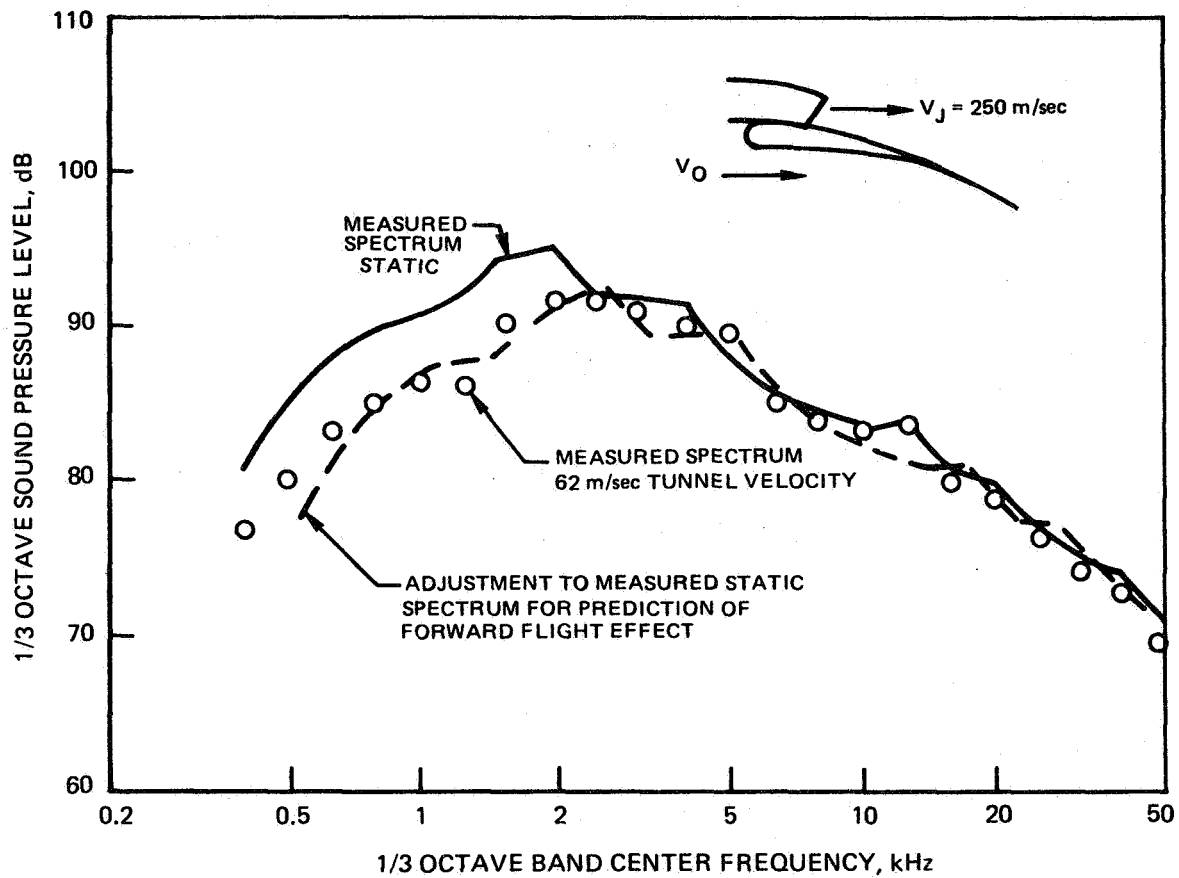


FIGURE 56- MEASURED AND PREDICTED EFFECT OF WIND TUNNEL VELOCITY ON FAR-FIELD SPECTRUM OF LOCKHEED-GEORGIA CO. UPPER SURFACE BLOWING CONFIGURATION, 250 m/sec JET VELOCITY

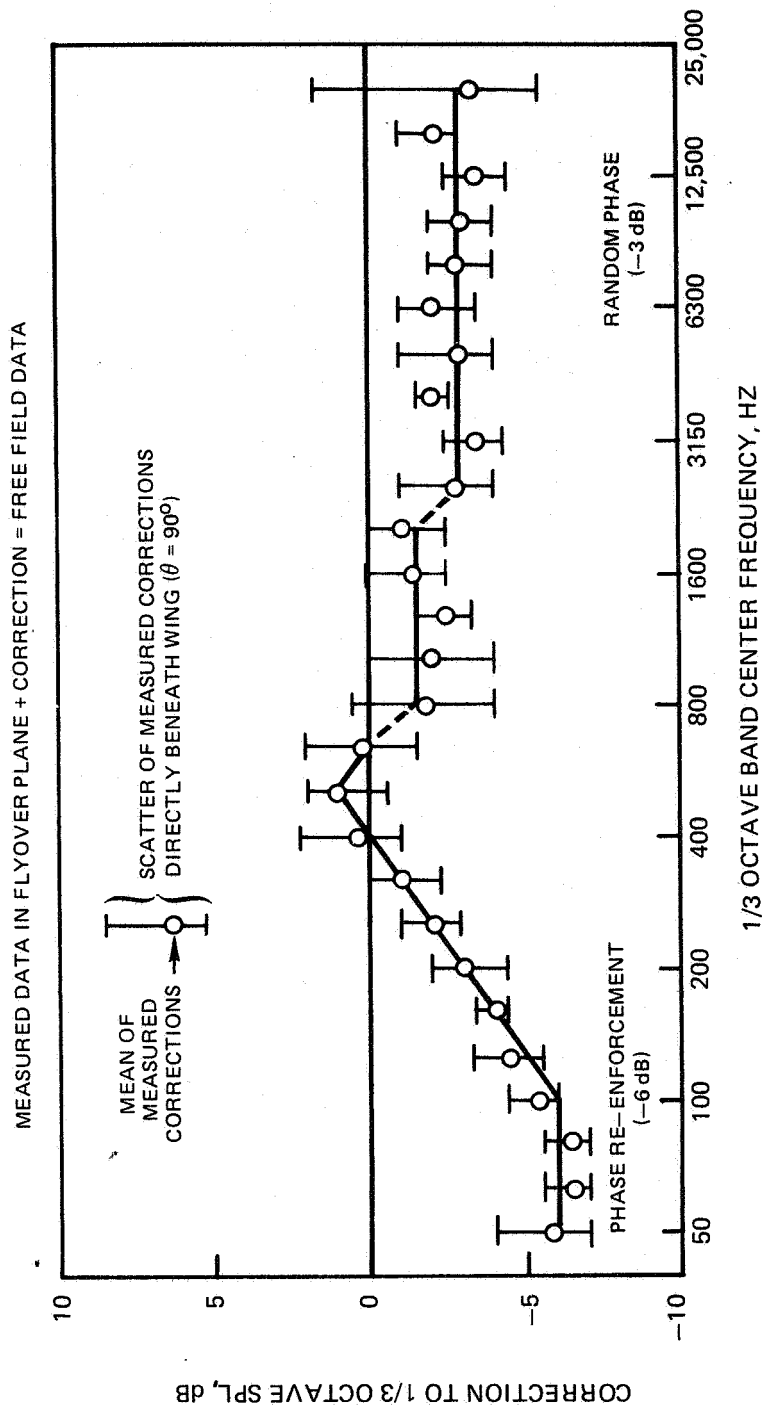
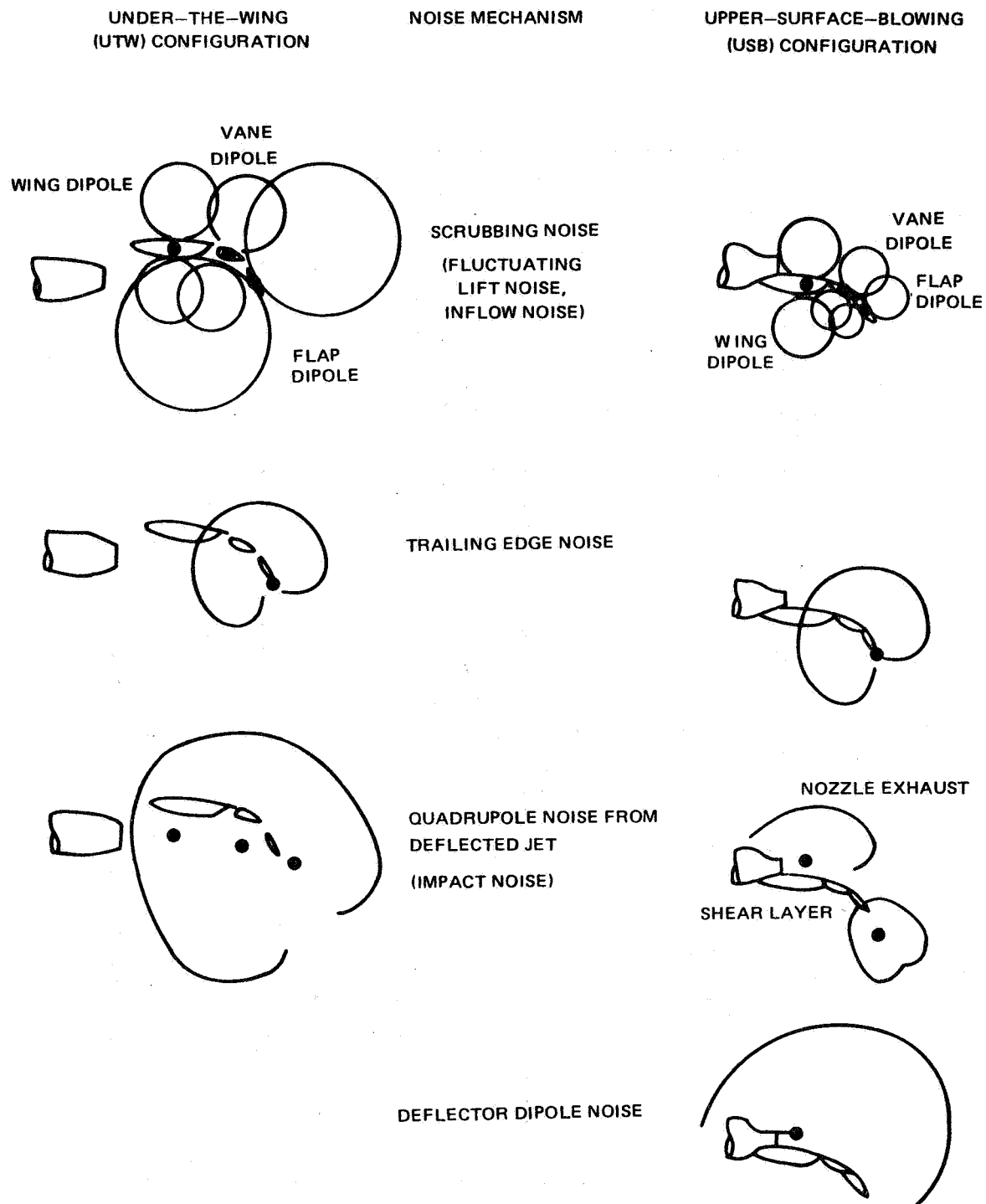


FIGURE 57 - EMPIRICAL CORRECTION FOR SPECTRA MEASURED WITH WING AND NOISE-SUPPRESSED TF-34 ENGINE IN FLYOVER PLANE



**FIGURE 58 – SKETCH OF DIRECTIVITIES FOR DIFFERENT MECHANISMS
OF EXTERNALLY BLOWN FLAP NOISE**

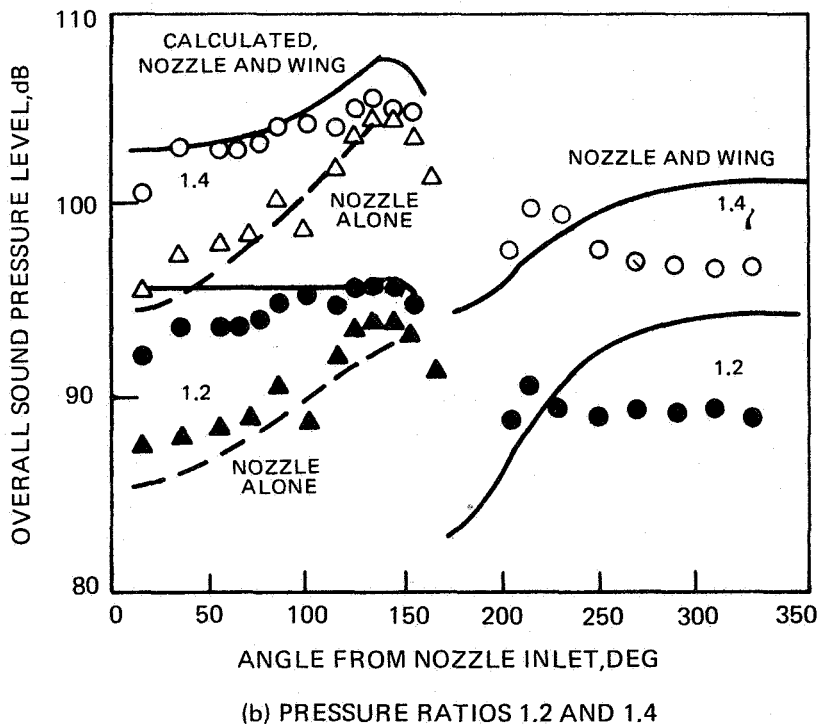
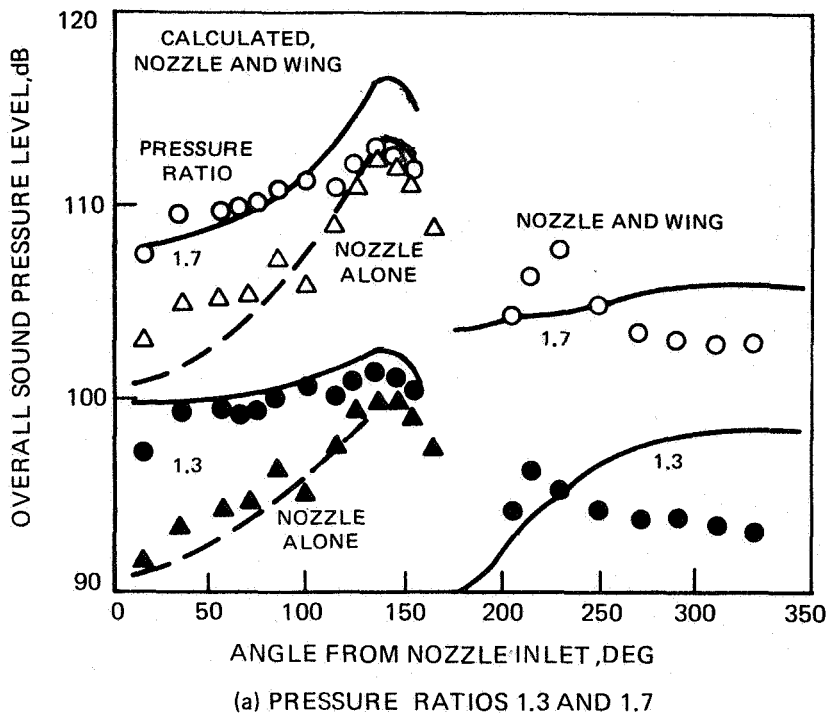


FIGURE 59—MEASURED AND CALCULATED OASPL DIRECTIVITY FOR LARGE MIXER NOZZLE ALONE AND WITH UTW WING WITH RETRACTED FLAPS

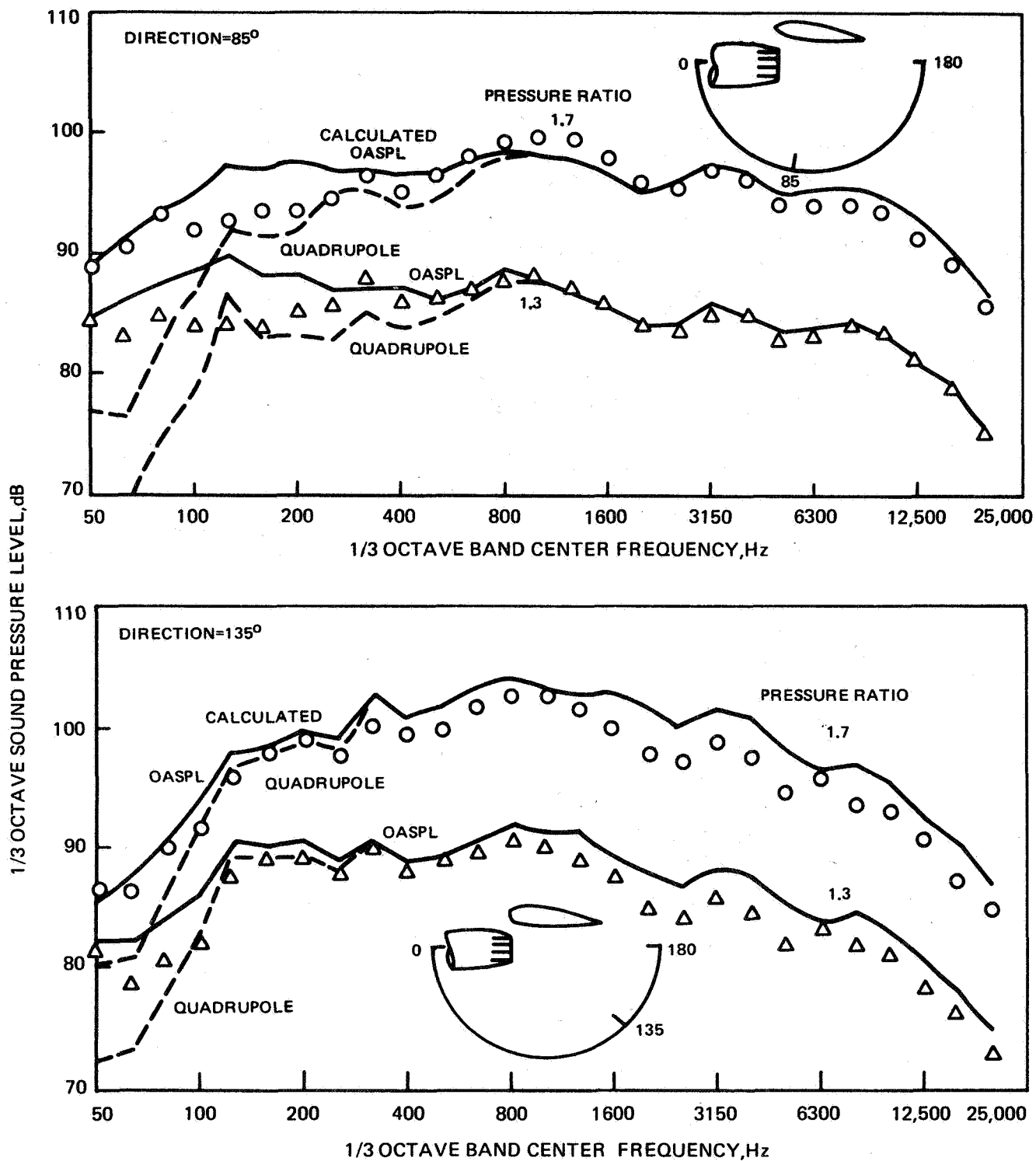
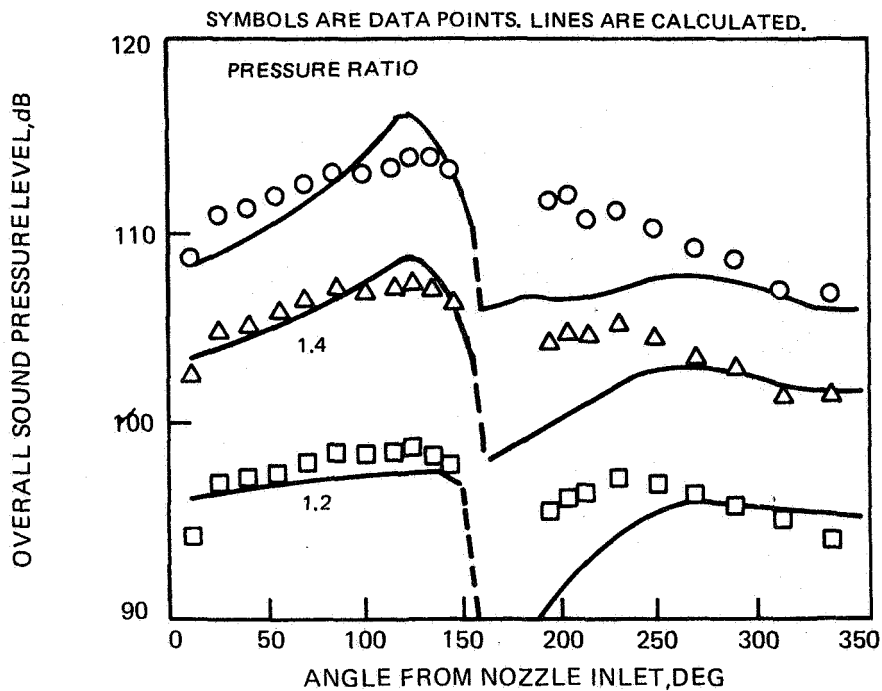
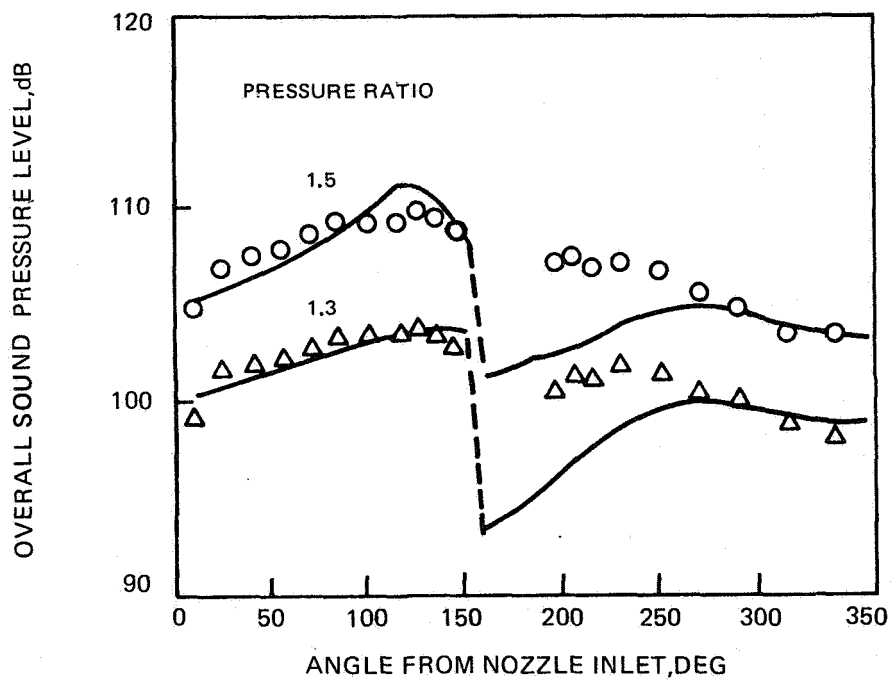
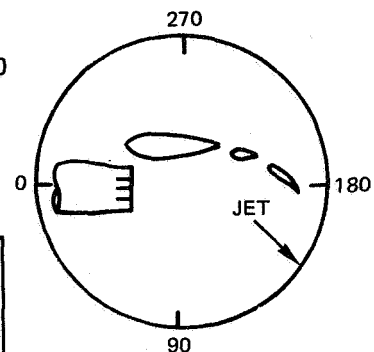


FIGURE 60 – MEASURED AND CALCULATED SPECTRA FOR LARGE UTW MIXER NOZZLE AND WING WITH RETRACTED FLAPS



(a) PRESSURE RATIOS 1.2, 1.4, AND 1.7



(b) PRESSURE RATIOS 1.3 AND 1.5

FIGURE 61—MEASURED AND CALCULATED OASPL DIRECTIVITY FOR LARGE MIXER NOZZLE AND UTW WING WITH 10°–20° FLAP DEFLECTION

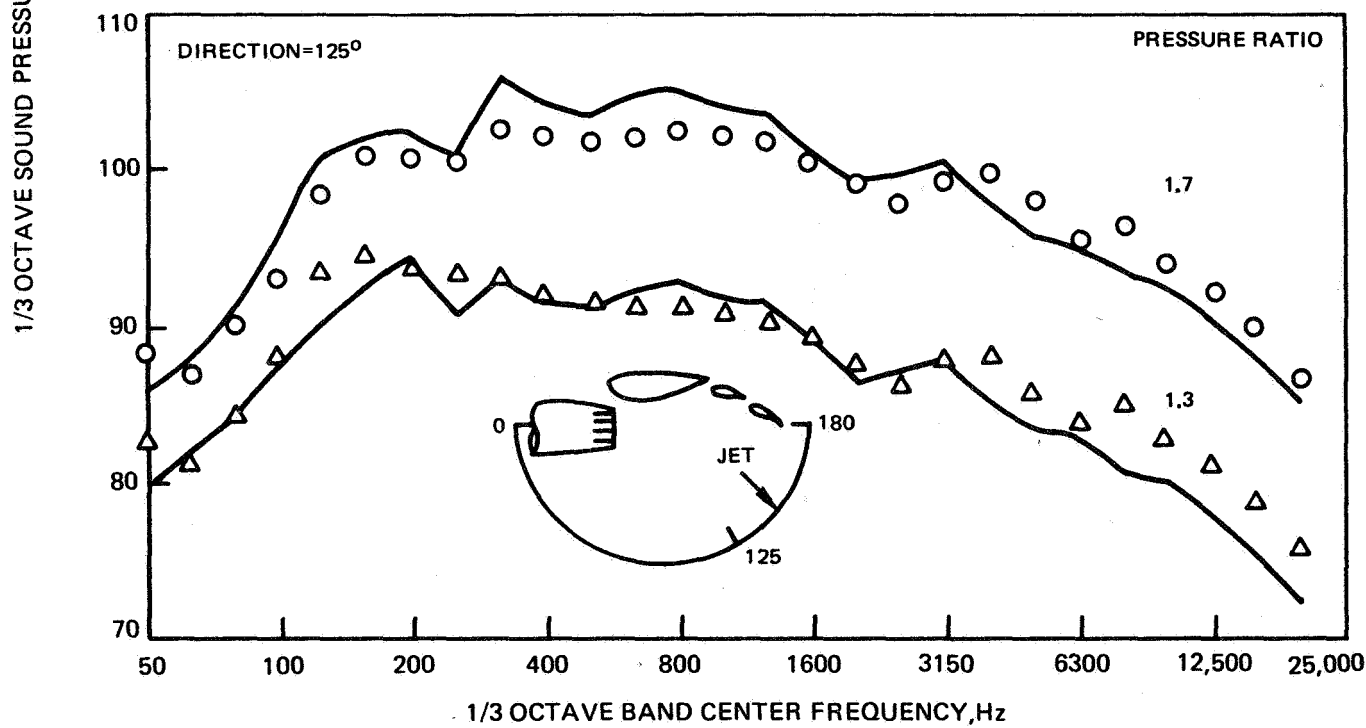
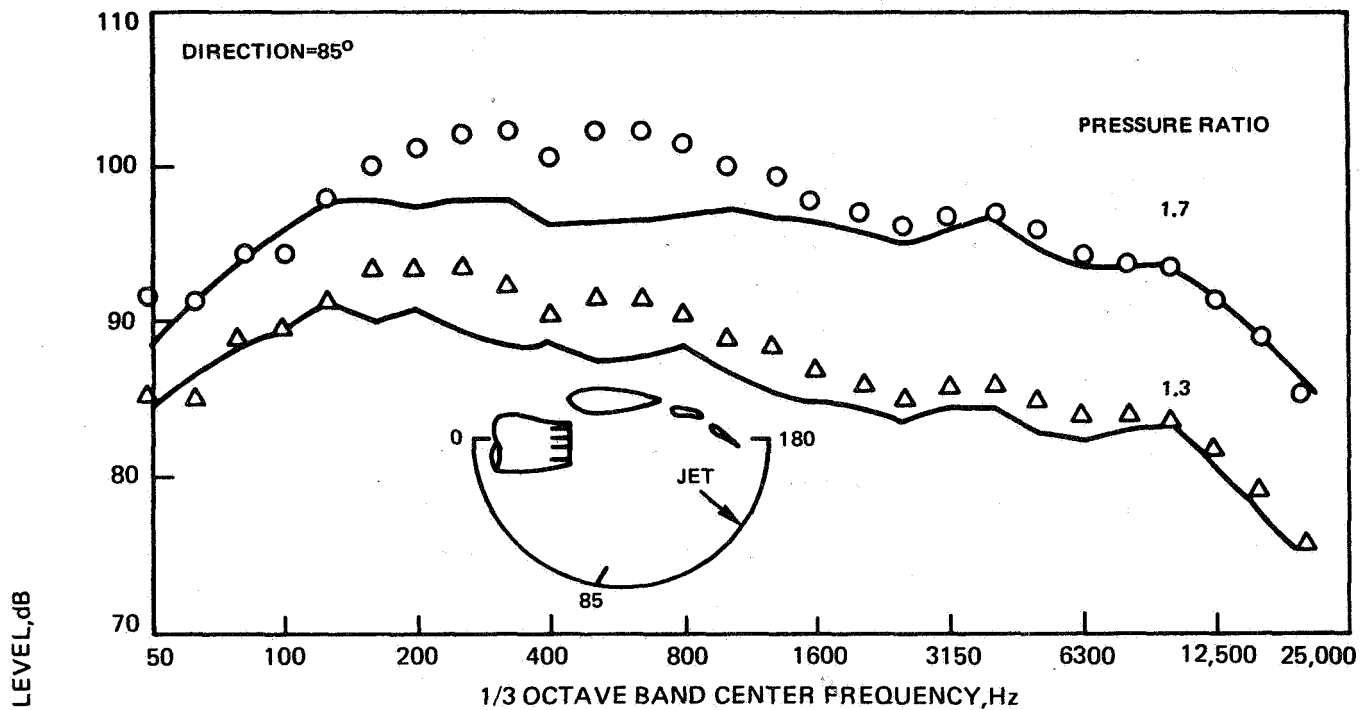
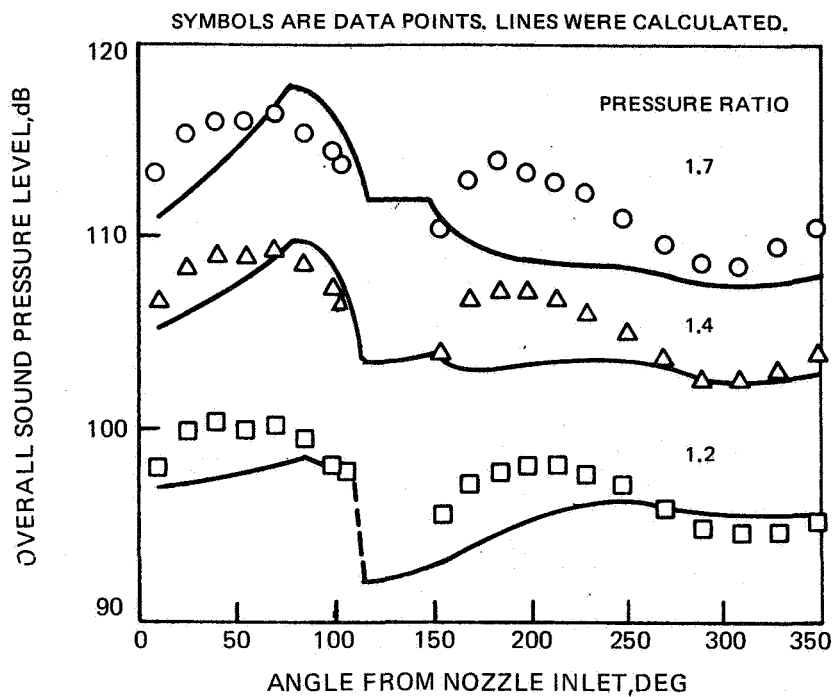
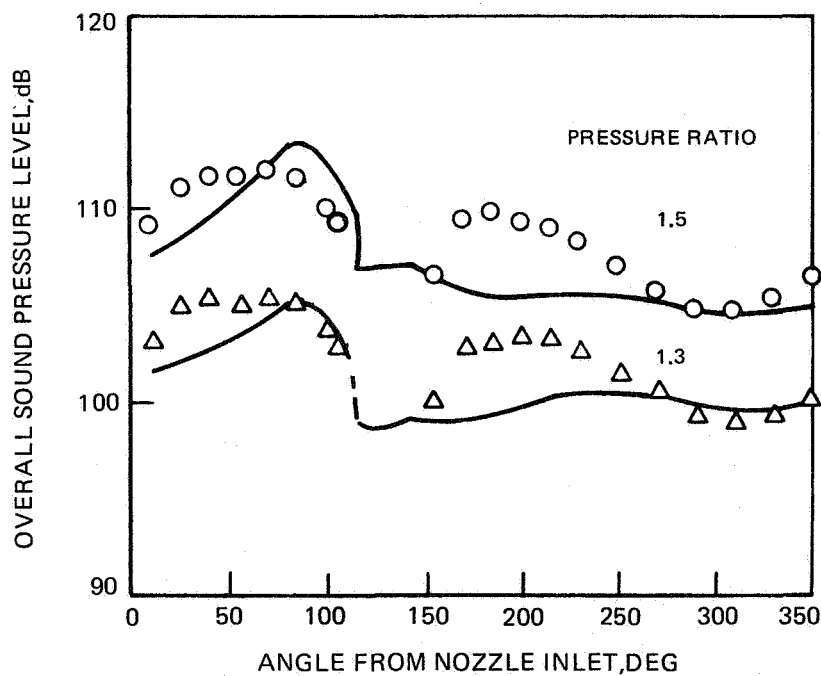
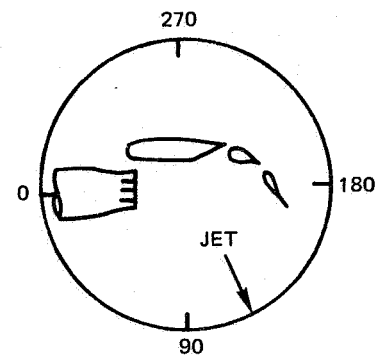


FIGURE 62 —MEASURED AND CALCULATED SPECTRA FOR LARGE MIXER NOZZLE AND UTW WING WITH 10°-20° FLAP DEFLECTION



(a) PRESSURE RATIOS 1.2, 1.4, AND 1.7



(b) PRESSURE RATIOS 1.3 AND 1.5

FIGURE 63 — MEASURED AND CALCULATED OASPL DIRECTIVITY FOR LARGE MIXER NOZZLE AND UTW WING WITH 30°–60° FLAP DEFLECTION

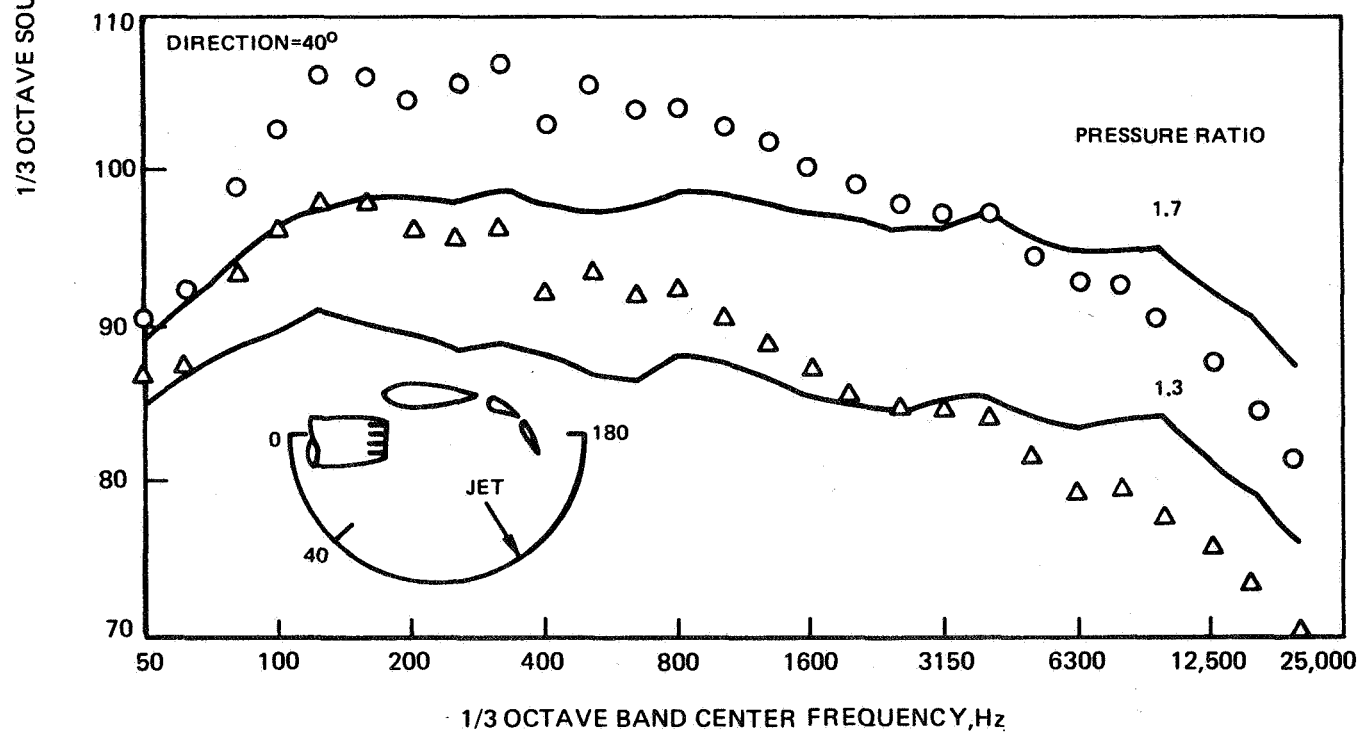
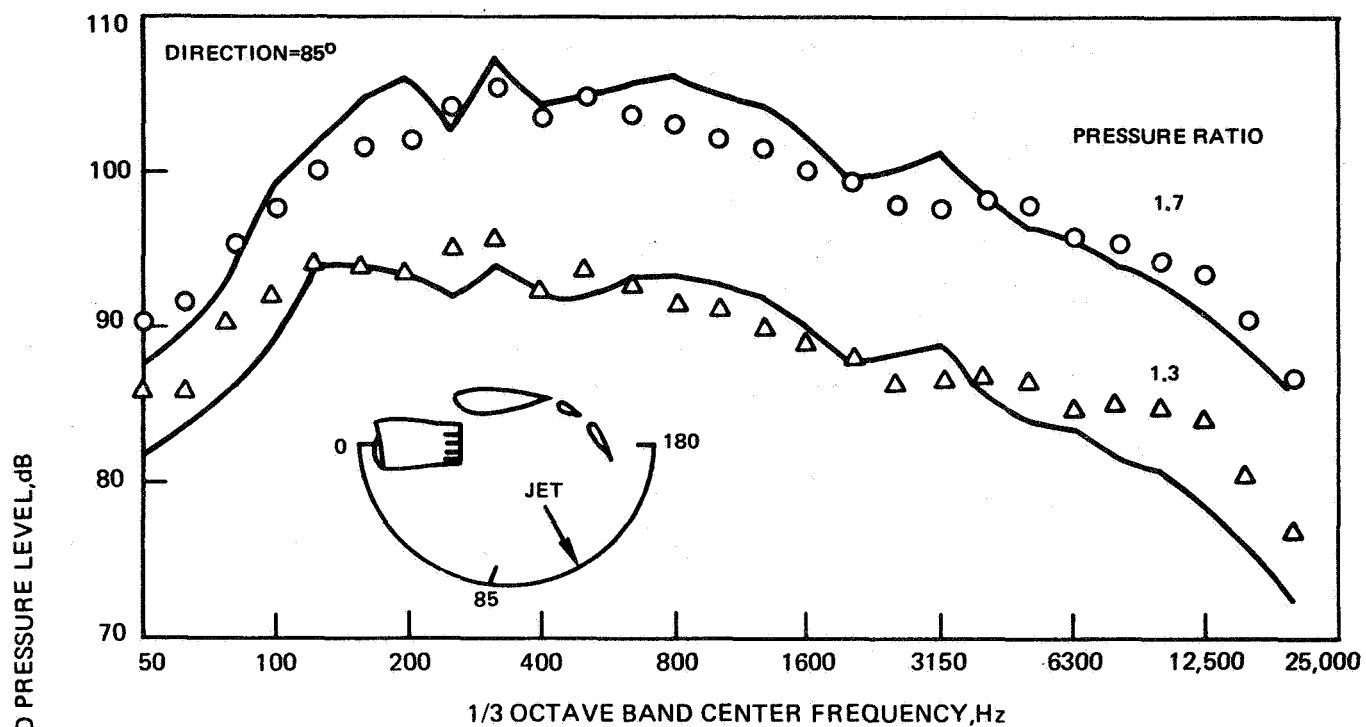
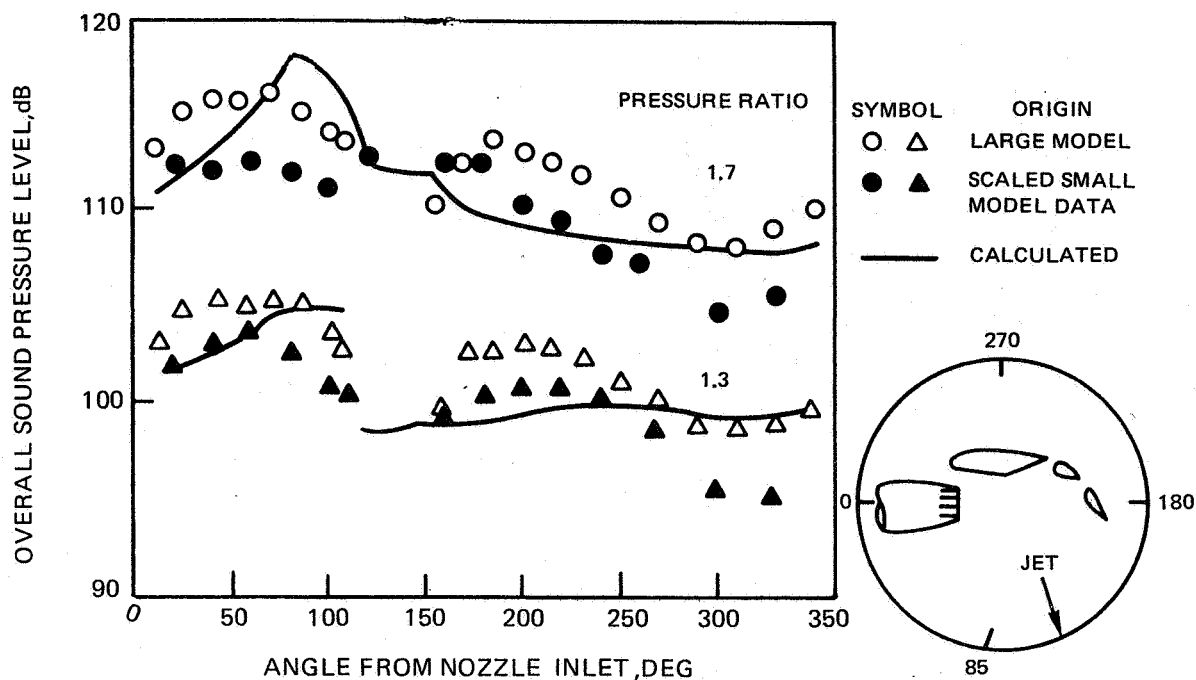
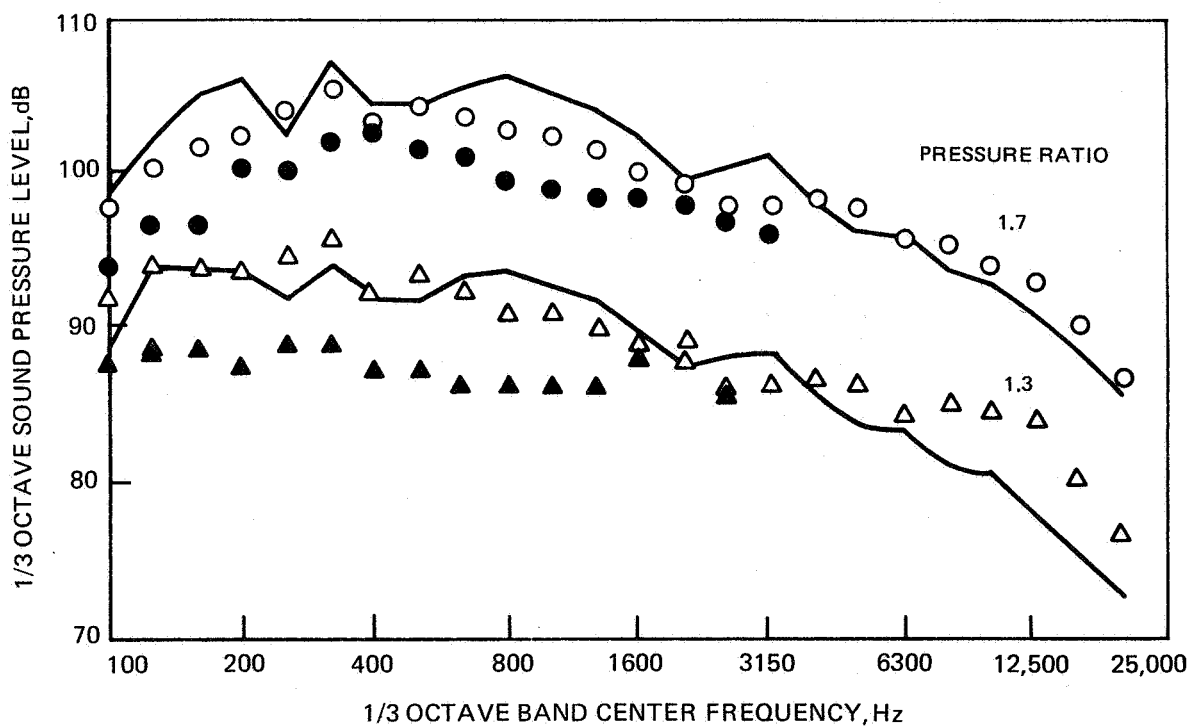


FIGURE 64 — MEASURED AND CALCULATED SPECTRA FOR LARGE MIXER NOZZLE AND UTW WING WITH 30°-60° FLAP DEFLECTION

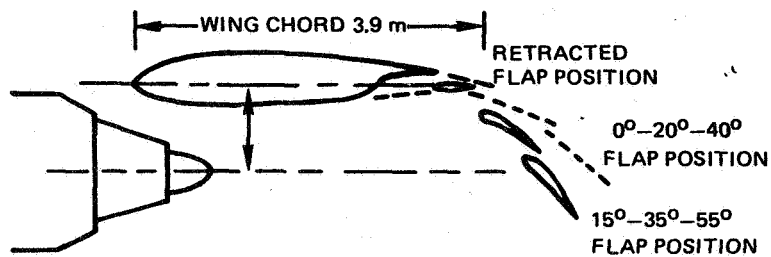


(a) OASPL DIRECTIVITY

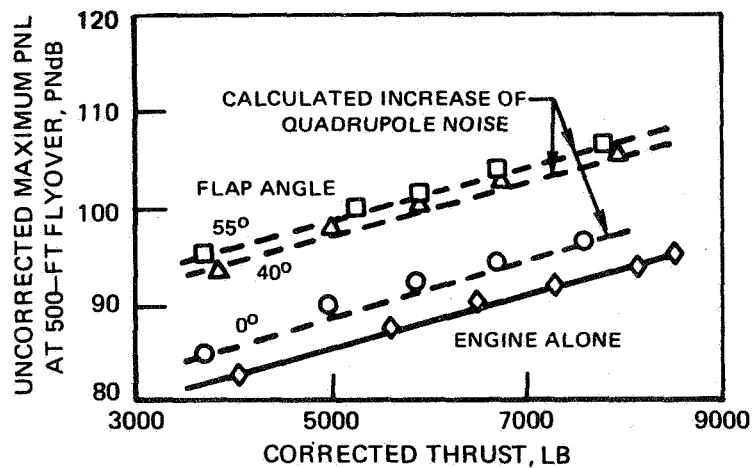


(b) SPECTRA AT 85° BENEATH WING

FIGURE 65 —COMPARISON OF ACOUSTIC DATA FOR LARGE MIXER NOZZLE AND UTW WING WITH 30°–60° FLAP DEFLECTION WITH DATA SCALED FROM SMALL MODEL



(a) SKETCH OF NOZZLE AND WING INSTALLATION



(b) VARIATION OF UNCORRECTED FLYOVER PNL WITH ENGINE THRUST

FIGURE 66 – ACOUSTIC COMPARISONS FOR FULL SCALE UTW INSTALLATION WITH NOISE-SUPPRESSED TF-34 ENGINE AND CO-ANNULAR NOZZLE

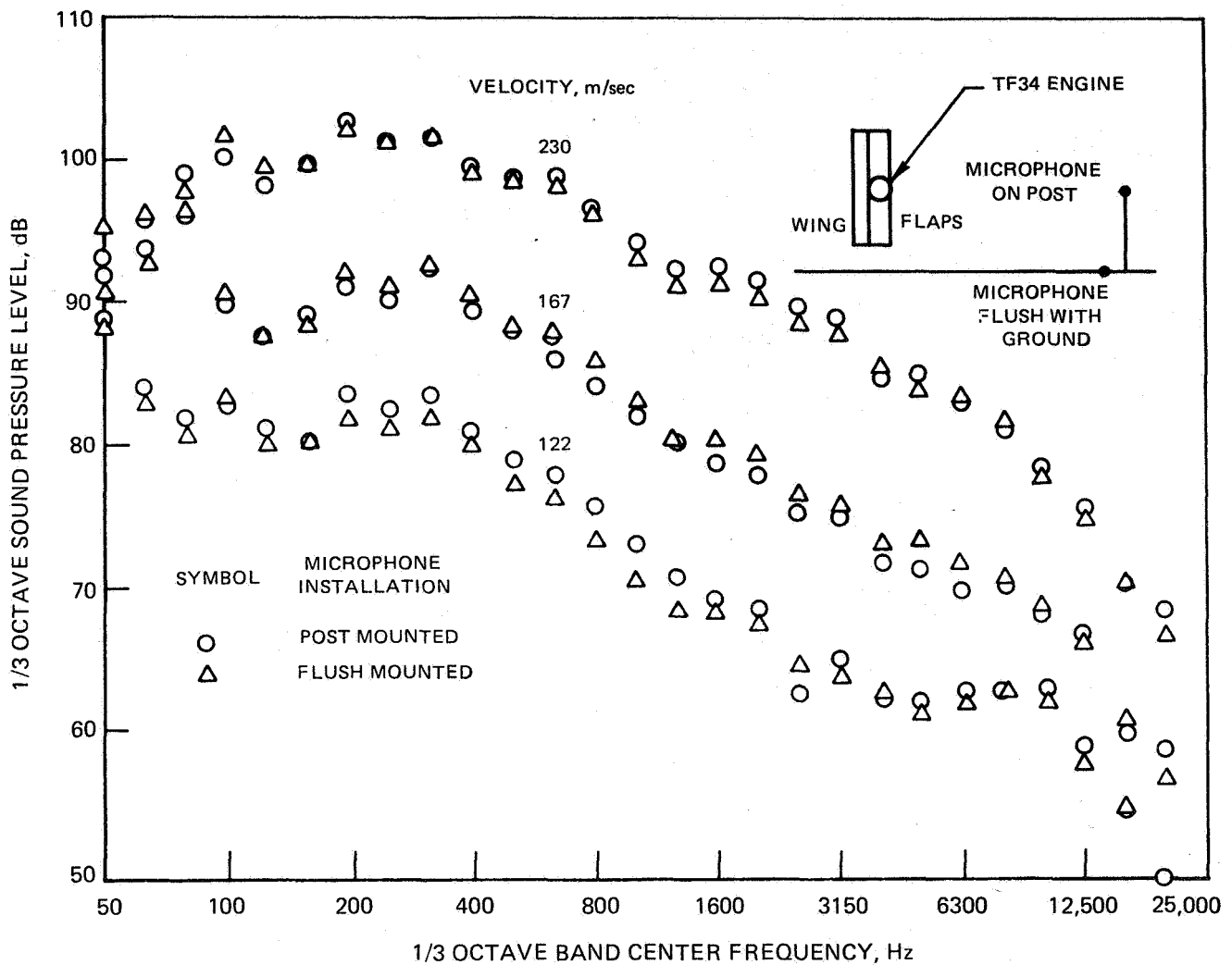


FIGURE 67 — CORRECTED SPECTRA IN FLYOVER PLANE AT 90° FROM NOZZLE CENTERLINE FOR TWO MICROPHONE INSTALLATIONS FOR TF-34 ENGINE AND THREE-FLAP UTW MODEL WITH 40° AFT FLAP DEFLECTION

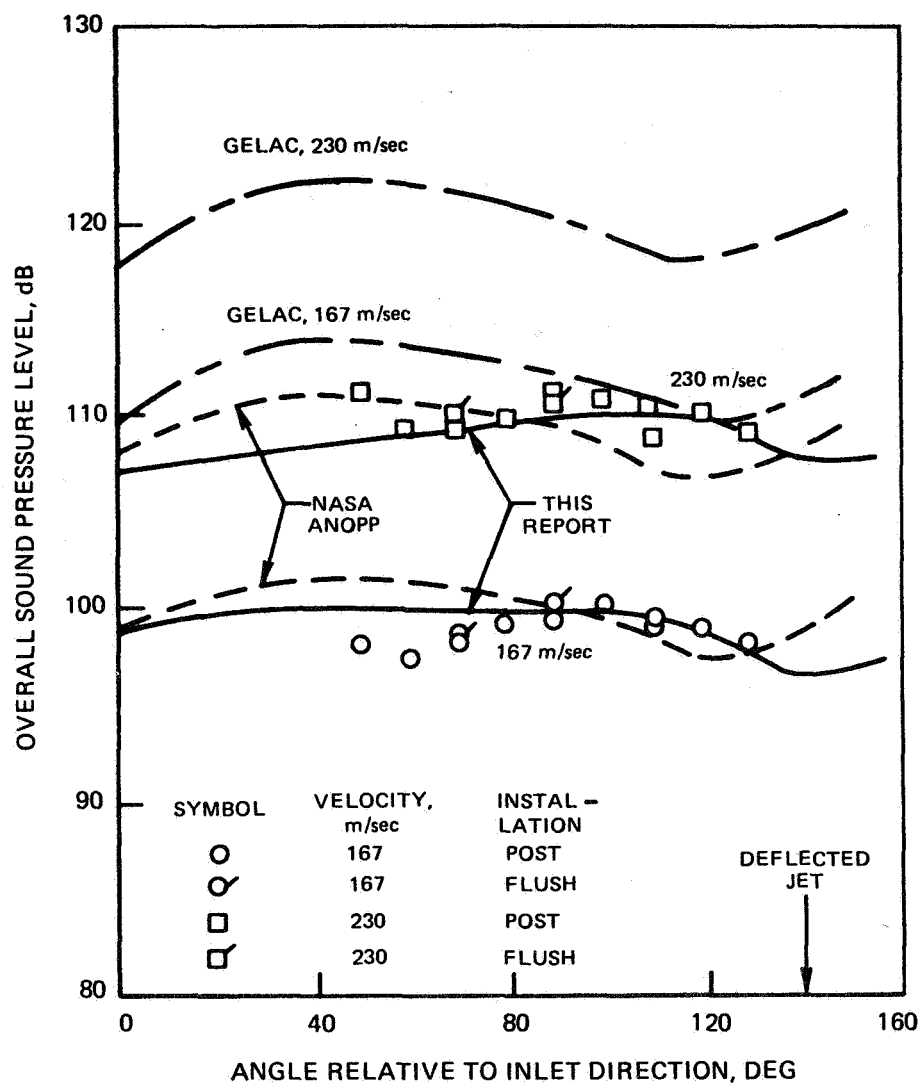


FIGURE 68 — COMPARISON OF MEASURED AND PREDICTED NOISE RADIATION PATTERNS IN FLYOVER PLANE FOR TF34 ENGINE AND THREE-FLAP UTW MODEL WITH 40° AFT FLAP DEFLECTION

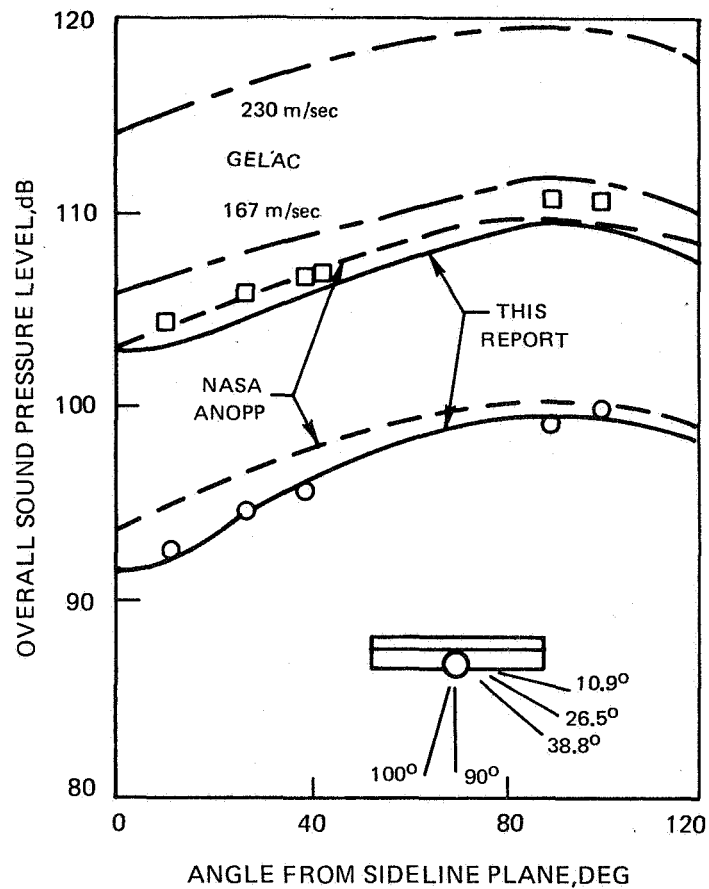


FIGURE 69 —COMPARISON OF MEASURED AND PREDICTED VARIATION OF OVERALL SOUND PRESSURE LEVEL WITH SIDELINE ANGLE IN 90° AZIMUTH PLANE FOR TF-34 ENGINE AND THREE-FLAP UTW MODEL WITH 40° AFT FLAP DEFLECTION

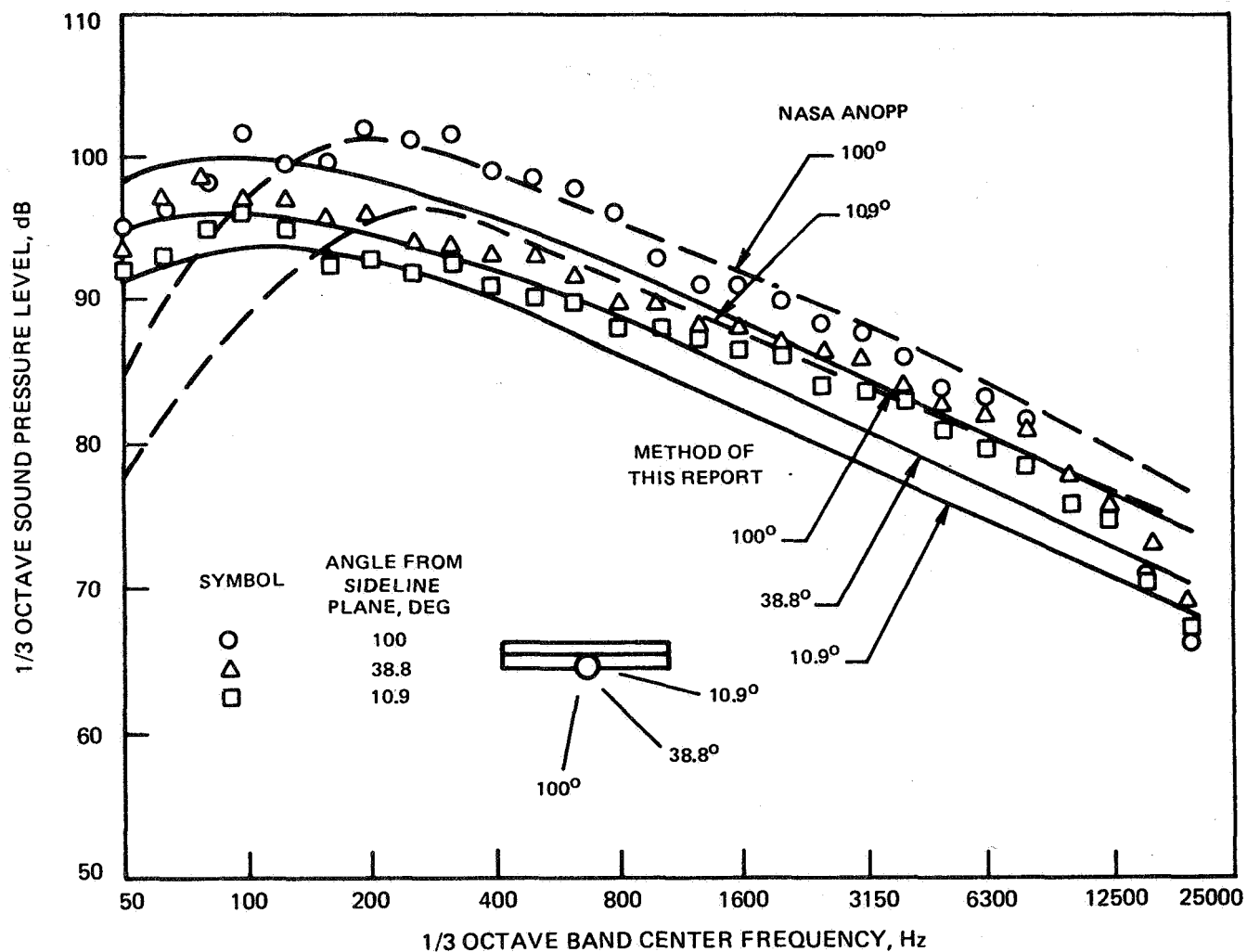


FIGURE 70 — EFFECT OF SIDELINE ANGLE ON SPECTRUM AT 90° AZIMUTH ANGLE TO TF-34 ENGINE AND THREE-FLAP UTW MODEL WITH 40° AFT FLAP DEFLECTION
(a) 122 m/sec EXHAUST VELOCITY

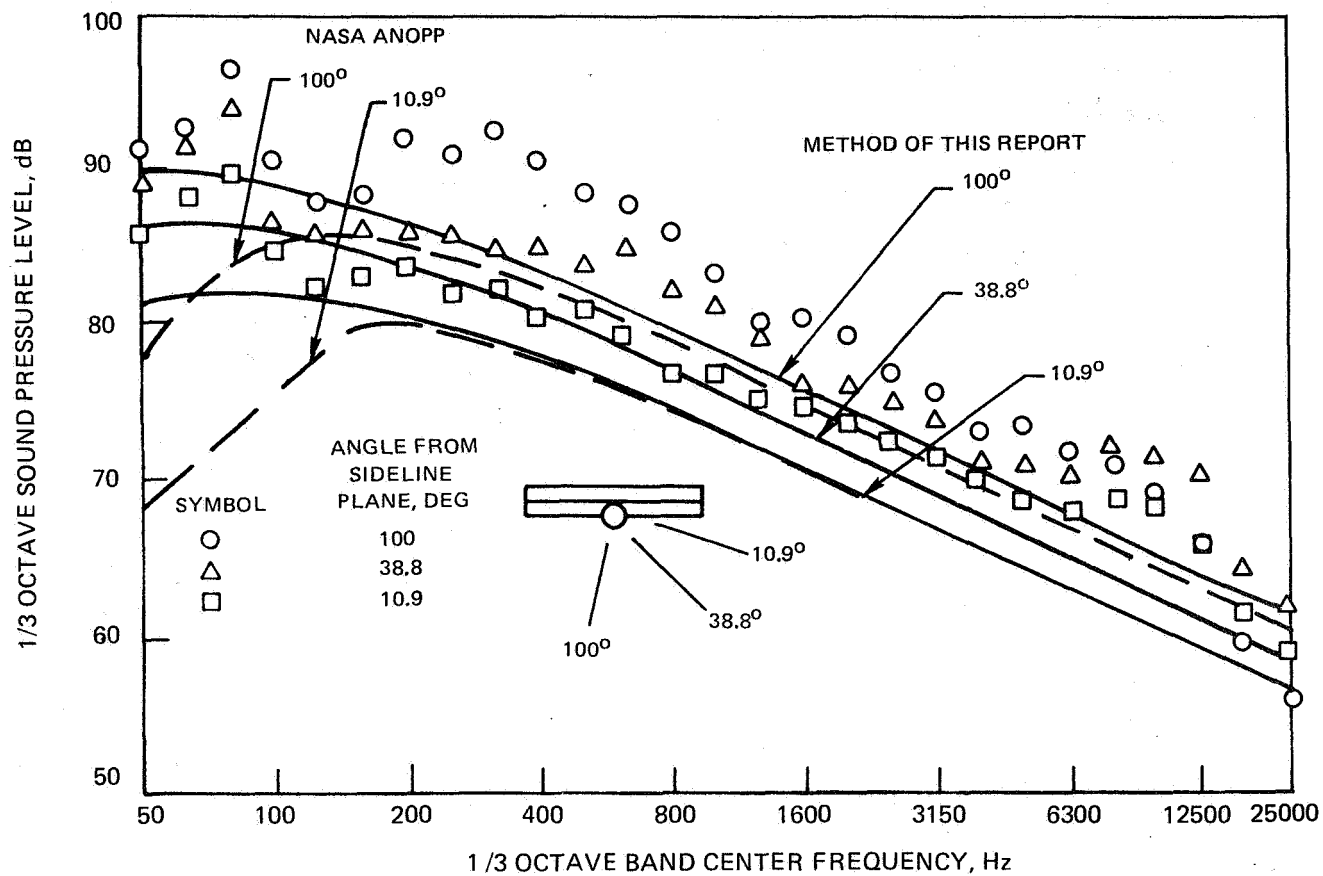


FIGURE 70 — CONTINUED (b) 167 m/sec EXHAUST VELOCITY

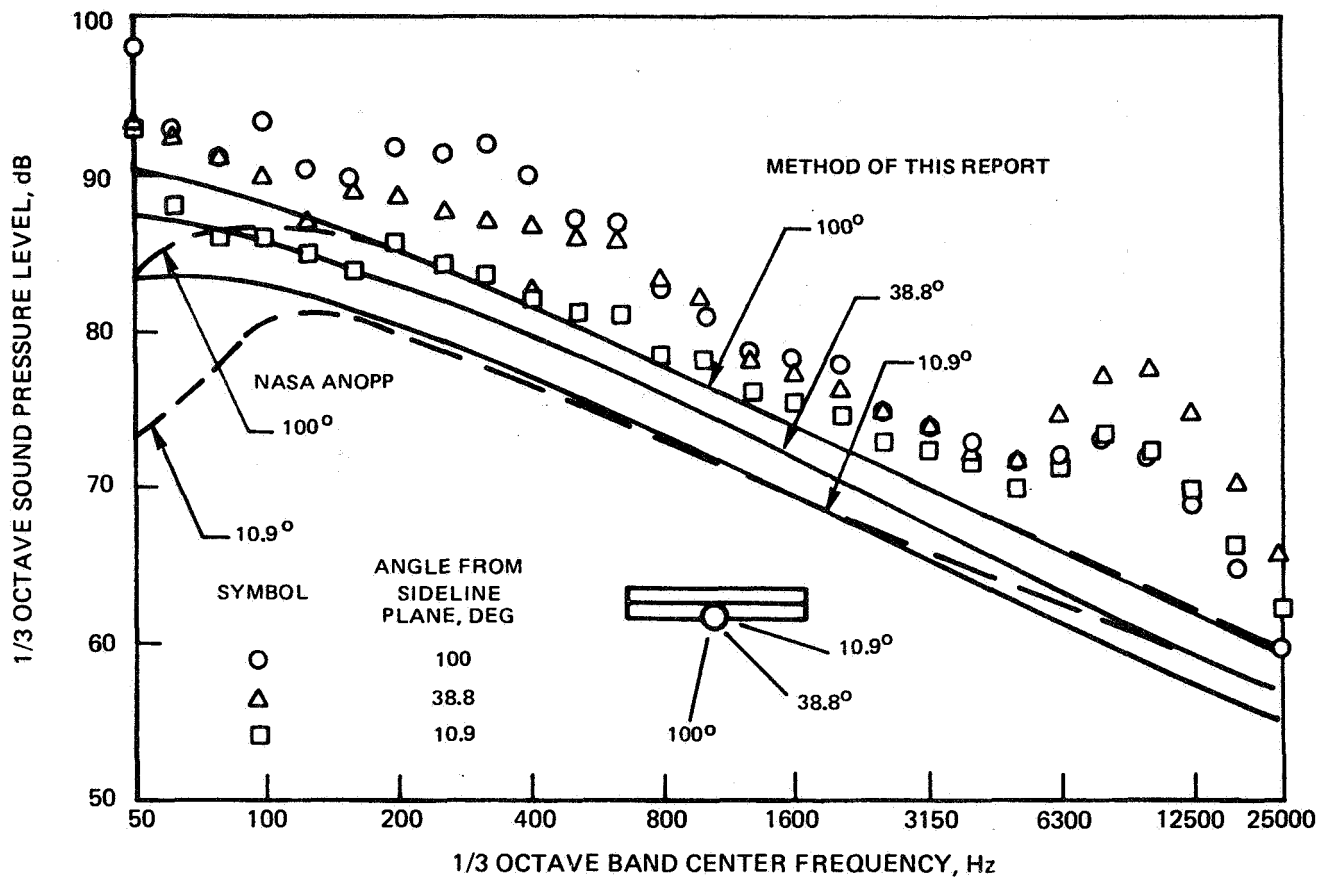
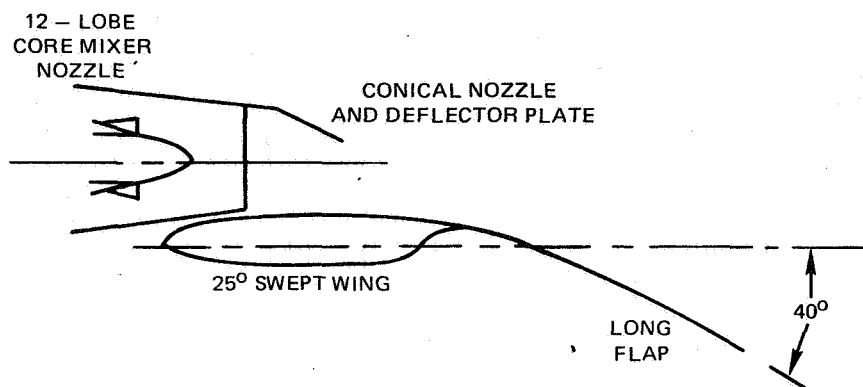
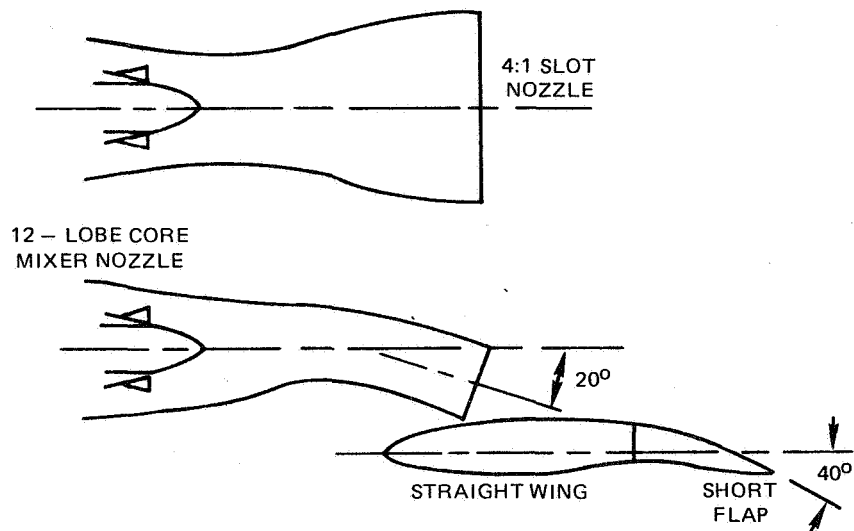


FIGURE 70 — CONCLUDED (c) 230 m/sec EXHAUST VELOCITY

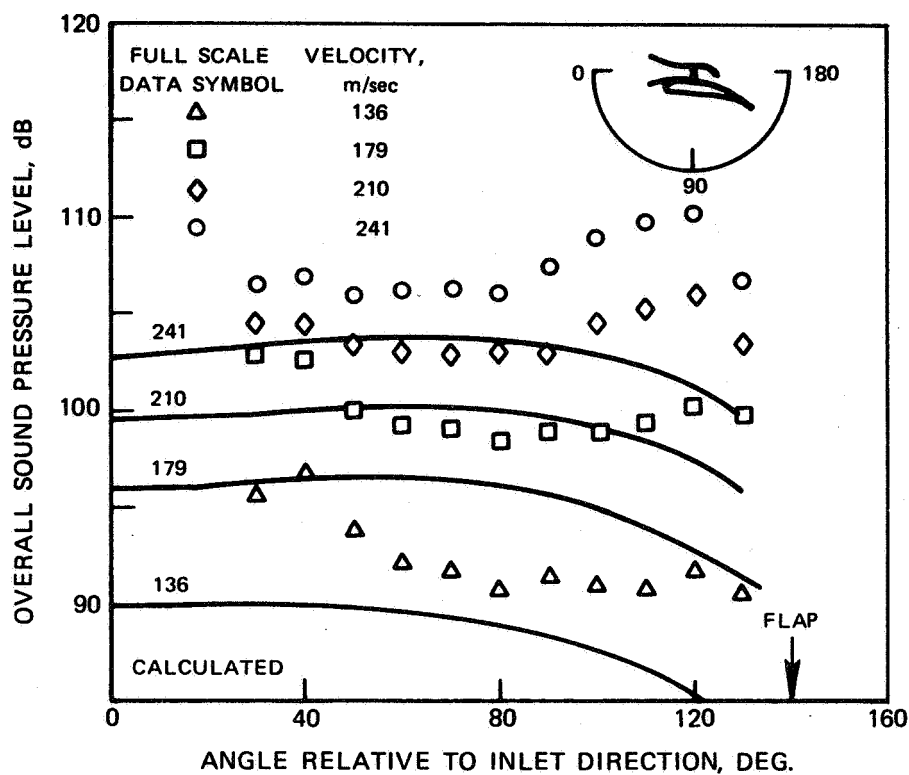


(a) CIRCULAR NOZZLE AND DEFLECTOR, LONG FLAP

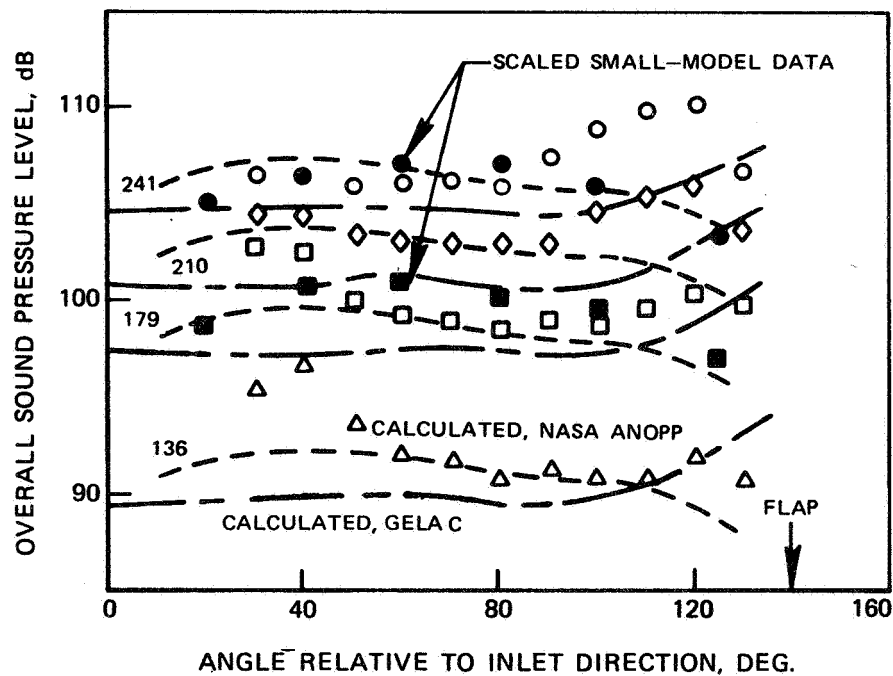


(b) CANTED 4:1 SLOT NOZZLE, SHORT FLAP

**FIGURE 71— FULL SCALE UPPER SURFACE BLOWING CONFIGURATIONS
WITH NOISE— SUPPRESSED TF-34 ENGINE**

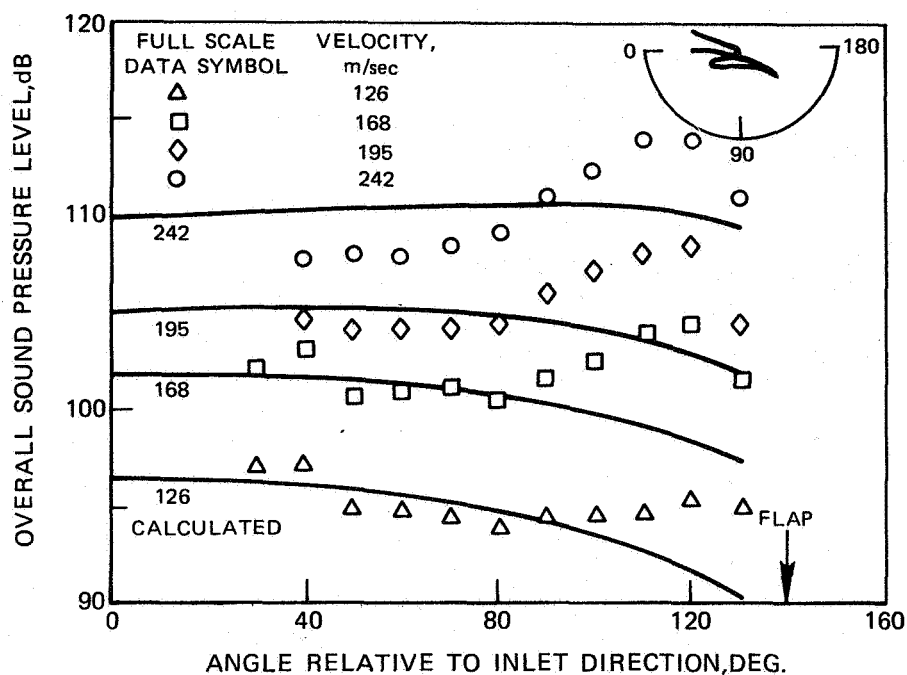


a) COMPARISON WITH METHOD OF THIS REPORT

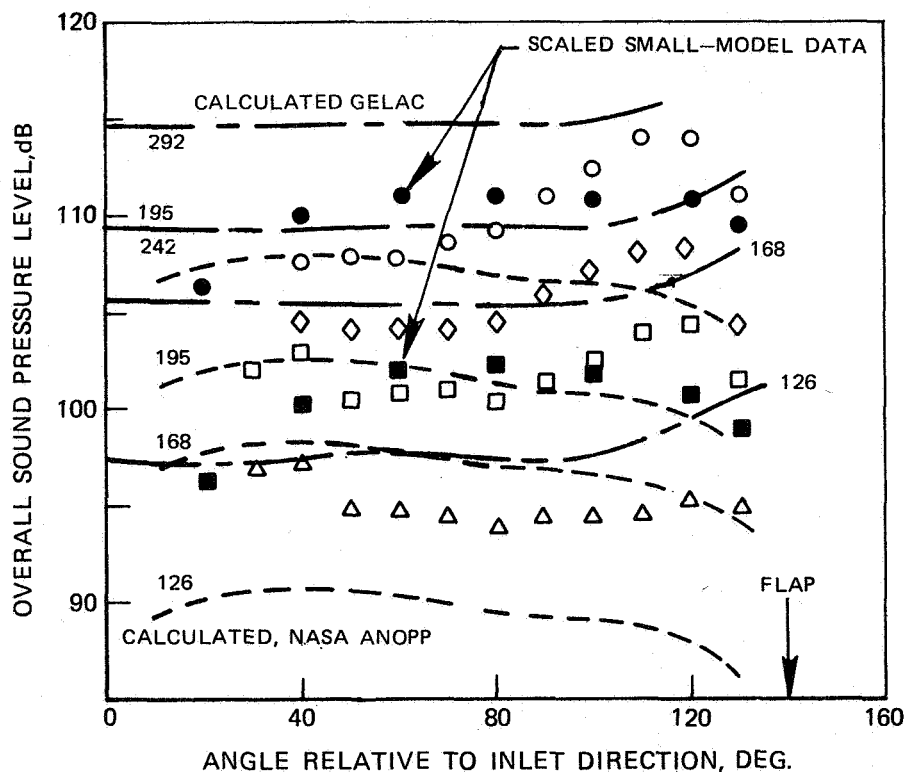


(b) TO COMPARISON WITH NASA ANOPP AND GELAC PREDICTIONS AND WITH SCALED SMALL-MODEL DATA

FIGURE 72 —COMPARISON OF MEASURED AND PREDICTED NOISE RADIATION PATTERNS FOR UPPER SURFACE BLOWING WITH TF-34 ENGINE, CIRCULAR NOZZLE AND DEFLECTOR, AND 40° DEFLECTION LONG FLAP

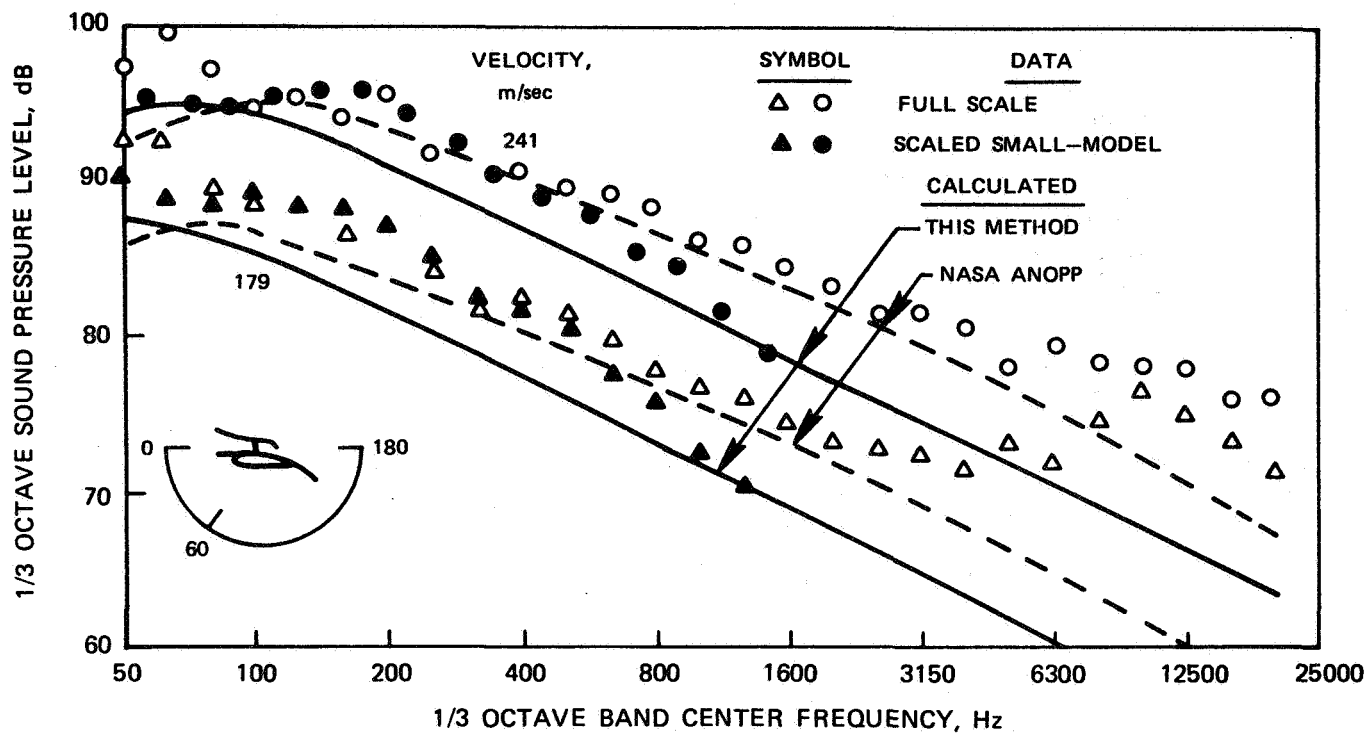


a) COMPARISON WITH METHOD OF THIS REPORT

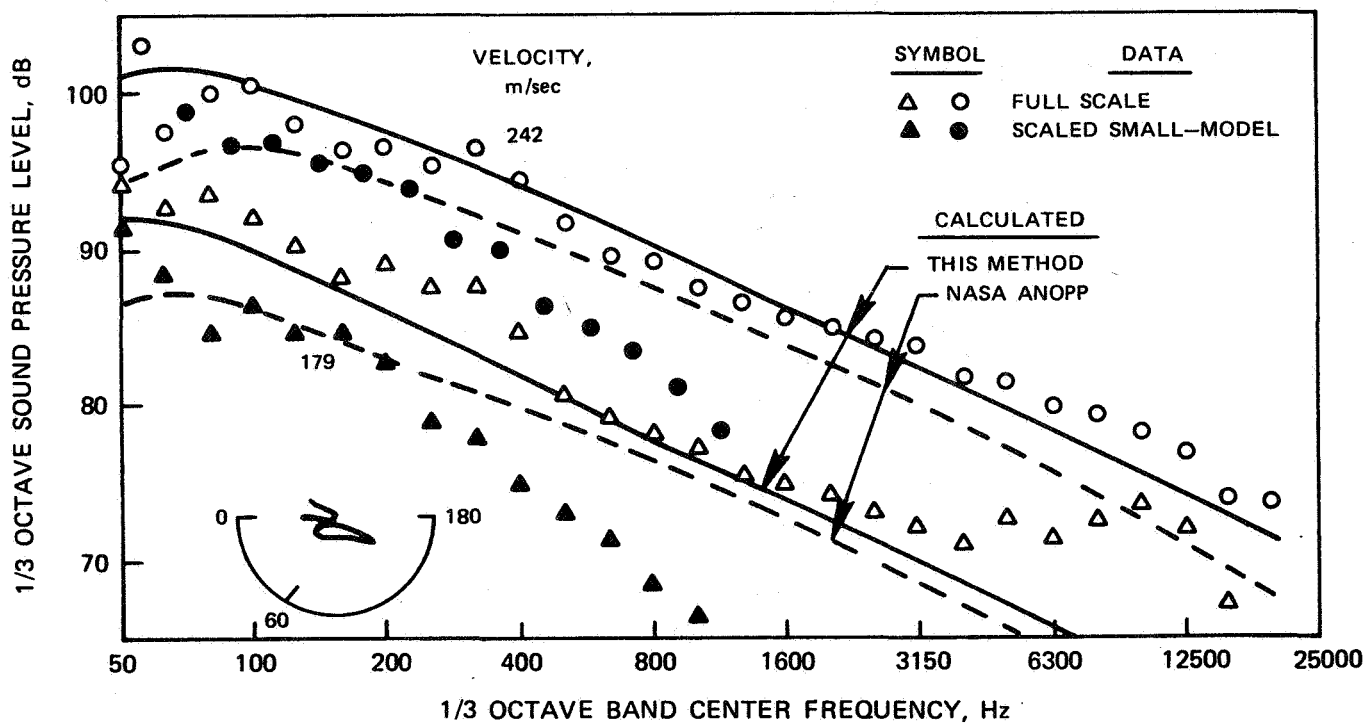


(b) TO COMPARISON WITH NASA ANOPP AND GELAC PREDICTIONS AND WITH SCALED SMALL-MODEL DATA

FIGURE 73—COMPARISON OF MEASURED AND PREDICTED NOISE RADIATION PATTERNS FOR UPPER SURFACE BLOWING WITH TF-34 ENGINE, CANTED 4:1 SLOT NOZZLE, AND 40° DEFLECTION SHORT FLAP

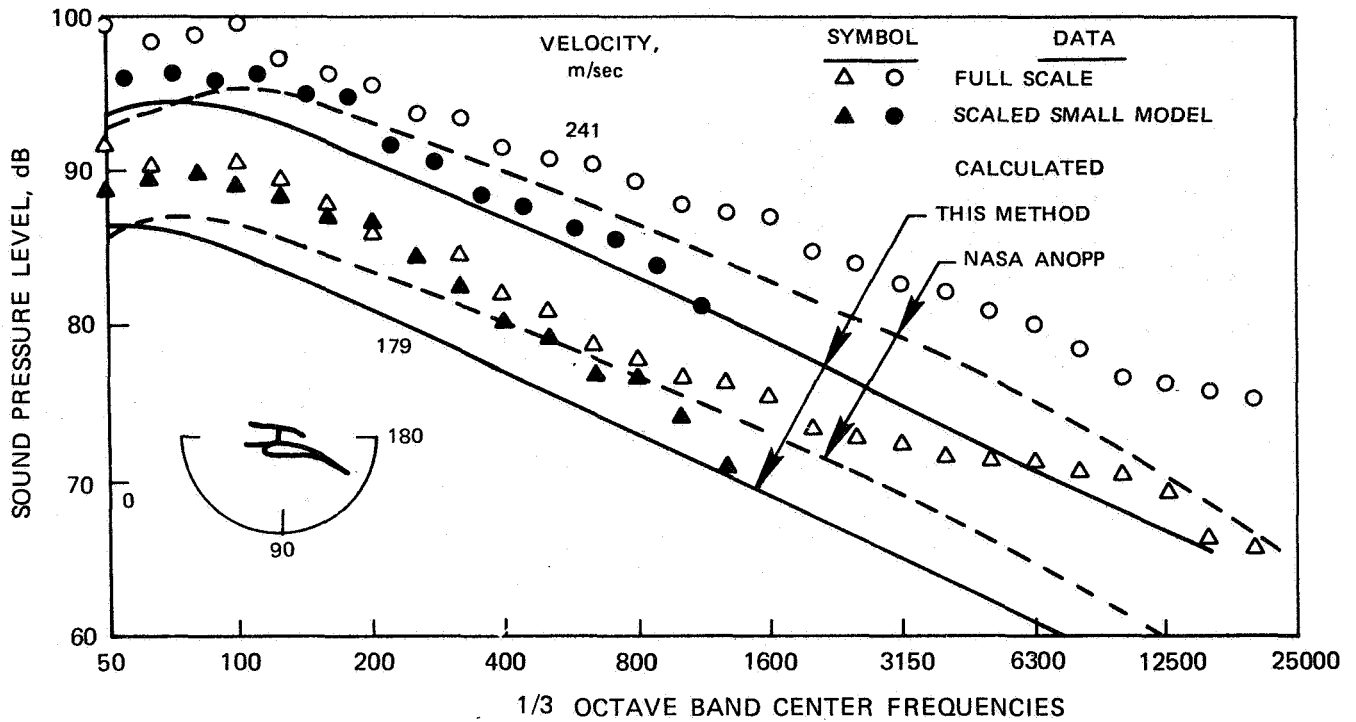


a) 60° FROM NOZZLE INLET, CIRCULAR NOZZLE WITH DEFLECTOR, LONG FLAP

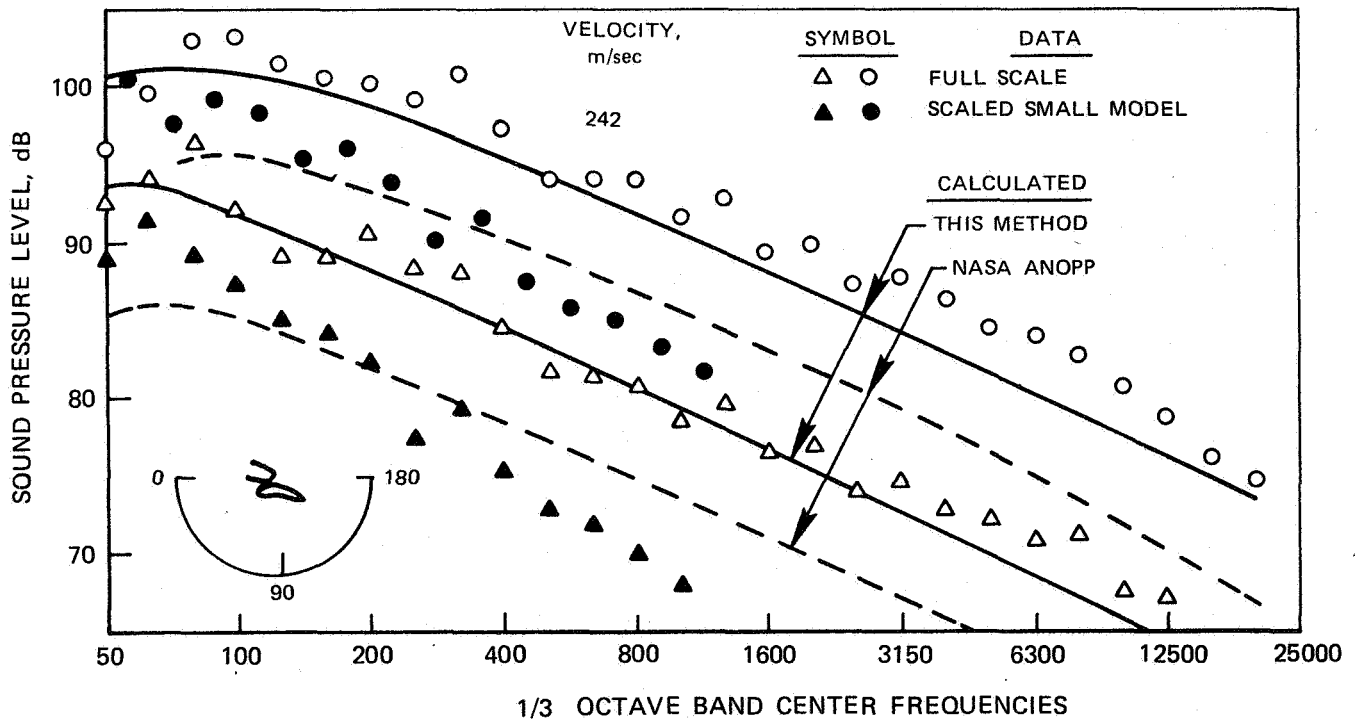


b) 60° FROM NOZZLE INLET, CANTED 4:1 SLOT NOZZLE, SHORT FLAP

FIGURE 74 —COMPARISON OF MEASURED AND PREDICTED SPECTRA FOR UPPER SURFACE BLOWING WITH TF-34 ENGINE AND 40° FLAP DEFLECTION

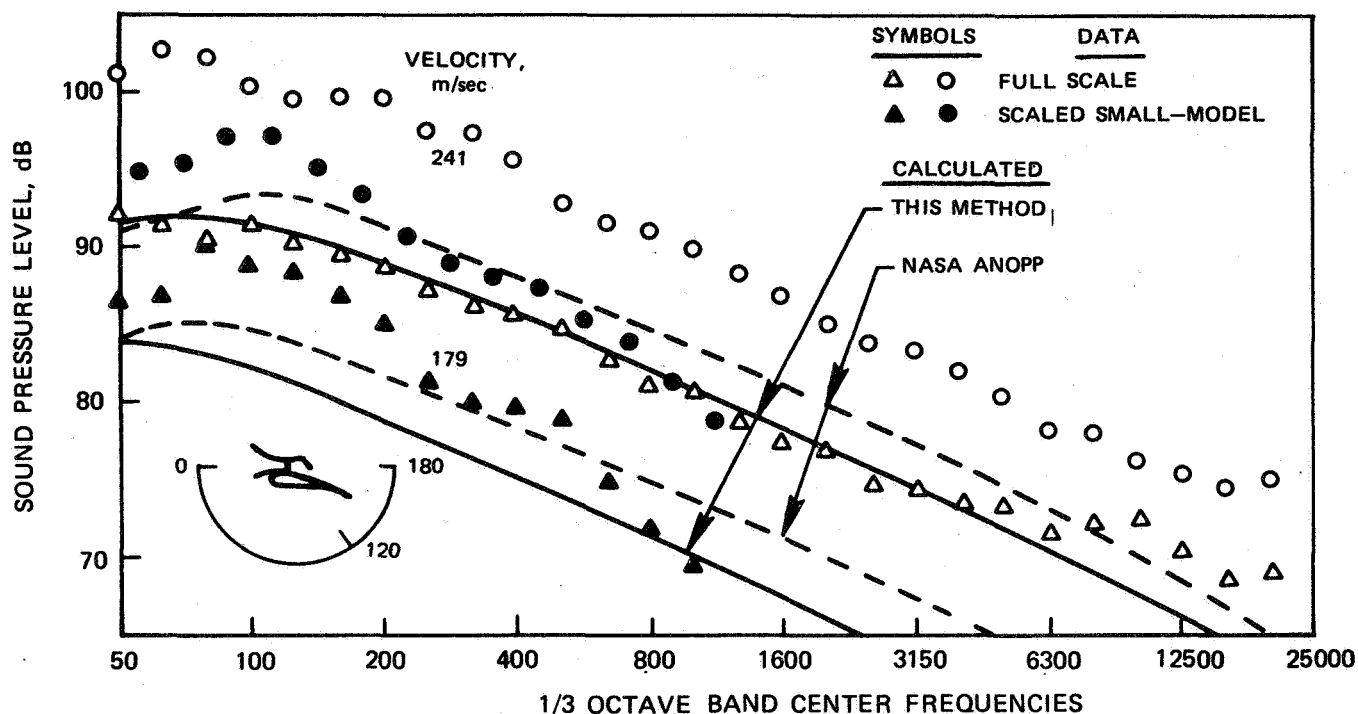


c) 90° FROM NOZZLE INLET, CIRCULAR NOZZLE WITH DEFLECTOR, LONG FLAP

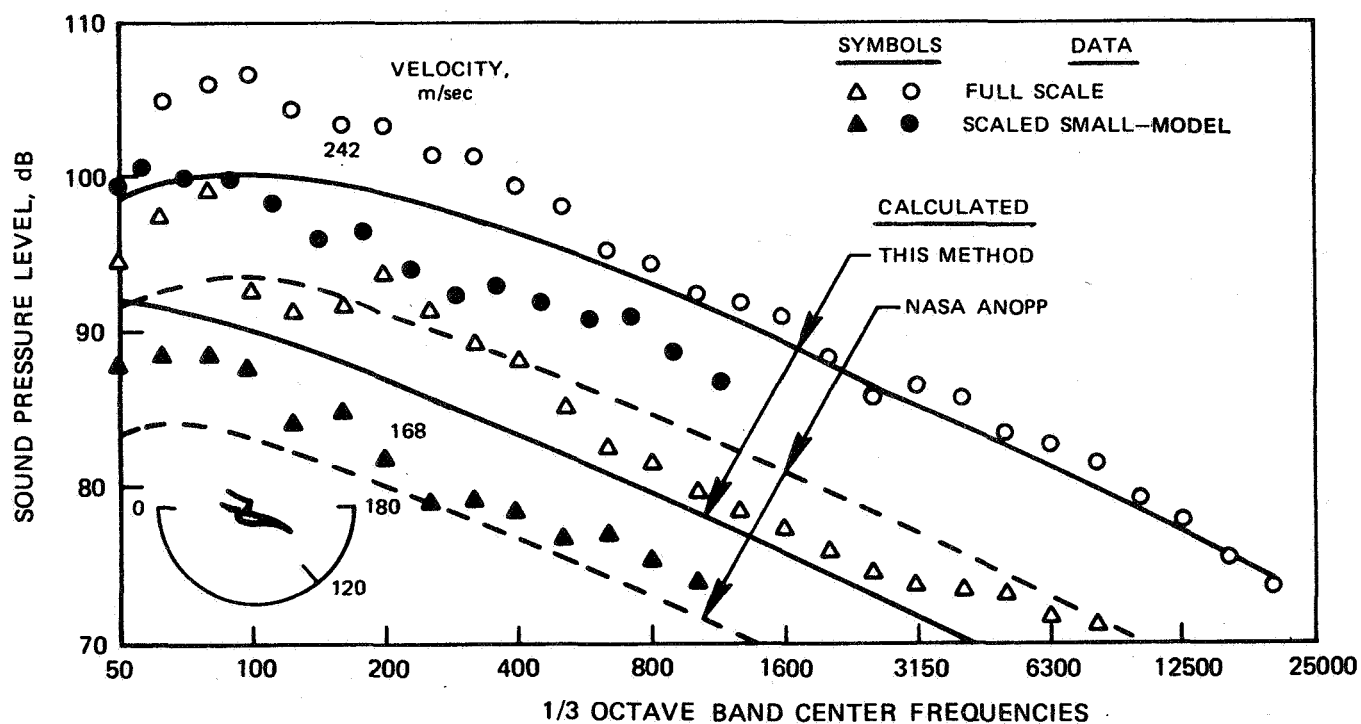


d) 90° FROM NOZZLE INLET, CANTED 4:1 SLOT NOZZLE, SHORT FLAP

FIGURE 74 - CONTINUED



e) 120° FROM NOZZLE INLET, CIRCULAR NOZZLE WITH DEFLECTOR, LONG FLAP



f) 120° FROM NOZZLE INLET, CANTED 4:1 SLOT NOZZLE, SHORT FLAP

FIGURE 74 – CONCLUDED.

1. Report No. NASA CR-135096	2. Government Accession No.	3. Recipient's Catalog No.	
4. Title and Subtitle Additional Studies of Externally Blown Flap Noise		5. Report Date August 1976	
		6. Performing Organization Code	
7. Author(s) Martin R. Fink		8. Performing Organization Report No.	
9. Performing Organization Name and Address United Technologies Research Center Silver Lane East Hartford, CT. 06108		10. Work Unit No.	
		11. Contract or Grant No. NAS3-17863	
12. Sponsoring Agency Name and Address National Aeronautics and Space Administration Washington, D.C. 20546		13. Type of Report and Period Covered Contract Report	
		14. Sponsoring Agency Code	
15. Supplementary Notes Project Manager, William A. Olsen, V/STOL and Noise Division, NASA Lewis Research Center, Cleveland, OH. 44135			
16. Abstract <p>Crosscorrelations were obtained among surface pressures on both sides of externally blown flap models and far-field acoustic pressures. Tests were conducted with both under-the-wing and upper-surface-blowing configurations. For both types of configurations at small deflection, the crosscorrelations showed that convection of jet exhaust turbulence to the trailing edge produces sound waves of opposite phase above and below the flap. For under-the-wing at larger flap deflection, dipole sound is generated by convection of turbulence past the forward part of the flap.</p> <p>Forward flight effects on externally blown flap noise were evaluated at ratios of wind tunnel velocity to exhaust jet velocity from 0 to 1/2 in increments of 1/8. Profiles of mean velocity and turbulence level were obtained along with surface pressure spectra and far-field acoustic spectra. The resulting predictions of forward speed effects on externally blown flap spectra and overall sound pressure levels agree with available data.</p> <p>Free-field directivity and spectra of large externally blown flap configurations were compared with predictions by the noise component method previously developed under this contract and with predictions by other methods. Good agreement was obtained with the noise component method for a mixer nozzle and two-flap under-the-wing configuration, a turbofan engine and three-flap under-the-wing configuration, and a turbofan engine with an upper-surface-blowing canted nozzle and short flap.</p>			
17. Key Words (Suggested by Author(s)) Acoustics; Aerodynamic noise, Externally blown flap noise, Aircraft noise.		18. Distribution Statement Unclassified - unlimited	
19. Security Classif. (of this report) Unclassified	20. Security Classif. (of this page) Unclassified	21. No. of Pages 170	22. Price* \$3.00

* For sale by the National Technical Information Service, Springfield, Virginia 22161